Study of B-H agostic interactions andc onsequence sfor hydrogen storage

Jingwen Zhu

To cite this version:

Jingwen Zhu. Study of B-H agostic interactions andc onsequence sfor hydrogen storage. Theoretical and/or physical chemistry. Sorbonne Université, 2018. English. NNT : 2018SORUS182 . tel-02452253

HAL Id: tel-02452253

https://theses.hal.science/tel-02452253

Submitted on 23 Jan 2020

HAL is a multi-disciplinary open access archive for the deposit and dissemination of scientific research documents, whether they are published or not. The documents may come from teaching and research institutions in France or abroad, or from public or private research centers.

L'archive ouverte pluridisciplinaire **HAL**, est destinée au dépôt et à la diffusion de documents scientifiques de niveau recherche, publiés ou non, émanant des établissements d'enseignement et de recherche français ou étrangers, des laboratoires publics ou privés.

Thèse de Doctorat de Sorbonne Université

Spécialité : Chimie Physique et Théorique

Ecole Doctorale de Chimie Physique et Chimie Analytique, Paris Centre (ED388)

Présentée par

Jingwen ZHU

Pour obtenir le grade de Docteur de Sorbonne Université

Study of B-H agostic interactions and consequences for hydrogen storage

Thèse soutenue le 12 septembre 2018

devant un jury composé de :

Mme Christine LEPETIT (DR)	LCC CNRS	Rapportrice
M. Laurent JOUBERT (Pr)	Université de Rouen	Rapporteur
M. Stéphane CARNIATO (Pr)	Sorbonne Université	Examinateur
Mme Corinne LACAZE-DUFAURE (Pr)	Université de Toulouse / CIRIMAT	Examinatrice
M. Christophe MORELL (Pr)	Université Claude Bernard Lyon 1	Examinateur
M. Esmaïl ALIKHANI (Pr)	Sorbonne Université	Directeur de thèse
Mme Emilie-Laure ZINS (MCF-HDR)	Sorbonne Université	Co-encadrante

Acknowledgments

Firstly, I would like to thank Prof. Christophe PETIT, director of laboratory MONARIS (de la Molécule aux Nano-objets : Réactivité, Interactions et Spectroscopies), to have housed me during these three years and to have provided me with optimal conditions for this thesis. Therefore, I consider myself as a very lucky individual as I was provided with an opportunity to be a part of MONARIS. I am also grateful for having a chance to meet so many wonderful people who led me though this three years' period. (Properly speaking five years ☺)

Bearing in mind previous I am using this opportunity to express my deepest gratitude and special thanks Professor Esmaïl ALIKHANI, supervisor of my thesis, who in spite of being extraordinarily busy with his duties, took time out to hear, guide and keep me on the correct path and allowing me to carry out my project at the esteemed organization and extending during this thesis.

I express my deepest thanks to Doctor Emilie-Laure ZINS, co-advisor of my thesis, for taking part in useful decision and giving necessary advises and guidance for me.

I would like to thank all the members of my PhD committee, M. Stephane CARNIATO, Mme Corinne DUFAURE-LACAZE, M. Christophe MORELL and especially my two referees Mme Christine LEPETIT and M. Laurent JOUBERT for accepting to review my work and to attend my defense.

A big thanks also to Doctor Bruno MADEBENE, tutor of my Master's internships, for his useful advice and guidance.

It is my radiant sentiment to place on record my best regards, deepest sense of gratitude to all the colleagues of Laboratory MONARIS and my dear friends for their kindness and precious guidance and helps.

I perceive as this opportunity as a big milestone in my career development. I will strive to use gained skills and knowledge in the best possible way, and I will continue to work on their improvement. Hope to continue cooperation with all of you in the future.

At the end, I would like to also express my particular gratitude to my cat for having been always with me for more than six years.

Contents

General Introduction **9**

I Energetic Transition: A Brief Panorama **11**

1 Hydrogen economy for transportation **13**

1.1 Search for a clean energy carrier 13
1.2 Sources of molecular hydrogen 14
  1.2.1 Hydrogen production from reforming methods 14
  1.2.2 Hydrogen production from renewable sources 15
1.3 Hydrogen storage 16
  1.3.1 Physical storage: Gaseous and liquid storage 18
  1.3.2 Material-based hydrogen storage 18

2 Catalyzed dehydrogenation/dehydrocoupling of ammonia borane and amine-borane adducts **23**

2.1 Ammonia borane and other related amine-boranes 23
  2.1.1 Structure and properties of ammonia borane 23
  2.1.2 Syntheses 24
2.2 Dehydrogenation reactions of amine-boranes 26
2.3 Transition metal-catalyzed dehydrogenations 28
  2.3.1 Early transition metals 28
  2.3.2 Mid-transition metals 31
  2.3.3 Late transition metals 33

II Computational and Theoretical Background **35**

3 Theoretical models for electronic structure **37**

3.1 The Hartree-Fock Approximation 38
  3.1.1 The Hartree-Fock Equations 38
  3.1.2 HF-limit 39
3.2 Density Functional Theory (DFT) 40
  3.2.1 Hohenberg-Kohn Theorems 41

3.2.2 Kohn-Sham Equation: KS-DFT . . . 41
3.2.3 Approximation of Exchange-Correlation Functionals . . . 42
3.3 Inclusion of dispersion in DFT methods . . . 44
3.3.1 Grimme's dispersion correction: DFT-GD . . . 45
3.3.2 APF-D method . . . 45

4 Wave function analysis in the real molecular space 49
4.1 QTAIM (Quantum Theory of Atoms in Molecules) . . . 49
4.1.1 The topology of electron density . . . 49
4.1.2 Zero-flux surface and bond paths . . . 51
4.1.3 Properties of bond critical point (BCP) . . . 51
4.1.4 Atomic properties . . . 54
4.2 ELF (Electron Localization Function) . . . 55
4.2.1 Definition of Electron Localization Function . . . 55
4.2.2 Topological analysis of Electron Localization Function . . . 56
4.2.3 Combined QTAIM and ELF analysis . . . 57
4.3 NBO (Natural Bond Orbital) . . . 58
4.3.1 Perturbation theory energy analysis . . . 59

III Theoretical Assessment of Amine-borane Dehydrogenation Process 61

5 Earlier experimental and theoretical studies of the reaction pathway: inconsistency proposals 63
5.1 Experimental observations . . . 64
5.2 Kinetic and mechanistic studies . . . 66
5.3 A two-cycle model . . . 67
5.4 DFT investigations in the literature . . . 68
5.5 Mechanism still remains uncertain since more than 10 years . . . 71

6 Characterization of M-H-B interactions involved in catalyzed dehydrogenation of amine-boranes 73
6.1 Characterization of agostic interactions . . . 74
6.1.1 History and definition . . . 74
6.1.2 Experimental characterization of C-H agostic interactions . . . 75
6.1.3 Topological descriptions of agostic interactions . . . 75
6.2 Benchmark studies . . . 78
6.2.1 Influence of exchange-correlation functionals . . . 79
6.2.2 Influence of the basis set . . . 85
6.3 Characterization of intramolecular M-H-B interactions . . . 90
6.4 Characterization of intermolecular M-H-B interactions . . . 92
6.4.1 Geometric considerations . . . 94
6.4.2 Topological considerations . . . 98

6.4.3 Energetic considerations . . . 104
6.4.4 Orbital approaches . . . 105

7 Mechanistic investigation of the titanocene-catalyzed dehydrogenation of amine-boranes 109
7.1 Look for a suitable level of theory . . . 110
7.1.1 Influence of the Grimme-D3(BJ) dispersion correction . . . 110
7.1.2 Influence of DFT functionals . . . 114
7.2 Mechanistic investigations . . . 116
7.2.1 Dehydrogenation/dehydrocoupling reactions of $HMe_2N{\cdot}BH_3$(DMAB) . . . 117
7.2.2 Titanocene-catalyzed dehydrogenation reaction of other amine borane adducts 134

IV Epilogue: General Conclusion and Some Prospect 141

General Conclusion 143

Some Prospect 145

Bibliography 147

Scientific production 169

General Introduction

Since the beginning of the 21st century, the increasing demand of clean energy carriers for industrial activities has been a major challenge: natural fossil fuel resources are limited and their use leads to the emission of greenhouse gases. A major shift towards the use of renewable and non-polluting energy sources is necessary. The dihydrogen molecule has several advantages: a high energy capacity, non-polluting nature, non-toxic and non-polluting combustion products (water). It is considered as an ideal energy carrier in the transport sector and electricity generation. The two main difficulties that limit its use concern its generation and its storage.

Ammonia borane ($H_3N{\cdot}BH_3$) and its related amine-borane compounds have emerged as attractive candidates for potential hydrogen storage vectors because of their relatively high weight percentage of available hydrogen (19.6% for ammonia borane) as well as the potential reversibility for the hydrogen release reactions. Actual applications would benefit from controlled reactions occurring close to room-temperature. In this context, mechanistic studies for the catalyzed dehydrogenation/dehydrocoupling of amine-boranes and phosphine-boranes have seen a quick development over the last decade. Inexpensive, environmentally friendly, easily synthesized and stable organometallic compounds that efficiently catalyze the reaction are worth studying.

This thesis mainly concentrates on the Group-IV metallocenes (Cp_2M, M = Ti, Zr and Hf) catalyzed dehydrogenation of amine-boranes. The investigation of the dehydrocoupling of $HMe_2N{\cdot}BH_3$ to form $[Me_2N{\cdot}BH_2]_2$ catalyzed by titanocene (Cp_2Ti) both experimentally and theoretically was already reported in the literature. However, despite extensive investigations, the exact mechanism of this reaction still remains uncertain at a molecular level.

The objective of this thesis is to investigate the dehydrogenation mechanism of amine-boranes at molecular level, following by the identification and characterization of intermolecular/intramolecular interactions involved in the intermediates among the reaction pathways. Theoretical studies based on DFT calculation and topological tools QTAIM (Quantum Theory of Atoms in Molecules) and ELF (Electron Localization Function), as well as the identification of donor-acceptor interaction with NBO (Natural Bond Orbital) are presented.

Part I

Energetic Transition: A Brief Panorama

Chapter 1

Hydrogen economy for transportation

1.1 Search for a clean energy carrier

Since the beginning of the 21st century, the growth of energy requirement for industrial activities results in problems demanding prompt solution for society. Natural fossil fuel resources are the main source of energy used to date. However, these resources are limited and their use leads to the emission of greenhouse gases causing climate change, as well as other environmental issues. In Figure 1.1 is shown the average annual temperature difference compared to the average temperature in the 1961-1990 period as baseline. It is clearly demonstrated that over the last few decades, temperature has risen sharply at the global level to approximately 0.8 °C higher than the 1961-1990 baseline. Glaciers are melting, sea levels are rising and forests are dying. It is clear that humans have caused most of the past century's warming by releasing greenhouse gases as we power our modern lives whose level is higher now than in the last 650,000 years.

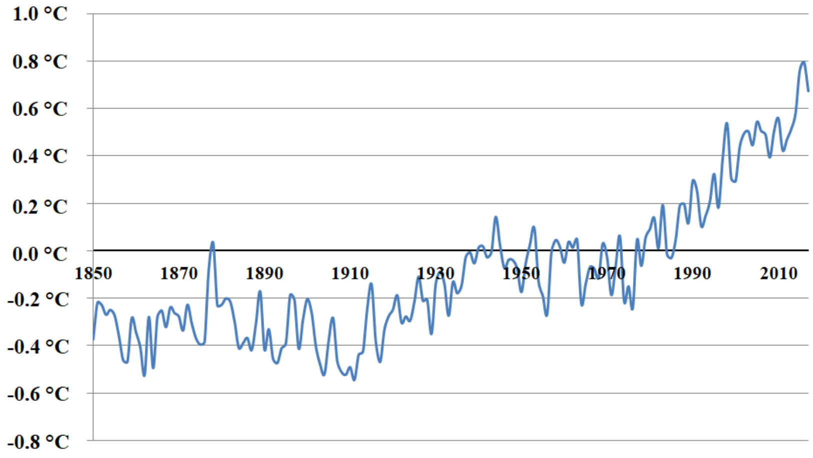

Figure 1.1: Average annual temperature difference trend through time with the average temperature during 1961-1990 period as baseline. [1]

What will we do to slow down this warming? How will we deal with the changes we've already set into motion?

Hydrogen is an ideal candidate as an energy carrier for future applications for industries and vehicles. It can be used to store and to transport energy from renewable resources such as electricity. Unlike fossil energy sources, combustion products obtained from dihydrogen are non-toxic and environmentally friendly. At present, the major challenge in utilization of hydrogen gas as a fuel is its unavailability in nature and the need for inexpensive production methods as well as the high capacity of hydrogen storage techniques. Researches on inexpensive and environmentally friendly production methods and the efficient, safe and stable hydrogen storage and transport techniques have become a key topic and the most important technical obstacles to the application of hydrogen energy.

1.2 Sources of molecular hydrogen

As a result of large demands for molecular hydrogen in industry, wide variety of processes have been developed for producing hydrogen which includes two main categories. The first category is based on the technology named conversional which converts fossil fuels using mainly hydrocarbon reforming as well as pyrolysis methods. In hydrocarbon reforming process, the participating chemical techniques are steam reforming, partial oxidation and auto-thermal steam reforming. The second category includes methods which produce H_2 from renewable resources, either from electrolysis of water or biomass process. Up to now, molecular hydrogen generation from fossil fuels (8% from natural gas, 30% from heavy oils and naphtha, and 18% from coal) is still the dominant way [2] and less often from renewable resources. [2–4]

1.2.1 Hydrogen production from reforming methods

Steam reforming method

Steam reforming of natural gas [5] is the most common method of producing H_2 with a high temperature steam (700 °C - 1000 °C). The steam reforming of methane (the main constituent of natural gas), is the most used and developed method for large-scale hydrogen production, with conversion efficiency between 74-85%.

Partial oxidation method

The partial oxidation process also generates hydrogen by reaction of methane and other hydrocarbons with limited quantity of oxygen in a less than stoichiometric ratio. The reaction temperature is about 950 °C for natural fossil fuels from methane to naphtha for the catalytic process. In the case of the non-catalytic process using heavy oil and coal, the temperature increase up to 1300-1500 °C. [6]

Auto-thermal reforming method

The auto-thermal reforming method adds steam to the catalytic partial oxidation process. This method employs the exothermic partial oxidation process to provide heat and the endothermic steam reforming process to increase the productive rate of H_2. The thermal efficiency is 60-75 % under the optimum temperature at about 700 °C. [7]

These methods presented above are efficient, well established and have required huge industrial demands for H_2, especially with the steam reforming technology. In Table 1.1 is shown the comparison of different hydrocarbon reforming methods with their corresponding general reactions, following by the water-gas shift process.

Table 1.1: Comparison of different hydrocarbon reforming methods.

Methods	General reaction	Advantages	Disadvantages
Steam reforming	$C_mH_n + mH_2O \longrightarrow mCO + (m + \frac{1}{2}n)H_2$	Oxygen not required Highest H_2/CO ratio	Highest air emissions Most commercial experience
Partial oxidation	$C_mH_n + \frac{1}{2}mO_2 \longrightarrow mCO + \frac{1}{2}H_2$	Non-catalytic reaction possible	Lowest H_2/CO ratio Highest temperature
Auto-thermal reforming	$C_mH_n + \frac{1}{2}mH_2O + \frac{1}{4}mO_2 \longrightarrow mCO + (\frac{1}{2}m + \frac{1}{2}n)H_2$	Lower temperature	Less commerial experience

At the same time, these hydrogen production methods release carbon dioxide and other pollutants. Meanwhile, a great number of energy should be furnished to supply a high reaction temperature. Other hydrogen production methods are therefore required to be carried out for the sustainable development requirement.

1.2.2 Hydrogen production from renewable sources

Electrolysis of water

Being a huge resource in Earth, electrolysis of water is also considered as a potential source of H_2. The splitting of water into H_2 and O_2 by electricity is a more environmentally friendly process if the electricity used for splitting the water comes from renewable energy sources, such as solar energy, wind energy, hydropower, biomass energy and other renewable sources. The typical electrolysis unit consists of an anode where oxygen is produced and a cathode which produces hydrogen *via* the following reaction:

$$H_2O \longrightarrow H_2 + \frac{1}{2}O_2 \tag{1.1}$$

Generally, there are three different water electrolysis methods used today and the main characters of these electrolysis systems are summarized in Table 1.2: [8]

Electrolysis is a promising option for hydrogen production from renewable resources. However, the water electrolysis is much less popular in H_2 generation industry, only a very small percentage (3%) of the world's hydrogen is produced by electrolysis. Because of the high cost for

Table 1.2: Characters of different water electrolysis methods. [8]

Method	**Temperature range**	**Cathodic reaction**	**Charge carrier**	**Anodic reaction**
AEC (Alkaline Electrolysis Cells) [9,10]	40 - 90 °C	$2\,H_2O + 2\,e^- \longrightarrow H_2 + 2\,OH^-$	OH^-	$2\,OH^- \longrightarrow \frac{1}{2}O_2 + H_2O + 2\,e^-$
PEMEC (Proton Exchange Membrane Electrolysis Cells) [10,11]	20 - 100 °C	$2\,H^+ + 2\,e^- \longrightarrow H_2$	H^+	$H_2O \longrightarrow \frac{1}{2}O_2 + 2\,H^+ + 2\,e^-$
SOEC (Solid Oxide Electrolysis Cells) [12,13]	700 - 1000 °C	$H_2O + 2\,e^- \longrightarrow H_2 + O^{2-}$	O^{2-}	$O^{2-} \longrightarrow \frac{1}{2}O_2 + 2\,e^-$

the current water electrolysis method, especially for the heavy-metal-contained electrodes for a large scale application, this technique still faces challenges in development with some optimization of electrodes and ions exchange membranes.

Hydrogen production from biomass

Biomass has been considered as a source of heat and energy since the beginning of recorded history but it is still widely employed all over the world at present. Various biomass sources, including agricultural or forest residues and wastes, industrial and municipal wastes, can be widely used to convert into diverse energies. There are two main categories of technologies for biomass-hydrogen conversion: [14] the **thermochemical process [15]** and the **biological process**. Hydrogen production through biomass provides a promising area for bio-energy generation due to its clean, recyclable and high efficient nature. But the existing methods are not commercially competitive because the rate of hydrogen production is still limited.

Table 1.3 summarizes various technologies for hydrogen production with different feed stock, efficiency, cost and their maturities. For the long-term environmental sustainability, seeking new technologies for reducing the costs to produce hydrogen with renewable and environmentally friendly resources as well as for enhancing the efficiency of hydrogen production methods has become the promising future.

1.3 Hydrogen storage

With a standard atomic weight of 1.008, hydrogen is the lightest element on the periodic table and the most abundant element in the universe. The density of the molecular hydrogen H_2

Table 1.3: Summary of hydrogen production technologies [4]

Technologies	Feed-stock	Efficiency	Cost ($US per kg of hydrogen)	Maturity
Steam reforming	Hydrocarbons	70-85%	1.03	Commercial
Auto-thermal reforming	Hydrocarbons	60-75%	/	Near term
Electrolysis	Water + Electricity	50-70%	6.64 (Electricity from wind)	Commercial
Biomass gasification	Biomass	35-50%	4.63	Commercial
Photolysis	Water + Sunlight	0.5%	/	Long term
Thermo-chemical water splitting	Water + Heat	/	1.63 (Heat from nuclear energy)	Long term

at STP (Standard conditions for temperature and pressure) is 0.09 g/L, which is approximately ten-thousandth of the density of water. Even if it can be liquefied below -239.7 °C, its density of liquid phase at melting point is about 70.8 g/L, only one-fifteenth of that of water.

Whether for vehicular on-board storage or stationary bulk storage, the storage of hydrogen in high density has been the major challenge due to hydrogen's low volumetric density and its resulting high cost. Hence, hydrogen storage basically implies the reduction of the enormous volume of the hydrogen gas. [16]

The issues that challenge the application of hydrogen vehicle imply to find a storage method or material that satisfies the following requirements: [3]

- High gravimetric/volumetric energy density of hydrogen;
- Reversibility of the release/charge cycle at moderate temperatures in 70-100 °C range to be compatible with the present generation of fuel cells;
- Fast release/charge kinetics with minimum energy barriers to hydrogen release and recharge.

To satisfy the requirements mentioned above, the materials should feature:

- A strong enough interaction between the hydrogen and the storage material;
- A relatively weak interaction between hydrogen and the storage material in an applicable temperature;
- The reversibility for the facile release/recharge processes.

As shown in Table 1.4, the U. S. Department of Energy (DOE) has set a goal (Update May 2017) that by 2020, the on-board hydrogen storage systems should achieve a target of 4.5 wt.% H_2 (1.5 kWh/kg) for gravimetric capacity, and a 0.030 kg hydrogen/L target (1.0 kWh/L) for a volumetric capacity, at a cost of \$333/kg H_2 stored (\$10/kWh).

Table 1.4: Technical system targets for on-board hydrogen storage for Light-Duty Fuel Cell Vehicles (Update May 2017) (wt.%=kg H_2/kg system, gge: gallon gasoline equivalent) [17]

		2020	2025	Ultimate
System gravimetric capacity	kWh/kg	1.5	1.8	2.2
	wt.%	4.5	5.5	6.5
System volumetric capacity	kWh/L	1.0	1.3	1.7
	kg H_2/L	0.03	0.04	0.05
Storage system cost	$/kWh	10	9	8
	$/kg Hydrogen	333	300	266
	$/gge at pump	4	4	4

The research and development of hydrogen storage technologies mainly focus on achieving the requirements to lower the cost and to increase both the gravimetric and volumetric storage capacity as well as efficiency. Two categories of storage technologies are generally discussed including **physical storage** and **material-based storage**.

1.3.1 Physical storage: Gaseous and liquid storage

The simplest and most common used hydrogen storage method is the **compression of hydrogen gas** at high pressure ($>$ 200 bars). Compressed hydrogen in tanks at 350 bars and 700 bars is used in hydrogen vehicles.

The **liquid storage** of hydrogen requires a temperature under -252.8 °C. The hydrogen tank must withstand high pressure and an extreme low temperature. With the density of liquefied hydrogen at 70.8 g/L, the tank necessary to store the 4 kg of hydrogen would be more than 56 liters, which is suitable for on-board application. But the liquefaction of hydrogen and its maintenance ask a high energy cost.

A method for increasing the gravimetric and volumetric capacity of storage for compressed hydrogen gas is using a cryogenic compression tank, called **cryo-compressed hydrogen storage**. The volumetric capacity increases by cooling the container from room temperature to liquid nitrogen temperature (at 77 K). To date, the volumetric capacity of cryo-compressed hydrogen storage tank reaches 40-45 g H_2/L. However, due to the volume occupied by the cooling system, the volume left to store compressed hydrogen further decreases, which further reduces the storage capacity of hydrogen.

1.3.2 Material-based hydrogen storage

Hydrogen storage materials should have the ability to adsorb and to release hydrogen under certain conditions. In practice, due to the frequent replenishment of hydrogen fuel, we require the material to have good reversibility in hydrogen adsorption. For hydrogen storage materials, the main parameters to considered are the hydrogen storage capacity, the reversibility, the limit of recycling, the time required for recharge and impurities (air and materials). The higher requirement is to adapt to the working conditions of the fuel cell. Material-based hydrogen storage technologies is currently based on developing materials that have the potential to meet the requirements for the on-board fuel cell for light-duty vehicle market, mainly including **absorbents**, **interstitial hydrides**, **metal hydrides** and **chemical hydrides**.

Sorbents materials

The metal-organic frameworks (MOFs) [18] and carbon-based materials [19] are mainly considered as sorbents for hydrogen by physisorption to their specific surface areas with weak van der Waals forces. Due to the relatively weak character of van der Waals forces between hydrogen molecules and adsorbents (on the order of 1 to 10 kJ/mol H_2 for most sorbents), the adsorbed gas could be released and gathered but also and also escape easily at room temperature and standard atmospheric pressure. Furthermore, because of the high porous nature of this kind of materials, the volumetric capacity is still low, although the higher gravimetric capacities were achieved.

Metal hydrides

Alternative technologies which involve storing hydrogen within **metal hydrides** also attract a lot of attentions in recent years. Other than the physisorption of hydrogen by sorbents, metal hydrides storage method is a chemical storage method where hydrogen is chemically stored by absorption process. A lot of metal hydrides own the potential for reversible on-board hydrogen storage and can release hydrogen at relatively mild conditions. According to different structures of metal hydrides and different hydrogen storage mechanisms, three metal hydrides are generally studied for the context of on-board hydrogen storage **[20]**: the simple hydrides,the interstitial hydrides and the complex hydrides. (Table 1.5)

Table 1.5: Examples of different type of metal hydrides for hydrogen storage with their theoretical weight percentage of hydrogen wt.%, reversibility, binding energies (ΔH in kJ/(mol H_2)).

Type of hydrides	**Reaction**	**wt.% of H_2**	**Reversibility**	**ΔH**	**Ref**
Simple hydrides	$MgH_2 \rightleftharpoons Mg + H_2$	7.7	yes	65.8-75.2	[21]
	$AlH_3 \rightarrow Al + \frac{3}{2}H_2$	10	no	7.8	[22]
Interstitial hydrides	$LaNi_5H_{6.5} \rightleftharpoons LaNi_5 + 3.25H_2$	1.5	yes	30.8	[23]
Complex hydrides	$LiBH_4 \rightleftharpoons LiH + B + \frac{3}{2}H_2$	13.9	yes	67	[21, 24, 25]
	$12LiBH_4 \rightleftharpoons Li_2B_{12}H_{12} + 10LiH + 12H_2$	10.0		44.4	[26, 27]
	$Mg(NH_2)_2 + 2LiH \rightleftharpoons Li_2Mg(NH)_2 + 2H_2$	5.6	yes	38.9-44.1	[28, 29]
	$NaAlH_4 \rightleftharpoons \frac{1}{3}Na_3AlH_6 + \frac{2}{3}Al + H_2$	3.7	yes	37	[30]

Chemical hydrides

The last class of hydrogen storage materials are the **chemical hydrides**. Compared to the metal hydrides, chemical hydrides possess higher gravimetric density of hydrogen since they contain light elements. In addition, they can release hydrogen in relatively mind conditions. Ammonia borane $H_3N{\cdot}BH_3$ is one of the most prominent examples of chemical hydrides with a relatively high gravimetric capacity at 19.6 wt.% of hydrogen and volumetric capacity at 145g H_2/L. Hydrogen can be released by hydrolysis, thermal decomposition as well as the catalyzed dehydrogenation of ammonia borane and its related adducts.

- Hydrolysis reaction provides low hydrogen yield because an excess of water is needed to achieve efficient H_2 release owning to the limited solubility of ammonia borane in water:

$$\mathrm{H_3N{\cdot}BH_3 + 3\,H_2O \longrightarrow B(OH)_3 + NH_3 + 3\,H_2} \tag{1.2}$$

- The thermolysis of ammonia borane can provide extremely high H_2 yield. The first step asks a decomposition temperature at approximately 100 °C while the second step ask a temperature at 150 °C. The final step requires high temperature ($>$ 1200 °C). The first two steps can be accessible at on-board conditions with a theoretical hydrogen density at 13.1 wt.%. However, the main obstacle of this method is the generation of unwanted gaseous byproduct such as NH_3 and $B_3N_3H_6$.

$$\mathrm{NH_3BH_3 \longrightarrow \frac{1}{n}(NH_2BH_2)_n + H_2} \tag{1.3}$$

$$\mathrm{\frac{1}{n}(NH_2BH_2)_n \longrightarrow \frac{1}{n}(NHBH)_n + H_2} \tag{1.4}$$

$$\mathrm{\frac{1}{n}(NHBH)_n \longrightarrow \frac{1}{n}(NB)_n + H_2} \tag{1.5}$$

- The catalyzed dehydrogenation of ammonia borane and its related adducts has been explored intensively in recent years as the potential method for on-board hydrogen supply and storage. This method is considered as a more efficient and more easily controlled approach for the hydrogen production. Compared to the thermolysis method, it requires a much more gental temperature and even at ambient conditions. It possesses a higher gravimetric capacity than the hydrolysis of ammonia borane, which makes it more attractive in the context of on-board hydrogen sources. In the following chapter, the catalyzed dehydrogenation of ammonia and other adducts will be the main content to be explored for the reason of its prominent potential for on-board hydrogen storage.

An overall summary of hydrogen production and storage techniques is shown in Figure 1.2.

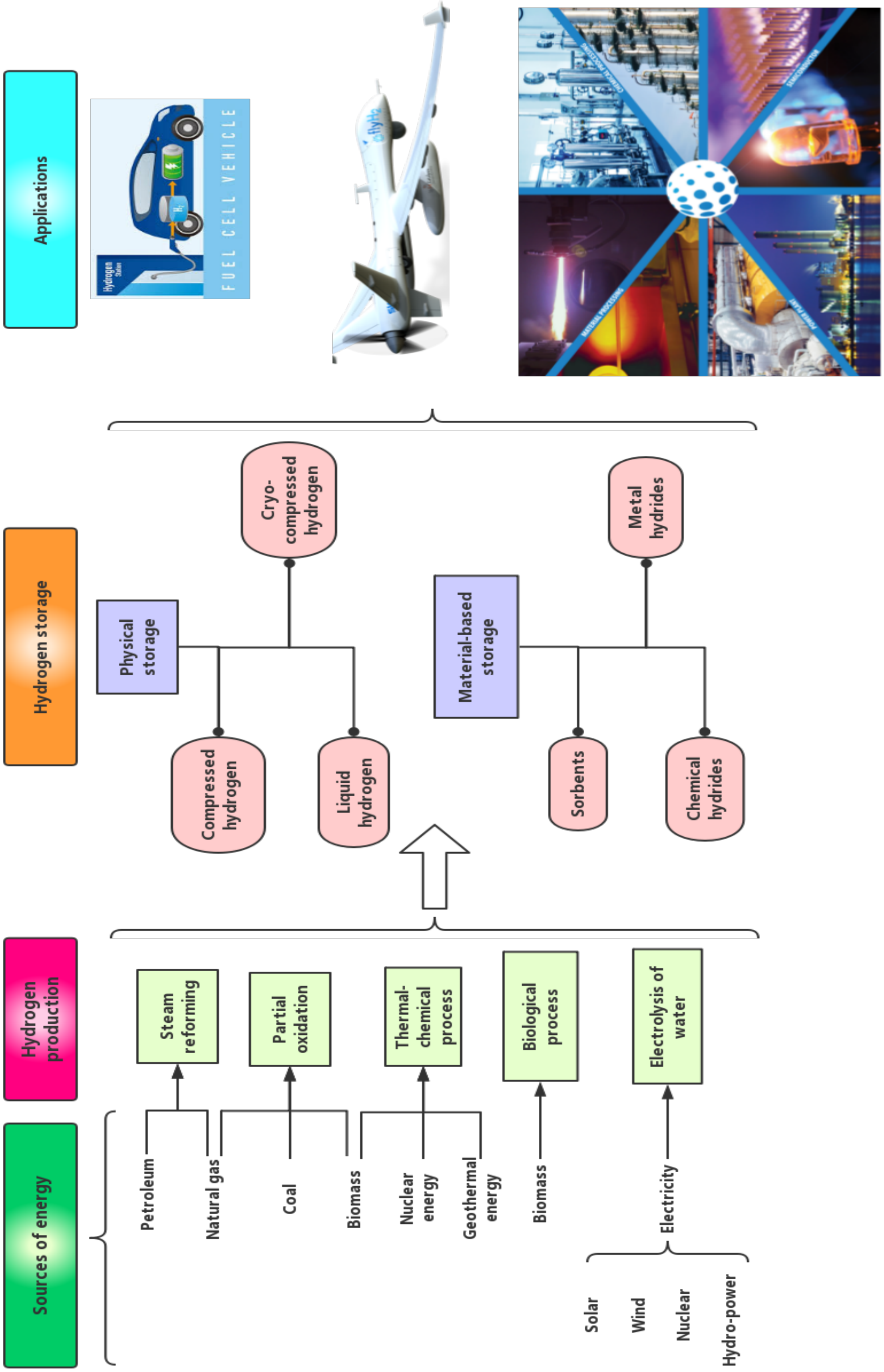
Sources of energy
Hydrogen production
Hydrogen storage
Applications
Petroleum
Natural gas
Coal
Biomass
Nuclear energy
Geothermal energy
Biomass
Electricity
Solar
Wind
Nuclear
Hydro-power
Steam reforming
Partial oxidation
Thermal-chemical process
Biological process
Electrolysis of water
Physical storage
Compressed hydrogen
Cryo-compressed hydrogen
Liquid hydrogen
Material-based storage
Sorbents
Metal hydrides
Chemical hydrides
Hydrogen Station
FUEL CELL VEHICLE
H2
flyH2

Figure 1.2: Summary of hydrogen production, storage and applications.

Chapter 2

Catalyzed dehydrogenation/dehydrocoupling of ammonia borane and amine-borane adducts

2.1 Ammonia borane and other related amine-boranes

2.1.1 Structure and properties of ammonia borane

Ammonia borane ($H_3N{\cdot}BH_3$) is a colorless solid, stable at room temperature and soluble in polar coordinating solvents. Its melting point is between 112 and 114 °C.

Because of the difference in electronegativity of B and N atoms ($\chi(B) = 2.04$ and $\chi(N) = 3.04$, electronegativity using the Allen scale), an heterogeneous distribution of charge is observed, which results in a transfer of electron from NH_3 moiety to BH_3 moiety. A N→B dative bond is formed between N and B atoms. Although ammonia borane is isoelectronic of ethane, it owns a lot of different properties. Because of the difference of electronegativities of BH_3 and NH_3 moieties, the protic $H^{\delta+}$ amine-hydrogen and hydridic $H^{\delta-}$ borane-hydrogen appear simultaneous in ammonia borane molecule with the polarization of B-H and N-H bonds. The electrostatic attraction between the $H^{\delta+}$ and $H^{\delta-}$ forms "BH$\cdots$HN" intermolecular interaction called dihydrogen bonds. These dihydrogen bonds further stabilize the system so that ammonia borane is solid at ambient conditions.

Both X-ray and neutron diffraction techniques have been used to determine the solid state structure of ammonia borane. Compared to the B-N distance in gas phase determined by microwave spectroscopy of 1.67 Å, the B-N dative bond distance becomes significant shorter in the solid state (from 1.58 Å to 1.60 Å depending on the different methods and conditions). Figure 2.1 displays a low temperature crystal structure of solid state ammonia borane. This structure exhibits short NH$\cdots$HB intermolecular contacts at 2.02 Å, constituting a dihydrogen bond [31], which is less than the van der Waals distances of 2.4 Å.

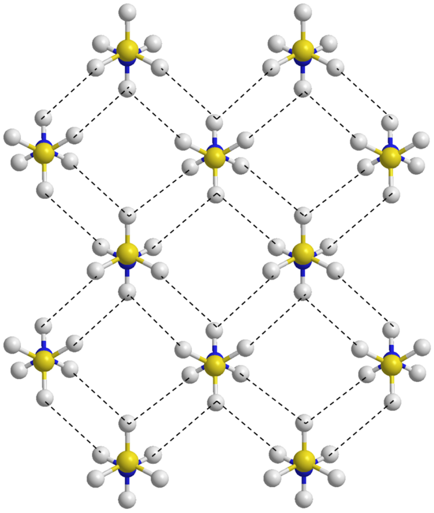

Figure 2.1: Low temperature crystal structure of solid state ammonia borane. [32] The yellow, blue and white balls represent the B, N and H atoms, respectively. The dihydrogen bonds are delineated by dashed lines.

Apart from the diffraction analyses for the structures determinations, ammonia borane has been analyzed by almost all spectroscopic techniques, including NMR, IR and Raman spectroscopies.

Because of the presence of the protic $H^{\delta+}$ amine-hydrogen and hydridic $H^{\delta-}$ borane-hydrogen which polarize the B-H and N-H bonds, it enables facile release of hydrogen from ammonia borane in mild conditions. Ammonia borane and amine-boranes are unique when compared with other chemical hydrides in their potential ability to store and deliver large amounts of molecular hydrogen through dehydrogenation and hydrolysis. A strong enough B-N bond indicates that under mild conditions, hydrogen removal is favored over dissociation of ammonia borane to ammonia and borane. There are two main ways of releasing hydrogen directly from ammonia borane: pyrolysis (thermal dehydrogenation) and hydrolysis which are already presented in Section 1.3.2.

2.1.2 Syntheses

Ammonia borane was first synthesized by Sheldon G. Shore and Robert W. Parry in 1955 [33] from lithium borohydride ($LiBH_4$) or from diammoniate of diborane ($[H_2B(NH_3)_2{}^+][BH_4{}^-]$) (Reaction 2.1 and 2.2):

$$LiBH_4 + NH_4Cl \longrightarrow LiCl + H_3N{\cdot}BH_3 + H_2 \tag{2.1}$$

$$[H_2B(NH_3)_2{}^+][BH_4{}^-] + NH_4Cl \longrightarrow [H_2B(NH_3)_2{}^+][Cl^-] + H_3N{\cdot}BH_3 + H_2 \tag{2.2}$$

From then on, many other synthesis methods of the ammonia borane and other amine-boranes have been developed. [34] Three general types of reactions are used : (1) the metathesis of $M[BH_4{}^-]$ and $[NH_4{}^+]X$; (2) the displacement of a ligand L from $L{\cdot}NH_3$ by BH_3 and (3) the decomposition reaction of diammoniate of diborane $[H_2B(NH_3)_2{}^+][BH_4{}^-]$.

Metathesis reaction

Ammonia borane can be synthesized by metathesis reactions by combining between different ammonium salts $[NH_4{}^+]X$ (X: $SO_4{}^-$, $CO_3{}^-$, Cl^- and Br^-) and borohydride salts $M[BH_4{}^-]$ (usually lithium borohydride $LiBH_4$ or sodium borohydride $NaBH_4$) in an organic solvent (CCl_4, CH_2Cl_2, $(C_2H_5)_2O$, toluene ...) at 25-45 °C. [33,35,36] The ammonium borohydride $[NH_4{}^+][BH_4{}^-]$ formed by the metathesis reaction undergoes instantaneously a dehydrogenation process to generate ammonia borane and dihydrogen because the ammonium borohydride is not stable under ambient conditions. (Reaction 2.3 and 2.4)

$$[NH_4{}^+]X + M[BH_4{}^-] \longrightarrow MX + [NH_4{}^+][BH_4{}^-] \tag{2.3}$$

$$[NH_4{}^+][BH_4{}^-] \longrightarrow NH_3BH_3 + H_2 \tag{2.4}$$

It was reported that the dehydrogenation of $[NH_4{}^+][BH_4{}^-]$ (reaction 2.4) in tetrahydrofuran (THF) containing a small amount of NH_3 is essential to the high yield at 99% and purity of ammonia borane. [34]

Displacement reaction

The syntheses of ammonia borane by displacement reaction (usually S_N2) are based on the Lewis acid-base exchange process. Ammonia NH_3, which is considered as a strong Lewis base, takes the place of the weaker base L in $L{\cdot}BH_3$ in an organic solvent (usually $(CH_3)_2O$, THF or toluene). This process undergoes generally under temperature below 0 °C. The L ligand can be $(CH_3)_2O$, $(CH_3)_2S$, THF and BH_3. [35,37,38]

$$NH_3 + L{\cdot}BH_3 \longrightarrow NH_3BH_3 + L \tag{2.5}$$

Room temperature displacement reaction in a large-scale was developed by both increasing the basicity of the Lewis base of the borane carrier and using a non-polar solvent. [39] Dimethylsulfide($(CH_3)_2S{\cdot}BH_3$, DMS) and dimethylaniline ($C_6H_5N(CH_3)_2$, DMA) were used as L ligand to process the displacement reaction with NH_3 at room temperature in anhydrous toluene. The yields were found to be higher than 90% under such conditions.

Decomposition reaction

Alternatively, the decomposition of diammoniate of diborane ($[H_2B(NH_3)_2{}^+][BH_4{}^-]$) is another way to synthesize ammonia borane. By solubilizing diammoniate of diborane into diethyl ether at -78 °C with a small amount of NH_3, a decomposition reaction takes place and leads to the formation of ammonia borane: [35]

$$[H_2B(NH_3)_2{}^+][BH_4{}^-] \longrightarrow H_3NBH_3 + H_2 + \frac{1}{n}(H_2NBH_2)_n \tag{2.6}$$

In the poly-ether solution with a small quantity of B_2H_6 at 25 °C, ammonia borane can be also formed by the decomposition of diammoniate of diborane as shown in Reaction 2.7: [40]

$$[H_2B(NH_3)_2{}^+][BH_4{}^-] \longrightarrow 2\,H_3NBH_3 \tag{2.7}$$

2.2 Dehydrogenation reactions of amine-boranes

Dehydrogenation process is a chemical reaction that involves the remove of hydrogen from a molecule. The dehydrogenation/dehydrocoupling of amine-boranes indicates a chemical process catalyzed by organometallic compounds wherein dihydrogen is released directly, or by the coupling of two or more amine-borane adducts. Dehydrogenation and dehydrocoupling of amine-borane adducts have attracted considerable interest in hydrogen storage for potential application of fuel cells for vehicles, preparation of new inorganic oligomeric compounds or polymeric materials with B-N (or B-P for phosphine borane) backbones. Inexpensive, environmentally friendly, easily synthesized and stable organometallic compounds that efficiently catalyze the reaction are worth studying. In this context, mechanistic studies of the catalytic dehydrogenation/dehydrocoupling of amine-boranes and phosphine-boranes have been put forward over the last decade. To date, a universal, detailed and well-established mechanism for these kinds of reaction remains uncertain. In general considerations, several possible reactions pathways of dehydrogenation/ dehydrocoupling of amine-borane adducts are summarized as below for ammonia borane, primary amine boranes and secondary amine boranes respectively:

- **Ammonia borane** $H_3N{\cdot}BH_3$

The ammonia borane molecule can release dihydrogen directly with a thermal decomposition over 100°C in generating the mixture of products including polyborazylene and polyaminoboranes with releasing at most 3 equiv. of molecular H_2.(Equation 1.3, 1.4 and 1.5) The catalyzed dehydrogenation of ammonia borane release generally equal or over 2 equiv. of H_2 to form polyborazylene as well as other oligomeric or polymeric materials. Figure 2.2 summaries the metal-catalyzed dehydrogenation mechanisms for ammonia borane. Many active catalysts generate linear polyaminoborane and a single equiv. of H_2 is released. [41,42] Most selective catalysts generate two equiv. of H_2 with concomitant formation of borazine (cyclic iminoborane trimer) and its BN-cross-linked polyborazylene. [43–46]

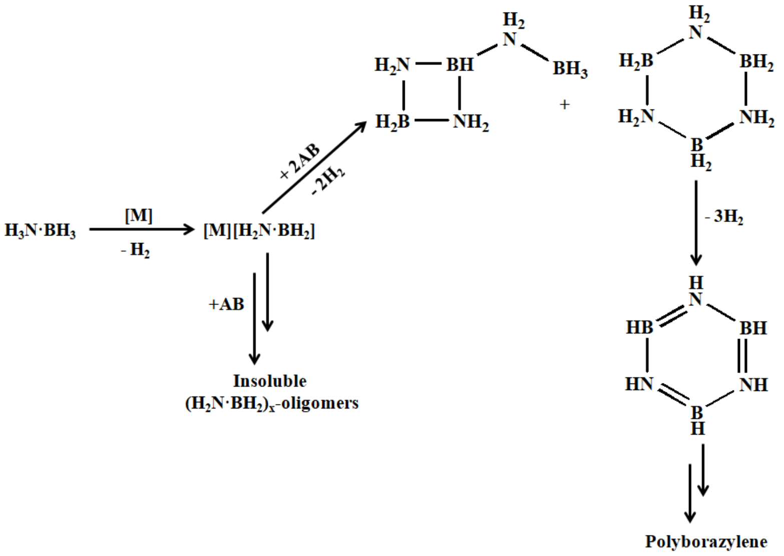

Figure 2.2: Metal-catalyzed dehydrogenation of ammonia borane. [47]

- **Primary amine-boranes** $H_2RN{\cdot}BH_3$

The primary amine-borane $H_2RN{\cdot}BH_3$ (R = H, Me and $^nBu\cdots\cdots$) can undergo a dehydrogenation of one equiv. of H_2 to form an aminoborane $HRN{=}BH_2$ (which can further undergo dimerization or trimerization reactions), or polyaminoboranes $[HRN{\cdot}BH_2]_n$. The loss of three equiv. of H_2 from primary amine-borane results in the formation of borazines $[RN{\cdot}BH]_3$. The general reaction paths of the primary amine borane is summarized in Figure 2.3.

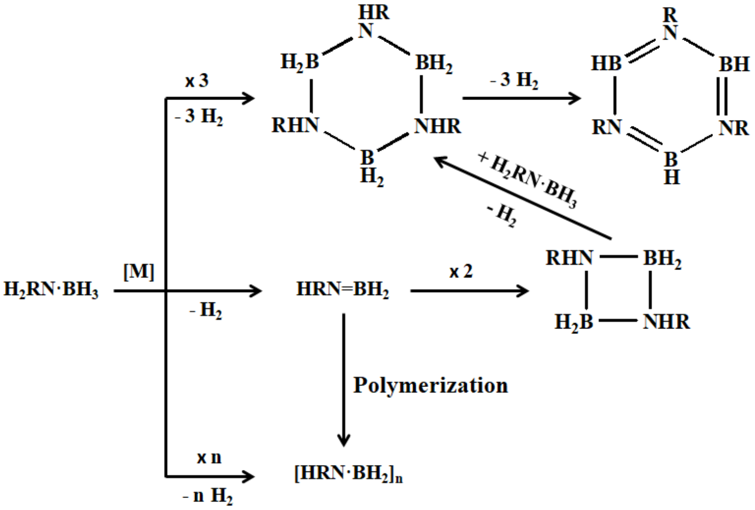

Figure 2.3: Summary of catalyzed dehydrogenation/dehydrocoupling pathways from primary amine-borane. [48]

- **Secondary amine-borane** $HR_2N{\cdot}BH_3$

The dehydrogenation reactions of the secondary amine-boranes $HR_2N{\cdot}BH_3$ (R = H, Me and Et$\cdots\cdots$) are relatively well-defined.

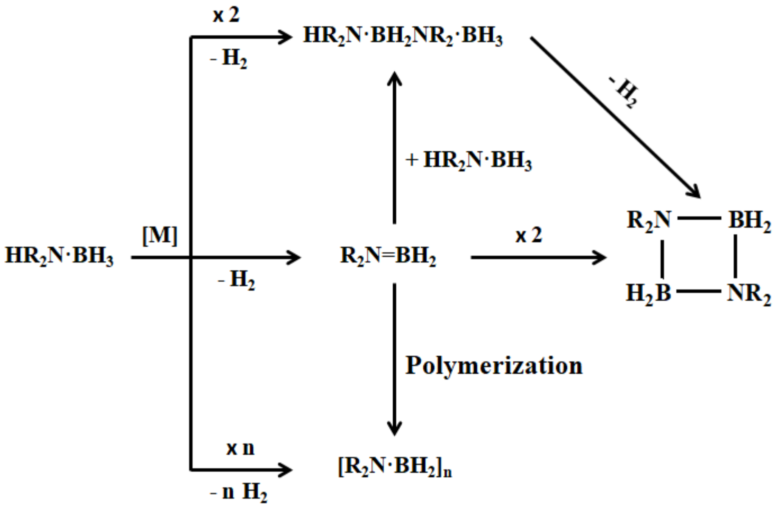

Figure 2.4: Possible catalyzed dehydrogenation/dehydrocoupling pathways of secondary amine-boranes.

Figure 2.4 summarizes the possible catalyzed dehydrogenation/dehydrocoupling reactions of secondary amine-borane $HR_2N{\cdot}BH_3$ (R = Me, Et and ^{i}Pr $\cdots\cdots$). As shown in Figure 2.4, the catalyzed dehydrogenation or/and dehydrocoupling of secondary amine-boranes has numerous possibilities. The loss of one molecule of H_2 from secondary amine-boranes mainly generates: 1) aminoborane ($R_2N{=}BH_2$) *via* a dehydrogenation process, that can further undergo dimerization or polymerization, *via* an off-/on-metal step; or reacts with another amine-borane to generate a linear dimer; 2) linear diborazane ($HR_2N{\cdot}BH_2R_2N{\cdot}BH_3$) *via* a dehydrocoupling reaction from two molecules. The linear diborazane may release a second molecule of hydrogen to form a cyclic diborazane ($[R_2N{\cdot}BH_2]_2$).

The dimethylamine borane, $HMe_2N{\cdot}BH_3$, is largely used for the investigations of catalyzed dehydrogenation studies of amine-boranes because of its well-defined products. The most commonly observed products are as follows: the aminoborane $Me_2N{=}BH_2$, the linear diborazane $HMe_2N{\cdot}BH_2Me_2N{\cdot}BH_3$, and cyclic diborazane $[Me_2NBH_2]_2$, all of which are soluble and easily experimentally identified.

2.3 Transition metal-catalyzed dehydrogenations

2.3.1 Early transition metals

Group IV transition metal catalysts were among the extensively studied catalysts for amine-boranes dehydrogenation/dehydrocoupling reactions due to their high abundance, high reactivity and low cost. Manners, [49–51] Chirik, [52] Rosenthal, [53] Wass, [54, 55], Beweries, [56] and Waterman [57] have presented detailed studies of related Group IV complexes, most of which are metallocene complexes.

Manners *et al.* presented the first Group IV metallocene catalyzed dehydrogenation investigation of amine-boranes by using the $[Cp_2Ti]$ catalyst (complex A in Table 2.1) generated *in situ* from Cp_2TiCl_2/^{n}BuLi. [49] After this study, the extensive kinetic/mechanistic investigations were carried out both experimentally [50] and theoretically. [58,59] Their studies have highlighted the efficient role of [Cp_2Ti] complex for homogeneous catalyzed dehydrogenation of secondary amine-boranes $HR_2N\cdot BH_3$ (R = Me and ${}^{i}Pr$). The turnover frequency (TOF) was determined to quantify the specific activity of a catalytic center. It is calculated as the number of molecular reactions or catalytic cycles occurring at the center per unit time. The [Cp_2Ti] catalyzed dehydrogenation of $HMe_2N\cdot BH_3$ reaction has a TOF value of 11.1 h^{-1} at 20 °C in toluene. The experimental studies also demonstrated the decreased activity on descending the periodic table (from Ti to Zr and Hf) and on substitution of the Cp (cyclopentadienyl) ligands by bulky or electron-donating groups. However, the mechanisms remain uncertain despite extensive studies. The detailed investigations for the mechanistic studies will be developed in following Chapters.

A subsequent work by Manners' group has demonstrated the significant role of the paramagnetic Ti^{III} species as precatalysts. [51] Experimental studies shown that the Ti^{III} complexes $Cp_2TiNMe_2\cdot BH_3$ and $Cp_2TiPPh_2\cdot BH_3$ (complexes B in Table 2.1) can act efficiently catalyze the dehydrogenation of $HMe_2N\cdot BH_3$, with a conversion of 83% (TOF 0.13 h^{-1}) and 97% (TOF 10.7 h^{-1}), respectively, after 2 hours. Under the same conditions, the Zr^{III} analogue $Cp_2ZrPPh_2\cdot BH_3$ as a precatalyst has been found to have only 1.5% conversion, while the diamagnetic $Cp_2Zr(H)NH_2\cdot BH_3$ complex shown no reactivity.

Table 2.1: Examples of early transition metal catalysts for amine-boranes dehydrogenation reactions.

	A	B	C
	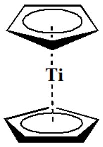	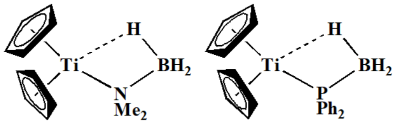	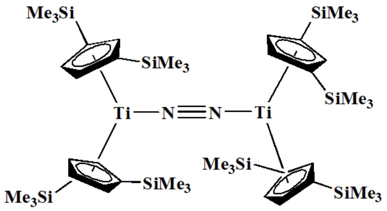 Me3Si SiMe3 SiMe3 SiMe3 Ti—N≡N—Ti Me3Si SiMe3 Me3Si SiMe3
Ref	[49,50,58,59]	[51]	[52]
	D	E	
	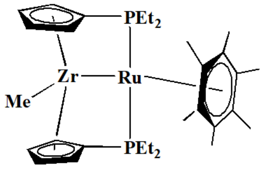	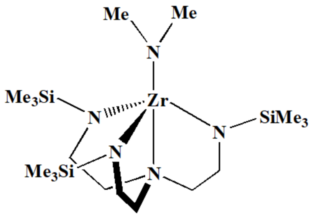 Me Me N Me3Si N Zr N SiMe3 N Me3Si N	
Ref	[60]	[57]	

Chirik *et al.* [52] have also studied the catalytic dehydrogenation of secondary amine-borane adducts promoted by a series of titanocenes and zirconocenes complexes, among which the silyl-substituted titanocene dinitrogen complex (complex C in Table 2.1) was found to be the most active catalyst. This complex shows a high efficiency for dehydrogenation of $HMe_2N\cdot BH_3$ with a TOF larger than 420 h^{-1} at 23 °C. Apart from the influence of the nature of metal center on the dehydrogenation efficiency, this work also highlighted the impact of cyclopentadienyl substitution on the H_2 loss reaction.

A family of Group IV (Zr, Hf) metallocene-Group VIII (Fe, Ru) heterobimetallic complexes has been studied by Nishibayashi *et al.* [60] A series of heterobimetallic complexes, including $[M^1M(\mu\text{-}\eta^5 : \eta^1\text{-}C_5H_4PEt_2)_2M^2Cp^*]$ (M^1=Zr, M^2=Ru (complex D in Table 2.1); M^1=Hf, M^2=Ru) have been investigated as catalysts for amine-borane dehydrogenation. In contrast to the previous works demonstrating that the $[Cp_2M]$ (M= Zr and Hf) [50] were completely inactive toward the dehydrogenation of $HMe_2N{\cdot}BH_3$, this study provides an alternative way to promote the reaction by cooperative effect of both metallic centers. The Zr-Ru bimetallic complex catalyzes the dehydrogenation of $HMe_2N{\cdot}BH_3$ to form $[Me_2N{\cdot}BH]_2$ with a TOF of 8 h^{-1} at 50 °C. The reactions with $H_3N{\cdot}BH_3$ and $H_2MeN{\cdot}BH_3$ have been found to be less active to form B-N oligomeric materials. Proposed catalytic mechanism of this heterobimetallic complex for $HMe_2N{\cdot}BH_3$ dehydrogenation is shown in Figure 2.5. A initial ligand exchange between the $HMe_2N{\cdot}BH_3$ and the methyl group results in the formation of bimetallic complex with a hydrogen bridge between Zr and Ru centers. An oxidative addition step of N-H on the Zr center is followed by a bimetallic reductive elimination of H_2. The B-H activation on the Ru center takes place, followed by a generation of $Me_2N{=}BH_2$ molecule and a regeneration of the hydrogen-bridged Zr-Ru bimetallic complex. This study demonstrates a cooperative role of both transition metals to promote a dehydrogenation reaction which could not be occurred with a simple monometallic catalyst. It may provide a potential application for future catalysts development.

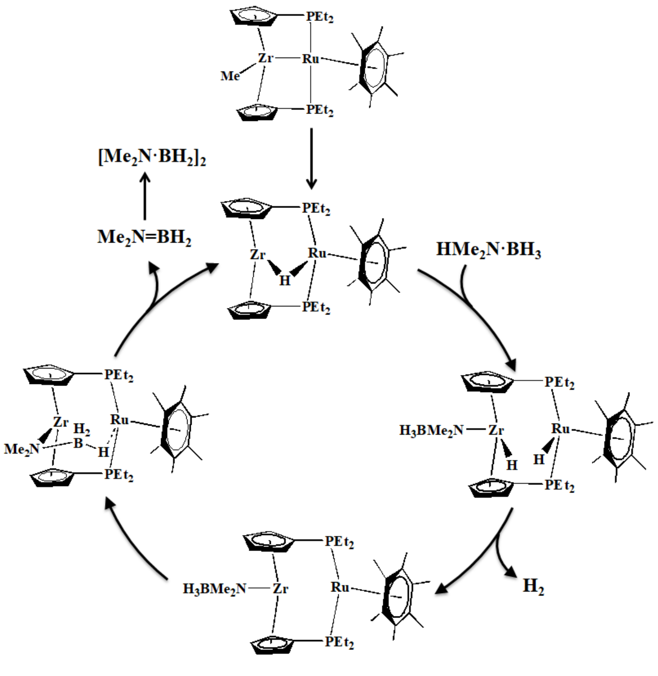

Figure 2.5: Proposed mechanism for the dehydrogenation of $HMe_2N{\cdot}BH_3$ catalyzed by Zr-Ru heterobimetallic complex. [60]

In addition, the efficient role of other zirconium-based complexes to catalyze this dehydrogenation reaction have also been reported in the literature. Waterman *et al.* [57] found that the $(N_3N)ZrR$ complex ($N_3N{=}\ N(CH_2CH_2NSiMeCH_2)_3$) with R = NMe_2 (complex E in Table 2.1), Cl and O^{t}Bu were good catalysts to dehydrogenate HRR′N·BH$_3$ (R = R′ = Me; R = R′ = Me; R = H, R′ = ^{t}Bu). In Figure 2.6 is shown an outer-sphere-type mechanism for molecular hydrogen and monomeric aminoborane releasing. This reaction may be considered in the hydrogenation for unsaturated molecule using the (N$_3$N)ZrNMe$_2$ complex and amine-boranes as hydrogen source.

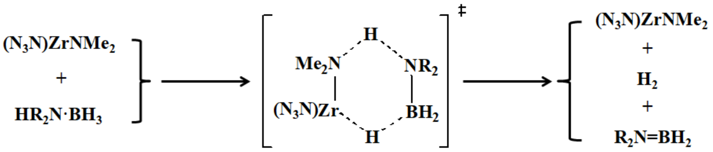

Figure 2.6: Proposed mechanism of dehydrogenation of amine-boranes by (N$_3$N)ZrNMe$_2$ complex. [57]

2.3.2 Mid-transition metals

Table 2.2: Examples of mid-transition metal catalysts for amine-boranes dehydrogenation reactions.

	F	G
	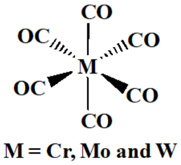	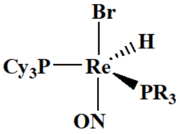
Ref	[61]	[62]

Group VI transition metal complexes catalyzing dehydrogenation of amine-boranes were studied by Shimo *et al.* [61] The reactions catalyzed by the Group VI metal carbonyl complexes [M(CO)$_6$] (M = Cr, Mo and W) with photo-irradiation lead to the generation of cyclic oligomers or monomeric aminoborane (R$_2$N=BH$_2$). The dehydrogenation of secondary amine-boranes HR$_2$N·BH$_3$ (R$_2$= Me$_2$, Et$_2$, C$_4$H$_8$ and C$_5$H$_{10}$) led to the formation of cyclic dimers [R$_2$N·BH$_2$]$_2$. Monomeric products R$_2$N=BH$_2$ were identified for the catalytic dehydrogenation of bulked amine-borane HR$_2$N·BH$_3$ (R= ^{i}Pr and cyclohexyl). Dehydrocoupling of primary amine-boranes H$_2$RN·BH$_3$ (R = Me, Et and ^{t}Bu) led to trimers [RN·BH]$_3$. A TOF value of 19 h^{-1} was reported in the case of HMe$_2$N·BH$_3$ dehydrogenation with [Cr(CO)$_6$]. Their DFT calculations of the mechanistic exploration suggested a stepwise intramolecular pathway based by the active [Cr(CO)$_4$] species, which is generated by the [Cr(CO)$_6$] precursor. (See Figure 2.7) A coordination step of amine-borane *via* Cr-H-B and Cr-H-N interactions is followed by the stepwise N-H and B-H breakages. The isomerization of the resulting dihydride takes place, followed by the release of H$_2$ and regeneration of the active catalytic center [Cr(CO)$_4$].

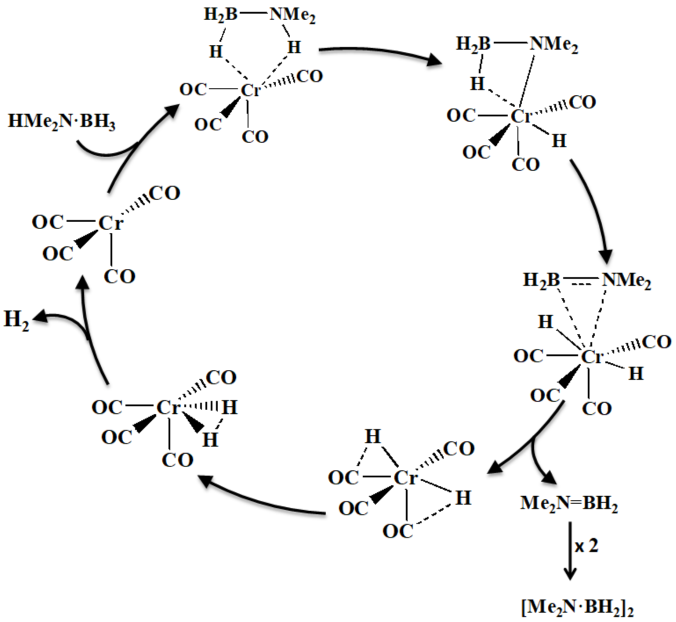
H₂B—NMe₂
H
H
OC
Cr
CO
OC
CO
HMe₂N·BH₃
H₂B—NMe₂
H
OC
Cr
CO
OC
H
CO
OC
Cr
CO
OC
CO
H₂
H₂B---NMe₂
H
OC
Cr
CO
H
OC
CO
OC
Cr
CO
H
OC
H
CO
H
OC
Cr
CO
OC
H
OC
Me₂N=BH₂
x 2
[Me₂N·BH₂]₂

Figure 2.7: Calculated mechanistic proposal for dehydrogenation of $HMe_2N{\cdot}BH_3$ by $[Cr(CO)_6]$ precatalyst. [61]

A range of rhenium-based catalysts were explored by Berke *et al.* [62] The five-coordinated rhenium(I) hydride complexes $[Re(Br)(H)(NO)(PR_3)_2]$ (R = cyclohexyl(Cy) and ^{i}Pr) were found to efficiently catalyze the dehydrogenation of $HMe_2N{\cdot}BH_3$ at 75 °C with a TOF of 77 h^{-1} (R = cyclohexyl) and a conversion of 100% in 1.3 h (for R = Cy) and a TOF of 55 h^{-1} with a conversion of 83% in 1.5 h (for R = ^{i}Pr). The proposed mechanism shown in Figure 2.8 for R = Cy starts with a coordination of $HMe_2N{\cdot}BH_3$ as a σ complex. Loss of PCy_3 ligand exposes a vacant coordination site, allowing a further activation and breakage of B-H bond to generate a dihydride complex. The reductive elimination of H_2 is carried out by insertion of the PCy_3 ligand, resulting a amidoborane intermediate. This intermediate undergoes N-H cleavage to regenerate the catalyst $[Re(Br)(H)(NO)(PR_3)_2]$ and to form a $Me_2N{=}BH_2$ which proceeds further cyclization. Interestingly, the amine-borane adducts can also serve as the source of hydrogen for the hydrogenation of olefins catalyzed by $[Re(Br)(H)(NO)(PR_3)_2]$ complexes.

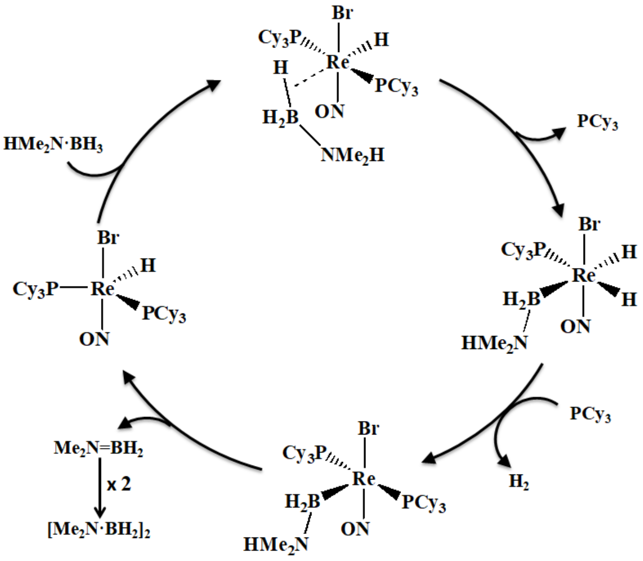

Figure 2.8: Proposed mechanism for the dehydrogenation of $HMe_2N{\cdot}BH_3$ catalyzed by $[Re(Br)(H)(NO)(PCy_3)_2]$. [62]

2.3.3 Late transition metals

Late transition metals catalyzing dehydrogenation reaction were extensively studied both experimentally and theoretically.

Table 2.3: Examples of late transition metal catalysts for amine-boranes dehydrogenation reactions.

	H	I	J
	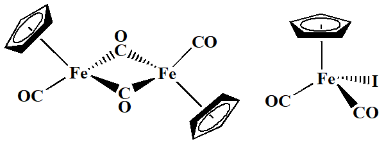	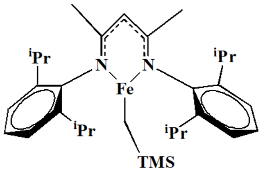	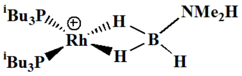
Ref	[63]	[64]	[65]
	K	L	M
	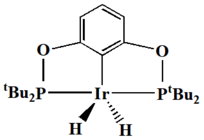	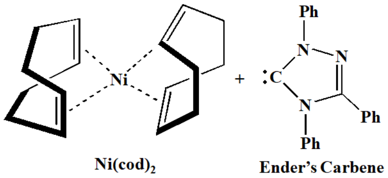	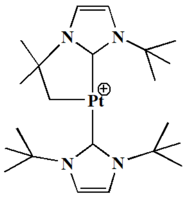
Ref	[41]	[43]	[66]

Iron carbonyl complexes like $[CpFe(CO)_2]_2$ and $CpFe(CO)_2I$ (complexes H in Table 2.3) were found to be efficient precatalyst under photo-irradiation at ambient temperature for the dehydrogenation of $HMe_2N{\cdot}BH_3$ by Manner and coworkers. [63] According to the experimental observations together with some DFT calculations, a two-step mechanism similar to the one proposed for titanocene-catalyzed reaction was suggested. (See Figure 2.9) The photoirradiation of $CpFe(CO)_2I$ species generate the $[CpFeCO]^+$ fragment, which reacts with the $HMe_2N{\cdot}BH_3$ molecule to form an $\eta^2-\sigma$ complex. The addition of a second molecule of $HMe_2N{\cdot}BH_3$ results in a dehydrocoupling process *via* the formation of B-N bond, followed by the generation of the linear dimer $HMe_2N{\cdot}BH_2Me_2N{\cdot}BH_3$ with the concomitant release of a H_2. The second step consists in the formation of a chelate σ complex involving $[CpFeCO]^+$ and linear dimer coordination. A further dehydrocoupling leads to the formation of cyclic dimer $[Me_2N{\cdot}BH_2]_2$.

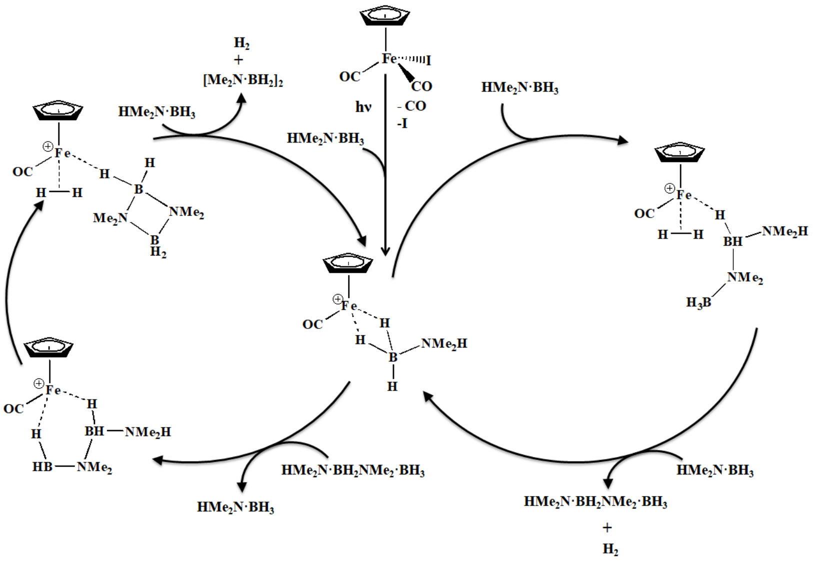

Figure 2.9: Proposed two-step mechanistic cycle of the dehydrogenation of $HMe_2N{\cdot}BH_3$ catalyzed by $CpFe(CO)_2I$ under photo-irradiation. [63]

More recently in 2017, Webster and coworkers reported a dehydrogenation of amine- and phosphine-boranes adducts using a series of iron(II) $\beta-$diketiminate complexes. (For example complex I in Table 2.3) The catalyzed dehydrogenation by complex I of $HMe_2N{\cdot}BH_3$ leads to the formation of $[Me_2N{\cdot}BH_2]_2$ with a conversion of 98% in 12h at ambient temperature. Under the same condition, the dehydrogenation of $HMeBnN{\cdot}BH_3$ results in $[MeBnN{\cdot}BH_2]_2$ product in 3h with 99% conversion. The dehydrogenation of $H^iPr_2N{\cdot}BH_3$ generates the monomeric aminoborane product, when complex I (in Table 2.3) is used as the catalyst. This is also the product identified with the titanocene A used as the catalyst. Similar mechanisms were proposed with both catalysts.(Figure 2.9) In addition, it was also reported in the study of Fe(II) complexes that the dehydrogenation of amine-boranes adducts is far more facile than the phosphine-borane counterpart.

Besides those complexes presented hereinbefore, many other late transition metal catalysts have also been found to be efficient for the dehydrogenation of amine-borane adducts, including the Rh-based complexes (complex J in Table 2.3), [65] Ir-based complexes (complex K in Table 2.3), [41, 67–69] the Ni-based complexes (complex L in Table 2.3) [43, 70] , Pt-based complexes (complex M in Table 2.3) [66] etc.

Part II

Computational and Theoretical Background

Chapter 3

Theoretical models for electronic structure

Principle

In quantum chemistry, the main objective is to describe the physical and chemical phenomena at the molecular level by solving the non-relativistic time-independent Schrödinger Equation mathematically:

$$\hat{H}\Psi = E\Psi \tag{3.1}$$

where

$$\hat{H} = \hat{T}_e + \hat{T}_N + \hat{V}_{eN} + \hat{V}_{ee} + \hat{V}_{NN} = \tag{3.2}$$

$$-\sum_{i=1}^{N}\frac{1}{2}\nabla_i^2 - \sum_{A=1}^{M}\frac{1}{2M_A}\nabla_A^2 - \sum_{i=1}^{N}\sum_{A=1}^{M}\frac{Z_A}{r_{iA}} + \sum_{i=1}^{N}\sum_{j>i}^{N}\frac{1}{r_{ij}} + \sum_{A=1}^{M}\sum_{B>A}^{M}\frac{Z_A Z_B}{R_{AB}}$$

is the Hamiltonian operator which contains the kinetic operator of electrons and nuclei, respectively, as well as different kinds of potential operators. The indices i and j refer to N electrons and the indices A and B refer to M nucleus in a system. The first two terms are associated with the kinetic energies of electrons and nuclei while the last three terms are respectively the operators of Coulomb attraction between the nuclei and electron, the Coulomb repulsion between electrons and the Coulomb repulsion between nuclei. Ψ corresponds to the wave function with the energy of system E.

The system is considered to be stationary in a vacuum. However, we cannot get the exact solution of this equation except for the one-electron systems. Several approximations must be used. The adiabatic approximation is introduced in considering that the study of dynamics of nuclei from that of electrons can be considered separately. Since the nuclei are much heavier than electrons, they move much more slowly. Hence, we can consider the electrons in a molecule to be moving in the field of the fixed nuclei called Born-Oppenheimer approximation to simplify the situation. With these approximations, the term of kinetic energy of nuclei can be neglected and the Coulomb repulsion of nuclei can be considered as a constant. The Hamiltonian becomes:

$$\hat{H}' = \hat{T}_e + \hat{V}_{eN} + \hat{V}_{ee} + \hat{V}_{NN} = \hat{H}_{el} + \hat{V}_{NN} \tag{3.3}$$

where $\hat{H}_{el}$ is the electronic Hamiltonian that describes the N electrons' movement in the field generated by M nuclei:

$$\hat{H}_{el} = -\sum_{i=1}^{N} \frac{1}{2}\nabla_i^2 - \sum_{i=1}^{N}\sum_{A=1}^{M} \frac{Z_A}{r_{iA}} + \sum_{i=1}^{N}\sum_{j>i}^{N} \frac{1}{r_{ij}} = \sum_{i=1}^{N} \hat{h}_i + \sum_{i=1}^{N}\sum_{j>i}^{N} \frac{1}{r_{ij}} \tag{3.4}$$

The total energy is obtained by adding a part of nuclear repulsion $\hat{V}_{NN}$ to the electronic energy E_{el}. According to these approximations, the strategy to solve the Schrödinger equation becomes to solve the electronic equation:

$$\hat{H}_{el}\mathit{\Psi}_{el} = E_{el}\mathit{\Psi}_{el} \tag{3.5}$$

To solve this electronic equation, the spatial description of electrons is needed. A spin-orbital $\mathit{\Phi}_i$ that describe the spatial distribution $\varphi_i(r)$ as well as the spin of an electron ω (α and β represent the spin up and spin down respectively) are introduced. The two possible descriptions of an electron are described as follows:

$$\mathit{\Phi}_i = \begin{cases} \varphi_i(r)\,\alpha(\omega) \\ \varphi_i(r)\,\beta(\omega) \end{cases} \tag{3.6}$$

with

$$\langle \alpha | \alpha \rangle = \langle \beta | \beta \rangle = 1$$

$$\langle \alpha | \beta \rangle = \langle \beta | \alpha \rangle = 0$$

However, this equation cannot be solved except for hydrogen-like species. For the other systems, it is necessary to introduce some additional approximations.

3.1 The Hartree-Fock Approximation

3.1.1 The Hartree-Fock Equations

The Hartree-Fock (HF) approximation provides some basic ideas to solve the electronic Schrödinger equation. The electronic wave function with N electrons is considered to be an anti-symmetric product of single electron functions, called the molecular orbitals (MO). In order to satisfy the Pauli's exclusion principle, the wave function should be written as the form of Slater determinant:

$$\Psi\left(x_1, x_2, \cdots, x_N\right) = (N!)^{-\frac{1}{2}} \begin{bmatrix} \Phi_1\left(x_1\right) & \cdots & \Phi_N\left(x_1\right) \\ \vdots & \ddots & \vdots \\ \Phi_1\left(x_N\right) & \cdots & \Phi_N\left(x_N\right) \end{bmatrix} \tag{3.7}$$

The Slater determinant has N electrons occupying N spin-orbitals. The factor $(N!)^{-\frac{1}{2}}$ is a normalization factor. Each spin-orbital $\Phi_i\left(x_i\right)$ is an eigenfunction of an eigenvalue equation:

$$\hat{F}_i \Phi_i\left(x_i\right) = \varepsilon_i \Phi_i\left(x_i\right) \tag{3.8}$$

with $\hat{F}_i$ an effective one-electron operator called Fock operator:

$$\hat{F}\left(x_i\right) = -\frac{1}{2}\nabla_i^2 - \sum_{A=1}^{M} \frac{Z_A}{r_{iA}} + \vartheta^{HF}\left(x_i\right) = \hat{h}\left(x_i\right) + \sum_{j \neq i}\left(\hat{J}_j - \hat{K}_j\right) \tag{3.9}$$

where $\hat{h}$ is the core Hamiltonian operator describing the kinetic energy and potential energy of electron i, ϑ^{HF} is the average potential experienced by the i-th electrons due to the presence of the other electrons called Hartree-Fock potential, written usually as algebraic sum of two terms $\left(\hat{J}_j - \hat{K}_j\right)$.

$\hat{J}_j$ refers to the Coulomb operator, defining the electron-electron repulsion energy due to each of the two electrons in the j-th orbital. $\hat{K}_j$ is called the exchange operator, defining the electron exchange energy due to the antisymmetry of the total N-electrons wave function.

For a closed-shell system, the spin-orbital is called restricted and the ground state wave function is only the combination of different spatial orbitals. And the Fock operator is thus simplified:

$$\hat{F}\left(r_1\right) = \hat{h}\left(r_1\right) + \sum_{i=1}^{N/2}\left(2\hat{J}_i\left(r_1\right) - \hat{K}_i\left(r_1\right)\right) \tag{3.10}$$

To solve the Hartree-Fock equations, a procedure called Self-Consistent-Field (SCF) method is proposed. Figure 3.1 illustrates the simplified algorithm of SCF method. The equation must be solved by an iterative procedure. An initial guess of input matrix of spin-orbital is generated to calculate the average potential field ϑ^{HF}. One can solve the eigenvalue equation 3.8 to obtain a new set of spin-orbitals in matrix form. Taking this new matrix, one can obtain a new potential field and iterate this procedure until the SCF is converged. After a SCF procedure, the converged orbital energies and the molecular orbital coefficients are obtained.

3.1.2 HF-limit

The Hartree-Fock approximation does not take into account the electron correlation energy, which comes from the influence of the movement of one electron with the presence of all other electrons. As a result, the limit-Hartree-Fock is always greater than the true energy with the correlation energy: $E_{corr} = E_{exact} - E_{HF}$. Electron correlation can be divided into dynamical and static correlation.

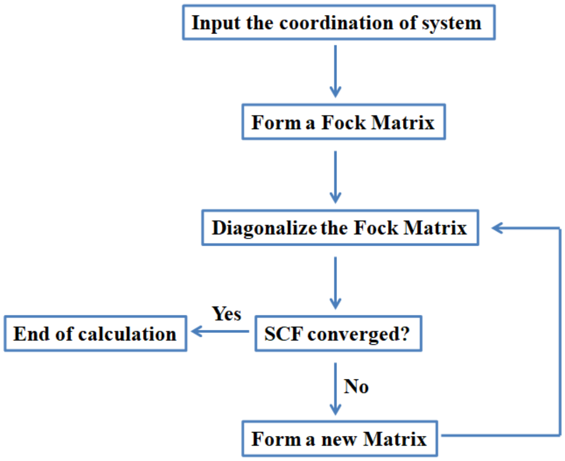

Figure 3.1: Illustration of SCF.

A general approach to treat correlation effect uses a truncated expansion of the wavefunction with several Slater determinants. Such an expansion can be constructed in several methods, like the Configuration Interaction (CI), Multi-Configuration Self Consistent Field (MCSCF), the Coupled-Cluster Method (CC). Static correlation is important for molecules where the ground state is well described with more than one Slater determinant. It is taken into account by multi-reference methods. Two families of methods take into account the dynamical correlation: the post-Hartree-Fock methods (for example: Configuration Interaction (CI), Coupled-Cluster Method (CC) and Moller-Plesset Perturbation Theory (MPx)) which add a correction to the Hartree-Fock result, and another approach called Density Functional Theory (DFT).

3.2 Density Functional Theory (DFT)

The Density Functional Theory (DFT) aims at the description of the polyatomic (molecular) systems on the basis of its electron density $\rho(r)$. For an ensemble of N electrons with the wavefunction Ψ, the electron density is defined as:

$$\rho(r) = N \int \cdots \int \mid \Psi \mid^2 dx_1 dx_2 \cdots dx_N \tag{3.11}$$

where x_i is the collective notation for the spatial and spin coordinate for the i-th electron.

DFT is a widely used approach nowadays for studies of large systems. An early precursor to modern DFT is the Thomas-Fermi (TF) model [71, 72] of a system with one nucleus and with many electrons. It is an instructive example of the kinetic energy of electrons, electron-nucleus and electron-electron interaction expressed as density functionals. The energy of electrons with the TF model is expressed as:

$$E[\rho] = T[\rho] + V_{eN}[\rho] + V_{ee}[\rho] \tag{3.12}$$

where $T[\rho]$ is the kinetic energy density functional, $V_{eN}[\rho]$ and $V_{ee}[\rho]$ are electron-nucleus and electron-electron density functionals respectively.

In order the describe the polyatomic systems in term of the electron density, an elaborate theoretical framework has been built upon two Hohenberg-Kohn Theorems.

3.2.1 Hohenberg-Kohn Theorems

The Density Functional Theory is based on the Hohenberg-Kohn theorems demonstrated by Hohenberg and Kohn in 1964 [73] which state that the ground state electronic energy E_0 is determined completely by the electron density in ground state ρ_0:

$$E_0 = E_0\left[\rho_0\right] \tag{3.13}$$

The first Hohenberg-Kohn theorem demonstrates that the ground state properties of a many-electrons system can be determined only by the ground state electron density, that is, the ground state electronic energy is the functional of electron density. The importance of this theorem is that the use of functionals of electron density can reduce the problem of N electrons with 3N spatial coordinates to only 3 spatial coordinates. The first Hohenberg-Kohn theorem had been extended to the case of excited states as well.

The second Hohenberg-Kohn theorem states that the functional $E\left[\rho\right]$ gives the lowest energy only if the density ρ is the same as that of the ground state. Thus, this density can be determined using the variational principle:

$$E\left[\rho\right] \geq E_0\left[\rho_0\right] \tag{3.14}$$

Based on these two Hohenberg-Kohn theorems, the energy of a polyatomic system is given by

$$E_v[\rho] = \int \rho(r)v(r)dr + F[\rho] \tag{3.15}$$

where $v(r)$ is the external potential felt by the electrons: $v(r) = V_{eN}[\rho]$ for an isolated molecular system. The functional $F[\rho]$ combines the kinetic energy $T[\rho]$ and the electron-electron interactions $V_{ee}[\rho]$:

$$F[\rho] = T[\rho] + V_{ee}[\rho] \tag{3.16}$$

3.2.2 Kohn-Sham Equation: KS-DFT

The Kohn-Sham Equation [74] is based on the idea that the many-body problem of interacting electrons could be resolved by making use of the system of non-interacting electrons in an effective potential. The effective potential includes the external potential and the Coulomb interaction between electrons which gives rise to the exchange and correlation. Specially, KS-DFT uses an ensemble of non-interacting electrons as a simple reference system and a new expression of $F\left[\rho\right]$ is donated:

$$F[\rho] = T_s[\rho] + J[\rho] + E_{xc}[\rho] \tag{3.17}$$

where $T_s[\rho]$ is the kinetic energy of the fictional system consists of particles without interaction and $J[\rho]$ accounts for classical Coulomb repulsion. $E_{xc}[\rho]$ is the exchange-correlation energy which is expressed as:

$$E_{xc}[\rho] = (T[\rho] - T_s[\rho]) + (V_{ee}[\rho] - J[\rho]) \tag{3.18}$$

The difficulty for KS-DFT is the actual exchange-correlation function $E_{xc}[\rho]$.

3.2.3 Approximation of Exchange-Correlation Functionals

The exact analytic expression of the functional $E_{xc}[\rho]$ is unknown. It is generally split into two separate terms, one is functional exchange which is associated with the electron-electron interaction energy of same spin $E_x[\rho]$ and the other is the correlation function $E_c[\rho]$ which is associated with the opposite spin electron-electron interaction:

$$E_{xc}[\rho] = E_c[\rho] + E_x[\rho] \tag{3.19}$$

LDA (Local Density Approximation)

The exchange-correlation functional in this approximation is expressed as:

$$E_{xc}^{LDA}[\rho] = \int \rho(r)\epsilon_{xc}(\rho)dr \tag{3.20}$$

where $\epsilon_{xc}(\rho)$ is the exchange-correlation energy per particle of a homogeneous electron gas of electron density ρ.

GGA (Generalized Gradient Approximation)

The electron density of the molecular and atomic compounds is generally non-homogeneous. The GGA approximation takes up the expression of LDA buy taking into account higher order terms, that is, by adding the gradient of electron density

$$E_{xc}^{GGA}[\rho] = \int \rho(r)\epsilon_{xc}^{GGA}(\rho, \nabla\rho)dr \tag{3.21}$$

Among the most widely used GGA functionals are the Becke 88 (B88) exchange functional, the Lee-Yang-Parr (LYP) correlation function, and the Perdew-Burke-Ernzerhof exchange-correlation functional (PBE), that takes important place in this GGA family, since it contains no empirical parameters. With the aim of improving these GGA functionals, it is possible to add supplementary density laplacian to improve the description of the electron density. These are the functionals of meta-GGA type.

Hybrid Functional

These functionals include a fraction of the exact nonlocal exchange energy as calculated in the Hartree-Fock theory. These hybrid methods have been extensively tested on the GGA functional and generally lead to a significant improvement in the accuracy of the results.

Example of hydrid functional: B3LYP

In 1993, Becke suggested the hybrid B3LYP functional. B3LYP exchange-correlation energy is expressed by a combination of Becke 88 (B88) exchange and Lee-Yang-Parr (LYP) correlation GGA functionals, Slater (S) exchange [75] and Vosko-Wilk-Nusair (VWN) correlation LDA functionals [76] and the HF exchange integral with 3 parameters:

$$E_{xc}^{B3LYP} = a_0 E_x^{HF} + (1 - a_0) E_x^S + a_x E_x^{B88} + (1 - a_c) E_c^{VWN} + a_c E_c^{LYP} \tag{3.22}$$

where a_0, a_x and a_c are 0.2, 0.72 and 0.81 respectively. B3LYP becomes one of the most popular DFT functionals in quantum chemistry because it gives relatively accurate results for a wide variety of chemical properties.

Long-range-corrected functional

The practical applications of Kohn-Sham density functional theory usually use local or semilocal approximations to the exchange-correlation functional. All the approximations have a common set of deficients, among which self-interaction error (that is defined as inexactness for one-electron densities) may be the most important. [77] In addition, the long-range behavior of the exchange-correlation potential is incorrect. The uniform addition of a part of the exact exchange from the Hartree-Fock model makes it possible to reduce only partially the self-interaction error. Thus, another category of functional has been developed, which are called the long-range corrected functional. The percentage of Hartree-Fock exchange, unlike conventional hybrid functionals, increases with the inter-atomic distance. [78–80] This growth will be governed by the ω, as shown by the following expression:

$$\frac{1}{r_{12}} = \frac{erf(\omega r_{12})}{r_{12}} + \frac{1 - erf(\omega r_{12})}{r_{12}} \tag{3.23}$$

where erf is the error function and $r_{12} = \mid r_1 - r_2 \mid$. The parameter ω defines the speed at which the value of 1 will be reached by this error function. So the bigger the ω value will be, the larger the transition from the Kohn-Sham exchange to the exact exchange Hartree-Fock will be. The upper equation has been generalized by Yanai *et al.* by introducing two new parameters α and β: [81]

$$\frac{1}{r_{12}} = \frac{\alpha + \beta erf(\omega r_{12})}{r_{12}} + \frac{1 - [\alpha + erf(\omega r_{12})]}{r_{12}} \tag{3.24}$$

where $0 \leq \alpha + \beta \leq 1$, $0 \leq \alpha \leq 1$ and $0 \leq \beta \leq 1$.

There are also functionals that are corrected at medium range. Their repulsion electronic operator has the following expression: [82, 83]

$$\frac{1}{r_{12}} = \frac{1 - erf(\omega_{SR} r_{12})}{r_{12}} + \frac{erf(\omega_{LR} r_{12})}{r_{12}} + \frac{[1 - erf(\omega_{LR} r_{12})] - [1 - erf(\omega_{SR} r_{12})]}{r_{12}} \tag{3.25}$$

with ω_{SR} and ω_{LR} the attenuation parameters at *short range* and at *long range* respectively.

The long-range correction was shown to improve the properties such as polarizability of long chains [84] and the dissociation of 2-center 3-electron bonds, for instance. [79]

Example of Long-range-corrected functional: LC-ωPBE

The exchange-correlation energy of PBE0 hybrid functional [85–88] was expressed as the following form:

$$E_{xc}^{PBE0} = 0.25E_x^{HF} + 0.75E_x^{PBE} + E_c^{PBE} \tag{3.26}$$

This hybrid functional is based on the PBE exchange-correlation functional by Perdew *et al.* [89, 90] To split all the exchange terms from the PBE0 exchange-correlation energy into their short- and long-range components, we have:

$$E_x^{PBE0} = aE_x^{HF,SR}(\omega) + aE_x^{HF,LR}(\omega) + (1-a)E_x^{PBE,SR}(\omega) + (1-a)E_x^{PBE,LR}(\omega) \tag{3.27}$$

Numerical tests based on realistic ω values show that the HF and PBE long-range exchanges, $aE_x^{HF,LR}(\omega)$ and $-aE_x^{PBE,LR}(\omega)$ terms respectively, contribute only a few percent to this functional. [91] In addition, these long-range exchange terms can cancel each other, making them negligible. An approximation may be introduced and we get a screened Coulomb potential hybrid density functional:

$$E_{xc}^{\omega PBE} = aE_x^{HF,SR}(\omega) + (1-a)E_x^{PBE,SR}(\omega) + E_x^{PBE,LR}(\omega) + E_c^{PBE} \tag{3.28}$$

where ω is an adjustable parameter governing the extent of short-range interactions. When ω value vanishes, this functional is equivalent to PBE0, and when $\omega \to \infty$, it will reach the PBE functional.

3.3 Inclusion of dispersion in DFT methods

The poor reproducibility of weak interaction like van der Waals interactions including London dispersion forces is one of the most important challenges with current DFT methods. [92] The dispersion forces can be empirically defined as the attractive part of a van der Waals interaction between atoms or molecules that are weakly bonded. The London dispersion interactions is given by the well-known $-\frac{C_6}{R^6}$ dependence in long-range distances. All common GGA functionals, including hybrid functionals, can not describe long-range electron correlations that are responsible for dispersive forces. [93] For a complex system, the poor reproducibility of such an attractive interaction my lead to the poor description of reaction barriers. The demands for improving the existing DFT methods to access a good description of van der Waals interactions has now become a very important field.

3.3.1 Grimme's dispersion correction: DFT-GD

An empirical-corrected method to take into account the van der Waals interactions in practical DFT calculations was introduced by Stefan Grimme. [93, 94] In DFT-GD method, a correction to standard functionals is introduced:

$$E_{MF-D} = E_{MF} + E_{disp} \tag{3.29}$$

where E_{MF} represents the usual meanfield energy (i.e. HF or DFT) and E_{disp} is the empirical dispersion correction. This empirical correction is given by:

$$E_{disp} = -S_6 \sum_{i=1}^{N_{atoms}-1} \sum_{j=i+1}^{N_{atoms}} \frac{C_6^{ij}}{R_{ij}^6} f_{damp}(R_{ij}) \tag{3.30}$$

where N_{atoms} is the number of atoms in the system, C_6^{ij} is the dispersion coefficient for atom pair ij with the interatomic distances R_{ij} and S_6 is the global scaling factor which only depends on the functional used. To avoid singularities for small R in the dispersion energy, a damping function $f_{damp}(R_{ij})$ is introduced:

$$f_{damp}(R_{ij}) = \frac{1}{1 + exp[-\alpha(R_{ij}/R_0 - 1)]} \tag{3.31}$$

In this expression, R_0 is the sum of the atomic van der Waals radii. It decays at small R fast to zero so that the dispersion forces between atoms with interatomic distances below van der Waals radii are negligible.

The up to date DFT-GD3 method (third version) has shown a significant improvement over the previous developed DFT-GD2 methods (second version), which is characterized by higher accuracy, a broader range of applicability and less empiricism compared to the DFT-GD2 method. [95] The dispersion correction with GD3 version is given by:

$$E_{disp} = -\sum_{i=1}^{N_{atoms}-1} \sum_{j=i+1}^{N_{atoms}} \sum_{g} [f_{d,6}(R_{ij,g}) \frac{C_{6,ij}}{R_{ij,g}^6} + f_{d,8}(R_{ij,g}) \frac{C_{8,ij}}{R_{ij,g}^8}] \tag{3.32}$$

For the reason that the $f_{d,6}$ and $f_{d,8}$ damping functions were constructed to approach zero when the inter-atomic distances vanish, a shortcoming of this method is that at small and medium distances, the atoms experience repulsive forces. The repulsive forces lead to even longer inter-atomic distances than those obtained without dispersion corrections. Becke and Johnson proposed the DFT-GD3(BJ) method which contains modified expressions for the $f_{d,6}$ and $f_{d,8}$ damping functions that lead to a constant contribution of dispersion energy to the total energy when $R_{ij} = 0$. The DFT-GD3(BJ) method provides an improved description of the weakly bonded structures and energies.

3.3.2 APF-D method

In 2012, Frisch and Petersson proposed the Austin-Petersson-Frisch functional (abbreviated as APF), which is a mixture of 41.1% B3PW91 and 58.9% PBE0 functionals. This functional “avoids the spurious long-range attractive or repulsive interactions that are found in most density functional theory (DFT) models”. [96] An addition of an empirical dispersion correction term is developed by a spherical atom model (SAM), which constitutes the APF-D method, also known as APF-PFD (Petersson-Frisch-Dispersion).

The authors considered this method to calculate the binding energy and geometrical structures of rare gas dimers, together with some small molecules dimers, and the obtained results were comparable to CCSD(T)/aug-cc-pVTZ calculations. [96] For the systems under consideration, in order to remove the spurious long-range interactions, the B3PW91 functional which shows consistent repulsive behavior both at intermediate and long distances, together with the PBE0 which shows consistent attraction in the same distance ranges, are combined in APF functional.

As it was shown in Equation 3.29, an empirical dispersion E_{disp} term is always demanded for such method.

An empirical term based on the Spherical Atom Model (SAM) for dispersion interactions is then developed to complete the APF-D method. The dispersion interaction is evaluated between two spherical shells of polarizable material A and B, and the radii of these were defined as $r_{s,A}$ and $r_{s,B}$. The interatomic potential can be given by:

$$V^{SAM}\left(R_{AB}\right) = \frac{C_{6,AB}}{\left[R_{AB}^2 - \left(r_{s,A} + r_{s,B}\right)^2\right]^3} \tag{3.33}$$

Taylor series expansion is used to expand this expression to:

$$V\left(R_{AB}\right) \approx \frac{C_{6,AB}}{R_{AB}^6}\left[1 + 3\left(\frac{r_{s,A} + r_{s,B}}{R_{AB}}\right)^2 + 6\left(\frac{r_{s,A} + r_{s,B}}{R_{AB}}\right)^4 + \cdots\right] \tag{3.34}$$

This equation diverges when R_{AB} goes to $r_{s,A} + r_{s,B}$. A suitable damping function $f\left(R_{AB}\right)$ is introduced since the interatomic potential does not describe the interactions at short-range:

$$f\left(R_{AB}\right) = \begin{cases} 0 & R_{AB} \leq R_{d,AB} \\ \left[1 - \left(1 + 2\frac{R_{AB} - R_{d,AB}}{R_{d,AB}}\right) \times e^{-4\left(\frac{R_{AB} - R_{d,AB}}{R_{d,AB}}\right)}\right]^2 & R_{AB} > R_{d,AB} \end{cases} \tag{3.35}$$

The SAM empirical dispersion potential is thus proposed as following by the authors:

$$V^{SAM}\left(R_{AB}\right) = \begin{cases} 0 & R_{AB} \leq R_{d,AB} \\ \frac{C_{6,AB}}{\left[R_{AB}^2 - R_{d,AB}^2\right]^3} f\left(R_{AB}\right) g\left(R_{AB}\right) & R_{AB} > R_{d,AB} \end{cases} \tag{3.36}$$

where $R_{d,AB} > R_{s,AB}$ and $g(x)$ is a switching function developed for the numerical quadrature in DFT. [97]

The empirical dispersion interactions are thus given by the sum of SAM potential in this APF-D model:

$$E_{disp} = \sum_{A>B} V^{SAM}\left(R_{AB}\right) \tag{3.37}$$

The APF-D model herein presented was designed and calibrated using a diverse sets of small molecules including rare gas dimers, argon complexes with nonpolar molecules and dimers of small hydrocarbons. Binding energies calculated within this model are found to be typically overestimated by up to 10% at shorter distances for dimers of larger molecules. In order to reduce the errors in describing the hydrogen bonded complexes and other larger complexes, further efforts should be promoted with this model.

Chapter 4

Wave function analysis in the real molecular space

4.1 QTAIM (Quantum Theory of Atoms in Molecules)

The Atoms in Molecules (AIM) theory or the Quantum Theory of Atoms in Molecules (QTAIM) [98] is based on the partitioning of the molecular electron density in real space. In the QTAIM formalism, two interacting atoms share three topological elements in an equilibrium geometry:

- BCP (Bond Critical Point) in electron density topology for which $\overrightarrow{\nabla}\rho(r) = \overrightarrow{0}$;
- BP (Bond Path), a line along which $\rho(r)$ is a maximum with respect to any neighboring line;
- IAS (InterAtomic Surface), formed by trajectories terminating at a BCP which separates the atomic basins of the neighboring atoms.

The QTAIM topological analysis of a chemical compound (molecule or crystal) enable us to answer in a clear and unambiguous manner to the following questions: [99]

- What is an atom in a molecule or a crystal?
- How can an atom or a group of atoms be transferable in an external potential?
- Can one define bonding in molecules unambiguously especially in borderline cases?

4.1.1 The topology of electron density

The critical point (CP) of electron density is a point in the molecular space at which the first derivative of electron density vanishes:

$$\overrightarrow{\nabla}\rho\,(r) = \overrightarrow{i}\frac{d\rho}{dx} + \overrightarrow{j}\frac{d\rho}{dx} + \overrightarrow{j}\frac{d\rho}{dx} = \overrightarrow{0} \qquad (4.1)$$

Considering the second derivative of electron density, we can discriminate between the local maximum, local minimum and saddle points. The Hessian matrix, second partial derivatives at a critical point r_c of the electron density, is given by the following:

$$A\left(r_c\right)=\left(\begin{array}{ccc} \frac{\partial^2\rho}{\partial x^2} & \frac{\partial^2\rho}{\partial x\partial y} & \frac{\partial^2\rho}{\partial x\partial z} \\ \frac{\partial^2\rho}{\partial y\partial x} & \frac{\partial^2\rho}{\partial y^2} & \frac{\partial^2\rho}{\partial y\partial z} \\ \frac{\partial^2\rho}{\partial z\partial x} & \frac{\partial^2\rho}{\partial z\partial y} & \frac{\partial^2\rho}{\partial z^2} \end{array}\right)_{r=r_c} \tag{4.2}$$

and its diagonalized form is:

$$H(r_c)=\left(\begin{array}{ccc} \frac{\partial^2\rho}{\partial x'^2} & 0 & 0 \\ 0 & \frac{\partial^2\rho}{\partial y'^2} & 0 \\ 0 & 0 & \frac{\partial^2\rho}{\partial z'^2} \end{array}\right)_{r'=r_c}=\left(\begin{array}{ccc} \lambda_1 & 0 & 0 \\ 0 & \lambda_2 & 0 \\ 0 & 0 & \lambda_3 \end{array}\right) \tag{4.3}$$

where λ_1, λ_2 and λ_3 are the eigenvalues of this matrix and also the curvatures of the electron density with respect to the three directions. Curvatures are positive at the minimum points and negative at maximum ones. The trace of this Hessian matrix of electron density is:

$$\nabla^2\rho\left(r\right)=\underbrace{\frac{\partial^2\rho}{\partial x^2}}_{\lambda_1}+\underbrace{\frac{\partial^2\rho}{\partial y^2}}_{\lambda_2}+\underbrace{\frac{\partial^2\rho}{\partial z^2}}_{\lambda_3} \tag{4.4}$$

A critical point is characterized by two number related to the curvatures: the rank of this matrix *rank*(ω) and the signature (the algebraic sum of the signs of curvatures) of matrix *signature*(σ). Each critical point is marked as a set of rank and signature as (ω, σ). Mathematically, a critical point with $\omega < 3$ is unstable. It can be vanished when presence of a little perturbation of electron density caused by a nuclear motion. For this reason, there is no critical points with $\omega < 3$ in the equilibrium state. Therefore, there are four types of stable critical points having three non-zero eigenvalues:

Table 4.1: Descriptions of different types of critical point

(ω, σ)	Description	Type of Critical Point
$(3, -3)$	Three negative curvatures: a local maximum	NCP (Nuclear Critical Point)
$(3, -1)$	Two negative curvatures: ρ(r) is a maximum in the plane defined by the corresponding eigenvectors but a minimum along the third axis which is perpendicular to this plane.	BCP (Bond Critical Point)
$(3, +1)$	Two negative curvatures: ρ(r) is a minimum in the plane defined by the corresponding eigenvectors but a maximum along the third axis which is perpendicular to this plane.	RCP (Ring Critical Point)
$(3, +3)$	Three positive curvatures: a local maximum	CCP (Cage Critical Point)

The number and type of critical points that can coexist in a molecule or in a crystal must strictly follow the topological relationship known as the Poincaré–Hopf [98] relationship for an isolated molecule and Morse equation [100] for infinite crystals as followed:

$$n_{NCP} - n_{BCP} + n_{RCP} - n_{CCP} = \begin{cases} 1 & (Isolated\ molecules) \\ 0 & (Infinit\ crystals) \end{cases} \tag{4.5}$$

where n denotes the number of critical points corresponding to the index.

4.1.2 Zero-flux surface and bond paths

The topology of the electron density dictates the shape of atoms in molecules. There exist several surfaces called zero-flux surface $S(\Omega)$ which separate the molecule 3D space into several mononuclear regions marked as Ω. On its surface, the gradient of electron density vanishes. For all the vector of positions $\overrightarrow{r}$, on this surface we have:

$$\overrightarrow{\nabla}\rho(r) \cdot \overrightarrow{n}(r) = 0 \tag{4.6}$$

where $\overrightarrow{n}(r)$ is the unit vector normal to the zero-flux surface $S(\Omega)$. The presence of an inter-atomic zero-flux surface between two bonded atoms is always accompanied by another topological feature, the Bond Path (BP). It is a line between two local maxima of the electron density and it serves as an indicator of chemical bindings. In the Figure 4.1 is shown the 2D isocurves of electron density of C_2H_4 as an example. A bond critical point (green points) can be found in the junction of an inter-atomic zero-flux surface (black dotted line) and a bond bath (black bold lines).

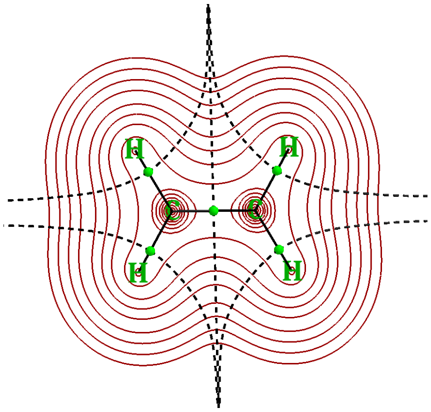

Figure 4.1: 2D isosurface of electron density of C_2H_4.

4.1.3 Properties of bond critical point (BCP)

The interactions between bonded atoms can be characterized and classified according to the properties of the electron density and the energy density at the bond critical point (BCP).

Electron density: ρ

The electron density ρ at BCP provides a measure of strength of a chemical bond. Generally, for a shared-interaction, that is for a covalent bond, the electron density at BCP is found higher than 0.10 a.u., [101] while the ρ(BCP) for a closed-shell interaction (ionic interaction, hydrogen bond, van der Waals interactions ...) has always been found smaller than 0.10 a.u.

Laplacian of electron density: $\nabla^2\rho$

The QTAIM theory provides not only a method to identify the chemical bonds, but also allows for characterization and classification of different bonding situations. The property that Bader has examined for this purpose is the Laplacian of the electron density at the bond critical point (BCP). [102] The Laplacian distribution of a molecular charge demonstrates the existence of local concentrations of electron density in both the bonded and non-bonded regions.

The Laplacian value at a bond critical point is of great importance for the identification of a chemical bond. It has been already shown in Table 4.1 that the second derivative of electron density at a BCP has a positive eigenvalue and two negative eigenvalues. The Laplacian of electron density at the BCP is the sum of the three curvatures at three directions (See Equation 4.4), the two perpendicular to the bond path, λ_1 and λ_2, being negative (by convention $|\lambda_1| > |\lambda_2|$), whereas the third curvature, λ_3, lying along the bond path, is positive. According to the relative values of λ_1, λ_2 and λ_3, the Laplacian at BCP can be either positive or negative. The negative curvatures measure the extent to which the density is concentrated along the bond path and the positive one measures the extent to which it is depleted in the region of the interatomic surface and concentrated in the individual atomic basins. [99]

A negative value of Laplacian $\nabla^2\rho < 0$ indicates that the negative curvatures λ_1 and λ_2 are dominant, which means the electron density is concentrated between two atoms. A covalent bond is thus identified in this case. For a positive Laplacian, λ_3 will be the dominant curvature and the electron density in this case is concentrated far from the interatomic region. Closed-shell interactions including ionic interactions, hydrogen bondings and van der Waals interactions are probably found in this case. Figure 4.2 shows the contours of the Laplacian of electron density of C_2H_4 molecule. The regions with negative Laplacian are marked in solid blue line, indicating a charge concentration region. The solid red lines around C atoms demonstrate a positive value of Laplacian, where a charge depletion region is displayed. BCPs are identified in the charge concentration region, indicating the presences of covalent bonds in this situation.

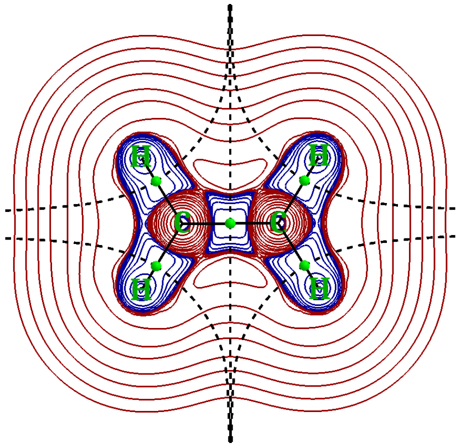

Figure 4.2: Laplacian of electron density isosurface of C_2H_4. Blue solid lines: $\nabla^2\rho < 0$ (Charge concentration region); red solid line: $\nabla^2\rho > 0$ (Charge depletion region).

In Figure 4.3 is shown the contours of the Laplacian of electron density isosurface of Al−C_2H_4 system. A BCP is also identified between the aluminium atom and the C_2H_4 molecule. Differently, this BCP locates in the charge depletion region, where the Laplacian value is positive. A weak interaction is thus proposed between Al and C_2H_4 in this system.

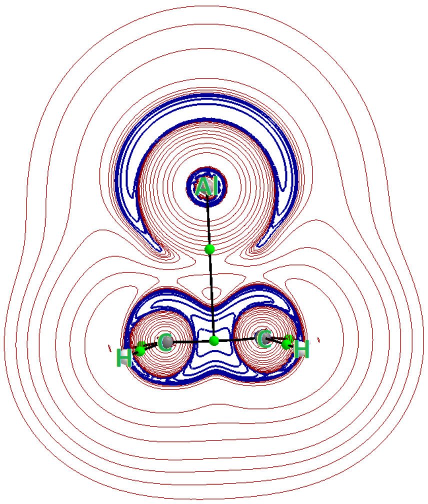

Figure 4.3: Laplacian of electron density isosurface of Al−C_2H_4 system. Blue solid lines: $\nabla^2\rho < 0$ (Charge concentration region); red solid line: $\nabla^2\rho > 0$ (Charge depletion region).

Ellipticity: ϵ

The ellipticity ϵ, that features the extent to which electron density is preferentially accumulated in a given plane containing the bond path, is given as:

$$\epsilon = \frac{\lambda_1}{\lambda_2} - 1 \tag{4.7}$$

where $|\lambda_1| \geqslant |\lambda_2|$.

This parameter provides a quantitative measurement of the anisotropy of the electron density at the BCP. The ellipticity has been originally associated to the π character of bonds, and therefore, it has been also employed as a measurement of delocalization and, ultimately, aromaticity. The number of applications of this parameter, however, has increased significantly in recent years and studies on the description of unusual bonds in charge transfer interactions, steric contacts, organometallic complexes, etc include the ellipticity as a useful chemical index.

Energy density: H

It is demonstrated that the Laplacian of electron density appears in the local expression of the virial theorem:

$$\left(\frac{\hbar}{4m}\right)\nabla^2\rho\left(r\right) = 2G\left(r\right) + V\left(r\right) \tag{4.8}$$

where $G\left(r\right)$ is the kinetic energy density and $V\left(r\right)$ is the potential energy density.

It is always known that $G\left(r\right) > 0$ and $V\left(r\right) < 0$. This equation thus demonstrates that the lowering of the potential energy $V\left(r\right)$ dominates the total energy in those regions of space where electronic charge is concentrated, where $\nabla^2\rho < 0$, while the kinetic energy is dominant in regions where $\nabla^2\rho > 0$.

The total electronic energy density was proposed:

$$H\left(r\right) = G\left(r\right) + V\left(r\right) \tag{4.9}$$

to compare the kinetic and the potential energy density. For a given bond critical point, the total energy density is: $H_{BCP} = G_{BCP} + V_{BCP}$

Unlike the Laplacian, whose sign is determined by the local virial expression (Equation 4.8), the sign of H_{BCP} is determined by the energy density itself and is found to be negative for all interactions which result from the accumulation of electron density at the BCP. [98]

4.1.4 Atomic properties

As an atom in molecule is a well-defined topological object, the atomic properties can be therefore determined. The atomic volume is the simplest property, which is defined as the space bounded by the zero-flux surface and the $\rho = 0.001$ a.u. contour when a molecule extends to infinity. The outer isodensity is chosen for $\rho = 0.001$ a.u. is due to the following two reasons: [98]

- This isosurface closely recovers the experimental van der Waals volume in the gas phase;
- It usually covers more than 99% of the electron population of a molecule.

The total electron population (charge) of an atom in molecule is given by:

$$N\left(\Omega\right) = \int_{\Omega}\rho\left(r\right)dr \tag{4.10}$$

It is obtained by integrating the electron density of a given volume over the atomic basin.

The atomic charge $q(\Omega)$ is obtained by the subtracting of electron population $N(\Omega)$ from the nuclear charge Z_Ω:

$$q(\Omega) = Z_\Omega - N(\Omega) \tag{4.11}$$

4.2 ELF (Electron Localization Function)

The Electron Localization Function (ELF) was introduced by Becke and Edgecombe in 1990 [103] which describes how much the Pauli repulsion is efficient at a given point of molecular space. In the study of the electron correlations, it was realized that, because of the Pauli principle, the movement of electrons of the same spin is more strongly correlated than the one between electrons of different spins.

4.2.1 Definition of Electron Localization Function

The probability of finding an electron of spin σ at a point $\overrightarrow{r_1}$ when a second electron of spin σ' is found at point $\overrightarrow{r_2}$ is proposed as : $\rho_2^{\sigma\sigma'}(\overrightarrow{r_1}, \overrightarrow{r_2})$. [104]

To reduce the number of variables of the electron interaction, the coordinate system was redefined as :

$$\overrightarrow{r} = \frac{1}{2}(\overrightarrow{r_1} + \overrightarrow{r_2}) \tag{4.12}$$

$$\overrightarrow{s} = (\overrightarrow{r_1} - \overrightarrow{r_2}) \tag{4.13}$$

The six variables were reduced into four variables: $\overrightarrow{r}$ and s. Hence, only the spherical average electron pair density is considered:

$$\rho_2^{\sigma\sigma'}(\overrightarrow{r_1}, s) = \frac{1}{4\pi}\int \rho_2^{\sigma\sigma'}(\overrightarrow{r_1}, s)\, d\Omega_s \tag{4.14}$$

Becke and Edgecombe [103] introduced a conditional probability of finding an electron at position $\overrightarrow{r_2}$ when there appeared an electron of the same spin at position $\overrightarrow{r_1}$. This probability is given by:

$$P^{\sigma\sigma'}(\overrightarrow{r}, s) = \frac{\rho_{2,av}^{\sigma\sigma'}(\overrightarrow{r}, s)}{\rho_\sigma(\overrightarrow{r})} \tag{4.15}$$

where $\rho_\sigma(\overrightarrow{r})$ is the electron density with spin with the Kohn-Sham approximation.

The Taylor Series expansion of this spherical average conditional pair density in the vicinity of $s = 0$ is know as:

$$P^{\sigma\sigma'}(\overrightarrow{r}, s) = \frac{1}{3}\left(\tau_\sigma - \frac{1}{4}\frac{(\nabla\rho_\sigma)^2}{\rho_\sigma}\right)s^2 + \cdots\cdots \tag{4.16}$$

It is convenient that the electron is found to be localized when the probability of finding a second electron with the same spin near the position where the reference electron is located is approaching to zero. A parameter D_σ is introduced to qualitatively describe this probability:

$$D_\sigma = \tau_\sigma - \frac{1}{4}\frac{(\nabla\rho_\sigma)^2}{\rho_\sigma} \tag{4.17}$$

D_σ vanishes only for H atom. A small value of D_σ indicates a region of space where the probability of finding a localized electron or a localized electron pair is really high. To simplify this average conditional pair density, Becke and Edgecombe proposed the following rule:

$$ELF = \left(1 + \chi_\sigma^2\right)^{-1} \tag{4.18}$$

where $\chi_\sigma = \frac{D_\sigma}{D_\sigma^0}$ and D_σ^0 is defined as the kinetic energy density of the homogeneous electron gas. In this way, we can also obtain that:

$$0 \leq ELF \leq 1 \tag{4.19}$$

As shown in Equation 4.19, the value of ELF can be found between 0 and 1. When the ELF value approaches to 1, it refers to a region of space where there is a very high probability of finding the electron localization. ELF value of 1 corresponds to perfect localization. When ELF reaches 0.5, this indicates a region with electron gas-like behaviors.

The ELF can be obtained by the calculation of electron density. Apart from the computational approaches, the electron density can also be obtained by means of experimental data. There has been approximative determination of ELF to use the electron density obtained by X-ray diffraction. [105] An important feature of ELF is the numerical stability. ELF stability can be understood as the qualitative attribute of the total electron density, and its independence with calculation levels. Of course, the calculation results of the expected value of the electron density, and the other characters of the density may be different, but their maximum, minimum position, particularly the position of the critical points are almost the same.

4.2.2 Topological analysis of Electron Localization Function

The topological analysis of ELF was proposed by Silvi and Savin [106], which allows a spatial partitioning of a molecule. It has been extensively used for study of chemical bonding [106], aromaticity problems [107], reactivity [108, 109] and chemical reactions. [110, 111]

The topological concept of domain was introduced to chemistry by P. Mezey in 1994. [112] In the context of ELF topological analysis, the concept of domain is of great importance, because it enables the definition of chemical units within a system and characterization of the valence domains belonging to a given chemical unit. A location domain is defined as a region delimited by a f value of the isosurface of the ELF function.

At low ELF values, all basins are contained in their respective localization domain. When the isosurface values become higher, the basins begin to split. At a certain ELF isosurface value, all the basins are found to be separated. This process is followed by a bifurcation. The bifurcation have be interpreted as a measure of the interaction among different basins and it provides also a measure of electron localization. [113] In Figure 4.4 are shown the representative ELF isosurface values for benzene molecule as an example.

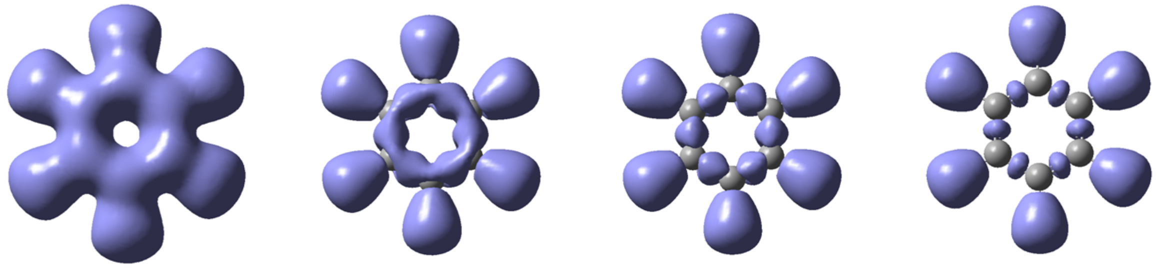

ELF = 0.50

ELF = 0.63
Bifurcation

ELF = 0.68
Bifurcation

ELF = 0.80

Figure 4.4: Localization domains of benzene molecule for different ELF isosurface values. The B3LYP/6-31G** level of theory was used for this example.

The graphical representations of the localization domains as a function of ELF values reveal that the domains merge with a low ELF value. When the isosurface value increases, the reducible domain splits into several domains. The V(C,H) basins appears when the isosurface value reaches to 0.63. The separation of the remaining reducible domain into irreducible domains which correspond to the C-C valence basins is then found when this value reaches 0.68. The bifurcation diagram of the benzene molecule is shown in Figure 4.5.

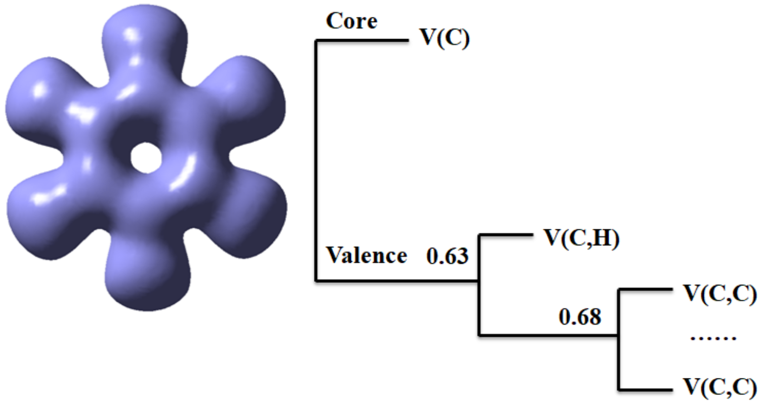

Figure 4.5: Bifurcation diagram corresponding to the ELF analysis of benzene molecule optimized with B3LYP/6-31G** level of theory.

4.2.3 Combined QTAIM and ELF analysis

The projection of the ELF basins onto the QTAIM ones enables us to determine the atomic contribution in every ELF valence basin. Figure 4.6 demonstrates an example of QTAIM and ELF basin analysis for CH_3CN molecule. The ELF topological approach makes it possible to identify the basins of core and valence associated with each atom as well as the population of each basin. In this case, the QTAIM analysis leads to the definition of the atomic surfaces, which divides the geometrical volume into different atoms. Each basin can be projected on each of the atomic surfaces, which allows to determine the atomic contribution in a given basin.

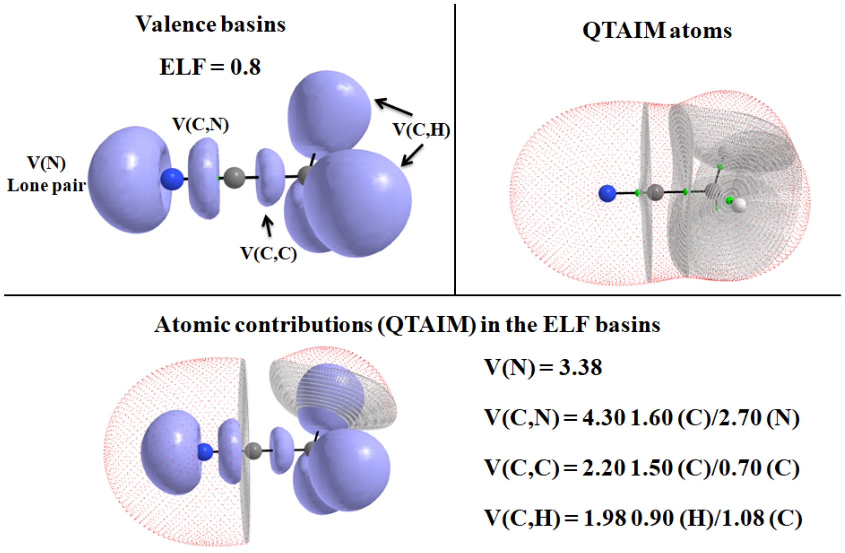
Valence basins
ELF = 0.8
V(C,N)
V(C,H)
V(N)
Lone pair
V(C,C)
QTAIM atoms
Atomic contributions (QTAIM) in the ELF basins
V(N) = 3.38
V(C,N) = 4.30 1.60 (C)/2.70 (N)
V(C,C) = 2.20 1.50 (C)/0.70 (C)
V(C,H) = 1.98 0.90 (H)/1.08 (C)

Figure 4.6: QTAIM and ELF basin analysis for CH_3CN molecule. For clarity, only two QTAIM atomic surfaces (H and N) are shown. [114]

4.3 NBO (Natural Bond Orbital)

Introduction

The concept of natural orbital was firstly defined by Löwdin in 1955 [115] to describe the unique set of orthonormal one-electron functions that are intrinsic to the N-electron wavefunction. It may be used for electron distribution into atomic and molecular orbitals, and thereby deriving atomic charges and molecular bonds. The Natural Atomic Orbital (NAO) and Natural Bond Orbital (NBO) analysis were developed by Weinhold *et al.* [116] who use the one-electron density matrix to define the shape of the atomic orbitals in molecular environment and to derive molecular bonds from electron density between atoms.

NBO analysis is based on a method for optimally transforming a given wavefunction into localized form, which corresponds to the one-center "lone pair" and two-center "bond" elements of the chemist's Lewis structure picture. The NBOs are obtained as local block eigenfunctions of the density matrix, having optimal convergence properties for describing the electron density. The set of high-occupancy NBOs, each taken doubly occupied, represents the "Natural Lewis Structure" (NLS). Delocalization effects appear as weak departures from this idealized localized picture.

NBOs can be described as a "chemist's basis set" that would correspond closely to the picture of localized bonds and lone pairs as basic units of molecular structures. [116]

The various natural localized sets can be considered to result from a sequence of transformations of the input atomic orbital basis set as shown in Figure 4.7 that includes NAOs (Natural Atomic Orbitals), NHOs (Natural Hybrid Orbitals), Natural Bond Orbitals (NBOs) and NLMOs

(Natural (semi-)Localized Molecular Orbitals).

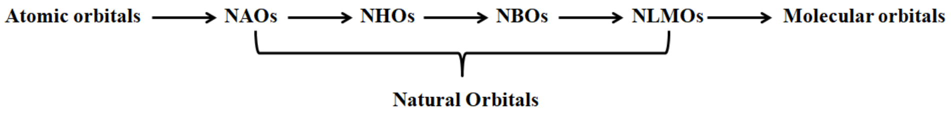

Figure 4.7: Overview of the basis sets between atomic orbitals and molecular orbitals.

For a localized σ bond σ_{AB} and antibond σ^*_{AB}, the NBO basis is generated directly by the linear combination of hybrids orbitals: NHOs h_A and h_B:

$$\sigma_{AB} = c_A h_A + c_B h_B \tag{4.20}$$

$$\sigma^*_{AB} = c_B h_A - c_A h_B \tag{4.21}$$

The coefficient c_A and c_B must satisfy the condition: $c_A^2 + c_B^2 = 1$. The NHOs are each made up by the optimized linear combination of NAOs.

The bonding NBOs are of the "Lewis orbital"-type (occupation numbers near 2) while the antibonding NBOs are of the "non-Lewis orbital"-type (occupation numbers near 0). In an idealized Lewis structure, full Lewis orbitals (two electrons) are complemented by formally empty non-Lewis orbitals. The main distinguishing feature of NBOs is the simultaneous demand for the orthonormality and the maximum occupancy, leading to compact expressions for atomic and bond properties. The NBO method is considered to translate the calculations into chemical insights, including the following concepts such as: [117]

- Atomic charge,
- Lewis structure,
- Nature of bond (covalent or ionic, σ or π,etc.),
- Hybridization,
- Charge transfer,
- Bond order, etc.

4.3.1 Perturbation theory energy analysis

In NBO analysis, the interaction and its energy between the occupied NBO (donor orbital) and empty NBO (acceptor orbital) can be estimated by second-order perturbation theory.

Figure 4.8 describes the interaction of an occupied orbital $\Phi_i^{(0)}$ of the Lewis structure with the empty orbital antibonding orbital $\Phi_{j^*}^{(0)}$ to give a second-order energy stabilization $\Delta E^{(2)}_{i \to j^*}$. The donor-acceptor stabilization energy associated with the $i \to j^*$ delocalization is estimated as follows:

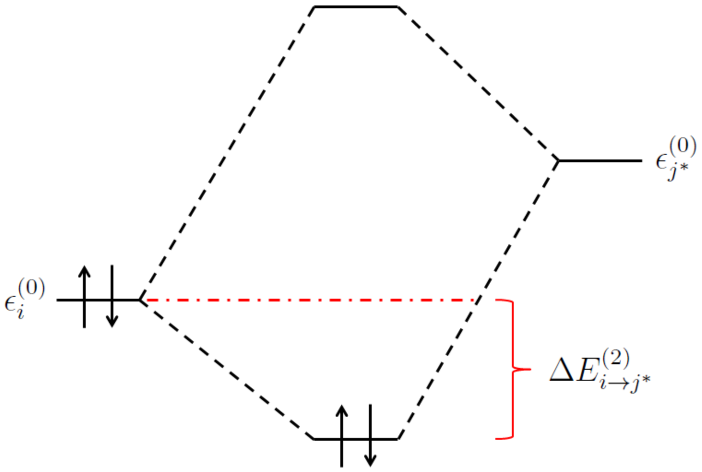

Figure 4.8: Two-electron stabilizing interaction between an occupied donor orbital $\Phi_i^{(0)}$ and an empty acceptor orbital $\Phi_{j^*}^{(0)}$.

$$\Delta E_{i\to j^*}^{(2)} = -n_i^{(0)} \frac{\left\langle \Phi_i^{(0)} \middle| \hat{F} \middle| \Phi_{j^*}^{(0)} \right\rangle^2}{\epsilon_{j^*}^{(0)} - \epsilon_i^{(0)}} \tag{4.22}$$

where $n_i^{(0)}$ is the number of electrons (2 for closed-shell and 1 for open-shell) occupying the spatial orbital $\Phi_i^{(0)}$, $\hat{F}$ is the Fock operator and $\epsilon_{j^*}^{(0)}$ and $\epsilon_i^{(0)}$ are the NBO orbital energies for the antibonding orbital and the occupied orbital, respectively.

The NBO perturbation theory energy analysis allows to apply qualitative concepts of valence theory to describe the noncovalent energy lowering.

Part III

Theoretical Assessment of Amine-borane Dehydrogenation Process

Chapter 5

Earlier experimental and theoretical studies of the reaction pathway: inconsistency proposals

Introduction

Transition-metal-catalyzed dehydrogenation/dehydrocoupling reactions of ammonia borane and its related amine-boranes or phosphine-boranes have been considered specifically for the synthesis of new materials and polymers with B-N (or B-P) backbones [118–121] as well as the potential applications for the hydrogen storage. [122, 123] Diverse catalysts have been developed to promote this kind of reaction, a lot of which are based on the homogeneous catalysis because the reaction processes can be easily controlled by modifying different parameters. The use of homogeneous catalysis is also helpful for fundamental researches, the comparison between experimental and theoretical studies is easier and the catalytically effective species can be identified more easily. Inexpensive, environmentally friendly, easily synthesized and stable organometallic compounds that efficiently catalyze the reaction are worth studying. In this context, mechanistic studies on the catalytic dehydrogenation/dehydrocoupling of amine-boranes and phosphine-boranes have attracted enormous attentions over the last decade. [124, 125] The understanding of detailed reaction pathway as well as the exact role of the metallic center and different parameters (such as ligands, substituents, oxidation states of metallic centers and solvation effect) could help in designing and choosing a good catalyst that is highly efficient under ambient conditions.

Experimental investigations have already recovered diverse kinds of efficient catalysts including almost all over the transition metals and s- and p-block metals complexes, especially from the beginning of 21st century. The efficiency of a catalytic species is easily quantified from the experimental observations, *via* the turnover frequency (TOF) calculation. However, the characterization of all the intermediates and transition states from the only experimental data is almost impossible. *In silicon* studies are particularly attractive for the elucidation of the whole reaction mechanism.

Recent advances in DFT methods in combination with the increase of computational resources make it possible to study whole reaction mechanisms of catalytic cycles. Both experimental and theoretical studies have underlined the crucial role of intermediates involving the 3-center 2-electron (3C/2e) interaction(s) for the dehydrogenation process.

The Group IV metallocenes, which are considered as promising catalysts with a relatively high activity for the dehydrogenation of amine-boranes and phosphine-boranes, have been studied intensively.

The dimethylamine borane molecule (DMAB), $HMe_2N{\cdot}BH_3$, is largely used for the investigations of catalyzed dehydrogenation studies of amine-boranes. [52,61,63,67,126] The most common observed products are : the amino-borane $Me_2N{=}BH_2$, the linear diborazane $HNMe_2{\cdot}BH_2Me_2N{\cdot}BH_3$ and the cyclic diborazane $[Me_2N{\cdot}BH_2]_2$, all of which are soluble and easily identified by experiments. [127] Furthermore, among the transition metals, iron and titanium are the most abundant elements on Earth. Titanocene complexes are easy to synthesize and use. [128] It is inexpensive, environmentally friendly and acts as an efficient catalyst for dehydrogenation of DMAB. Understanding the detailed reaction mechanism may help to better control the dehydrogenation reactions, towards a possible development of marketable systems.

5.1 Experimental observations

The catalyzed dehydrogenation/dehydrocoupling reaction of DMAB by group 4 metallocenes ($[Cp_2M]$, M=Ti, Zr and Hf) was firstly experimentally investigated by Clark *et al.* in 2006. [49] The DMAB was treated with a catalytic amount (2 mol%) of $[Cp_2Ti]$ generated *in situ* ($Cp_2TiCl_2/^nBuLi$). The reaction was followed by ^{11}B NMR spectroscopy under ambient conditions. Apart from the aminoborane $[Me_2N{\cdot}BH_2]_2$ as the main product, a relative large signal which was identified lately as a linear diborazane $HMe_2N{\cdot}BH_2Me_2N{\cdot}BH_3$ was observed. Significantly, small signals of $Me_2N{=}BH_2$ and $(Me_2N)_2BH$ were also identified.

$$2\,HMe_2N{\cdot}BH_3 \xrightarrow[20\ ^\circ C,\ 4h,\ toluene]{2\ mol\%,\ Cp_2Ti} [Me_2N{\cdot}BH_2]_2 \tag{5.1}$$

The titanocene also acts as an efficient catalyst for the dehydrogenation reaction of a much more sterically hindered amine-borane: the di-isopropylamine borane $H^iPr_2N{\cdot}BH_3$ (DiPrAB) treated 2 mol% of $[Cp_2Ti]$ in toluene at 20 °C forms the aminoborane $^iPr_2N{=}BH_2$, instead of the cyclic dimer product observed through the reaction with DMAB:

$$H^iPr_2N{\cdot}BH_3 \xrightarrow[20\ ^\circ C,\ 1h,\ toluene]{2\ mol\%,\ Cp_2Ti} {}^iPr_2N{=}BH_2 \tag{5.2}$$

This study provided a first insight of the high efficiency of titanocene to catalytically dehydrogenate secondary amine-boranes. Furthermore, the substituent effect or steric hindrance effect may be considered as main factors to influence the dehydrogenated products and the efficiency of reactions.

Four years later, Manners *et al.* [50] carried out an extensive experimental study to elucidate the reaction mechanism of titanocene-catalyzed dehydrogenation of amine-boranes ($HR_1R_2N{\cdot}BH_3$).

A mixture with DMAB in toluene solution was treated with 2 mol% of $[Cp_2Ti]$. As in the case of the previous experimental study, the catalyst $[Cp_2Ti]$ was not directly introduced. Instead, it was generated *in situ* at room temperature from the precatalyst $Cp_2TiCl_2/2\,^nBuLi$ or $Cp_2Ti(PMe_3)_2/2\,^nBuLi$, following a classical procedure.

The combined ^1H NMR and ^{11}B NMR spectroscopies (noted as $^{11}B\{^1H\}$NMR) were employed to *in situ* follow the dehydrogenation reaction of DMAB. Five different species containing boron were identified during the reaction. They are $HMe_2N{\cdot}BH_3$, the linear dimer $HMe_2N{\cdot}BH_2Me_2N{\cdot}BH_3$, the cyclic dimer $[Me_2N{\cdot}BH_2]_2$, and also traces of $(Me_2N)_2BH$ and aminoborane $Me_2N{=}BH_2$. At t = 0 min, the reagent DMAB is the only observed species. At t = 15 min, a consequent decrease of the signal of DMAB is already noticeably. Two new species are also identified: the major one is attributed to the linear diborazane, the other one is due to a small amount of cyclic diborazane. From t = 75 to 240 min, gradual decrease of the signal of DMAB is observed. The amount of linear diborazane also gradually decreases, with a concomitant increase of the amount of cyclic dimer. This observation indicates that the linear diborazane serves as an intermediate in this reaction. A trace of by-products (1%), $(Me_2N)_2BH$ and $Me_2N{=}BH_2$, can always be identified during the reaction.

It is important to note that the linear diborazane is stable in standard conditions without catalyst. Other supplementary experiments showed that in presence of titanocene, the entire quantity of the linear diborazane was converted into the cyclic diborazane.

The catalytic activities of $[Cp_2Ti]$ towards ammonia borane $H_3N{\cdot}BH_3$, primary amine borane $H_2MeN{\cdot}BH_3$, and more sterically hindered species, $H^iPr_2N{\cdot}BH_3$ and $HMeBnN{\cdot}BH_3$ ($Bn{=}CH_2Ph$) were also investigated. The treatment with 2 mol% $[Cp_2Ti]$ generated *in situ* with ammonia borane showed no reaction at all and less than 1% conversion with primary amine-borane was observed. A full conversion toward $^iPr_2N{=}BH_2$ and $[MeBnN{\cdot}BH_2]_2$ was observed respectively in 1 hour and 1.5 hours from $H^iPr_2N{\cdot}BH_3$ and $HMeBnN{\cdot}BH_3$ respectively:

$$H_3N{\cdot}BH_3 \xrightarrow[20\text{–}45\ ^\circ C,\ 16h,\ toluene]{2\ mol\%,\ \mathrm{Cp_2Ti}} \text{No Reaction}$$

$$H_2MeN{\cdot}BH_3 \xrightarrow[20\ ^\circ C,\ 16h,\ toluene]{2\ mol\%,\ \mathrm{Cp_2Ti}} [HMeN{\cdot}BH_2]_3 \text{ (Less than 1\%)}$$

$$H^iPr_2N{\cdot}BH_3 \xrightarrow[20\ ^\circ C,\ 1h,\ toluene]{2\ mol\%,\ \mathrm{Cp_2Ti}} {}^iPr_2N{=}BH_2$$

$$2\,HMeBnN{\cdot}BH_3 \xrightarrow[20\ ^\circ C,\ 1.5h,\ toluene]{2\ mol\%,\ \mathrm{Cp_2Ti}} [MeBnN{\cdot}BH_2]_2$$

The substitution effect on the N atom on the reaction is another aspect for which it is worth studying the whole detailed reaction pathway. In addition, the zirconocene and hafnocene counterparts for the dehydrogenation of amine-boranes were also studied. No activity was observed with these catalysts.

5.2 Kinetic and mechanistic studies

Manners *et al.* also proposed a simple mechanistic model that represents their experimental evidences with a four-step process:

$$[Cp_2Ti] + HMe_2N{\cdot}BH_3 \longrightarrow [IntA] \tag{5.3}$$

$$[IntA] + HMe_2N{\cdot}BH_3 \longrightarrow H_2 + HMe_2N{\cdot}BH_2Me_2N{\cdot}BH_3 \tag{5.4}$$

$$[Cp_2Ti] + HMe_2N{\cdot}BH_2Me_2N{\cdot}BH_3 \longrightarrow [IntB] \tag{5.5}$$

$$[IntB] \longrightarrow [Me_2N{\cdot}BH_2]_2 + H_2 \tag{5.6}$$

They carried out the exploration of the kinetic isotope effects (KIE) associated with the dehydrocoupling reaction of DMAB. This method bases principally on the difference of zero-point energy (ZPE) for the X-D bond stretch and X-H bond stretch for a bond cleavage/formation process. For the mechanism with a X-H bond cleavage/formation step, the isotope effect is controlled by the difference in ground state ZPE. The ZPE for X-D bond stretch is lower than that of X-H bond stretch. As a result, the activation energy for X-D cleavage step is higher than the one of X-H bond.

They performed the catalytic dehydrocoupling of different deuterated reagents in comparison with the non-deuterated DMAB. The phenomenological k_H/k_D values in considering each step as a pseudo-zero-order reaction and the reaction time for 100% conversion to cyclic dimer of each reagents are summarized in Table 5.1.

Table 5.1: Phenomenological k_H/k_D value of the catalytic dehydrocoupling reactions of different deuterated DMAB. Reaction time for 100% conversion for each reactant are also given.

1a	1aND	1aBD	1aNDBD
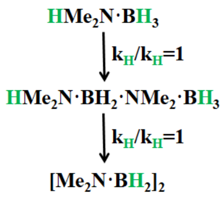 HMe₂N·BH₃ kH/kH=1 HMe₂N·BH₂·NMe₂·BH₃ kH/kH=1 [Me₂N·BH₂]₂	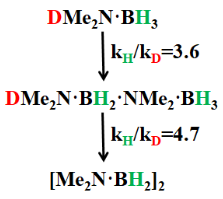 DMe₂N·BH₃ kH/kD=3.6 DMe₂N·BH₂·NMe₂·BH₃ kH/kD=4.7 [Me₂N·BH₂]₂	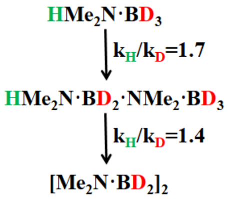 HMe₂N·BD₃ kH/kD=1.7 HMe₂N·BD₂·NMe₂·BD₃ kH/kD=1.4 [Me₂N·BD₂]₂	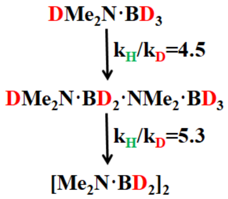 DMe₂N·BD₃ kH/kD=4.5 DMe₂N·BD₂·NMe₂·BD₃ kH/kD=5.3 [Me₂N·BD₂]₂
7h	32h	9h	33h

This KIE exploration leads to the following conclusions:

- The hydrogen transfer from N-H moiety occurs during the turnover limiting step in both the conversion to linear diborazane and to cyclic diborazane according to their relatively high k_H/k_D values observed in the case of the dehydrogenation of 1aND. The reaction time was also found to highly increase when the deuteriation is done on the nitrogen atom.

- Low k_H/k_D value associated with the B-H(D) cleavage process is found in both the steps. In the same way, the total reaction time for the conversion of 1aBD adduct has found no significant increase compared to the non-deuterated species. This observation may arise from small transfer angles of B-H moiety, or may be on account of the possibility that the B-H/D step cleavage was outside of the turnover limiting step.

The experimental results presented above suggest that the metal mediated N-H cleavage be the time-determining step in both the linear diborazane formation process and the linear diborazane cyclization process.

5.3 A two-cycle model

Regarding the overall experimental observations, Manners *et al.* proposed a two-cycle process of catalytic dehydrocoupling reaction of $HMe_2N{\cdot}BH_3$ that is summarized in Figure 5.1:

- At first, they proposed a two-step cycle leading to a coordination complex $[Cp_2Ti{-}\eta^2\text{-}H_3B{\cdot}NMe_2H]$ involving two 3C/2e (Ti-H-B) interactions. This complex further undergoes a proton transfer by formation of an η^2 agostic intermediate $Cp_2Ti(H)NMe_2BH_3$. When adding a second molecule of DMAB, another two-body reaction is expected to lead to the formation of the linear dimer with the concomitant loss of one dihydrogen molecule.
- The second cycle consists of the dehydrocoupling of the linear diborazane generated during the first cycle, *via* an intermediate with several Ti$\cdots$H$-$B and Ti$\cdots$H$-$N interactions, to form the final product, the cyclic diborazane $[Me_2N{\cdot}BH_2]_2$.

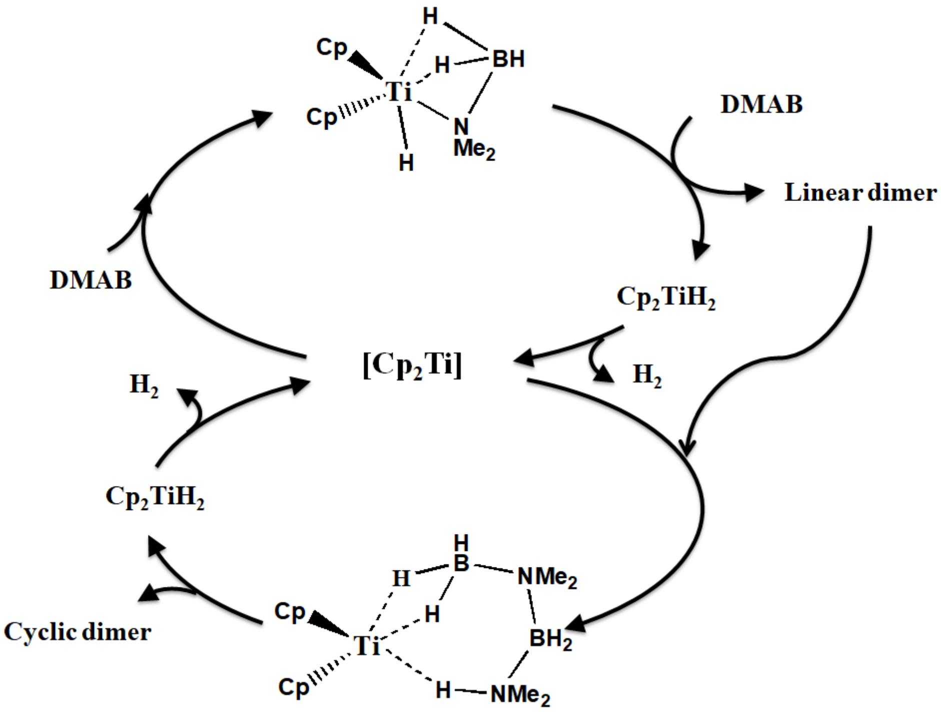

Figure 5.1: Two-cycle model of catalytic dehydrocoupling of DMAB proposed by Manners *et al.*

5.4 DFT investigations in the literature

A DFT investigation of mechanisms of this system was firstly carried out by Luo and Ohno in 2007. [58] They performed the geometry optimizations and energy calculations with the hybrid functional B3LYP associated with the relativistic pseudo-potential LanL2DZ for the metallic center, the Pople basis set 6-31G* for the Cp (cyclopentadienyl anion: $C_5H_5{}^-$) and Me groups, as well as the 6-31++G** basis set for all the atoms involved in the formation and dissociation of bonds during the pathways. The solvation effect of toluene was taken into account with the implicit solvent model CPCM (Conductor-like Polarizable Continuum Model).

Two different dehydrogenation mechanisms were proposed according to their computational results (Figure 5.2):

- **The intramolecular process (two-body reaction)** is calculated to be the most energetically favorable one. The DMAB molecule firstly coordinates with titanocene by forming a $\mathrm{Ti}\cdots\mathrm{H{-}B}$ interaction. This step is followed by a proton transfer from the nitrogen atom to the metallic center. The energy barrier (relative free energy with solvation effect) for this rate-determining step was calculated to be +95.8 kJ/mol. A further B-H bond cleavage generates $Me_2N{=}BH_2$ and Cp_2TiH_2 species. The metal hydride Cp_2TiH_2 releases a dihydrogen molecule to regenerate the catalyst Cp_2Ti. The aminoborane intermediate then undergoes an off-metal 2+2 dimerization, leading to a cyclic dimer with an energy barrier of 119.5 kJ/mol.

- The second mechanism called **intermolecular pathway (three-body reaction)** was predicted to be less energetically favored. It is an intermolecular catalyzed dehydrocoupling of two DMAB molecules which leads to the formation of a linear dimer $HMe_2N{\cdot}BH_2Me_2N{\cdot}BH_3$. A three-body complex with a titanocene and two DMAB molecules is firstly formed. A step-wise proton transfer from the nitrogen atom of the first DMAB, followed by a second hydrogen transfer from the boron atom of the second DMAB is proposed. The rate-determining energy barrier was calculated to be 155.6 kJ/mol for this mechanism.

Their results on the detailed mechanisms and the calculated relative free energy in considering the solvation effect are summarized in Figure 5.2.

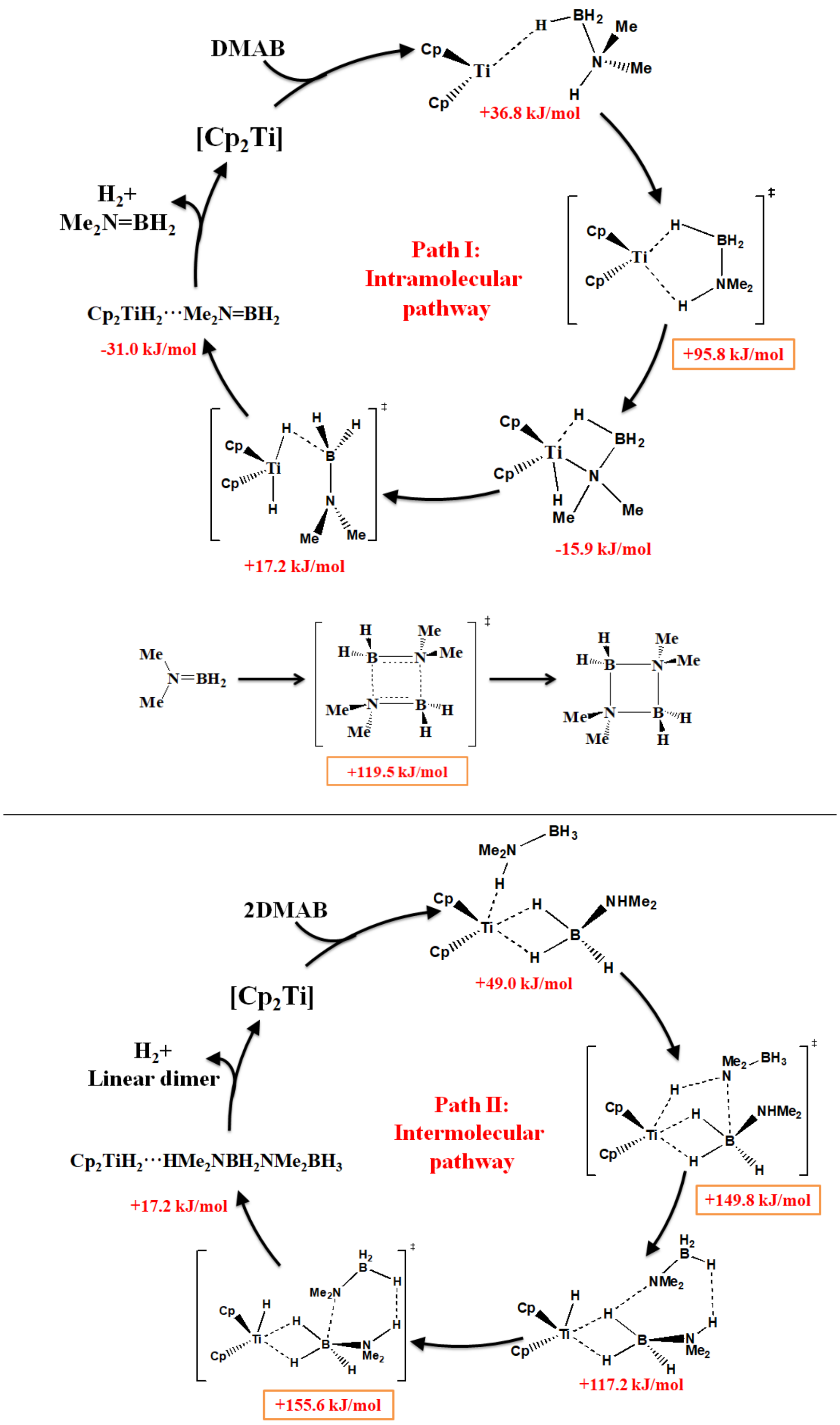
DMAB
[Cp$_2$Ti]
+36.8 kJ/mol
Path I:
Intramolecular
pathway
+95.8 kJ/mol
-15.9 kJ/mol
+17.2 kJ/mol
-31.0 kJ/mol
Cp$_2$TiH$_2$···Me$_2$N=BH$_2$
H$_2$+
Me$_2$N=BH$_2$
+119.5 kJ/mol
2DMAB
[Cp$_2$Ti]
+49.0 kJ/mol
Path II:
Intermolecular
pathway
+149.8 kJ/mol
+117.2 kJ/mol
+155.6 kJ/mol
+17.2 kJ/mol
Cp$_2$TiH$_2$···HMe$_2$NBH$_2$NMe$_2$BH$_3$
H$_2$+
Linear dimer

Figure 5.2: The intramolecular (Path I) and intermolecular (Path II) catalytic dehydrocoupling of DMAB by [Cp$_2$Ti] proposed by Luo and Ohno with their calculated relative free energies (in kJ/mol) that takes into account the solvation effect is shown. The calculated off-metal 2+2 dimerization of aminoborane Me$_2$N=BH$_2$ to form the cyclic diborazane [Me$_2$N·BH$_2$]$_2$ is also given.

Their calculations suggested that the two-body step-wise intramolecular pathway was preferential rather than the three-body intermolecular one.

A computational re-investigation of the titanocene-catalyzed dehydrocoupling reaction was performed by Tao and Qi in 2013. [59] Their calculations were carried out using the B3LYP functional, the same as Luo and Ohno did, associated with the 6-31G(d) basis set for the description of the cyclopentadienyl groups, a modified LanL2DZ relativistic pseudo-potential for the titanium atom and the 6-311++G(d,p) basis set for all atoms of DMAB molecule.

Their conclusion was similar to the one of Luo and Ohno: the intramolecular mechanism leading to the $Me_2N{=}BH_2$ aminoborane intermediate, followed by an off-metal cyclization, was calculated to be energetically more favorable than the intermolecular mechanism. In addition, a detailed reaction pathway for the dehydrocoupling of the linear diborazane was proposed in this study. As presented in Figure 5.3, this dehydrocoupling process of linear diborazane was also calculated to be endothermic at their theoretical level of theory.

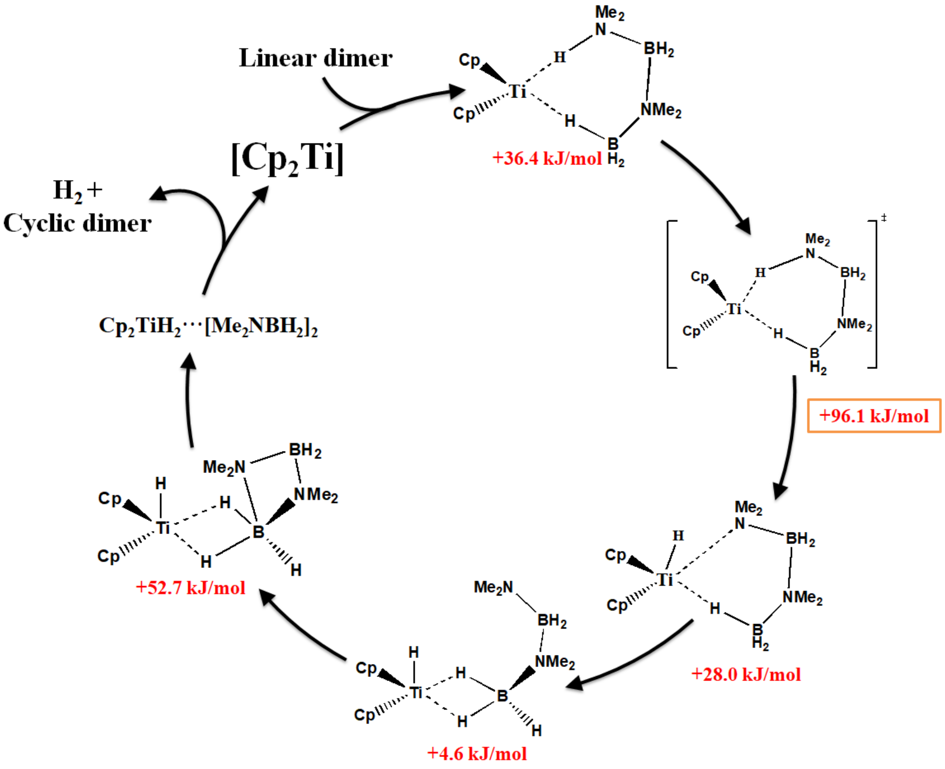

Figure 5.3: The titanocene-catalyzed dehydrocoupling of linear diborazane calculated by Tao and Qi in 2013 with their calculated relative free energies (in kJ/mol) including solvation effect. The B3LYP functional associated with the 6-31G(d) basis set for Cp groups, the 6-311++G(d,p) basis set for all the DMAB atoms and a modified LanL2DZ relativistic pseudo-potential for Ti atom was used.

5.5 Mechanism still remains uncertain since more than 10 years

Despite two extensive theoretical studies, the dehydrocoupling mechanism of DMAB catalyzed by titanocene remains unexplained. Indeed, inconsistencies between theoretical and experimental results are summarized in Table 5.2. According to the experiments, the linear diborazane is considered as a key intermediate for the on-metal cyclic diborazane formation reaction, and not the monomeric aminoborane as suggested by the DFT calculations. This inconsistency has also been highlighted in two recent reviews on the catalyzed dehydrogenation of amine boranes, by Weller *et al.* and Rossin & Peruzzini. [48,129] In addition, the substitution effect on the nitrogen atom that leads to different reactivities and different products has not been studied theoretically.

Table 5.2: Summary of experimental and theoretical results and conclusions of the titanocene-catalyzed dehydrogenation of DMAB reaction.

	Titanocene-catalyzed dehydrogenation of DMAB		Effect of substitution on the N atom
	Intermediate formed	Cyclization step	
Experimental evidences	Linear diborazane $HNMe_2{\cdot}BH_2Me_2N{\cdot}BH_3$	On-metal dehydrocoupling	Different natures of substituent group studied
Theoretical results	Aminoborane $Me_2N{=}BH_2$	Off-metal with an energy barrier of 117 kJ/mol	Not studied

Understanding the reaction pathway, however, would be an essential stage towards the investigation of the early transition metal catalyzed dehydrogenation process. The present work aims at further exploring the catalytic dehydrogenation/dehydrocoupling pathways of DMAB and other amine-borane adducts. Considering the importance of different theoretical levels in predicting, describing and understanding divers parameters and properties for a chemical reaction, primarily, a suitable level of theory should be proposed.

Our studies aim at investigating the following points:

- The structure, properties and free energies of intermediates and transition states;
- The possible existence of consecutive and competitive mechanisms;
- The influence of solvent and substituents on the reaction barriers and reaction mechanisms;
- The underlying question is: “How to choose a suitable method for a relatively accurate description of all the parameters mentioned above with a reasonable computational cost?”.

Chapter 6

Characterization of M-H-B interactions involved in catalyzed dehydrogenation of amine-boranes

Introduction

Chapter 5 has presented the homogeneous dehydrogenation studies of amine-borane adducts catalyzed by titanocene complex generated *in situ*. Experimental results demonstrated that the titanocene complex has a high activity on the dehydrocoupling of DMAB while the zirconocene and hafnocene analogues shown nearly no activity. As presented in their proposed two-cycle titanocene-catalyzed dehydrocoupling pathway of DMAB (see Figure 5.1 shown in Chapter 5) different non-covalent interactions involved in the dehydrocoupling cycles including 3-center 2-electron interactions in both intermolecular and intramolecular (agostic) Ti-H-B intermediates, are considered to play an important role in the reaction because of the activation of B-H σ-bond.

More works have highlighted the significant role of the paramagnetic Ti(III) species in the dehydrogenation reactions. $Cp_2TiNMe_2{\cdot}BH_3$ and $Cp_2TiPPh_2{\cdot}BH_3$complexes, which were isolated experimentally, were found to be efficient catalysts for the dehydrogenation reactions of amine-boranes. [51]

For an in-depth understanding of the reaction mechanism, the effect of the nature of metallic centers, substituent groups and ligands on the activation of B-H bonds will be presented. A detailed identification and characterization of 3C/2e interactions at molecular scale is a needed prerequisite *prior to* this mechanistic investigation. The aim of this study is to propose specific descriptors with both the QTAIM (Quantum Theory of Atoms in Molecules) and ELF (Electron Localization Function) topological approaches that would allow a qualitative and quantitative comparison of the strength of 3C/2e interactions.

6.1 Characterization of agostic interactions

6.1.1 History and definition

The term "agostic" was firstly proposed by Maurice Brookhart and Malcolm L. H. Green in 1983 [130] and in a second review in 1988 [131] which are today the cornerstones of the agostic interactions studies. The term agostic initially described "a covalent interactions between carbon-hydrogen groups and transition metal centers in organometallic compounds" 3-center 2-electron intramolecular C-H-M system when a hydrogen atom is covalently bonded simultaneously to both a carbon atom and a transition metal.

The discovery and introduction of this term was based on several experimental observations: [132]

- The unusual high field shifts for the ethyl hydrogen in ^{1}H NMR spectrum of an organometallic complex;
- The geometric deformation;
- The changes in reactivity, especially an activation of the C-H bond related to other chemical reactions.

Different types of C-H agostic interactions were then found and characterized. They are usually grouped according to the position of the bond involved in the intramolecular interaction related to the metal center, including α-, $\beta-$, $\gamma-$,.... agostic interactions. [133] (Figure 6.1) The most common type of interaction is β agostic interaction.

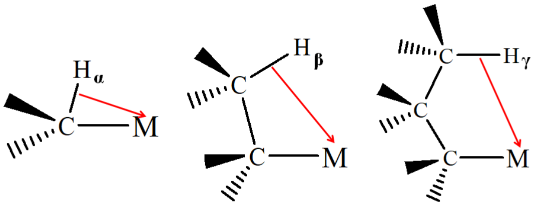

Figure 6.1: Illustration of C-H agostic interaction and different types of C-H agostic interactions. For clarity purposes, all the agostic interactions and other non-covalent interactions will be marked as dotted lines in the following sections. (For example M$\cdots$H-X for an agostic interaction)

The metals in the C-H-M agostic interaction system should match the conditions as follows: (1) a high Lewis acidity/positive charge at the metal atom; (2) an available acceptor orbital (an empty d orbital) suitable to the electron donors at the metal; (3) a relatively low degree of steric congestion at M; (4) more than 16 valence electrons displayed by the transition metal. [134]

Apart from the C-H agostic interaction, many other similar interactions between an X-H (B-H [135], Si-H [136]) or X-C (C-C [137], Si-C [138]) σ bond and a metallic center were experimentally discovered and characterized. Particularly, some B-H bonds present in the organometallic systems attend to form interactions with the metal center, similar to those of agostic interactions of C-H bonds, have attracted considerable attention for its potential application in dehydrogenation of amine-borane and the hydrogen storage.

6.1.2 Experimental characterization of C-H agostic interactions

According to the crystallographic studies of M-H-C systems, there appeared to be an unusually close approach of the hydrogen to a metal center. A 3C/2e M-H-C agostic interaction is characterized by a relatively short M-H distance (in the [1.8 Å, 2.3 Å] range) and a small M-H-C angle (approximately from 90 ° to 140 °). However, there is no evidence to distinguish whether geometric distortions come from the attraction of C-H σ bond to the metallic center, or from the ligands structures (sterical hindrance, pincer ligands). Several M-H-C interactions are not classified as agostic interaction but are described by the term "anagostic" because the interaction between a σ bond and a metallic center also leads to a geometric distortion whereas some agostic criteria are not met. The following table summarizes different geometric features of the "agostic" and "anagostic" interactions: [139]

Table 6.1: Different geometric features to distinguish the M-H-C agostic and anagostic interactions.

	M-H-C agostic	M-H-C anagostic
M-H distance	1.8 Å - 2.3 Å	2.3 Å - 2.9 Å
$\widehat{M-H-C}$ angle	$90° - 140°$	110° - 170°

Apart from the geometric data, many other experimental methods including NMR and IR are used to characterize the C-H agostic interaction. The agostic interactions feature: [132]

- NMR chemical shifts to high field δ = -5 to -15 ppm with the reduced NMR coupling constants ^{1}J = 75 to 100 Hz for the C-H agostic interactions *versus* the 125 Hz expected for a normal C-H σ bond;
- low vibrational frequencies $\upsilon(\mathrm{C{-}H_{agostic}}) = 2700\text{-}2300\ \mathrm{cm^{-1}}$ compared with the 2700-3000 $\mathrm{cm^{-1}}$ for free C-H bond.

6.1.3 Topological descriptions of agostic interactions

Despite the experimental observations mentioned above to characterize the 3C/2e interactions, some theoretical approaches are also of particularly importance for the identification and description of these specific interactions on the basis of electron density analysis. Topological approaches of electron density such as QTAIM (Quantum Theory of Atoms in Molecules) as well as ELF (Electron Localization Function) were proposed to be particularly suitable tools for the description of 3C/2e interactions. In addition, the NBO (Natural Bond Orbital) approach also allows a quantitative characterization of the electron delocalization of 3C/2e systems.

QTAIM

P.L.A. Popelier and G. Logothetis [132] firstly proposed criteria for the identification of 3C/2e interactions based on the QTAIM (Quantum Theory of Atoms in Molecules) approach.

A common question to be addressed in the studies of interaction involving hydrogen and transition metal atoms is to distinguish hydrogen bondings and agostic interactions. To that propose, Popelier and Logothetis have demonstrated the relevance of the QTAIM topological analysis. According to their extensive investigations of different systems including $CH_3TiCl_2{}^+$, $C_2H_5TiCl_2{}^+$ and $C_3H_7TiCl_2{}^+$, the existence of agostic bonds should be proven by the following concomitant topological features: the identification of a BCP (Bond Critical Point) and BP (Bond Path) between metallic center M and hydrogen atom from C-H bond.

The following Table summaries the main QTAIM characters of agostic interactions compared to the hydrogen bonds proposed by Popelier *et al.* The QTAIM analysis can provide a qualitative and also quantitative insight of an agostic interaction.

Table 6.2: QTAIM features of hydrogen bonds and agostic interactions proposed by Popelier *et al.* [132, 140, 141] All the values presented here are in atomic unit. (a.u.)

Properties of BCP at $M\cdots H$	Hydrogen Bond	Agostic Interaction
ρ(BCP)	$0.002 < \rho(BCP) < 0.035$	$0.035 < \rho(BCP)$
$\nabla^2\rho$(BCP)	$+0.024 < \nabla^2\rho(BCP) < +0.139$	$+0.15 < \nabla^2\rho(BCP) < +0.25$
ϵ(BCP)	$\epsilon \approx 0$	$\epsilon \neq 0$
H(BCP)	$H(BCP) > 0$ for weak H bonds $H(BCP) < 0$ for medium and strong H bonds	$H(BCP) < 0$

However, above mentioned QTAIM criteria were only evaluated for limited systems. Other topological investigations on the characterization of agostic interactions by considerable enlarging systems were carried out. Adamo *et al.* [142] demonstrated the study for 23 representative complexes including all first line transition metals (with different oxidation states) as well as different positions of agostic hydrogen (α, β, γ and δ). The electron density of BCP($M\cdots H$) interactions extends to a larger range from 0.01 a.u. to 0.13 a.u. The corresponding $\nabla^2\rho$(BCP) values were found in the [0.03, 0.25] range.

Above mentioned QTAIM criteria make it possible to identify agostic compounds. However, caution should be taken with systems that exhibit particularly weak agostic interactions, typically involved in the α-agostic compounds. It can be difficult to identify the bond path and bond critical point in these cases, leading to a mis-identification within the QTAIM approach. For that reason, other methods are needed for a further identification of all the compounds containing 3C/2e interactions.

ELF

Complementarily to the QTAIM approach, the ELF (Electron Localization Function) topological analysis has been found to be a valuable approach for characterizing chemical bondings. This method makes it possible to identify not only the core basins but also the valence basins associated with each atom as well as the population (number of electrons) of each basin.

In the case of the 3C/2e interaction herein studied, a trisynaptic basin labelled V(M, H, X) can be featured for an agostic interaction. The ELF signature of such an interaction should consist in a trisynaptic protonated basin containing approximate 2 e which belongs to three atoms: the metallic center M, the hydrogen atom H and the X atom which carries the hydrogen atom. [114] When combined with the QTAIM approach, the contribution of each atom (that is the attractor according to the QTAIM definition) can be quantified in a given basin.

This approach enables to ensure the presence of a 3C/2e interaction, in all the cases of α-, β- or γ- agostic systems.

As already stated, the identification of non-covalent interactions involving a hydrogen atom and a metal center has often been unclear and debatable. [143, 144] ELF topological analysis provides a good solution to distinguish the 3C/2e interaction and the hydrogen bond. An example for which the identifications of the C-H$\cdots$M interaction have been discussed in the literature is illustrated in Figure 6.2. X-ray crystallography demonstrated a relatively short (C-)H$\cdots$Cu interatomic distance of 2.454 Å and a bond critical point was also identified between H and Cu atoms in the same study, [143] suggesting a C-H$\cdots$Cu agostic interaction. Disagreement was pointed out in the literature on the basis of the geometric features (Table 6.1) and QTAIM characters (Table 6.2) of an agostic interaction. [144] We carried out an additional study using the ELF topological approach, which provides a convincing proof of the ono-existence of an agostic interaction, since no contribution of metal center to the protonated basin was identified.

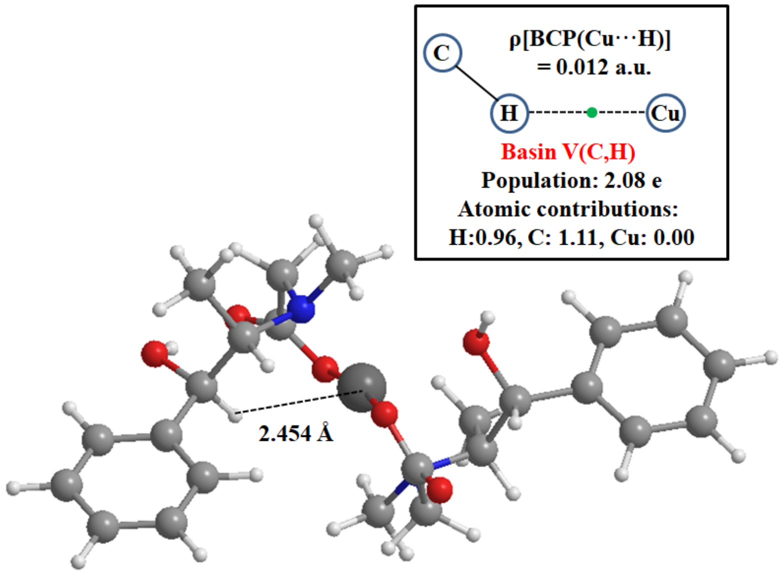

Figure 6.2: X-ray crystallography study [143] as well as QTAIM and ELF topological characterization of the C-H$\cdots$M interaction in the Cu(II) compound.

The ELF and QTAIM analyses are therefore complementary tools to quantitatively identify agostic interactions. Moreover, if such a 3C/2e interaction is identified, the contribution of the metallic center to the protonated basin can be quantified, allowing a quantitative determination of the strength of interaction.

In addition, the covariance Cov(V(H)/C(M)) [145] calculated from the ratio between the protonated basin's population V(H) and the population of the core basin C(M) of metallic center also provides an important insight to characterize the interaction between these two basins. It measures the electron delocalization between the two basins. A covariance larger than 0.03 (in absolute value) is considered as a proof of an agostic interaction between the X–H bond and M. [114]

6.2 Benchmark studies

Introduction

For a sake of a systematic investigation of the systems with 3C/2e interactions involved in the group 4 metallocene dehydrogenation of amine-boranes and phosphine-boranes, an appropriate geometric and electronic description is required. Previous investigations have demonstrated that the density functional theory (DFT) can be employed to describe the agostic interactions. [133] The suitable DFT calculation levels that allow a good geometric and electronic description of non-covalent interactions at a reasonable computational cost should be identified. Herein is proposed an estimation of the "minimum level of theory" leading to accurate enough descriptions of 3C/2e interactions within the DFT framework. The following benchmark studies will be developed:

- Firstly, geometric parameters will be used to characterize the ability of the DFT methods to describe the agostic systems;
- Secondly, correct description for the topological QTAIM and ELF features will also be evaluated for a set of DFT method.

A series of group 4 metallocenes in combination with amine-boranes or phosphine-boranes fragments for which experimental data were already reported in the literature: $Cp_2TiNH_2BH_3$, [135] $Cp_2Zr(H)NH_2BH_3$ and its isomer, [146] $Cp_2TiNMe_2BH_3$, [51] $Cp_2Zr(H)NMe_2BH_3$, [51] $Cp_2TiPPh_2BH_3$ [51] and $Cp_2ZrPPh_2BH_3$. [51]

The effects of several exchange-correlation functionals as well as basis sets (including the treatment of relativistic effects) on the geometric and electronic description of the agostic interaction in the metallocenes were evaluated. This calibration step was carried out based on the paramagnetic $Cp_2TiNH_2BH_3$ complex for which experimental data are available, as well as the diamagnetic $Cp_2Ti(H)NH_2BH_3$ species.

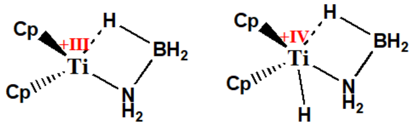

Ti^{+III} Ti^{+IV}

Figure 6.3: The paramagnetic $Cp_2TiNH_2BH_3$ complex which was characterized by X-ray diffraction and the diamagnetic $Cp_2Ti(H)NH_2BH_3$.

All the geometry optimizations were carried out with Gaussian 09 Rev D.01 software. The ELF and QTAIM calculations have been carried out using the TopMod and AIMAll softwares, respectively. Prior to the use of these softwares, the generation of a specific wave function file called "wfn" or "wfx" is needed. This file was generated with the Gaussian 09 software.

6.2.1 Influence of exchange-correlation functionals

For this calibration step, we were looking for satisfactory levels of theory, that correctly reproduce experimental parameters for "good" theoretical reasons. Indeed, it is known that in several cases, incomplete theoretical description of exchange-correction interactions can lead to apparent satisfactory description of the systems due to error compensation. The Minnesota and range-separated hybrid functionals, dedicated to the study of weak interactions, were considered for the present methodological study. Additionally, the effect of the Grimme's empirical dispersion correction within the framework of the Becke-Johnson damping function (GD3BJ), was evaluated. The following functionals were considered:

Table 6.3: Selected exchange-correlation functionals for the calibration study of the agostic systems.

	Local	GGA	Meta-GGA	Hybride	RSH (Range-Separated Hybrid)
Exchange-correlation functional	M06-L	BP86	TPSSTPSS	B3LYP B3PW91 PBE0 M06 TPSSh	LC-ωPBE ($\omega = 0.4$ a.u.$^{-1}$)

Geometric considerations

Influence of exchange-correlation functionals

To begin with, the calibration of different exchange-correlation functionals on several representative geometric parameters were carried out in the case of the paramagnetic $Cp_2TiNH_2BH_3$ complex shown in Figure 6.3. The 6-311++G(2d,2p) basis set was chosen for all the atoms. Table 6.4 displays the calculated values of selected inter-atomic distances and angles, as well as the experimental data obtained by X-ray diffraction.

For a sake of a more visible comparison, deviations between experimental and calculated parameters were calculated as follows:

$$\delta d_{X-Y} = \frac{d^{calc}_{X-Y} - d^{exp}_{X-Y}}{d^{exp}_{X-Y}} \times 100 \tag{6.1}$$

where d^{exp}_{X-Y} represents the experimental obtained inter-atomic distance and d^{calc}_{X-Y} means the theoretical calculated one. Similarly, deviations of $X-\widehat{Y}-Z$ angle were calculated as follows:

$$\delta_{X-\widehat{Y}-Z} = \frac{X-\widehat{Y}-Z^{calc} - X-\widehat{Y}-Z^{exp}}{X-\widehat{Y}-Z^{exp}} \times 100 \tag{6.2}$$

The bar chart which represents all the deviations between experimental and calculated parameters is given in Figure 6.4.

Table 6.4: Influence of the functionals on the geometric description of the $Cp_2TiNH_2BH_3$ complex

Class	Functional	d_{Ti-N}	d_{Ti-B}	$d_{B-H_{free}}$	d_{B-H_a}	Δd_{B-H}	d_{Ti-H_a}	$Ti - \widehat{H_a} - B$	$Ti - \widehat{N} - B$	$N - \widehat{B} - H_a$
Local	M06L	2.178	2.525	1.200	1.282	0.082	1.899	103.4	83.4	105.8
GGA	BP86	2.184	2.530	1.212	1.312	0.100	1.882	103.4	83.4	105.4
Meta-GGA	TPSSTPSS	2.181	2.532	1.205	1.305	0.100	1.878	103.9	83.4	104.9
Hybrid	B3LYP	2.182	2.542	1.203	1.297	0.094	1.895	104.0	84.0	104.9
	B3PW91	2.170	2.519	1.206	1.303	0.097	1.880	103.1	83.6	105.5
	PBE0	2.163	2.510	1.207	1.303	0.096	1.879	102.7	83.5	105.7
	M06	2.163	2.517	1.204	1.294	0.090	1.892	102.8	83.6	105.7
	TPSSh	2.174	2.526	1.204	1.302	0.098	1.877	103.7	83.5	104.9
Range-separated	LC-ωPBE	2.155	2.501	1.206	1.297	0.091	1.877	102.4	83.2	105.9
Exp		2.153	2.52	1.13&1.09	1.21	0.100	/	/	84.5	107.1

The experimental measured Ti-N and Ti-B inter-atomic distances are 2.153 Å and 2.52 Å respectively. The corresponding calculated values are found in the [2.155 Å, 2.184 Å] and [2.501 Å, 2.542 Å] ranges, respectively. The δd_{Ti-N} deviations between the experimental and the calculated distances are thus found in the [+0.1%, +1.5%] range, whereas the δd_{Ti-B} deviations are in the [-0.8%, +0.9%] range within all the DFT methods used in this calibration study. Thus, the calculated Ti-N and Ti-B distances are in good agreement with the experimental data.

With all the levels of theory used, the two B-H bonds which have no interaction with the Ti atom ($B-H_{free}$) are calculated to be identical in length. However, from crystallographic structures, two different lengths are measured for these non-agostic B-H bonds: 1.09 and 1.13 Å. This suggests the existence of additional weak intermolecular interactions either with the solvent during the evaporation, or between molecules in the solid phase.

The corresponding $B-H_{free}$ distances are calculated in the [1.200 Å, 1.212 Å] range. Thus, the deviation between the experimental and the calculated distance is in the [+8.1%, +9.2%] range. Similarly, the deviations of $B-H_a$ bond that interacts with the metallic center have been found in the the [+6.0%, +8.4%] range. The deviations observed for B-H distances ($B-H_{free}$ and $B-H_a$) are much larger than those obtained for the Ti-N and Ti-B distances. Such discrepancy may be due to the difficulty to locate the hydrogen atoms accurately by X-ray diffraction.

For this reason, the lengthening of the agostic B-H bond due to the interaction with the metallic center is further studied. The difference between agostic and free B-H distance is labelled as Δd_{B-H}. This parameter provides a measure of the B-H bond lengthening due to the agostic interaction:

$$\Delta d_{B-H} = d_{B-H_a} - d_{B-H_{free}} \tag{6.3}$$

These Δd_{B-H} values are shown in Table 6.4. X-ray diffraction data lead to an experimental Δd_{B-H} value of 0.100 Å. The calculated values are in the [0.090 Å, 0.100 Å] range for all the

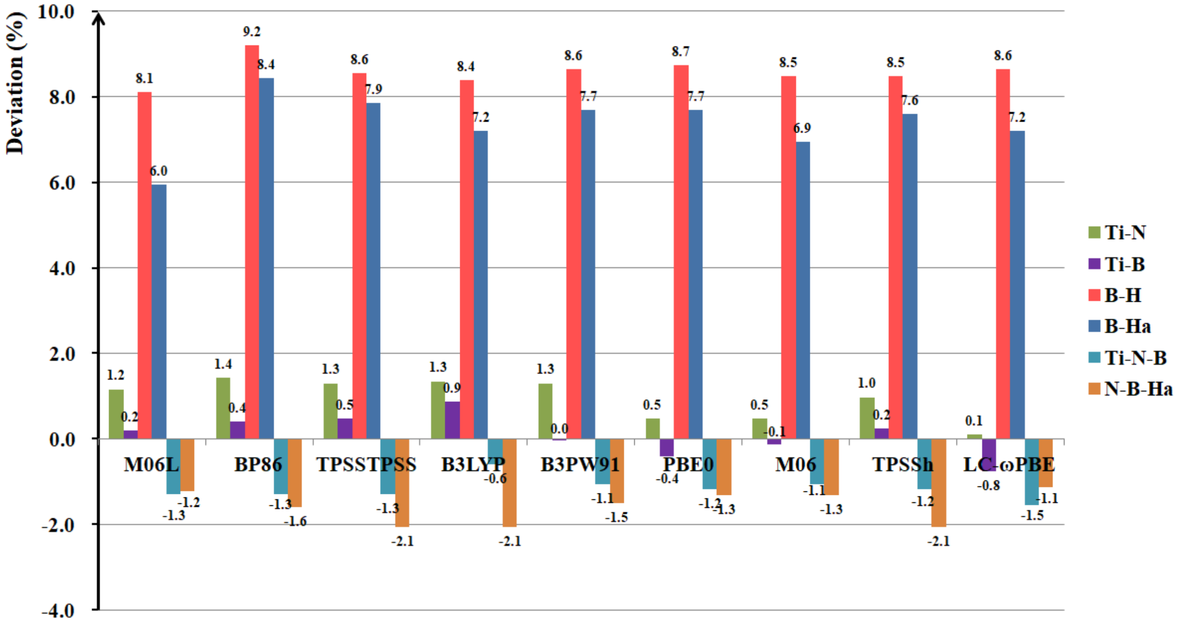

Figure 6.4: Deviations between calculated and experimental geometric features for the $Cp_2TiNH_2BH_3$ complex.

chosen levels of theory except for the case of M06L functional that it was found at 0.800 Å. It can be concluded that the lengthening of the B-H bond due to the interaction with the metallic center is correctly described by the selected functionals, apart from the local M06L functional.

Complementary $Ti{-}H_a$ distances also provide a geometric insight to the characterization of 3C/2e interaction. All the calculated $Ti{-}H_a$ distances are found between 1.877 Å and 1.899 Å. (Table 6.4) According to the geometric features for M-H-C systems presented in Table 6.1, this in indeed in agreement with agostic interactions.

In addition to distances, angles are also used as criteria in the identification of 3C/2e interactions. In the case of the C-H bonds summarized in Table 6.1, it is generally considered that a $Ti - \widehat{H} - C$ angle in the [90°, 140°] range corresponds to an agostic interaction. Table 6.4 shows that the calculated $Ti - \widehat{H} - B$ angles are in the [102.4°, 104.0°] range. By analogy between Ti-H-B and Ti-H-C interactions, the calculated angles confirm the formation of 3C/2e interaction. The deviation between experimental and calculated $Ti - \widehat{N} - B$ and $N - \widehat{B} - H_a$ angles are found in the [-1.5%, -0.6%] and [-2.1%, -1.1%] ranges, respectively.

In summary, the DFT functionals herein chosen correctly reproduce the geometric parameters for the titanocene-amidoborane complex. The 3C/2e characters of an agostic complex are well described within all the considered functionals. In other word, the 3C/2e characters are not too sensitive to the exchange-correlation functionals chosen, at least from the geometric point of view.

The influence of the empirical correction of dispersion within the GD3BJ framework will be further evaluated.

Influence of the GD3BJ empirical correction

The 3C/2e interactions have often been compared to the hydrogen bondings. In the latter case, the dispersion forces may notably contribute to the stabilization of the system. A substantial effort was recently made to take into account these forces in DFT calculations. In the present study, the effect of the GD3BJ empirical correction was evaluated in the case of several functionals. To this end, the relative deviation between geometric parameters calculated with and without the GD3BJ correction were calculated as follows:

$$\delta_{X-Y}^{GD3BJ} = \frac{d_{X-Y}^{GD3BJ} - d_{X-Y}}{d_{X-Y}} \times 100 \tag{6.4}$$

$$\delta_{\widehat{X-Y-Z}}^{GD3BJ} = \frac{\widehat{X-Y-Z}^{GD3BJ} - \widehat{X-Y-Z}}{\widehat{X-Y-Z}} \times 100 \tag{6.5}$$

The relative deviations between dispersion corrected values and un-corrected ones (Table 6.5) demonstrate that the GD3BJ correction has minor influence on the geometric description for the system herein studied. Concerning to the Ti-N and Ti-B inter-atomic distances, the relative deviations are found in the [-0.5%, -0.2%] and [-0.7%, -0.3%] ranges, respectively. Moreover, the deviations are even much smaller in the case of $B-H_{free}$ and $B-H_a$ bonds with relative deviations in the [-0.2%, 0.0%] range. Deviations are found in the [-0.5%, -0.1%] and [+0.1%, +0.2%] ranges for $\widehat{Ti-N-B}$ and $\widehat{N-B-H_a}$ respectively.

Table 6.5: Influence of the GD3BJ dispersion correction on the geometric description of the $Cp_2TiNH_2BH_3$ complex: relative deviation δ_{X-Y}^{GD3BJ} and $\delta_{\widehat{X-Y-Z}}^{GD3BJ}$ are given in %.

Functionals	δ_{Ti-N}^{GD3BJ}	δ_{Ti-B}^{GD3BJ}	$\delta_{B-H_{free}}^{GD3BJ}$	$\delta_{B-H_a}^{GD3BJ}$	$\delta_{\widehat{Ti-N-B}}^{GD3BJ}$	$\delta_{\widehat{N-B-H_a}}^{GD3BJ}$
BP86	-0.5	-0.6	-0.1	-0.1	-0.4	0.2
TPSSTPSS	-0.4	-0.5	0.0	-0.1	-0.2	0.1
B3LYP	-0.5	-0.7	-0.1	-0.2	-0.5	0.2
PBE0	-0.3	-0.3	0.0	-0.1	-0.2	0.1
LC-ωPBE	-0.2	-0.4	0.0	0.0	-0.1	0.1

As a conclusion, in the present case, the GD3BJ correction does not impact the geometric description of the system.

Topological considerations

For the characterization of a 3C/2e interaction, the previously proposed methodology relies in the combined use of the QTAIM and ELF topological tools. First of all, the 3C/2e nature of the interactions should be ascertained. To this end, the protonated basin within the ELF topological framework should be a trisynaptic basin with a total population close to 2 e. Then, a combined QTAIM/ELF study is carried out to determine the atomic contributions to the protonated basin. The strength of the agostic interaction is evaluated on the basis of the atomic contribution of the metallic center. Besides, if a BCP is found between M and H_a atoms within the QTAIM framework, the electron density ρ(BCP) provides an alternative way to estimate the strength of agostic interaction.

Thus, besides an accurate geometric characterization of the organometallic complex, the electronic description of the system obtained from DFT calculations should be also accurate enough prior to the topological investigation. To evaluate the accuracy of this description, the topological characters of the agostic interaction were evaluated for the paramagnetic $Cp_2TiNH_2BH_3$ complex with all the above considered functionals in combination with the 6-311++G(2d,2p) basis set.

ELF topological description

The influence of the choice of the functionals as well as the GD3BJ empirical correction on the topological description of the protonated basins was studied. The characteristic results obtained for the $Cp_2TiNH_2BH_3$ complex are summarized in Table 6.6.

Table 6.6: Influence of the functionals on the ELF topological description of the protonated basin involved in the agostic interaction of the $Cp_2TiNH_2BH_3$ complex.

Class	Functionals	Protonated basin	Atomic contribution		
		$V(H_a)$	Ti-$V(H_a)$	B-$V(H_a)$	H_a-$V(H_a)$
Local	M06L	1.92	0.11	0.24	1.57
GGA	BP86	1.91	0.14	0.26	1.51
	BP86-D3	1.92	0.14	0.25	1.51
Meta-GGA	TPSSTPSS	1.90	0.12	0.23	1.55
	TPSSTPSS-D3	1.91	0.13	0.23	1.55
Hybrid	B3LYP	1.92	0.12	0.24	1.56
	B3LYP-D3	1.91	0.12	0.24	1.55
	B3PW91	1.92	0.13	0.25	1.54
	PBE0	1.92	0.13	0.24	1.55
	PBE0-D3	1.92	0.13	0.24	1.55
	M06	1.92	0.12	0.25	1.55
	TPSSh	1.89	0.12	0.22	1.55
Range-separated	LC-ωPBE	1.92	0.12	0.24	1.56
	LC-ωPBE-D3	1.91	0.12	0.23	1.56

Considering all the exchange-correction functionals in combination with 6-311++G(2d,2p) basis set, with and without the GD3BJ empirical correction, the total population of the trisynaptic protonated basin V(Ti, H_a, B) (labelled as $V(H_a)$) is calculated in the [1.89 e, 1.92 e] range. The contribution of the titanium atom to this basin, noted as Ti-$V(H_a)$, varies from 0.11 to 0.14 e. These values are fully consistent with a 3C/2e character of the Ti-H-B interaction herein studied.

From the quantitative point of view, it is found that the ELF topological characterization of the 3C/2e interactions is not sensitive to the exchange-correlation functionals.

QTAIM topological description

The QTAIM approach is also considered as a quantitative and qualitative method to estimate the strength of a particular chemical bond, including 3C/2e interactions. In this case, QTAIM was used to characterize (i) the interaction between the metallic center and the hydrogen atom carried by boron atom: Ti-H_a, (ii) the B-H_a bond and (iii) the B-H_{free} bond.

3C/2e interactions are generally characterized by a such interactions are generally characterized by a BCP(Ti-H_a). The electron density at BCP(B-H_a) should be smaller than the one of the B-H_{free} bond. The electron density ρ, the Laplacian of electron density $\nabla^2\rho$, the ellipticity ϵ and the total energy density H can be used to estimate the strength and characters of interactions herein studied. The calibration of the influence of functionals are thus important for an accurate QTAIM description for a 3C/2e system.

The results obtained for the $Cp_2TiNH_2BH_3$ complex with the selected functionals in combination of the 6-311++G(2d,2p) basis set are presented in Table 6.7.

Table 6.7: Effect of functionals on the QTAIM topological description of the agostic interaction and other important interactions involved in the $Cp_2TiNH_2BH_3$ complex. All the values are given in atomic units.

Functional	BCP(Ti-H_a)				BCP(B-H_a)				BCP(B-H_{free})		
	ρ	$\nabla^2\rho$	ϵ	H	ρ	$\nabla^2\rho$	ϵ	H	ρ	$\nabla^2\rho$	ϵ
M06L	0.055	0.162	0.430	-0.006	0.130	0.027	0.161	-0.117	0.169	-0.159	0.047
BP86	0.059	0.143	0.373	-0.010	0.122	-0.051	0.143	-0.108	0.170	-0.270	0.038
BP86-D3	0.061	0.146	0.372	-0.010	0.123	-0.051	0.141	-0.109	0.170	-0.269	0.038
TPSSTPSS	0.059	0.156	0.374	-0.009	0.122	0.003	0.147	-0.108	0.171	-0.218	0.037
TPSSTPSS-D3	0.060	0.159	0.372	-0.010	0.123	0.003	0.146	-0.108	0.171	-0.217	0.037
B3LYP	0.057	0.150	0.436	-0.009	0.125	-0.014	0.149	-0.112	0.174	-0.259	0.044
B3LYP-D3	0.059	0.154	0.434	-0.009	0.126	-0.012	0.147	-0.113	0.174	-0.258	0.044
B3PW91	0.059	0.151	0.441	-0.010	0.123	-0.010	0.145	-0.110	0.171	-0.241	0.043
PBE0	0.060	0.153	0.464	-0.010	0.123	-0.004	0.142	-0.110	0.171	-0.235	0.043
PBE0-D3	0.060	0.155	0.463	-0.011	0.124	-0.004	0.141	-0.110	0.171	-0.234	0.043
M06	0.058	0.154	0.429	-0.009	0.128	-0.024	0.133	-0.116	0.171	-0.226	0.044
TPSSh	0.059	0.159	0.408	-0.009	0.122	0.017	0.147	-0.108	0.171	-0.208	0.039
LC-ωPBE	0.060	0.157	0.517	-0.010	0.125	-0.004	0.131	-0.112	0.172	-0.253	0.048
LC-ωPBE-D3	0.061	0.160	0.516	-0.011	0.125	-0.004	0.130	-0.112	0.172	-0.253	0.048

- **Ti-H interaction**

First of all, it is worth noticing that the agostic interaction is identified by a BCP(Ti-H_a) for all the selected functionals. The electron density at BCP(Ti-H_a) is calculated in the [0.055 a.u., 0.061 a.u.] range. This indicates a stability of functionals for the QTAIM electron density description of the system being studied. In addition, the positive value of the Laplacian of electron density at this BCP is found from +0.143 to +0.162 a.u., suggesting in a qualitative manner that, the agostic interaction is a closed-shell (non-covalent) interaction. The negative values of total energy density H are in the [-0.011 a.u., -0.009 a.u.] range, which indicates a stabilization of this interaction.

- **Free B-H bond**

A high electron density at BCP(B-H_{free}) in combination with a negative $\nabla^2\rho$ indicates a presence of a covalent bond. In this case, the ρ[BCP(B-H_{free})] value varies from 0.169 a.u. to 0.174 a.u. within different functionals and the $\nabla^2\rho$[BCP(B-H_{free})] values lie in the [-0.325 a.u., -0.051 a.u.] ranges. The Laplacian values are found to be more sensitive to the functionals chosen. Nonetheless, all the calculated results lead to a consistent description of the covalent character of the free B-H bond involved in the $Cp_2TiNH_2BH_3$ complex.

- B−H_a **bond connected to the Ti center**

Compared to the free B-H bond, the B-H_a bond is characterized by lower values of ρ and $\nabla^2\rho$ at BCP. The difference $\Delta\rho$ of electron density between B-H_{free} and B-H_a may provide a preliminary insight of the weakening of B-H bond due to the interaction with the metallic center. This value is found in the [0.047 a.u., 0.049 a.u.] range, except in the case of the calculation with the M06L functional, for which the $\Delta\rho$ is calculated to be 0.039 a.u. Additionally, the Laplacian value at BCP(B-H_a) is found to be very close to zero for all the chosen exchange-correlation functionals. The characterization of bonds by the sign of the Laplacian at the BCP is not always unambiguous, especially in the case of weak bonds. [147] It is therefore difficult to determine the nature of the bonding where the Laplacian values are close to zero.

In addition to these QTAIM descriptors, the ellipticity ϵ associated with different BCP measures the extent to which charge is preferentially accumulated. The ellipticity values at BCP(Ti-H_a) varies from 0.372 to 0.517, which is substantially larger than that in the case of BCP(B-H_{free}) ($0.037 < \epsilon < 0.048$) and BCP(Ti-H_a) ($0.130 < \epsilon < 0.149$). (Table 6.7) Substantial bond ellipticities reflect structural instability. The 3C/2e interaction affects the Ti-H_a and B-H_a bonds in this case. This may explain the higher ellipticities calculated at the BCP(Ti-H_a) and BCP(B-H_a) relative to the BCP(B-H_{free}).

These results demonstrate that all the selected functionals in combination with the 6-311++G(2d,2p) basis set lead to consistent descriptions of the interactions within QTAIM approach. There is no significant difference among exchange-correlation functionals applied in this study.

6.2.2 Influence of the basis set

The influence of the basis sets was also studied. In the case of the titanocene compounds, Pople basis sets can be used for all the elements. This is not the case for the Group IV zirconocene and hafnocene compounds. For these latter cases, the use of a pseudopotential is needed. To determine how these pseudopotentials will affect the description of the agostic interactions, investigations using the following basis sets were carried out:

- The Ahlrichs' basis sets Def2-TZVP, Def2-TZVPP and Def2-QZVPPD for all the atoms,
- The Pople 6-311++G(2d,2p) and 6-311++G(3df,3pd) basis sets for all the atoms,
- The Pople 6-311++G(2d,2p) basis set for the main-elements in combination with the SDD pseudopotential for the titanium atom, (this basis set will be further referred to as 6-311++G(2d,2p)+SDD)
- The Pople 6-311++G(2d,2p) basis set for the main-elements in combination with the relativistic LanL2DZ pseudopotential for the titanium atom, (this basis set will be further referred to as 6-311++G(2d,2p)+LanL2DZ)
- The DZP and TZP basis sets,
- The relativistic second-order Douglas-Kroll-Hess Hamiltonian calculation [148–150], in combination with all-electron contracted Gaussian basis sets DZP-DKH and TZP-DKH,
- The relativistic RESC approach, in combination with the DZP-DKH basis set.

Since it has been demonstrated in the previous section that both the geometrical and topological descriptions of 3C/2e interactions are not sensitive to the exchange-correlation functional, we thus took the B3LYP functional, which is considered as one of the most popular functionals for various properties predictions, in the following investigations.

Geometric considerations

As previously, the $Cp_2TiNH_2BH_3$ complex was chosen as a case study. For this compound, a large choice of basis sets is available, including triple- and quadruple-zeta all electron basis sets and relativistic pseudopotentials. However, for the zirconocene (Cp_2Zr) and hafnocene (Cp_2Hf), pseudopotentials should be used for calculations, in order to reduce the number of primitive Gaussians. Moreover, relativistic effects may play prominent role in organometallic complexes. In addition with relativistic pseudopotentials (SDD and LanL2DZ), the scalar relativistic Douglas-Kroll-Hess Hamiltonian was used. (Table 6.8) In order to clearly demonstrate the impact of basis sets on the selected parameters, a graphic representation of the deviations between calculated distances and experimental ones, as well as the total deviation for each basis set, is shown in Figure 6.5.

At a first glance, it appears that the Ti-N and Ti-B experimental distances are correctly reproduced, with a deviation within ± 0.03 Å. The lengthening of the B-H bond involved in the agostic interaction (Δd_{B-H}) is also well reproduced, with a deviation below 1.4%. Thus, from a geometrical point of view, all the considered basis sets combined with the B3LYP functional lead to a suitable description of the $Cp_2TiNH_2BH_3$ system.

Table 6.8: Effect of the basis set on the geometric description of the $Cp_2TiNH_2BH_3$ complex. The distances are given in Å.

Type of basis set	Basis set	d_{Ti-N}	d_{Ti-B}	$d_{B-H_{free}}$	d_{B-H_a}	Δd_{B-H}	d_{Ti-H_a}
Ahlrichs' basis sets	Def2-TZVP	2.182	2.540	1.204	1.299	0.095	1.894
	Def2-TZVPP	2.182	2.541	1.203	1.298	0.095	1.895
	Def2-QZVPP	2.182	2.540	1.202	1.297	0.095	1.894
Pople's basis sets	6-311++G(2d,2p)	2.182	2.542	1.202	1.297	0.095	1.895
	6-311++G(3df,3pd)	2.182	2.540	1.203	1.297	0.094	1.894
Pople's basis sets with pseudopotential for metal	6-311++G(2d,2p) +SDD	2.174	2.535	1.202	1.297	0.095	1.889
	6-311++G(2d,2p) +LanL2DZ	2.177	2.529	1.202	1.298	0.096	1.879
Double and triple zeta basis sets	DZP(9v)	2.176	2.540	1.219	1.312	0.093	1.894
	DKH2/ DZP-DKH(9v)	2.173	2.536	1.219	1.314	0.095	1.890
	RESC/ DZP-DKH(9v)	2.174	2.537	1.219	1.314	0.095	1.891
	TZP(9v)	2.183	2.539	1.204	1.301	0.097	1.887
	DKH2/ TZP-DKH(9v)	2.180	2.535	1.204	1.300	0.096	1.885
Exp.		2.153	2.52	1.13&1.09	1.21	0.1	

The use of either LanL2DZ or SDD pseudopotential for the metallic center, in combination with the 6-311++G(2d,2p) basis set for the other atoms, leads to a little improvement of the accuracy of the calculated distances, especially for description of the Ti-N and Ti-B distances in which the metallic center is involved.

The influence of the use of a scalar relativistic Hamiltonian was also studied with the two-component relativistic Douglas-Kroll-Hess Hamiltonian in combination with the all electron contracted DZP-DKH and TZP-DKH basis sets. For a sake of comparison, non-relativistic calculations were also carried out with the DZP and TZP basis sets. Due to a limitation of variables (for a maximum 50 variables) and high computational cost for such calculations with the Gaussian 09 software, only partial optimizations were carried out. All but nine parameters were frozen. In this case, the positions of the Ti, N, B and H atoms were optimized in Z-matrix representation which is shown in Figure 6.6. Nine variables are optimized for the partial optimizations and the frozen parameters were optimized with B3LYP/6-311++G(2d,2p)+LanL2DZ level of theory.

The same variables were used for the relativistic DKH2/DZP-DKH, RESC/DZP-DKH, DKH2/TZP-DKH and for the non-relativistic DZP and TZP calculations. No dramatic change is observed between the structure partially optimized at the B3LYP/DZP level and those at relativistic calculations, including the DKH2 and RESC methods. (Figure 6.5) However, compared to the above mentioned basis sets, the deviations of calculated parameters are larger within these double-zeta

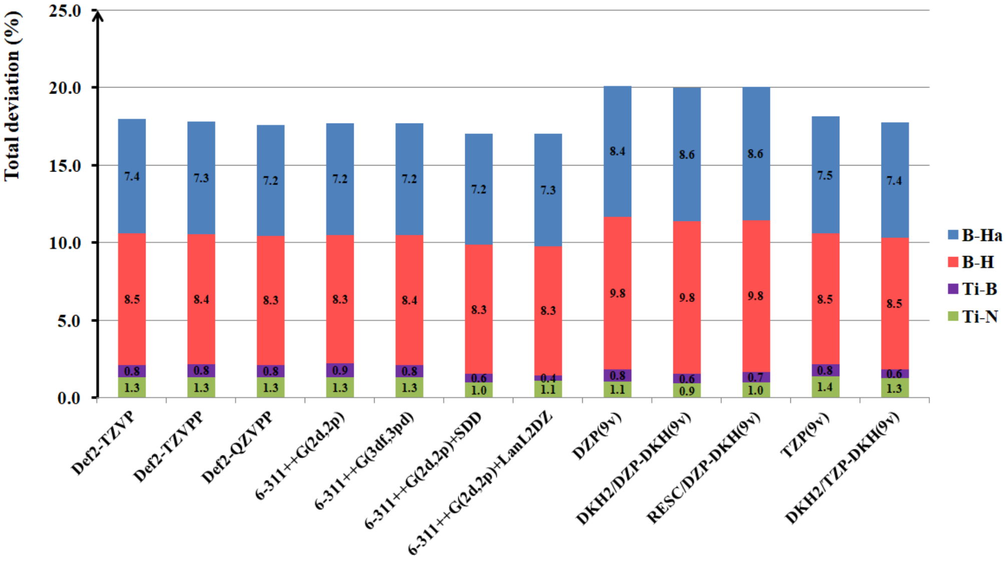

Figure 6.5: Total deviations between calculated geometric values (with B3LYP functional in combination with different basis sets) and experimental values for the $Cp_2TiNH_2BH_3$ complex.

Ti						
B	1	a				
N	2	b	1	c		
H_a	2	d	3	e	1	f
H_{free1}	2	g	3	h	1	i
H_{free2}	2	g	3	h	1	-i

Figure 6.6: Z-matrix representation for the partial optimization of the $Cp_2TiNH_2BH_3$ complex.

basis sets, especially for the cases of B-H_{free} and B-H_a bond. The employment of triple-zeta basis sets, alone or with relativistic calculations, slightly improves the geometrical descriptions. This suggests that the relativistic effect should have a limited impact on the calculated structures in the case of $Cp_2TiNH_2BH_3$ complex. In addition, the larger triple-zeta basis sets are more suitable compared to the double-zeta ones.

To sum up the effect of the size of basis sets, the increasing size of these three Ahlrichs' basis sets and two Pople's basis sets presented in this study leads to no improvement for a geometric description. It means that the Def2-TZVP and the 6-311++G(2d,2p) (which is used for the calibration of different functionals) basis sets are sufficient to describe the system herein studied. The use of the LanL2DZ and SDD relativistic pseudopotential for metallic center leads to a small improvement of the geometric description. Besides, the partial optimizations within the relativistic DKH2 or RESC calculations in combination with all-electron basis sets were also performed. Results have shown that the double-zeta DZP(-DKH) basis sets are not enough while the triple-zeta TZP(-DKH) ones allow for a better geometrical description. Additionally, the effect of relativistic calculations is found to be negligible for the titanocene.

Topological considerations

The B3LYP functional was further used to evaluate the influence of basis sets on the electronic description of the 3C/2e interaction. The results obtained with ELF analysis are presented in Table 6.9. With all the combinations of basis sets selected in this study, calculations carried out with the B3LYP functional lead to the identification of a synaptic protonated basin $V(H_a)$ with a total population in the [1.90 e, 1.94 e] range for the case of $Cp_2TiNH_2BH_3$ complex. Non-negligible contribution of metallic center to this basin is identified with all the selected levels of theory. Thus, whatever the levels of theory chosen, the topological analysis leads to the identification of a 3C/2e agostic interaction.

However, the calculated contribution of the metallic center on this protonated basin very much depends on the basis set. At the B3LYP/6-311++G(2d,2p)+LanL2DZ and B3LYP/6-311++G(2d,2p)+SDD levels of theory, the atomic contribution of the Ti atom in the hydrogen atom, is calculated to be 0.06 e. With all the other selected combinations of basis set, without the use of a pseudopotential for the metallic atom, the atomic contribution of the Ti atom in the hydrogen atom, is 0.12 e. We thus consider that the use of a relativistic pseudopotential for the metallic center leads to an accurate description of the agostic interaction from a geometric point of view, but not from a topological point of view. The use of a basis set that takes into account of the core electrons is necessary *prior to* ELF topological analysis of an agostic interaction when the contribution of metallic center is quite important for further investigations.

Table 6.9: Effect of different combinations of basis set on the ELF topological description of the protonated basin involved in the Ti-H-B interaction in $Cp_2TiNH_2BH_3$ compound. All the calculations were carried out with the B3LYP functional and all the values are given in e.

Type of basis set	Basis sets	$V(H_a)$	Atomic contribution		
			Ti-$V(H_a)$	B-$V(H_a)$	H_a-$V(H_a)$
Ahlrichs' basis sets	Def2-TZVP	1.91	0.12	0.23	1.56
	Def2-TZVPP	1.91	0.12	0.23	1.56
	Def2-QZVPP	1.92	0.12	0.23	1.57
Pople's basis sets	6-311++G(2d,2p)	1.92	0.12	0.24	1.56
	6-311++G(3df,3pd)	1.91	0.12	0.23	1.56
Pople's basis sets with pseudopotential for metal	6-311++G(2d,2p)+SDD	1.90	0.06	0.23	1.61
	6-311++G(2d,2p)+LanL2DZ	1.91	0.06	0.24	1.61
Double and triple zeta basis sets	DZP(9v)	1.92	0.12	0.22	1.58
	DKH2/DZP-DKH(9v)	1.91	0.12	0.21	1.58
	RESC/DZP-DKH(9v)	1.94	0.12	0.24	1.58
	TZP(9v)	1.93	0.12	0.23	1.58
	DKH2/TZP-DKH(9v)	1.91	0.12	0.23	1.56
B3LYP-DKH2/DZP-DKH//B3LYP/6-311++G(2d,2p)+LanL2DZ		1.91	0.11	0.21	1.59

For a sake of computational time saving, we carried out a single point calculation with the relativistic DKH2/DZP-DKH all electron contracted basis set, at the geometry optimized with the B3LYP/6-311++G(2d,2p)+LanL2DZ. When the topological study is carried out from this single point calculation, the atomic contribution of the metallic center in the trisynaptic agostic basin is calculated to be 0.11 e with the population of corresponding basin of 1.91 e. Thus, a single point calculation using the DKH2 Hamiltonian in combination with the B3LYP/DZP-DKH level of theory from a correct geometry obtained with a pseudopotential for the metallic center is sufficient to accurately describe the agostic interaction from a topological point of view. Since the DKH2/DZP-DKH basis set is available for all the atoms including the Group IV and V metals, and the single point calculations of electron density with double-zeta basis set have already been proven to be enough for a correct topological description, it will be employed for further investigations.

Summary

A calibration based on the $Cp_2TiNH_2BH_3$ compound was carried out to estimate the ability of several DFT levels of theory to reproduce the geometric and topological properties of the 3C/2e interaction involved in this compound. It has been found that there is no significant influence of different exchange-correlation functionals on both the geometric and topological descriptions. However, for an accurate topological description of this interaction, especially in the case of electron localization function (ELF), all electron basis sets that take account the relativistic effects should be considered. Thus, a minimum methodology was proposed for the following investigations:

- First of all, the geometry of the compounds were built up from the information available from the literature, and fully optimized with the B3LYP functional, in combination with the LanL2DZ basis set for the metallic atom and the 6-311++G(2d,2p) basis set for all the other atoms,
- Then, a single point calculation was carried out using the DKH2 Hamiltonian in combination with the B3LYP/DZP-DKH level of theory for further topological analyses of selected systems.

6.3 Characterization of intramolecular M-H-B interactions

Various experimental investigations as well as computational propositions of transition metal catalyzed-dehydrogenation mechanisms of amine-boranes have revealed the important role of the supporting M-H-B 3C/2e interactions. These include:

- intramolecular interactions, which are called agostic interactions;
- intermolecular interactions involved in so-called σ complexes.

In this section, 54 metallocene agostic complexes were selected to further understand the impact of different parameters on the 3C/2e characters. The effect of this interaction on the catalytic role of the metallocene was further evaluated. In Figure 6.7 are shown different series of metallocene compounds with several features:

- different natures of the metallic center M (M = Ti, Zr and Hf) as well as different oxidation states of M: +III (paramagnetic) and +IV (diamagnetic);
- different ligands including amido-borane and phosphido-borane (X = N and P);
- different natures of substituent groups carried by X atoms (R= H, Me and Ph).

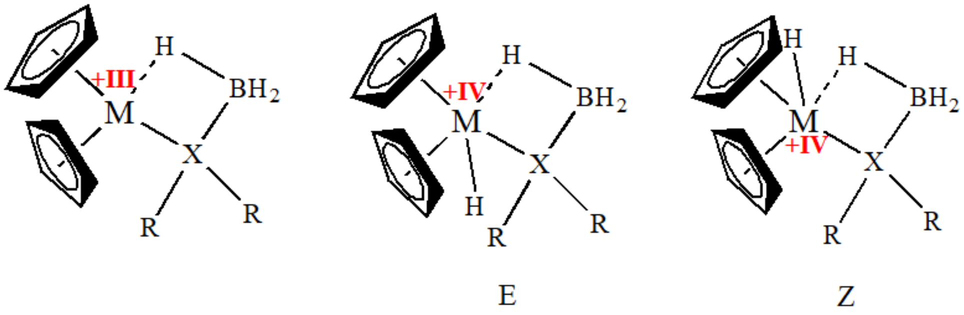

Figure 6.7: Group IV metallocene compounds involving a 3C/2e intramolecular M-H-B interaction that were considered for the present study.

Two isomers of diamagnetic compounds (+IV oxidation state) are also considered in this case:

- the E isomers where E (entgegen) stands for opposite position of hydrogen atom carried by the metal and the hydrogen atom from BH_3 moiety,
- the Z isomers where Z (zusammen) represents the close position of the two hydrogen atoms.

Figure 6.8 presents the variation of the electron density ρ[BCP(M-Ha)] (“Ha” stands for the hydrogen atom from BH_3 moiety in interaction with the metallic center) as a function of the corresponding M-Ha distances involved in the 54 complexes. The strength of the interaction increases with the ρ(BCP) value and with the decrease of the interatomic distance. As a consequence, points located in the left hand side and in the top side of the graph correspond to the strongest interactions. This graph clearly suggests that the β B-H agostic interaction is systematically stronger with amido-borane ligands compared to phosphido-borane ones. The comparison of the strength of agostic interactions in similar complexes with different metal centers demonstrates that the agostic interaction is stronger in titanocene compounds than in zirconocene and hafnocene counterparts. The strength of the interaction is slightly affected by the oxidation state of the metal, as well as the Z and E isomers.

It is interesting to compare these results with experimental observations, based on the study of the whole dehydrogenation process including the global turnover of the reaction, identification of products, and structural characterization of intermediates. The experimental results have unveiled several features of the amine-borane dehydrogenation:

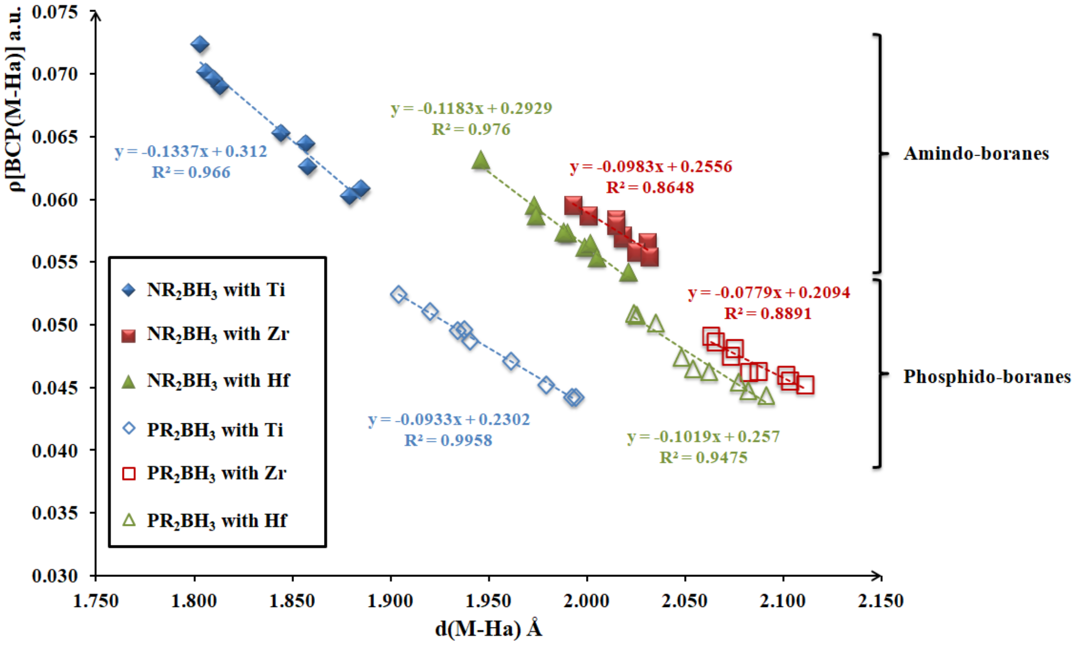

Figure 6.8: Variation of ρ[BCP(M-Ha)] as a function of M-Ha distances involved in $Cp_2MXR_2BH_3$ and $Cp_2M(H)XR_2BH_3$ complexes.

- In a study dealing with Rh-containing organometallic catalysts, Manners *et al.* have demonstrated that dehydrogenation reaction proceeds more efficiently with amine-boranes compared to phosphine-borane ones. [151]
- The turnovers of the dehydrogenation reactions with titanocene catalysts are reported to be higher than the ones obtained with zirconocene and hafnocene counterparts. [50, 52]

The close agreement between the calculated strength of the agostic interactions and the experimental efficiency of the dehydrogenation processes may suggest that the agostic intermediate might have a prominent role in the reaction mechanism.

6.4 Characterization of intermolecular M-H-B interactions

As far as the dehydrogenative coupling of amine-boranes is concerned, σ complexes involving 3C/2e M-H-B intermolecular interactions are also considered as important intermediates. Figure 6.9 illustrates the simplified dehydrogenation reaction course of amine-boranes. Generally, σ complexes can be isolated experimentally when tertiary amine-boranes e.g. $H_3B{\cdot}NMe_3$ are involved, as the lack of N-H bonds prevents further dehydrogenation process. [65, 152, 153] The isolation of such a σ complex is also possible when the dehydrogenation reaction is inactive. This might be the case if the metallic center is already fully coordinated, for instance. [65, 153]

The aim of the present study is to propose specific descriptors that would allow a comparison of the strength of intermolecular M-H-B interactions involved in a σ complex. Previous study of intramolecular M-H-B interactions has already demonstrated the linear relationship of calculated

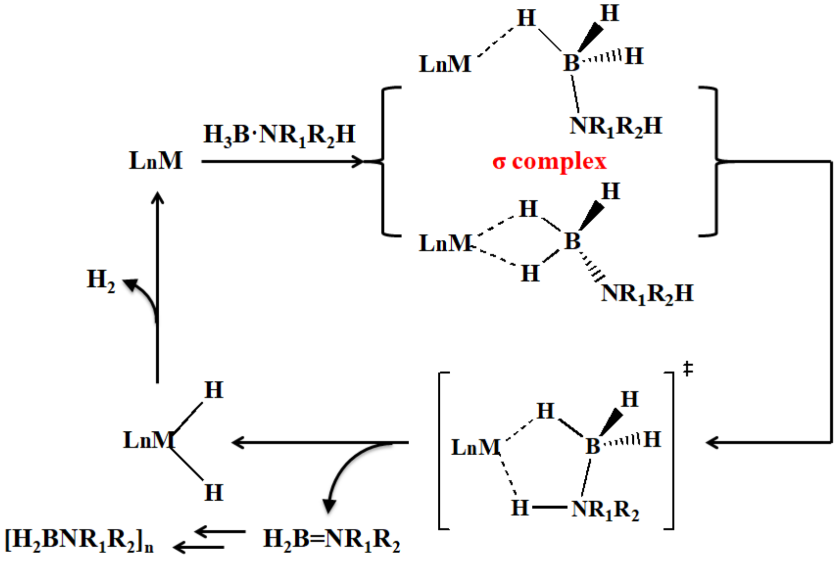

Figure 6.9: Simplified pathway for dehydrogenation of amine-borane adducts.

inter-atomic distances as function of their corresponding electron density at BCPs. In the present section, I will extend the previous study to cases of intermolecular M-H-B interactions involved in σ complexes. In addition, other descriptors for comparison of the strength of 3C/2e interactions will be sought. Owing to lack of experimental data for such systems, hydroborates anions interacting with metallocenes cations (Figure 6.10) were chosen as simple prototypes. Indeed, experimental data are available for these systems in the literature.

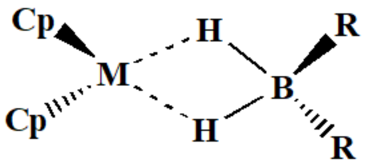

Figure 6.10: σ complex that contains a cationic metallocene and an anionic hydroborate ligand.

σ complexes associated with Group IV and Group V metallocenes were mainly characterized experimentally, by means of X-ray and neutron diffraction crystallography. Table 6.10 shows characteristic distances involved in the M-H-B interactions in nine Cp_2M−hydroborate complexes. Both the experimental values from the literature and the calculated ones obtained by geometry optimization at B3LYP/6-311++G(2d,2p)+LanL2DZ level of theory are given.

As a first approximation, the experimentally determined B-H and M-H distances could be considered as simple indicators of the strength of the interaction. A lengthening of the B-H bond, combined with a relatively short M-H distance should be an indicator of a relatively strong interaction. The graph plotted in Figure 6.11 clearly demonstrates that these simple indicators do not allow an easy classification of the {metallocene + hydroborate} systems. This may be explained by several reasons:

- a physico-chemical phenomenon: the nature of the metallic center and the ligand influences the interaction. Different {metallocene + hydroborate} systems cannot be directly compared;
- a technical phenomenon: the experimental determination of the M-H and B-H distances

Table 6.10: Characteristic distances involved in the M-H-B iterations in the Cp_2M-hydroborate complexes identified with diffraction techniques (Exp). Calculations (Calc) were carried out by geometry optimization at B3LYP/6-311++G(2d,2p)+LanL2DZ level of theory. All the distances are given in Å.

Complex		M-H(B)	B-H($\cdots$M)
$Cp_2Ti-H_2BH_2$	Exp [154]	1.75(8)/1.75(8)	1.23(8)/1.23(8)
	Calc	1.897/1.897	1.270/1.270
$Cp_2Ti-H_2BC_4H_8$	Exp [155]	1.83(3)/1.84(3)	1.23(3)/1.27(3)
	Calc	1.875/1.875	1.290/1.290
$Cp_2Ti-H_2BC_5H_{10}$	Exp [155]	1.88(3)/1.88(4)	1.18(3)/1.35(3)
	Calc	1.891/1.889	1.300/1.295
$Cp_2Ti-H_2BC_8H_{14}$	Exp [155]	1.89(2)/1.90(1)	1.23(1)/1.29(2)
	Calc	1.892/1.892	1.292/1.292
$Cp_2Ti-H_2B(C_6F_5)_2$	Exp [156]	1.973/2.031	1.320/1.320
	Calc	1.963/1.963	1.254/1.254
$Cp_2Nb-H_2BH_2$	Exp [155]	1.83(4)/1.83(4)	1.39(4)/1.39(4)
	Cal	1.921/1.921	1.313/1.312
$Cp_2Nb-H_2BC_4H_8$	Exp [155]	1.82(3)/1.76(3)	1.30(3)/1.27(3)
	Calc	1.899/1.899	1.339/1.339
$Cp_2Nb-H_2BC_5H_{10}$	Exp [155]	1.85(3)/1.85(3)	1.26(3)/1.26(3)
	Calc	1.915/1.911	1.345/1.341
$Cp_2Nb-H_2BC_8H_{14}$	Exp [155]	1.87(4)/1.89(4)	1.32(3)/1.26(3)
	Calc	1.916/1.916	1.335/1.335

by X-ray diffraction is entangled by errors due to the difficulty in locating H atoms;

- the size of sample is really limited and the properties of these selected systems are similar.

Therefore, accessible experimental data are not enough for in-depth exploration of such systems. As can be seen from Figure 6.12, representative models of $Cp_2M-H_2BR_2$ complexes in combination with cationic metallocenes $[Cp_2M]^+$ and anionic hydroborate $[H_2BR_2]^-$ are proposed. Among the representative systems, nine complexes have been already experimentally synthesized and identified.

6.4.1 Geometric considerations

In the first place, the presence of a relatively strong electrostatic interaction between cationic metallocene and anionic hydroborate ligand in combination with metal-ligand interactions may cause a series of structure distortions. Similar to the case of agostic systems studied hereinbefore, a relatively short M-H distance accompanied by elongation of the corresponding B-H bond may provide a first insight on the strength of intermolecular interactions.

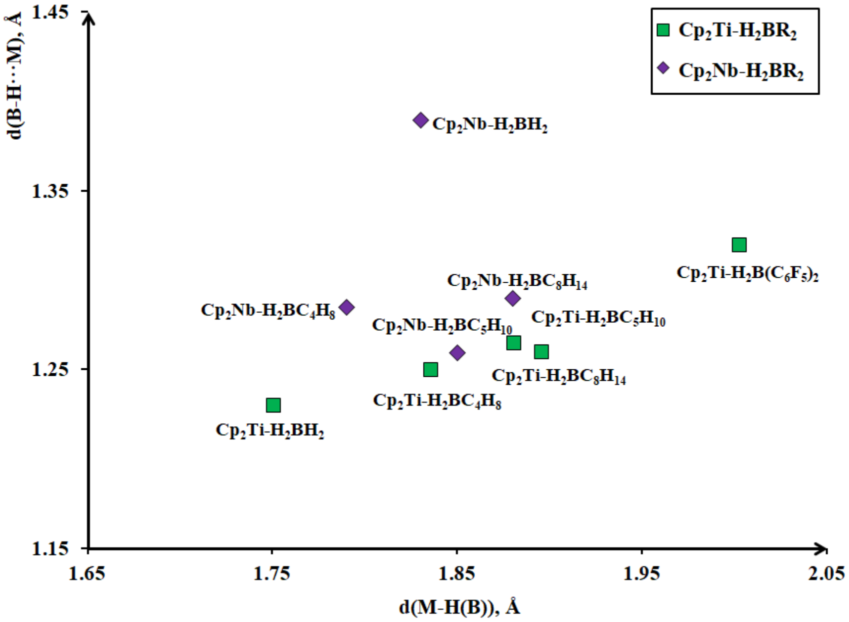

Figure 6.11: Representation of the experimental B-H(···M) and M-H(B) distances in the {metallocene + hydroborate} complexes.

Table 6.11 shows the calculated B-H bond length in the isolated hydroborate ligands, as well as the B-H and M-H distances involved in the $Cp_2Ti{-}H_2BR_2$ complexes. The strength of the B-H bond in different complexes is dominated by mainly two effects:

- Firstly, the intrinsic effect of hydroborate ligand, indicating the influence of the nature of substituent group R carried by the boron atom should be considered. Isolated ligands are taken into consideration for the first time to evaluate the impact of R groups on the B-H length involved in the $[H_2BR_2]^-$ ligands. Regarding the alkylated hydroborates, the B-H distances are found in the [1.230 Å, 1.244 Å] range. It is noteworthy that almost all the structures are symmetric except from the case of $R_2 = C_5H_{10}$ and $R_2 = (CH_2)_2C_6H_4$. Compared to the reference value at 1.235 Å in the case of $[BH_4]^-$, the substitution of aliphatic groups has minor effect on the B-H bonds. The strong electron-withdrawing effect of the pentafluorophenyl (C_6F_5) group results in a significantly shortened B-H distance of 1.204 Å.

- Secondly, the effect induced by the intermolecular interactions between B-H bond and metallocene is worth studying. From Table 6.11, evidence for the presence of M-H-B interaction is identified by the elongation of B-H bonds in the complexes and the relative short M-H distances in the [1.875 Å , 1.963 Å] range, which were similar in the agostic systems.

The elongations of B-H bond in interaction with titanocene compared to the distance in the isolated ligand is donated as Δ(B-H):

$$\Delta(B-H) = d(B-H_{complex}) - d(B-H_{isolated\ ligand}) \tag{6.6}$$

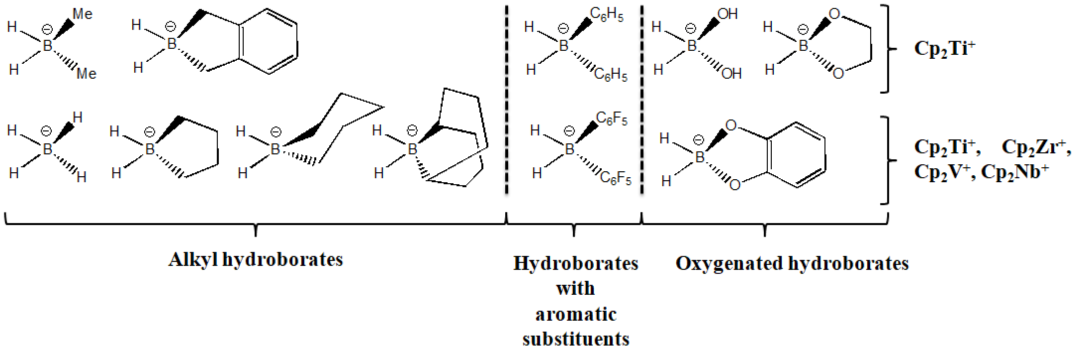
Me
Me
H
H
C6H5
C6H5
C6F5
C6F5
OH
OH
O
O
Cp2Ti+
Cp2Ti+, Cp2Zr+,
Cp2V+, Cp2Nb+
Alkyl hydroborates
Hydroborates with aromatic substituents
Oxygenated hydroborates

Figure 6.12: Combinations of cationic metallocenes and anionic hydroborates selected for the present study of the M-H-B interactions involved in $Cp_2M{-}H_2BR_2$ complexes.

Δ(B-H) values can be divided into three categories:

- the $Cp_2Ti{-}H_2BH_2$ complex has the smallest B-H elongation that is calculated to be 0.035 Å;
- in the case of other complexes containing alkylated hydroborate and aromatic hydroborate, the Δ(B-H) values are found from 0.050 Å to 0.057 Å;
- Δ(B-H) become even greater in the complexes with oxygenated ligands in the [0.080 Å, 0.091 Å] range.

The graphical representation of B-H bond length as function of the corresponding M-H distances for the titanocene complexes is given in Figure 6.13. It provides a general measure of the force of intermolecular interactions, in other words the extent of B-H activation, in $Cp_2Ti{-}H_2BR_2$ systems with different substituent group. The longer the B-H bond is, the smaller the M-H distance is and the stronger the intermolecular interactions are. Figure 6.13 shows the activation of B-H bond from the geometric point of view. In the complexes with oxygenated ligands, the B-H activation is stronger than the one in alkyl-substituent complexes. The complexes with aromatic substituents have even inconspicuous activation effect, especially in the case of $Cp_2Ti{-}H_2B(C_6F_5)_2$ complexes.

Table 6.11: Calculated B-H distances in the isolated hydroborate ligands as well as the B-H and M-H distances involved in the $Cp_2Ti{-}H_2BR_2$ complexes.

Type of hydroborate	$[H_2BR_2]^-$	Isolated ligand	$Cp_2Ti{-}H_2BR_2$ complex		Δ(B-H)
		B-H	B-H(···M)	M-H(B)	
Alkylated hydroborate	$[H_2BH_2]^-$	1.235	1.270	1.897	0.035
	$[H_2BC_4H_8]^-$	1.236	1.290	1.875	0.054
	$[H_2BC_5H_{10}]^-$	1.238/1.244	1.295/1.300	1.891/1.889	0.057/0.056
	$[H_2BC_8H_{14}]^-$	1.237	1.292	1.892	0.055
	$[H_2BMe_2]^-$	1.242	1.298	1.889	0.056
	$[H_2B(CH_2)_2C_6H_4]^-$	1.230/1.233	1.285/1.286	1.889/1.884	0.055/0.053
Aromatic hydroborate	$[H_2B(C_6F_5)_2]^-$	1.204	1.254	1.963	0.050
	$[H_2B(C_6H_5)_2]^-$	1.227	1.279	1.921	0.052
Oxygenated hydroborate	$[H_2B(OH)_2]^-$	1.241	1.321	1.848	0.080
	$[H_2BO_2C_2H_4]^-$	1.239	1.319	1.839	0.080
	$[H_2BO_2C_6H_4]^-$	1.224	1.315	1.856	0.091

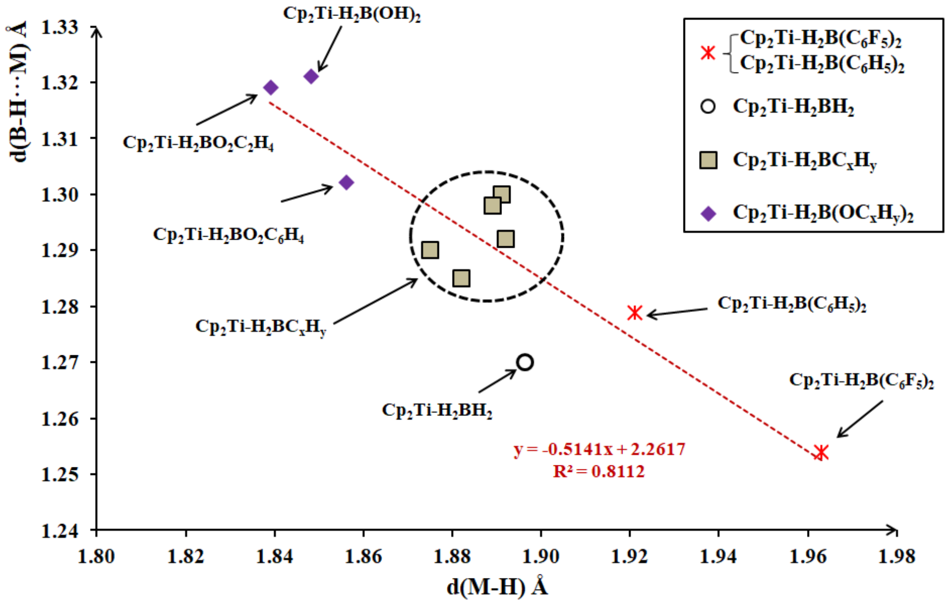

Figure 6.13: B-H distances as a function of M-H distances involved in the titanocene complexes.

In addition, concerning complexes with other Group IV and Group V metallocenes, the calculated geometric parameters also demonstrate the nature of metal-dependence for the B-H activation. Figure 6.14 demonstrates that the strongest B-H activation effect is systematically observed in the vanadocene and titanocene complexes rather than their corresponding niobiocene and zirconocene ones.

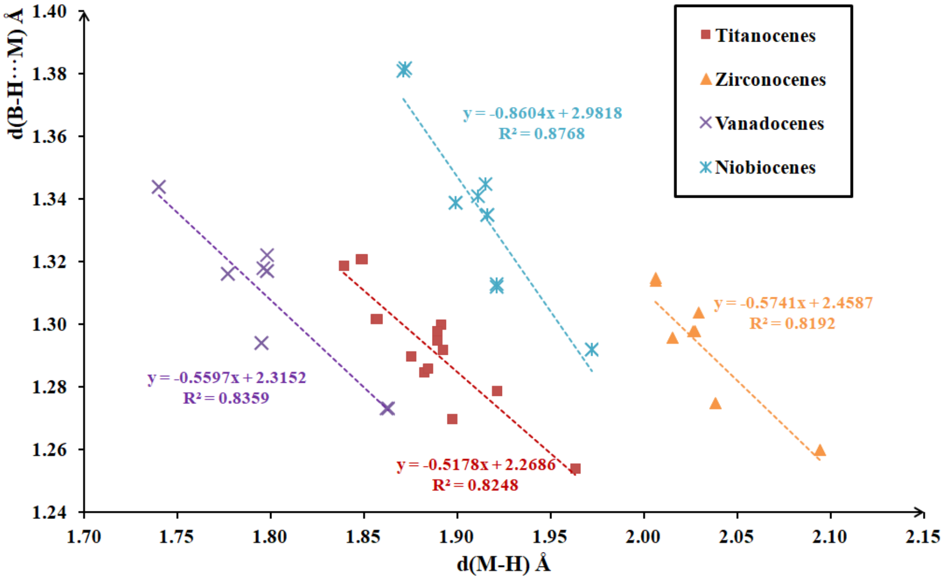

Figure 6.14: Evolution calculated B-H distance as function of M-H distance.

Can these geometric parameters serve as good descriptors for the ability of B-H activation in different systems? How can we speculate the strength of corresponding B-H or M-H distances in a given system? Further investigations and discussion will be carried out within the topological analyses.

6.4.2 Topological considerations

Previous studies have already allowed the proposal of some topological descriptors based on the QTAIM and ELF topological approaches to estimate the B-H activation and to prove the presence of 3C/2e interactions involved in agostic systems.

The QTAIM approach for all the {metallocenes + hydroborates} systems demonstrates the identification of a bond bath (BP) and a bond critical point (BCP) between the metal center and hydrogen atoms for each of these systems. A example is given in Figure 6.15 that displays the 2D representation of Laplacian of electron density of $Cp_2Ti{-}H_2BH_2$ complex. Two topological quantities, the electron density ρ[BCP(B-H)] and ρ[BCP(M-H)], are worth studying to quantitatively characterize the interactions between metallocenes and hydroborates.

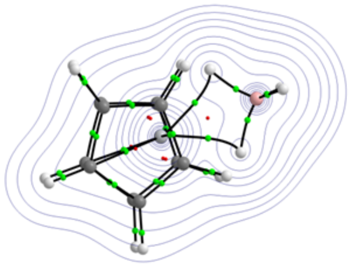

Figure 6.15: 2D representation of Laplacian of electron density of $Cp_2Ti{-}H_2BH_2$ complex.

Electron density at BCP of B-H bonds $Cp_2M - H_2BR_2$ complexes

The weakening of B-H bond is a determining factor of the B-H activation for a given system. In the first place, to investigate the influence of hydroborate substituents and also nature of metal center on this weakening effect, the studies of each BCP(B-H) are carried out. Figure 6.16 shows the variations of ρ[BCP(B-H)] as a function of the length of the B-H bond involved in the isolated ligands and in the $Cp_2Ti{-}H_2BR_2$ complexes respectively. This direct comparison of the ligands is of interest to the experimenters, since it directly reflects the propensity of the B-H bond to be broken for a further dehydrogenation reaction. The longer the B-H bond, the lower the electronic density at the BCP of the bond, the more reactive the B-H bond will be. This graphical representation makes it possible to classify the hydroborates depending on the activation of the B-H bond. Three families of ligands are identified: $H_2BC_xR_y^-$ ligands (with R = H and F) on the one hand, $H_2B(OC_xH_y)_2^-$ ligands on the other hand, and the $H_2BH_2^-$ ligand.

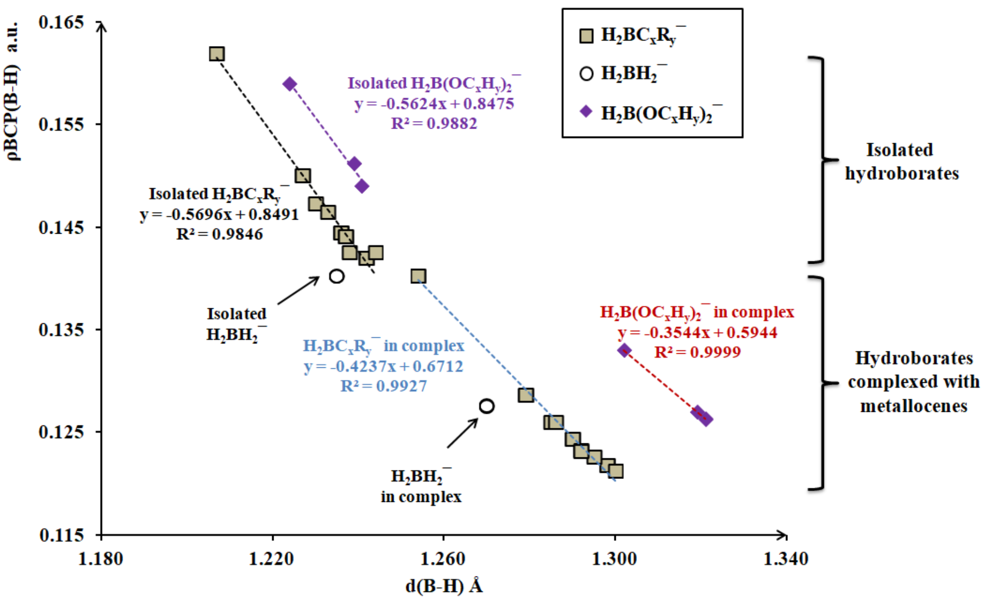

Figure 6.16: Effects of the substituent groups carried by boron atom on the strength of B-H bonds in isolated hydroborate and in the hydroborates interacting with titanocene cation.

When interacting with the titanocene cation, a right and down shift of these three families is observed. Thus, the interaction of the hydroborate anions with the titanocene cation leads to a lengthening of the B-H bond with a concomitant decrease of ρ[BCP(B-H)]. The displacement of each group of plotted points provides a visual impression about the activation of B-H bond. The B-H bond is found to be mostly activated in the complexes with oxygenated ligands $H_2B(OC_xH_y)_2^-$ when interacting with the titanocene complex.

Electron density at BCP of M-H bonds $Cp_2M - H_2BR_2$ complexes

The presence of BCP(M-H) in all the studied complexes within the QTAIM framework makes it possible to evaluate the strength of the interaction by following the evolution of ρ[BCP(M-H)] as a function of the M-H distance. Figure 6.17 presents the results obtained for the hydroborates interacting with titanocene: ρ[BCP(M-H)] decreases linearly with the distance M-H, whatever the nature of the substituents on the borate is. The interaction is strongest with the oxygenated hydroborates with respect to alkylated borates, and a weaker interaction is identified with hydroborates bearing aromatic substituents, with a particularly weak interaction in the case of the $H_2B(C_6F_5)_2{}^-$.

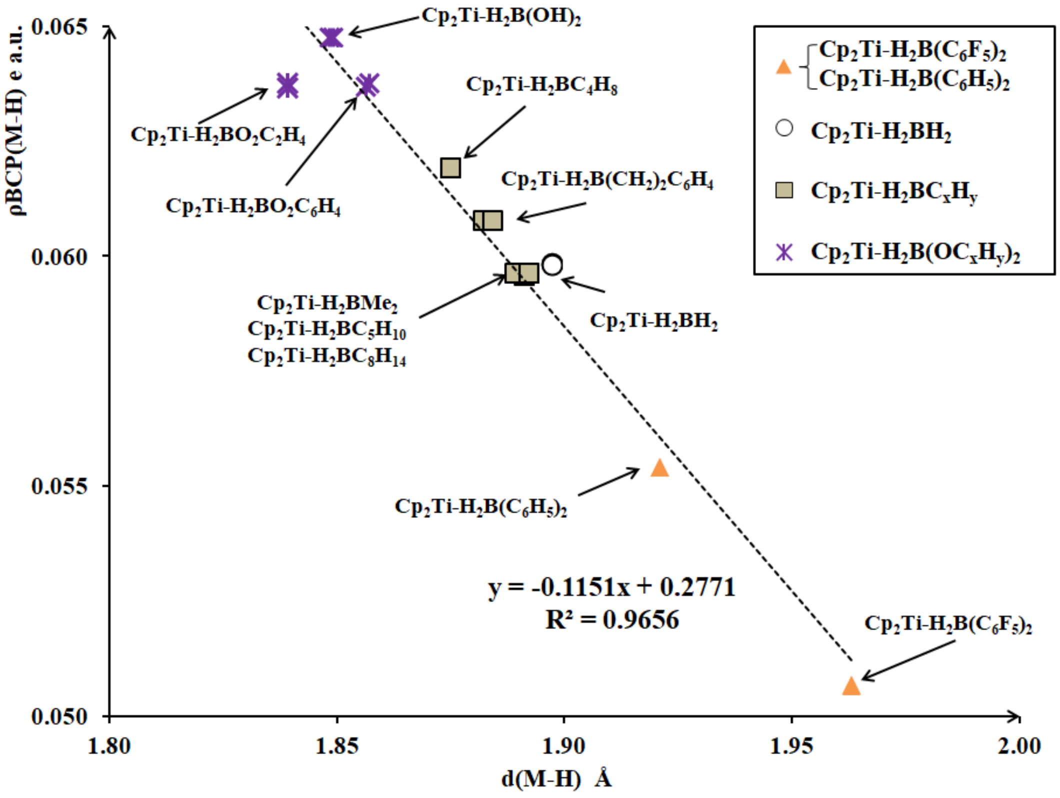

Figure 6.17: Quantification of the strength of the M-H interaction for differently substituted hydroborates interacting with titanocene.

When the nature of the metal center is modified, the strongest M-H interactions are systematically observed with the oxygenated substituents, and the weakest interactions with the aromatic substituents (Figure 6.18). For a given borate, the value of ρ[BCP(M-H)] suggests that the $Cp_2M{-}H_2BR_2$ interactions are systematically stronger with vanadocene (respectively Niobiocene) compared to titanocenes (respectively zirconocene).

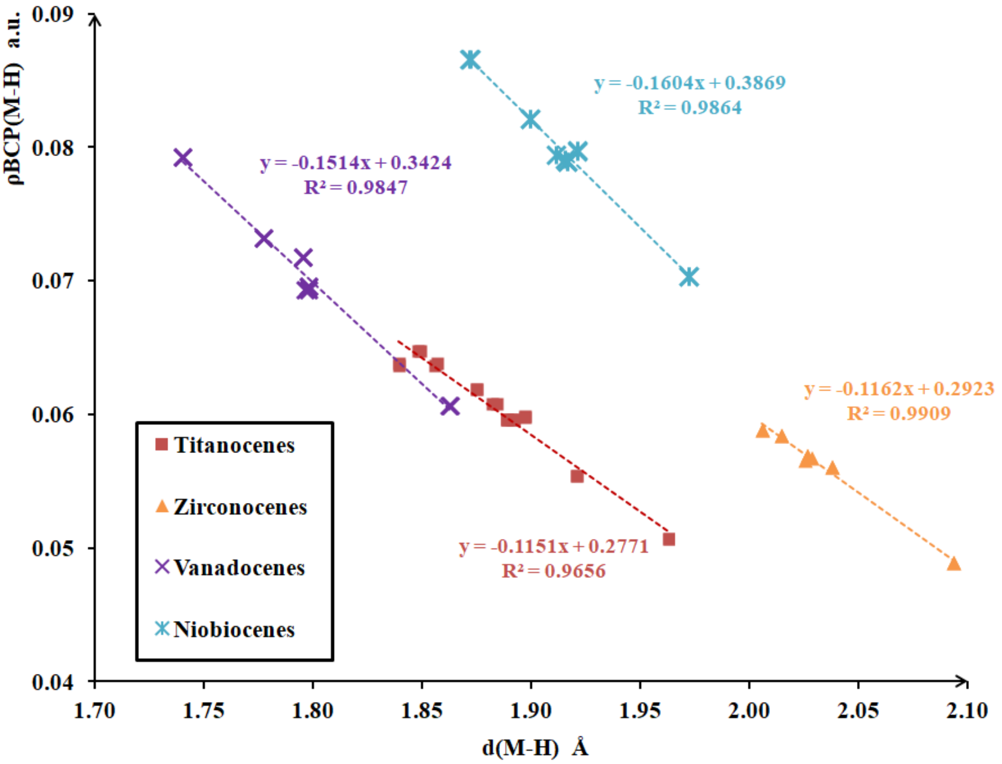

Figure 6.18: Influence of the metal center on the strength of the M-H interaction.

An ELF/QTAIM combined analysis of the $Cp_2M - H_2BR_2$ interactions

The topological characterizations of the B-H bond and M-H interactions are complementary in these $Cp_2M{-}H_2BR_2$ complexes: the geometric and electronic characteristics of the B-H bonds will play a fundamental role in the B-H activation reactivity, whereas the M-H distance and ρ[BCP(M-H)] are direct measurements of the strength of the interaction with the metal center. However, the QTAIM analysis of the B-H and M-H bond paths is not sufficient for a full quantitative description of these M-H-B interactions. The ELF analysis was already employed to identify the presence of a 3C/2e interaction in previous section. It allows to quantify the contribution of the metallic center C(M) within the protonated basin (V(H)) involved in the 3C/2e interactions. In the case of the $Cp_2M{-}H_2BR_2$ complexes, trisynaptic protonated basins are identified in all the considered systems, indicating a 3C/2e character of the intermolecular interactions between B-H σ bond and metallocene. In Table 6.12 are reported the population of protonated basin as well as the contribution of each atom to this basin of all the σ complexes with titanocene.

Table 6.12: ELF features of Ti-H-B interactions involved in $Cp_2Ti{-}H_2BR_2$ including the population of protonated basin V(H), the atomic contribution of each atom to this basin, all of them are given in e. The contributions of metal center to the protonated basin $100\times\frac{C(M)}{V(H)}$ are also given.

	Protonated basin	Atomic contribution			$100\times\frac{C(M)}{V(H)}$
	V(H)	C(M)	C(B)	C(H)	
$Cp_2Ti{-}H_2BH_2$	1.90	0.07	0.21	1.61	3.69
	1.90	0.07	0.21	1.61	3.69
$Cp_2Ti{-}H_2BC_4H_8$	1.93	0.08	0.23	1.61	4.00
	1.93	0.08	0.23	1.61	4.00
$Cp_2Ti{-}H_2BC_5H_{10}$	1.92	0.07	0.23	1.61	3.86
	1.91	0.08	0.22	1.60	3.98
$Cp_2Ti{-}H_2BC_8H_{14}$	1.92	0.08	0.23	1.61	3.96
	1.92	0.08	0.23	1.61	3.96
$Cp_2Ti{-}H_2BMe_2$	1.91	0.07	0.23	1.61	3.88
	1.91	0.07	0.23	1.61	3.88
$Cp_2Ti{-}H_2B(CH_2)_2C_6H_4$	1.94	0.08	0.24	1.62	3.92
	1.91	0.07	0.22	1.61	3.87
$Cp_2Ti{-}H_2B(C_6F_5)_2$	1.93	0.06	0.26	1.60	2.91
	1.93	0.06	0.27	1.60	2.91
$Cp_2Ti{-}H_2B(C_6H_5)_2$	1.92	0.07	0.24	1.61	3.60
	1.92	0.07	0.24	1.61	3.60
$Cp_2Ti{-}H_2B(OH)_2$	1.95	0.08	0.26	1.59	4.20
	1.95	0.08	0.26	1.59	4.20
$Cp_2Ti{-}H_2BO_2C_2H_4$	1.96	0.09	0.28	1.58	4.33
	1.96	0.09	0.28	1.58	4.33
$Cp_2Ti{-}H_2BO_2C_6H_4$	1.98	0.08	0.28	1.60	3.97
	1.98	0.08	0.28	1.60	3.97

The use of the following topological and geometric quantities is introduced to classify the 3C/2e interactions involved in {metallocene + hydroborate} systems:

$$\frac{d(B-H)}{d(M-H)} \tag{6.7}$$

$$100\times\frac{C(M)}{V(H)} \tag{6.8}$$

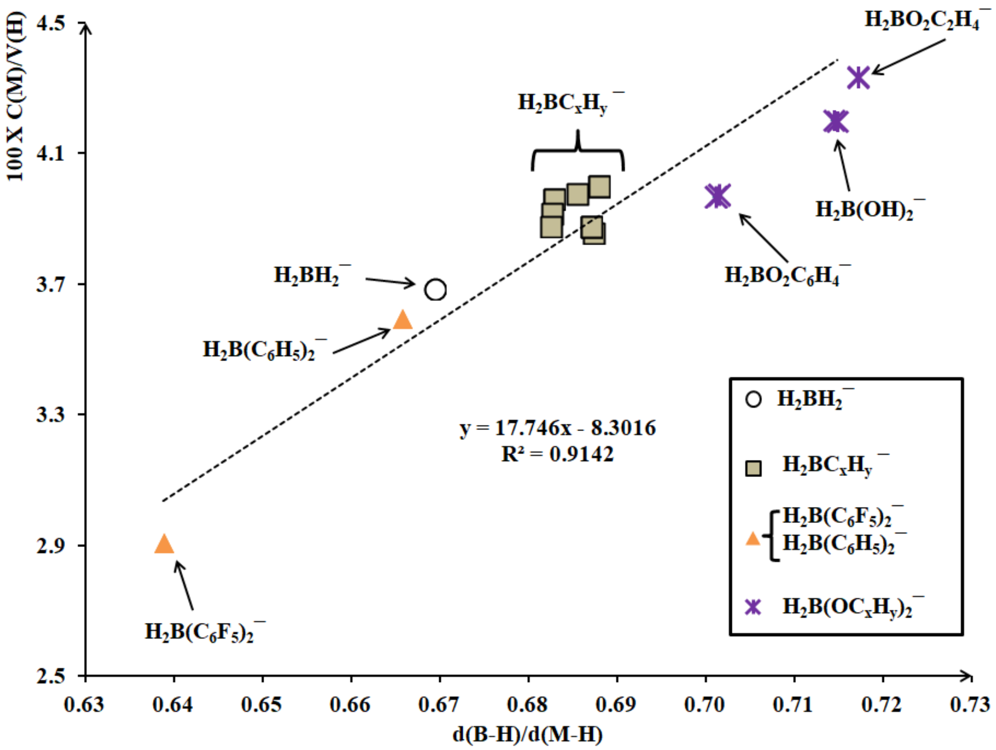

Figure 6.19: Graphical representation of contribution of metal center (M=Ti) to the basin $(100\times\frac{C(M)}{V(H)})$ as function of geometric properties $(\frac{d(B-H)}{d(M-H)})$.

In the present study, the graphical representation of contribution of metal center to the protonated basin $(100\times\frac{C(M)}{V(H)})$ as function of geometric properties $(\frac{d(B-H)}{d(M-H)})$ (Figure 6.19) allows classifying the borates in their order of increasing interaction with the titanocene:

- As already mentioned, the use of these descriptors shows that the $H_2B(C_6F_5)_2^-$ ligand is the one for which the interaction with the titanocene is the weakest;
- Thereafter $H_2B(C_6H_5)_2^-$ and BH_4^- hydroborates are characterized by a similar normalized contribution of the metallic center within the protonated basins;
- All alkyl borates comparably interact with the titanocene;
- The oxygenated borates systematically lead to the strongest interactions with the titanocene.

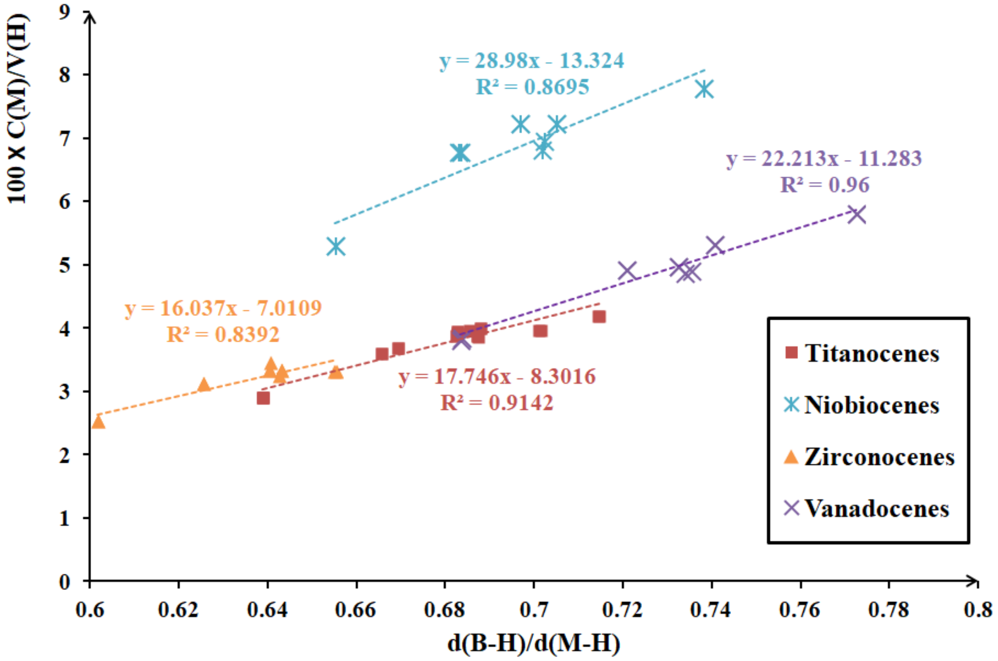

Figure 6.20: Graphical representation of contribution of metal center (M=Ti, Zr, V and Nb) to the protonated basin ($100\times\frac{C(M)}{V(H)}$) as a function of geometric properties ($\frac{d(B-H)}{d(M-H)}$).

Figure 6.20 shows that similar results are obtained with zirconocene, vanadocene and niobiocene. These descriptors suggest that vanadocene complexes should lead to stronger B-H activation compared to the titanocene and zirconocene analogues.

6.4.3 Energetic considerations

In addition to the geometric and topological descriptors mentioned above, the binding energy of two isolated molecules also provides a fundamental measure of the interaction strength between these two species.

$$\mathrm{Cp_2M^+ + H_2BR_2{}^- \longrightarrow Cp_2M{-}H_2BR_2} \tag{6.9}$$

The energy of the intermolecular interactions can be estimated as follows:

$$\Delta E = E_{Cp_2M-H_2BR_2} - (E_{Cp_2M^+} + E_{H_2BR_2^-}) \tag{6.10}$$

In the case of $\mathrm{Cp_2Ti{-}H_2BH_2}$ system for instance, the binding energy was calculated to be 633.6 kJ/mol (151.6 kcal/mol) according to the level of theory used. It is much larger than the usual value for an intermolecular 3C/2e interaction:

- experimental determination of an approximate binding energy of 10-15 kcal/mol for an intermolecular 3C/2e interaction was proposed based on the bond dissociation enthalpy determined by photoacoustic calorimetry for heptane binding to $\mathrm{W(CO)_5}$; [157]

- results obtained from computational approaches indicate that the binding energy of a 3C/2e interaction ranges from very small to more than 10 kcal/mol.

In the present study, the ionic interaction involving the attraction between cationic metallocene (Cp_2M^+) and anionic hydroborate ($H_2BR_2{}^-$) may play the dominant role but not the 3C/2e interactions in the stabilization of $Cp_2M{-}H_2BR_2$ systems.

For a sake of estimating the stabilization energy that is brought by the intermolecular 3C/2e interactions in this σ complex, a modified conformation of $Cp_2Ti{-}H_2BH_2$ (Complex (b) in Figure 6.21) is introduced. In an approximative manner, the rotation of BH_4 fragment leads to the modified conformation (b), in which the 3C/2e interactions are largely reduced. The Ti-H distances extend from 1.897 Å where the 3C/2e interaction is significant to 2.216/2.210 Å where this interaction becomes negligible. The Ti-B distance is maintained unchanged in order to exclude the influence of other interactions including the ionic interaction.

A single-point calculation of structure (b) was carried out within the same level of theory. Energetic difference is found to be 87.6 kJ/mol. The stabilization energy arisen by the intermolecular Ti-H-B interaction is thus estimated to be 43.8 kJ/mol (10.5 kcal/mol) for each of the interaction. This is in good agreement with the reported energy value of a 3C/2e interaction in former experimental determinations and theory calculations.

(a)$Cp_2Ti{-}H_2BH_2$	(b) Modified $Cp_2Ti{-}H_2BH_2$
ΔE = 0.0 kJ/mol	ΔE = +87.6 kJ/mol

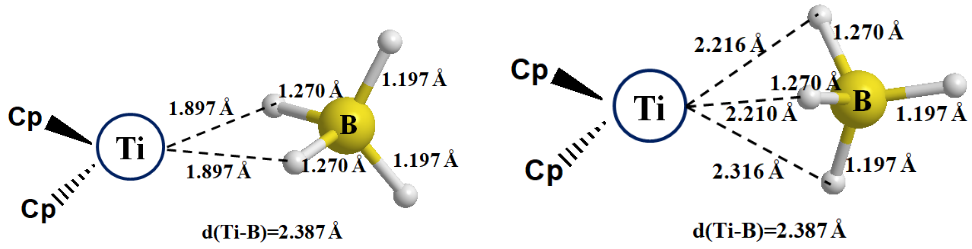

Figure 6.21: Some important geometrical parameters of optimized $Cp_2Ti{-}H_2BH_2$ complex (a) and its modified structure (b). The relative energy of (b) compared to (a) is also given.

However, this estimation method can not be employed for other systems in which a lot of intermolecular interactions exist when the tetrahydroborate fragment is substituted. For that reason, no general rule is considered from the stabilization energy point of view for the comparison of strength of 3C/2e interaction involved in systems herein studied.

6.4.4 Orbital approaches

With the nature of 3C/2e, the intermolecular interactions between the metallocenes and hydroborates involved in the σ complexes in the present study can also be recognized as donor-acceptor interactions. It is thought that the B-H σ bond from the hydroborate ligands acts as an orbital donor whereas the acceptor orbital could be an empty molecular orbital from metal center.

In a first approach, it could be considered that the highest occupied molecular orbital (HOMO) of hydroborate ligands establishes a donor-acceptor interaction with the metal center lowest unoccupied molecular orbital (LUMO). Although the activation of B-H bonds does not depend in any regular way on the ligand HOMO energy, it was always understood that ligands with very low lying occupied orbitals would be unlikely to interact with a metal center. A poor Lewis base would thus be difficult to access a Lewis acidic metal center. For that reason, the HOMO energy of each isolated hydroborate are thus considered. The higher the value of the HOMO is, the stronger the M-H-B interaction will be.

Table 6.13: Energies of highest occupied molecular orbital (HOMO) of each isolated hydroborate ligand.

Ligands	Energy of HOMO (a.u.)	Ligands	Energy of HOMO (a.u.)
$[H_2BH_2]^-$	-0.066	$[H_2B(C_6F_5)_2]^-$	-0.138
$[H_2BC_4H_8]^-$	-0.063	$[H_2B(C_6H_5)_2]^-$	-0.091
$[H_2BC_5H_{10}]^-$	-0.066	$[H_2BO_2C_6H_4]^-$	-0.029
$[H_2BC_8H_{14}]^-$	-0.063	$[H_2BO_2C_2H_4]^-$	-0.028
$[H_2BMe_2]^-$	-0.059	$[H_2B(OH)_2]^-$	-0.039
$[H_2B(CH_2)_2C_6H_4]^-$	-0.071		

The energies of the HOMOs of all the isolated hydroborate anions considered in the present study are reported in Table 6.13. The $H_2B(C_6F_5)_2{}^-$ ligand is found to have a lowest HOMO value at -0.138 a.u. while the HOMO value of the oxygenated hydroborates ($[H_2BO_2C_2H_4]^-$ and $[H_2BO_2C_6H_4]^-$) lies higher, at -0.028 a.u. The aliphatic hydroborates have a HOMO value in the [-0.071 a.u., -0.059 a.u.] range (Table 6.13).

Thus, using such an approach, the oxygenated hydroborates are predicted to form stronger interactions with a given metallocene. Conversely, the aromatic ligands are predicted to form weaker interaction. This classification is consistent with the one obtained using both the geometric and topological descriptors for a M-H-B interaction involved in a σ complex.

Summary

In this chapter, the combined geometric and topological approaches were carried out to qualitatively and quantitatively describe the intramolecular (in agostic complexes) and the intermolecular (in σ complexes) M-H-B 3C/2e interactions which are considered as key intermediates in the transition-metal catalyzed dehydrogenation reactions of amine-boranes and phosphine-boranes. The preliminary benchmark investigations have proposed a two-step level of theory for the computational investigations of the systems herein considered:

- The geometric optimization undergoes with the B3LYP functional, in combination with the LanL2DZ basis set for the metallic atom and the 6-311++G(2d,2p) basis set for all the other atoms.

- A single-point calculation of the optimized structure should be carried out using the DKH2 Hamiltonian in combination with the B3LYP/DZP-DKH level of theory for further topological analyses.

Different geometric and topological descriptors were studied to estimate the strength of the 3C/2e interaction. Taking the case of the $Cp_2M{-}H_2BR_2$ systems, the descriptors and their corresponding classifications are summarized in Table 6.14.

Table 6.14: Geometric and topological descriptors to estimate the strength of the 3C/2e interactions.

Strength of 3C/2e interaction according to different descriptors		
Descriptor	$Cp_2Ti{-}H_2BR_2$ system	$Cp_2M{-}H_2BR_2$ system
$\Delta(B - H)$	oxygenated > alkylated, aromatic > tetrahydroborate	titanocenes, vanadocenes > niobiocenes, zirconocenes
$\rho[BCP(B - H)] = f[d(B - H)]$	oxygenated > alkylated, aromatic	/
$\rho[BCP(M - H)] = f[d(M - H)]$	oxygenated > alkylated > aromatic	titanocenes > zirconocenes & vanadocenes > titanocenes
$\frac{C(M)}{V(H)} = f[\frac{d(B-H)}{d(M-H)}]$	oxygenated > alkylated > aromatic	vanadocenes > titanocenes > zirconocenes

It was shown that the following parameters have significant contribution to the strength of 3C/2e interactions:

- The nature of metal center which the B-H σ bond is connected to;
- The nature of ligand, the amido- (NR_2BH_3) and phosphido-boranes (PR_2BH_3) in this study:
- The nature of the substituent groups carried by N atom.

Chapter 7

Mechanistic investigation of the titanocene-catalyzed dehydrogenation of amine-boranes

Density Functional Theory (DFT) has been successfully applied in the modeling of reactivity and in generating insight into the chemistry of a variety of transition-metal complexes. It thus underlines the immense role played by computational approach in better understanding of chemistry properties as well as reaction mechanisms. [158–160] However, in the present study for the titanocene-catalyzed dehydrogenation of dimethylamine borane (DMAB), inconsistency between experimental and theoretical results which was detailed in Chapter 5 and summarized in Figure 7.1 still remains to be problematic.

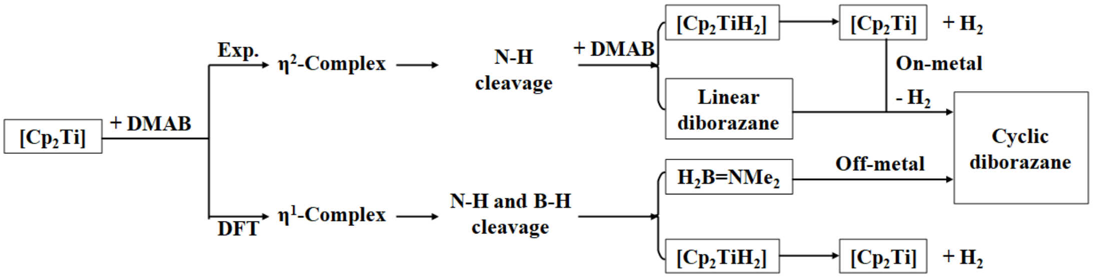
[Cp₂Ti]
+ DMAB
Exp.
η²-Complex
N-H cleavage
+ DMAB
[Cp₂TiH₂]
[Cp₂Ti]
+ H₂
On-metal
- H₂
Linear diborazane
Cyclic diborazane
DFT
η¹-Complex
N-H and B-H cleavage
H₂B=NMe₂
Off-metal
[Cp₂TiH₂]
[Cp₂Ti]
+ H₂

Figure 7.1: DMAB dehydrocoupling mechanism from both experimental (Exp.) and theoretical (DFT) points of view.

This chapter aims to look for a good agreement between the experimental observations and DFT calculations for the dehydrogenation mechanism of DMAB and other amine-borane adducts. To this end, we reconsider the previously proposed mechanisms using the dispersion-corrected density functional theory (DFT-D) that enables a suitable description of non-covalent interactions. A detailed electronic and bonding description of each compound involved in the reaction path will be performed within the topological frameworks.

7.1 Look for a suitable level of theory

7.1.1 Influence of the Grimme-D3(BJ) dispersion correction

It was recently shown that the London dispersion corrections are indispensable for consistent geometrical and energetic prediction. [161,162] This dispersion force is found very important not only for systems with non-covalent interactions, such as van der Waals complexes, but also for metal-ligand binding energies calculations. In addition, Liptrot and Power [163] have highlighted recently in their review that London dispersion forces can be of considerable importance in stability, structure and reactivity of inorganic and organometallic systems with sterically large substituents.

The DFT-D method in which a damped, atom pairwise potential is added to a standard Kohn-Sham DFT result is one of the most widely used approach to take into consideration of dispersion interactions. A previous study on the performance of DFT methods for the activation energies of a similar system (the C-H activation reactions mediated by zirconocene [Cp_2Zr] fragment) [161] has put forward an improvement with DFT empirical dispersion correction DFT-D3 of Grimme et *al*, [95,164] especially for the OLYP and B3LYP, [165,166] as well as the Minnesota M06-2X functional for the energy barrier calculations.

How is the performance of the dispersion-corrected DFT theory on the energetic description concerning the titanocene-catalyzed dehydrogenation mechanism? Can the dispersion correction play a pivotal role on the inconsistency of experimental and theoretical results?

In this study, the performance of the DFT-D method on the mechanistic investigation of the dehydrogenation reaction of DMAB will be evaluated from both a geometry and an energy point of view.

To be able to compare our results with those obtained by Luo and Ohno [58], we chose the same functional and the same pseudopotential, as well as the same basis sets. (See in section 5.4. In following sections, this level of theory is noted as B3LYP/6-31G*+6-31++G**+LanL2DZ for clarity.) The GD3BJ correction (D3 version of empirical dispersion correction of Grimme with Becke-Johnson damping) will be taken into consideration for all of the optimizations of intermediates and transition states in this work. The solvation effect of toluene will also be taken into account by the implicit solvent model PCM (Polarizable Continuum Model) in this study.

Geometric description

The influence of the dispersion correction on structures was first investigated by considering the selected inter-atomic distances involved in S_1 intermediate. Due to the lack of experimental data, the relative deviation (Dev) is also introduced, as shown in the following expressions:

$$\Delta d_{X-Y} = d_{X-Y}^{without\ GD3BJ} - d_{X-Y}^{within\ GD3BJ} \tag{7.1}$$

$$Dev[\%] = \frac{\Delta d_{X-Y}}{d_{X-Y}^{within\ GD3BJ}} \tag{7.2}$$

Table 7.1: Selected inter-atomic distances and their relative deviations involved in S_1 intermediate.

	B3LYP/6-31G*+6-31++G**+LanL2DZ					S_1
	Ti$\cdots$H(B)	B$-$H$\cdots$(Ti)	B$-$H$_{\text{free}}$	N-H	N-B	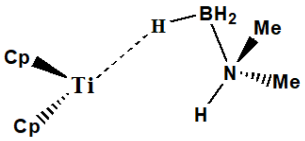
Distance (in Å) with GD3BJ	1.986	1.231	1.205/1.208	1.023	1.623	
Distance (in Å) without GD3BJ	1.946	1.232	1.207/1.204	1.027	1.627	
Relative deviation	-2.01%	0.08%	-0.08%	0.39%	0.25%	

By comparing the relative deviations (Table 7.1), it is obvious that the dispersion correction has negligible impact on the geometric description for the current studied system. The relative deviations are found in the [-2.01%, 0.39%] range. Our previous investigations (Chapter 6) have shown the same conclusion that the dispersion correction plays insignificant role on the molecular structures involved in the amine-boranes dehydrogenation with Group IV metallocenes.

Energetic description

A second major prerequisite for an accurate description of a reaction pathway relies on an energetic description which is comparable to the experimental evidences.

Figure 7.2 illustrates both the intramolecular and intermolecular dehydrogenation pathways proposed by Luo and Ohno within the DFT framework (blue line) and relative energies including GD3BJ correction (green line). This Figure clearly demonstrates that the dispersion correction contributes significantly to the stabilization of systems involved in both the two-body intermolecular pathway (Path I) and the three-body intramolecular pathway (Path II). Both mechanisms are calculated to be much more favorable when the dispersion correction is taken into account.

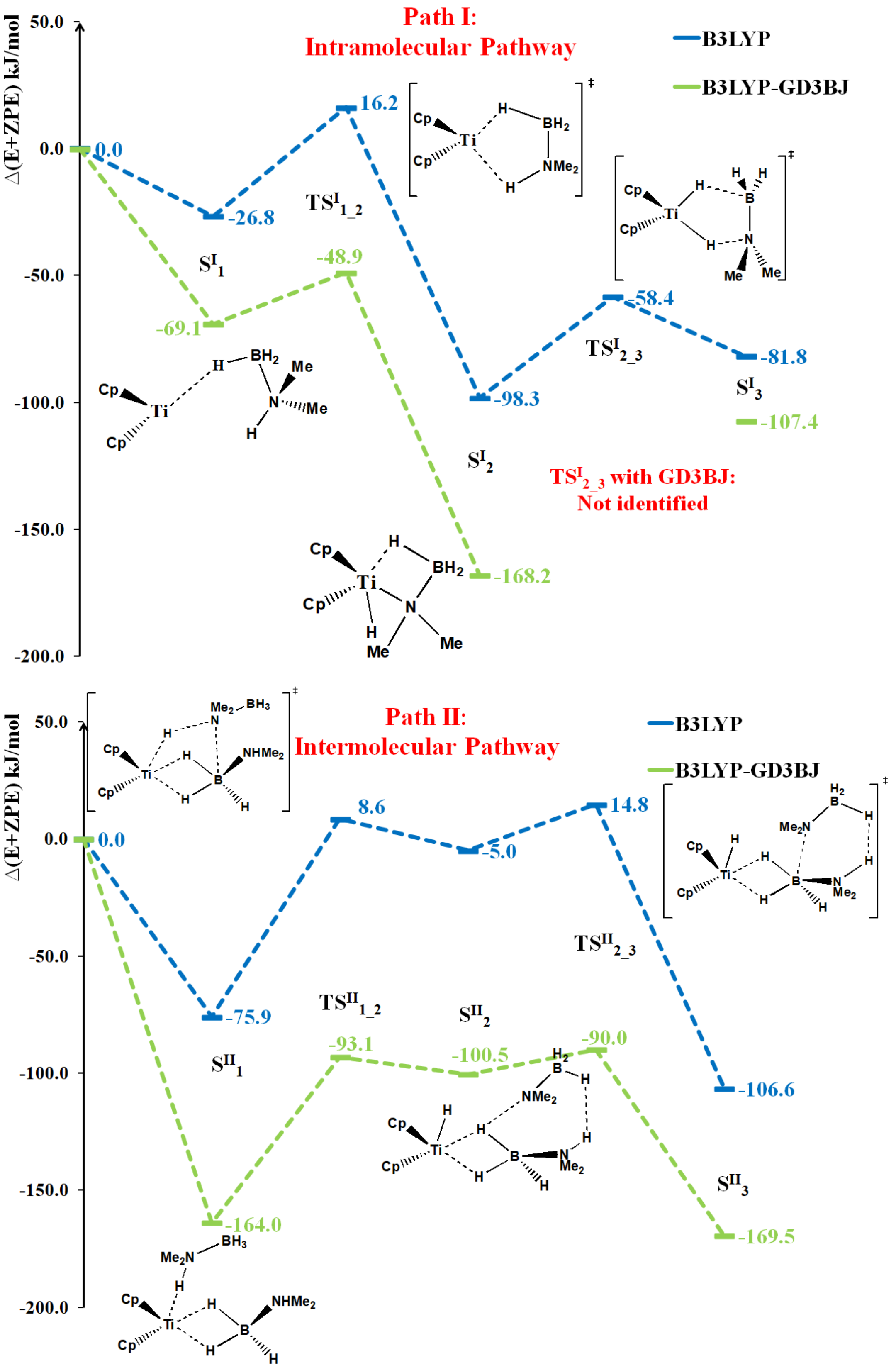

Figure 7.2: Effect of the dispersion correction on the energy profile associated with the intramolecular and intermolecular pathways: comparison of relative electronic energies (in kJ/mol) without or with GD3BJ corrections

To further compare the stabilization by the inclusion of the dispersion correction, the difference of relative energies within GD3BJ correction and those within non-dispersion corrected DFT method, noted as E^{corr}_{GD3BJ}, is also considered among different systems involved in these two reaction pathways proposed by Luo and Ohno:

$$E^{corr}_{GD3BJ} = E_{DFT-GD3BJ} - E_{DFT} \tag{7.3}$$

Table 7.2: E^{corr}_{GD3BJ} values (in kJ/mol) for each intermediate and transition state involved in Path I and Path II .

	E^{corr}_{GD3BJ}	
	Path I	**Path II**
Cp_2Ti	-117.2	
DMAB	-42.2	
S_1	-206.3	-298.8
TS_{1_2}	-227.8	-308.5
S_2	-232.1	-305.9
TS_{2_3}	/	-313.9
S_3	-191.5	-270.2

With the E^{corr}_{GD3BJ} energies obtained for the reaction intermediates as well as the isolated substrates (Table 7.2), contributions of the attractive energies to the stabilization of systems is shown in Figure 7.3. This stabilizing effects of attractive dispersion forces is due to different interactions, such as the predominance of electrostatic, hydrogen bindings and other van der Waals interactions in the reaction pathways herein considered. The non-covalent intermolecular or intramolecular interactions, the inter-ligand contacts may contribute to extra London dispersion interactions. As expected, the three-body intermolecular pathway is more affected by the GD3BJ correction. The GD3BJ correction of the two-body pathway (Path I) are found in the [-72.7, -32.1] kJ/mol range, smaller than the ones of three-body pathway (Path II) which are in the [-112.3, -68.6] kJ/mol range. This may be due to the presence of more complicated interactions that occur in the system during the reaction.

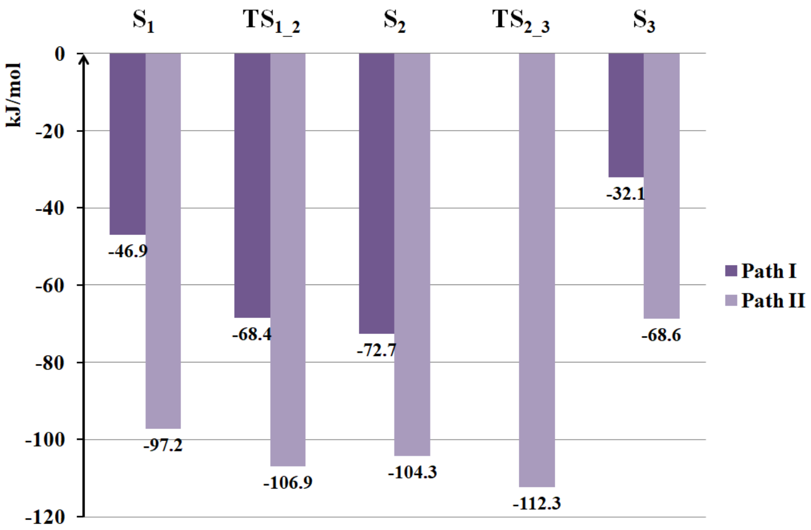

Figure 7.3: Contributions of the GD3BJ dispersion correction energy to relative electronic energy (in kJ/mol) of each intermediate involved in both the Path I and Path II proposed by Luo and Ohno.

In conclusion, the dispersion forces, although appear as a weak component among diverse intermolecular or intramolecular interactions, can arise to strongly influence the energetic description of systems. Different from the results obtained by the pioneering theoretical studies conducted by Luo & Ohno [58] and Tao & Qi [59] within DFT framework, both the intramolecular and intermolecular pathways are calculated to be more favorable when the GD3BJ correction is taken into account. The calculations implementing the dispersion correction to the previous DFT framework may be an alternative explanation to solve the inconsistency between experiments and theories.

7.1.2 Influence of DFT functionals

It is previously shown in section 7.1.1 that the GD3BJ dispersion has a significant impact on the energetic description of the reaction pathways herein studied. In this case, the hybrid B3LYP functional was taken into consideration. However, is there any dependency of different exchange-correlation functionals on the energetic description for this mechanistic study that strongly influence the conclusion?

To evaluate the performance of different DFT functionals for the energetic description of the titanocene-catalyzed dehydrogenation reaction, the binding energy of the $[\mathrm{Cp_2Ti}-\eta^1\text{-}\mathrm{H_3B{\cdot}NMe_2H}]$ complex as well as the $[\mathrm{Cp_2Ti}-\eta^2\text{-}\mathrm{H_3B{\cdot}NMe_2H}]$ complex (a hypothetical intermediate involved on the two-cycle model proposed by Manners *et al.* [50]) were calculated using three functionals, including or not empirical dispersion corrections:

- the B3LYP functional, which was already chosen by Luo & Ohno and Tao & Qi, alone and with the GD3BJ correction;
- the RSH (Range-Separated Hybrid) functional LC-ωPBE [167, 168] were considered both

alone and with the GD3BJ correction;

- the ωB97XD [169, 170] that is known as a range-separated functional which has already been constructed to account for dispersion.

For sake of comparison, single point calculations were also carried out:

- energetic calculation at the B3LYP-GD3BJ level on structures optimized at the B3LYP level,
- energetic calculation at the high level *ab initio* CCSD(T) [171,172] on structures optimized at the B3LYP level (without GD3BJ correction).

Table 7.3: Gas-phase relative electronic energies and free energies (in kJ/mol) are given. (a) Basis set: 6-31G*/6-31++G**/LanL2DZ. (b) ΔG for all the single-point calculations are obtained by the addition of the reference value (that is the value with B3LYP-GD3BJ method) to their corresponding relative electronic energies.

Method (a)	$[Cp_2Ti-\eta^1-H_3B\cdot NMe_2H]$			$[Cp_2Ti-\eta^2-H_3B\cdot NMe_2H]$		
	ΔE	ΔG	ΔG-ΔE	ΔE	ΔG	ΔG-ΔE
B3LYP	-33.2	+27.2	60.4	-53.4	+16.8	70.2
LC-ωPBE	-44.1	+20.4	64.5	-72.0	+1.4	73.4
B3LYP-GD3BJ	-77.6	-10.9	66.7	-103.5	-31.2	72.3
LC-ωPBE-GD3BJ	-74.8	-13.6	61.2	-105.5	-36.1	69.4
ωB97XD	-72.8	-8.4	64.4	-97.4	-29.3	68.1
B3LYP-GD3BJ//B3LYP	-74.5	-7.8(b)	66.7(b)	-102.4	-30.1(b)	72.3(b)
CCSD(T)//B3LYP	-75.5	-8.8(b)	66.7(b)	-104.5	-32.2(b)	72.3(b)

Table 7.3 presents the gas-phase electronic energies and free energies obtained at all these levels of theory. The choice of functionals appears to slightly affect the binding energy of these complexes. The systems are slightly stabilized by using the long-range-corrected functional LC-ωPBE which is considered to solve the poor reproducibilities of van der Waals interactions instead of hybrid B3LYP functional. In the case of $[Cp_2Ti-\eta^2-H_3B\cdot NMe_2H]$ complex, the stabilization brought by taking advantage of LC-ωPBE functional is found to be larger compared to the the η^1- complex. However, the use of LC scheme does dramatically affect the energetic description of these systems.

The functional dependency becomes even minor when the dispersion correction is included, not only within the DFT-GD3BJ framework but also within the functional which has already been constructed to account for dispersion (ωB97XD). In addition, as previously studied, the dispersion correction increases the binding energy by approximately 30-40 kJ/mol, compared to the results obtained without dispersion correction, in the case of the $[Cp_2Ti-\eta^1-H_3B\cdot NMe_2H]$ complex. For the $[Cp_2Ti-\eta^2-H_3B\cdot NMe_2H]$ complex, the difference becomes larger, especially for the case within B3LYP functional. It is interesting to notice that the energetic calculations with the GD3BJ corrected B3LYP and LC-ωPBE functionals gives the same results, different from the un-corrected case.

Furthermore, energy calculations carried out within the DFT-D framework are consistent with single points calculations at the CCSD(T) level. Thus, the importance of the dispersion correction applied to the mechanistic investigations is proven again, and the B3LYP-GD3BJ approach appears as being a satisfactory level for the present systems.

Summary

In summary, the titanocene-catalyzed dehydrogenation reaction mechanisms of DMAB proposed by Luo and Ohno in 2007 were re-investigated. The dispersion correction was found to be indispensable for the mechanistic exploration of this system. The energetic description of systems in the present work within B3LYP-GD3BJ framework was further proven to be feasible in proceeding a single-point energetic calculation within *ab initio* CCSD(T) method. The empirical dispersion correction GD3BJ is thus considered for the investigations developed hereinafter.

7.2 Mechanistic investigations

With the detailed reaction mechanism remaining uncertained since more than ten year, the present study aims at re-investigating the reaction pathways using combined density functional theory (DFT) and interpretative methods.

As already employed in our previous work, two quantum topological approaches were used to further characterize electron density flux along the dehydrogenation reactions of DMAB. To begin with, QTAIM (Quantum Theory of Atoms in Molecules) [98, 173, 174] framework leads to the identification of bond paths (BPs) and bond critical points (BCPs) between DMAB and the metallocene, allowing to qualitatively and quantitatively characterize the intermolecular and intramolecular interactions. To further identify 3C/2e interactions, the topology of ELF (Electron Localization Function) [103, 106, 113] was used. The ELF signature of a 3C/2e interaction consists in a trisynaptic protonated basin. [114, 175] Furthermore, NBO (Natural Bond Orbital) analysis [176] of intermolecular interactions were also employed in this investigation.

All of the structure optimizations presented in the following sections were performed using B3LYP/6-31G*+6-31++G**+LanL2DZ level of theory with GD3BJ correction, with the Gaussian 09 Rev D.01 software (see section 7.1). [177] We have also accounted for the effect of solvent in energy along the reaction pathways by performing the calculation with PCM (Polarizable continuum model) [178] as solvent model and toluene as solvent. The transition state is located for a local maximum on a potential energy surface (PES) and it is characterized by one imaginary frequency of the vibrational spectrum. All the necessary wfn files for the topological investigations have been generated from single point calculations with B3LYP functional using the second-order Douglas-Kroll-Hess Hamiltonian (DKH2) [179] in conjunction with the DZP-DKH [179–181] all electron basis sets. The ELF and QTAIM topological data have been calculated using the TopMod and the AIMAll softwares, respectively. The NBO analyses were carried out using NBO 6.0 program. [182]

In the following sections, the detailed mechanistic studies of catalyzed dehydrogenation of DMAB will be discussed. Besides, in an attempt to be able to explain the difference of reactivity of different amine-borane adducts (ammonia borane, primary amine-borane and secondary amine-borane with diverse steric hindrance), we also explored the [Cp_2Ti] catalyzed dehydrogenation of these related species.

7.2.1 Dehydrogenation/dehydrocoupling reactions of $HMe_2N{\cdot}BH_3$(DMAB)

First catalytic cycle: Formation of the linear diborazane intermediate

In the entrance channel, the two-body interaction between one Cp2Ti and one DMAB molecule may lead to the formation of two σ complexes in which one or two hydrogen atoms of the BH_3 moiety interact *via* a 3-center 2-electron (3C/2e) bonding motif with Ti center: the [$Cp_2Ti{-}\eta^1$-$H_3B{\cdot}NMe_2H$] and the [$Cp_2Ti{-}\eta^2$-$H_3B{\cdot}NMe_2H$] complexes.

Path I: A two-body pathway

The [$Cp_2Ti{-}\eta^1$-$H_3B{\cdot}NMe_2H$] complex is considered at first as an initial step. It features a stepwise N-H then B-H transfers from DMAB molecule to metallic center and generates an aminoborane $Me_2N{=}BH_2$ and a dihydride intermediate Cp_2TiH_2. The aminoborane intermediate can then subsequently undergoes an off-metal dimerization to produce the cyclic dimer $[Me_2N{\cdot}BH_2]_2$. The corresponding energy profiles of the relative gas-phase zero-point corrected energies (E+ZPE) and the calculated inter-atomic distances are presented in Figure 7.4 and Table 7.4 respectively.

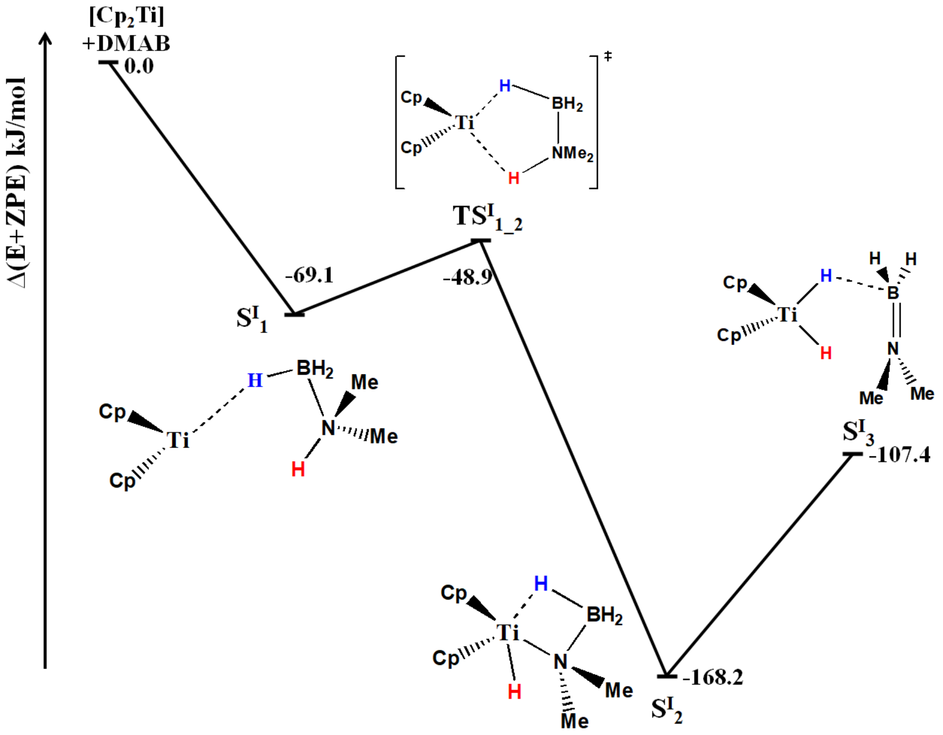

Figure 7.4: Energy profile for the intramolecular dehydrogenation mechanism of DMAB: Path I. Relative gas-phase zero-point corrected energies (E+ZPE) are given in kJ/mol.

According to our dispersion-corrected calculations, the dehydrogenation reaction starts with a formation of a two-bodies complex with a stabilization energy of 69.1 kJ/mol. A slight lengthening of B-H bond from 1.204 Å in an isolated DMAB molecule to 1.232 Å as well as a relative short Ti-H distance implies a weak η^1 Ti$\cdots$H$-$B interaction in $\mathrm{S^I}_1$ intermediate. This intermediate then proceeds a further elongation of both B-H bond and N-H bond, which results in the shortening of both Ti$\cdots$H(B) and Ti$\cdots$H(N) distances through a formation of a five-membered Ti-H-B-N-H ring involved in $\mathrm{TS^I}_{1\_2}$. The formation of $\mathrm{S^I}_2$ intermediate proceeds *via* a N-H oxidation addition at the formally Ti(II) center. This process needs to overcome an activation energy of 20.2 kJ/mol. At the meantime, the B-H bond undergoes a further lengthening from 1.232 Å in $\mathrm{S^I}_1$ to 1.296 Å in $\mathrm{S^I}_2$ accompanying with a shortening of B-N bond from 1.627 Å to 1.537 Å. This $\mathrm{S^I}_2$ intermediate proceeds directly a dehydrogenation from BH_3 moiety *via* $\mathrm{S^I}_3$ to form a titanium dihydride and aminoborane $Me_2N{=}BH_2$. This process is found to be endothermic with an energy barrier of 60.8 kJ/mol between $\mathrm{S^I}_2$ and $\mathrm{S^I}_3$. A B-N double bond is formed which features by the shortening of B-N distance from 1.627 Å in initial complex $\mathrm{S^I}_1$ to 1.399 Å in $\mathrm{S^I}_3$. It is important to remark that the transition state between $Cp_2Ti(H)NMe_2BH_3$ intermediate ($\mathrm{S^I}_2$ in this work) and the complex $Cp_2TiH_2\cdots Me_2N{=}BH_2$ proposed by Luo and Ohno in 2007 (and also by Tao and Qi in 2013) can not be obtained in this study with the DFT-D framework. The searching of such a transition state with the empirical corrected dispersion leads directly to a stationary point, that is $\mathrm{S^I}_3$ shown in Figure 7.4.

Table 7.4: Main inter-atomic distances (in Å) of calculated intermediates and transition state of Path I

Path I	Ti-H(B)	B-H(···Ti)	B−H$_{\text{free}}$	Ti-H(N)	N-H(···Ti)	N-B	Ti-B	Ti-N
S^{I}_{1}	1.946	1.232	1.207/1.204	2.915	1.027	1.627	3.079	3.503
$TS^{I}_{1\_2}$	1.878	1.274	1.204/1.204	1.826	1.208	1.623	2.558	2.467
S^{I}_{2}	1.858	1.296	1.206/1.208	1.858	2.342	1.537	2.557	2.266
S^{I}_{3}	1.673	2.153	1.197/1.197	1.687	3.172	1.399	3.760	3.967

The solvent was also taken into account to study its effect on structures and energetic properties. The relative Gibbs free energies in gas phase and in toluene were calculated under standard state (298.15 K, 1 atm). Free energy which contains solvation effect ΔG_{sol} represents a very important property for the thermodynamic description of a chemical process. The relative electronic energies with zero point energy (ZPE) correction, as well as the Gibbs free energies both in gas phase and in toluene solution, provide a qualitative insight to determine whether a process will occur spontaneously under the given conditions and environment surroundings in the system. (Table 7.5) The solvation effect offers a minor changes on potential energy surface for this system as the energy barriers keep nearly unchanged. This reaction is found to be exothermic under standard state in solution, which is close to the experimental conditions.

Table 7.5: Relative electronic energies with zero point energy (ZPE) correction and Gibbs free energies (in kJ/mol) both in gas phase and in toluene solution with PCM model for Path I.

	Gas phase		PCM with toluene	
	Δ(E+ZPE)	ΔG	Δ(E+ZPE)sol	ΔGsol
Cp_2Ti+ DMAB	0.0	0.0	0.0	0.0
S^{I}_{1}	-69.1	-10.9	-58.9	-3.9
Energy barrier ($TS^{I}_{1\_2}$-S^{I}_{1})	**20.3**	**28.3**	**23.2**	**32.2**
$TS^{I}_{1\_2}$	-48.9	17.4	-35.7	28.3
S^{I}_{2}	-168.2	-101.1	-152.7	-87.6
S^{I}_{3}	-107.4	-55.9	-91.3	-47.5

Competitively, the S^{I}_{2} intermediate can also lead to the formation of a van der Waals complex S^{I}_{3B} through a further addition of a second DMAB molecule. This alternative 2+1 reaction pathway is exothermic (Route B in Figure 7.5) and leads to a stabilization of almost 15 kJ/mol fromS^{I}_{2}. From S^{I}_{3B} , the formation of the precursor of the linear dimer and titanium hydride (S^{I}_{4B}) is an exothermic process which releases approximate 25 kJ/mol energy related to the S^{I}_{3B} intermediate .

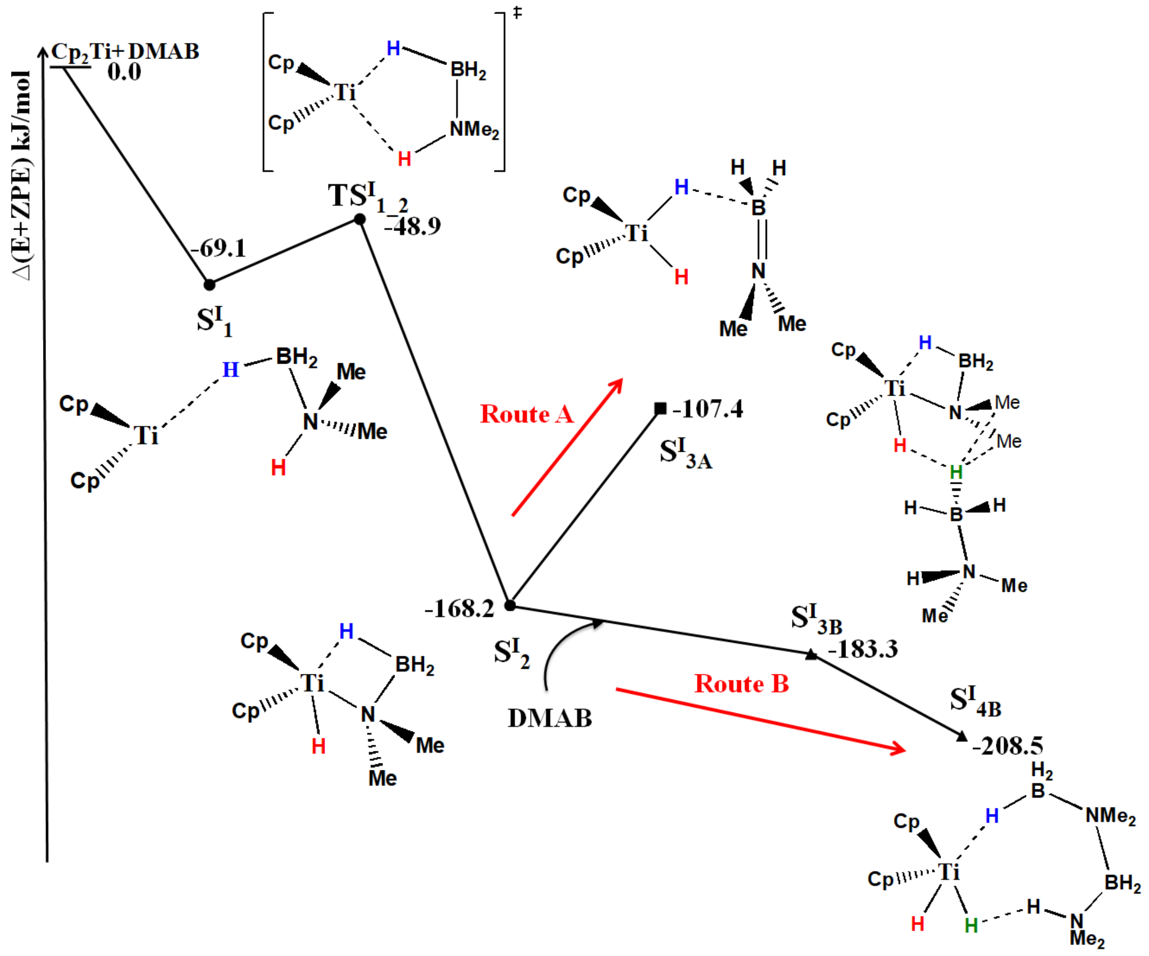
Δ(E+ZPE) kJ/mol
Cp2Ti+DMAB
0.0
‡
Cp
Cp
Ti
H
BH2
NMe2
H
TS^I_1_2
-48.9
-69.1
S^I_1
Route A
-107.4
S^I_3A
-168.2
S^I_2
DMAB
Route B
S^I_3B
-183.3
S^I_4B
-208.5
Me
Me
NMe2
BH2
Me2

Figure 7.5: Energy profiles for the titanocene-catalyzed dehydrogenation/dehydrocoupling of DMAB. Relative gas-phase zero-point corrected energies (in kJ/mol) are shown.

Rory Waterman proposed a similar possibility that complements Manners' mechanistic model (in Figure 5.1) in the formation of the linear diborazane. [183] The coupling of a titanium-amidoborane $Cp_2Ti(H)NMe_2BH_3$ with a BH_3 moiety of the second DMAB molecule was proposed with the hypothetical transition state shown in Figure 7.6, which may be considered as one of the possible path from S^{I}_{3B} intermediate to S^{I}_{4B}.

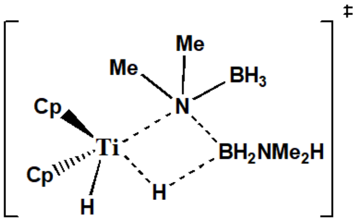
‡
Me
Me
BH3
N
Cp
Ti
Cp
BH2NMe2H
H
H

Figure 7.6: Transition state for a 2+1 dehydrocoupling process proposed by Waterman to complement the Manners' mechanistic model.

Despite several attempts, the transition state between S^{I}_{3B} and S^{I}_{4B} can not be identified at the chosen level of theory: all the calculations converge to either S^{I}_{3B} or S^{I}_{4B} intermediates, probably because the interactions are particularly weak. Besides, the attempt for the addition of a second DMAB molecule to the S^{I}_{3A} intermediate leads to the reformation of B-H bond. This type of addition from S^{I}_{3A} will not be further discussed here, as the pathway to add the second DMAB molecule toS^{I}_{2} intermediate is obviously more energy-efficient than this pathway. Compared to the direct dehydrogenation of DMAB (Route A in Figure 7.5), the dehydrocoupling process *via* a van der Waals complex (Route B in Figure 7.5) is energetically more favored according to the calculations. The Route B is in good agreement with experimental evidences and mechanistic proposal of Manners' group that the linear dimer intermediate is predominant.

The Bader's analyses of the intermediates ${S^I}_1$, ${S^I}_2$, ${S^I}_{3B}$ and ${S^I}_{4B}$ are presented in Table 7.6 and the ELF features of the Ti-H-B interactions are presented in Table 7.7.

The intermolecular interactions between the titanium atom and B-H bond contained in the ${S^I}_1$ intermediates are identified as a 3C/2e interaction on the basis of both the QTAIM criteria and ELF features. A bond critical point (BCP) and a bond path (BP) between Ti and the hydrogen atom carried by the boron atom was identified with an electron density ρ[BCP(Ti$\cdots$H(B))] of 0.039 a.u. Meanwhile, a non-negligible contribution of Ti atom to the tri-synaptic protonated basin V(Ti, H, B) with a population close to 2 e was also found in ${S^I}_1$ intermediate (Table 7.7), which indicates a 3C/2e character of the Ti-H-B interaction.

The ρ[BCP(Ti$\cdots$H(B))] is significantly higher in ${S^I}_2$ intermediate than that in ${S^I}_1$ intermediate, suggesting a strengthening of the intermolecular interaction. Besides, an additional interaction is formed between the titanium atom and the nitrogen of the DMAB. Additionally, a hydrogen atom previously linked to the nitrogen atom has formed an interaction with the titanium atom, leading to the formation of a metal hydride.

The properties of BCP(Ti-H(N)hydride) and BCP(Ti-N) are almost equivalent in the ${S^I}_2$ and ${S^I}_{3B}$ intermediates. Thus, the interaction between the first DMAB molecule and the titanocene is almost not affected by the addition of the second DMAB molecule. Bond ellipticities ϵ, which measure the extent to which the density is preferentially accumulated in a given plane are also given in the Table 7.6. The ϵ values of BCP(Ti-H(N)hydride) in ${S^I}_1$ and ${S^I}_{4B}$ (around 0.6) are larger than those in ${S^I}_2$ and ${S^I}_{3B}$ (around 0.2). The bond ellipticity in this case could be related to structural stabilities. The ${S^I}_2$ and ${S^I}_{3B}$ intermediate are considered as β-agostic complexes where intramolecular 3C/2e interactions are involved. Besides, the Ti-H-B interactions in ${S^I}_1$ and ${S^I}_{4B}$ intermediates are intermolecular 3C/2e interactions.

Table 7.7: Topological characterization of the dehydrocoupling of DMAB via the van der Waals complex: the ELF protonated basins interacting with the titanium atom and the atomic contribution of each atom are presented.

Intermediates	Population of basin	Atomic contribution		
	V(Ti, H, B)	Ti	B	H
${S^I}_1$	2.02	0.09	0.26	1.65
${S^I}_2$	1.91	0.11	0.22	1.57
${S^I}_{3B}$	1.91	0.11	0.22	1.57
${S^I}_{4B}$	1.93	0.05	0.26	1.62

Furthermore, the addition of the second DMAB molecule leads to three intermolecular interactions involving the same B-H bond (${S^I}_{3B}$), as demonstrated by the QTAIM approach in Table 7.6. The QTAIM analysis of the bonding motif in the ${S^I}_{3B}$ complex clearly reveals the formation of a dihydrogen bond-like interaction, with ρ[BCP(H$\cdots$H)] = 0.004 a.u. and

Table 7.6: QTAIM features of the stationary points of the titanocene-catalyzed dehydrocoupling pathway of DMAB *via* the van der Waals complex. The electron density ρ at BCP, the Laplacian of electron density $\nabla^2\rho$ and the ellipticity ϵ are presented for each BCP in this table are all in a.u.. The gray, pink, blue and white balls represent the Ti, B, N and H atoms respectively. (a): Values at BCPs from top to bottom in the $S^{I}{}_{3B}$ intermediate are written from left to right.

Intermediates		First DMAB molecule				Second DMAB molecule					
		Ti···H(B)	Ti-H(N) hydride	B-H(Ti)	Ti-N	(B)H···H$^{(a)}$			Ti-H(B) hydride	(N)H···H-Ti	N-H
$S^{I}{}_{1}$	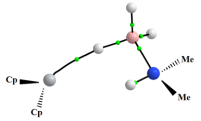	0.039 0.139 0.552		0.140 0.057 0.210							
$S^{I}{}_{2}$	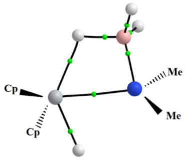	0.064 0.132 0.200	0.118 -0.011 0.005	0.120 0.105 0.153	0.059 0.167 0.221						
$S^{I}{}_{3B}$	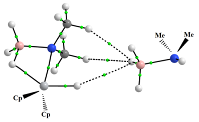	0.063 0.133 0.220	0.122 -0.025 0.008	0.121 0.101 0.146	0.059 0.167 0.222	0.005 0.018 0.680	0.003 0.011 0.053	0.004 0.012 0.506			0.329 -1.429 0.018
$S^{I}{}_{4B}$	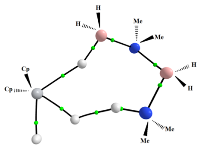	0.036 0.125 0.577	0.118 0.001 0.024	0.134 0.061 0.185					0.097 0.082 0.096	0.045 0.044 0.007	0.301 -1.271 0.009

$\nabla^2\rho$[BCP(H$\cdots$H)] = +0.01 a.u. between the second DMAB molecule and the hydrogen atom directly linked to the Ti center. However, a thorough charge analysis shown in Figure 7.7 demonstrates that the net atomic charge borne by both hydrogen atoms engaged in the H$\cdots$H interaction is negative, with q(H(B)) = -0.68 e and q(H(Ti)) = -0.34 e. As a consequence, this interaction could be labelled as X$-$H$^{\delta-}\cdots{}^{\delta-}HML_n$, unlike to classical dihydrogen bond that correspond toX$-$H$^{\delta+}\cdots{}^{\delta+}H-$Y pattern. The concept of "homopolar dihydrogen bond", expressed as X$-$H$^{\delta-}\cdots{}^{\delta-}H-$X or X$-H^{\delta+}\cdots{}^{\delta+}H-$X, is a well-known concept for B-H$\cdots$H-B or C-H$\cdots$H-C interactions. [184–186] It drew the attention of researchers, because of the dominant role of van der Waals attractive interactions rather than the classical electrostatic interactions in the stabilization of the intermediate complexes. However, the kind of interaction identified in $S^I{}_{3B}$ appears to be slightly different. Generally speaking, in dihydrogen bondings involving transition-metal hydride complexes, the hydride ligand acts as an intermolecular hydrogen-bond acceptor in a X$-$H$^{\delta+}\cdots{}^{\delta-}H-ML_n$ interaction. [187–189] An X$-$H$^{\delta-}\cdots{}^{\delta-}HML_n$ homopolar dihydrogen bond was identified in this case. Other dihydrogen bonds are also identified in this intermediate. B-H$\cdots$H-C interactions between the BH_3 moiety and methyl groups or Cp ligands (which are not presented in Figure 7.7) have electron density in the [0.004 a.u., 0.006 a.u.] range.

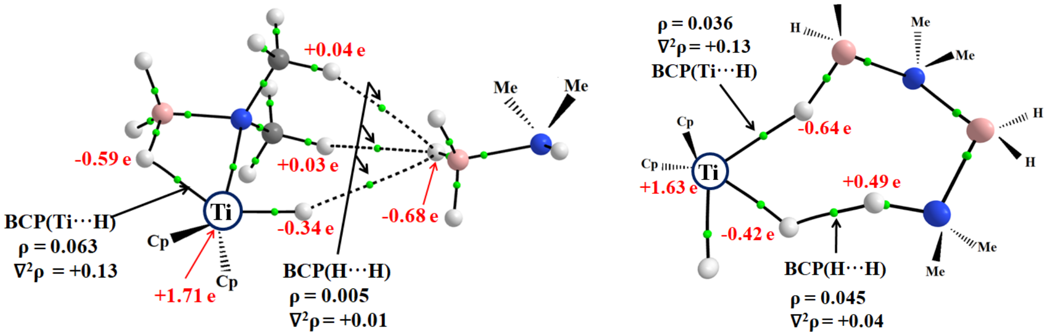

$S^I{}_{3B}$ $S^I{}_{4B}$

Figure 7.7: Bond critical points and Bader's charge analyses in the $S^I{}_{3B}$ and $S^I{}_{4B}$ intermediate.

In the last intermediate $S^I{}_{4B}$, the linear dimer is already formed and it interacts with the organometallic complex via two main inter-atomic interactions: a 3C/2e interaction involving the B-H bond, and a (N)H$\cdots$H-Ti dihydrogen bonding. The cleavage of Ti-N bond in $S^I{}_2$ and $S^I{}_{3B}$ and the Ti-H-B-N ring opening process makes the 3C/2e interaction decreasing again from 0.063 to 0.036 a.u. The dihydrogen bonding present in$S^I{}_{4B}$ is not the same with the dihydrogen-bond-like interaction involved in the $S^I{}_{3B}$ intermediate. Indeed, the hydrogen atom of the DMAB involved in this interaction is linked to the boron atom in the case of the $S^I{}_{3B}$ intermediate. On the other hand, the hydrogen atom of the linear dimer involved in the dihydrogen bond is linked to a nitrogen atom in the case of the $S^I{}_{4B}$ intermediate. Thus, in the latter case, the hydride ligand acts as an intermolecular hydrogen-bond acceptor in a X$-$H$^{\delta+}\cdots{}^{\delta-}H-ML_n$ interaction, in a "classical fashion" (Figure 7.7). This standard dihydrogen bonding is found to be much stronger than those involved in $S^I{}_{3B}$. The electron density at BCP((N)H$\cdots$H-Ti) in this case is 0.045 a.u..

In line with the outcomes of discussion on the energy profile along the Path I, a full mechanistic cycle for the catalytic formation of linear diborazane and release of an equivalent H_2 could be therefore proposed (Figure 7.8). This mechanistic proposal is in agreement with the experimental scheme proposed by Manners' team.

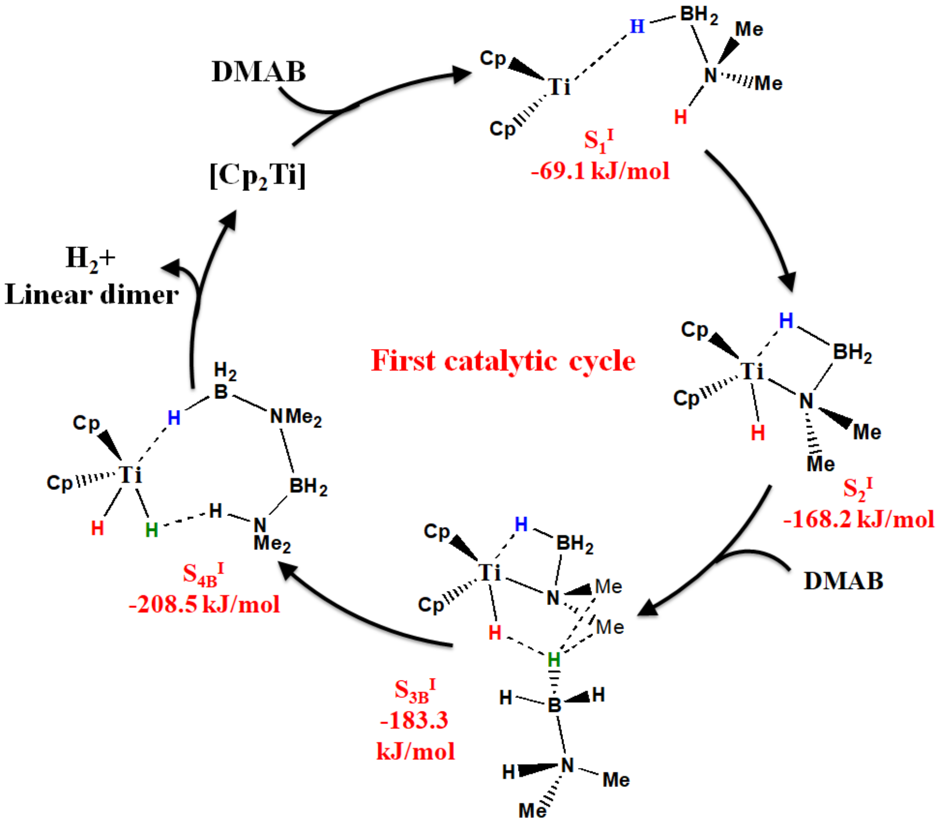

Figure 7.8: First catalytic cycle from [$Cp_2Ti{-}\eta^1$-$H_3B{\cdot}NMe_2H$] complex to linear diborazane *via* a van der Waals complex. Relative energies calculated in the gas-phase including zero-point energy (ZPE) correction in kJ/mol are mentioned.

Path II: A three-body pathway

Complementarily, a possible intermediate shown in Figure 7.9 was also studied as an initial step. This complex is stabilized by the formation of two Ti-H-B intermolecular interactions with a stabilization energy of 90.6 kJ/mol. It is found to be more stable than the S^I_1 complex (the stabilization energy is 69.1 kJ/mol in this case) that is generated by the formation of η^1 3C/2e interactions in the first catalytic cycle presented above.

One further question arisen from the higher stability of this complex in comparison to the S^I_1 complex considered for further dehydrogenation reaction as presented in Figure 7.5. The η^2-complex is calculated to be more stable than the η^1-complex by about 20 kJ/mol. However, in the η^2-complex, the migration of a protic hydrogen atom from the nitrogen atom to the metal center appears to be highly improbable, due to obvious geometrical constraints. In the two-body intermolecular dehydrocoupling of the DMAB, the key step of the reaction is the hydrogen transfer from nitrogen atom to the metal center, thus is, the N-H cleavage process. This

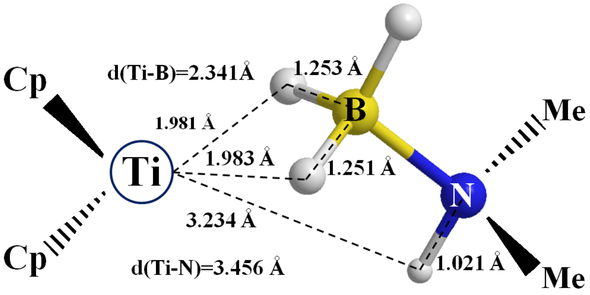

Figure 7.9: Two-body complex $Cp_2Ti-\eta^2$-DMAB involving the η^2 Ti···H−B interactions between Cp_2Ti and DMAB molecule.

standpoint was proposed by Manners et *al* according to their KIE investigation, and was further confirmed from the mechanistic studies with DFT framework. Since the formation of the η^2-complex prevents a further hydrogen migration process from the nitrogen to the titanium atoms, this intermediate can only been involved in a three-body mechanism, as in the intermediate $S^{II}{}_1$. (Figure 7.10)

Such a catalytic cycle involving the three-body complex was already proposed in the previous theoretical work, but it has been ruled out because its highly endoergic nature of reaction. In the present work, this three-body intermolecular mechanism is calculated to be energetically possible within the DFT-D framework. The corresponding energy profiles of the relative gas-phase zero-point corrected energies (E+ZPE) are shown in Table 7.8

Table 7.8: Relative electronic energies with zero point energy (ZPE) correction and Gibbs free energies both in gas phase and in toluene solution with PCM model for Path II.

	Gas phase		PCM with toluene	
Path II	Δ(E+ZPE)	ΔG	Δ(E+ZPE)sol	ΔGsol
Cp_2Ti + 2DMAB	0.0	0.0	0.0	0.0
$S^{II}{}_1$	-164.0	-54.1	-143.8	-34.6
Energy barrier ($TS^{II}{}_{1\_2}$-$S^{II}{}_1$)	**70.9**	**77.6**	**72.7**	**77.9**
$TS^{II}{}_{1\_2}$	-93.1	23.5	-71.1	43.3
$S^{II}{}_2$	-100.5	12.9	-88.4	23.6
Energy barrier ($TS^{II}{}_{2\_3}$-$S^{II}{}_2$)	**10.5**	**17.3**	**17.3**	**22**
$TS^{II}{}_{2\_3}$	-90.0	30.2	-71.1	45.6
$S^{II}{}_3$	-169.5	-61.4	-147.5	-42.6

Two molecules of DMAB are required to interact with the catalyst by forming a three-body intermediate $S^{II}{}_1$. This complex is stabilized by forming an η^2 Ti···H−B interactions and an η^1 Ti···H−N interaction with a binding energy of -164.0 kJ/mol related to the isolated species. On

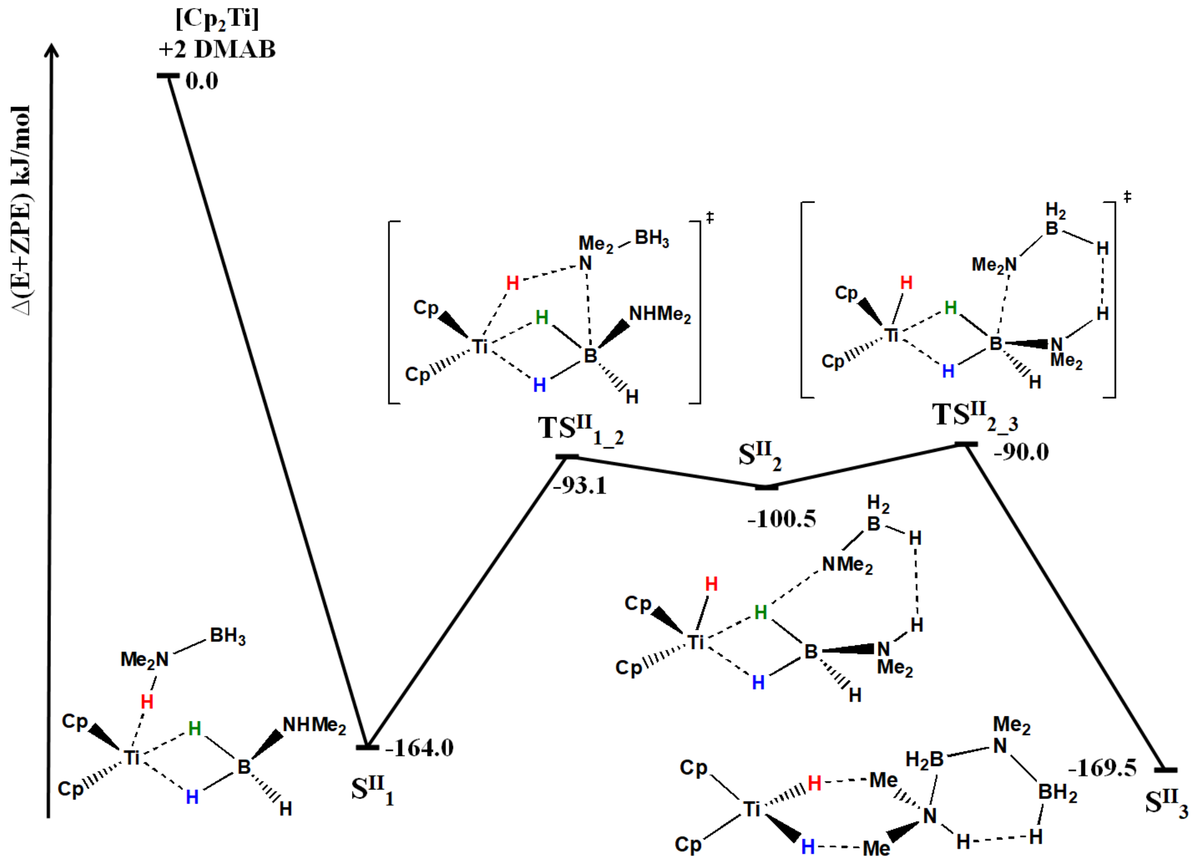

Figure 7.10: Energy profiles for the titanocene-catalyzed dehydrocoupling of two DMAB molecules: a three-body intermolecular pathway. Relative gas-phase zero-point corrected energies (in kJ/mol) are shown.

the basis of the Bader's AIM topological analyses (Table 7.10), only one 3C/2e intermolecular Ti-H-B interaction is identified with ρ[BCP(Ti$\cdots$H(B1))] $=$ 0.053 a.u. and $\nabla^2\rho$[BCP(Ti$\cdots$H(B1))] $=$ 0.135 a.u. However, from the geometric point of view, two η^2 3C/2e interactions involving two B-H bondings can be hypothesized. Indeed, as shown in Figure 7.11, both Ti$\cdots$H(B) and B-H bond lengths are similar. The fact that only one BCP is identified could come from a similar difficulty than the one reported in the case of the identification of α-agostic interactions. [132] The high ellipticity value (ϵ= 6.075) of BCP(Ti$\cdots$H(B1)) also indicates the easy and probable evolution of this point to the formation of two BCPs connecting the Ti center to two hydrogen atoms of BH_3.

The ELF topological approach was further used to characterize the nature of intermolecular interactions involved in the $Cp_2Ti-\eta^2$-DMAB complex and $S^{II}{}_1$ intermediate (Table 7.9). This analysis confirms the presence of 3C/2e interactions between titanium and B-H bonds in both the two complexes by the identification of non-negligible contribution of titanium to the trisynaptic protonated basin V(Ti,B,H).

A bond path and bond critical point were also identified between the titanium and the hydrogen atom carried by the nitrogen atom in the second DMAB molecule in $S^{II}{}_1$ intermediate. Differently to the previously discussed intermolecular interactions involving an hydrogen atom

Table 7.9: ELF characters of the intermolecular interactions involved in $Cp_2Ti-\eta^2$-DMAB complex and S^{II}_1 intermediate.

Complex	Protonated basin	Population of basin	Atomic contribution		
			Ti	B or N	H
$Cp_2Ti-\eta^2$-DMAB	V(Ti, B, H)	1.99	0.06	0.30	1.63
	V(Ti, B, H)	2.07	0.07	0.37	1.63
S^{II}_1	V(Ti, B, H)	2.01	0.07	0.32	1.63
	V(Ti, B, H)	2.09	0.07	0.32	1.64
	V(N, H)	2.12	/	1.61	0.51

and the metallic center, the present interaction is not a 3C/2e one. (Table 7.9) In the this case, a protic hydrogen, with a Bader's charge of +0.44 e, linked to the nitrogen atom, interacts with the titanium. This weak non-covalent interaction is characterized by a BCP with a ρ[BCP(Ti$\cdots$H-N)] value of 0.017 a.u.

The NBO (Natural Bond Orbital) analysis, which provides a measure of the electron donor-acceptor delocalization, was carried out to further characterize these intermolecular interactions. The molecular orbitals (MOs) involved in the intermolecular interactions are shown in Figure 7.12. Two electrons are donated from the B-H σ bond (BD(B-H)) to an unoccupied orbital of metal center (LV(Ti)) both in the case of $Cp_2Ti-\eta^2$-DMAB complex and S^{II}_1 intermediate. These Ti-H-B interactions are thus confirmed as 3C/2e interactions. In addition, an orbital overlap between the lone pair (LP(Ti)) of titanium and the anti-bonding (BD*(N-H)) of N-H bond from the second DMAB molecule is found in the case of S^{II}_1. As a consequence, a weak intermolecular Ti-H-N interaction was also identified as a result of the overlap of two accessible molecular orbitals.

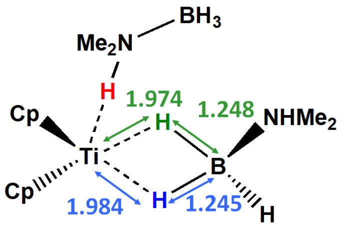

Figure 7.11: Geometric features of 3C/2e interactions in S^{II}_1.

Table 7.10: QTAIM features of the stationary points of the titanocene-catalyzed intermolecular dehydrocoupling pathway of two DMABs . The electron density ρ at BCP, the Laplacian of electron density $\nabla^2\rho$ and the ellipticity ϵ are presented for each BCP in this table and are all in a.u.. The grey, pink, blue and white balls represent the Ti, B, N and H atoms respectively.

	Intermediates	Ti···H(B1)	Ti···H(N2)	Ti-H hydride	N1-H···H-B2	B1-N1	B2-N2	B1-N2	Ti-H···H-C
$S^{II}{}_1$	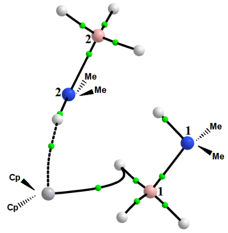	0.053 0.135 6.075	0.017 0.011 0.170			0.125 0.388 0.124	0.117 0.420 0.034		
$S^{II}{}_2$	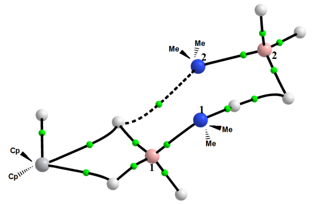	0.058 0.061 0.170 0.154 0.781 0.640		0.121 -0.022 0.018	0.042 0.063 0.248	0.143 0.341 0.175	0.146 0.378 0.075		
$S^{II}{}_3$	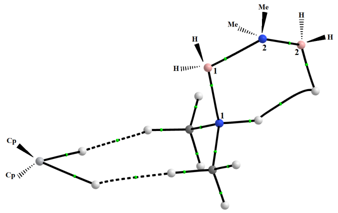			0.113 0.113 -0.003 -0.003 0.071 0.071	0.032 0.061 0.207	0.123 0.348 0.199	0.121 0.361 0.063	0.140 0.283 0.206	0.011 0.010 0.027 0.026 0.014 0.096

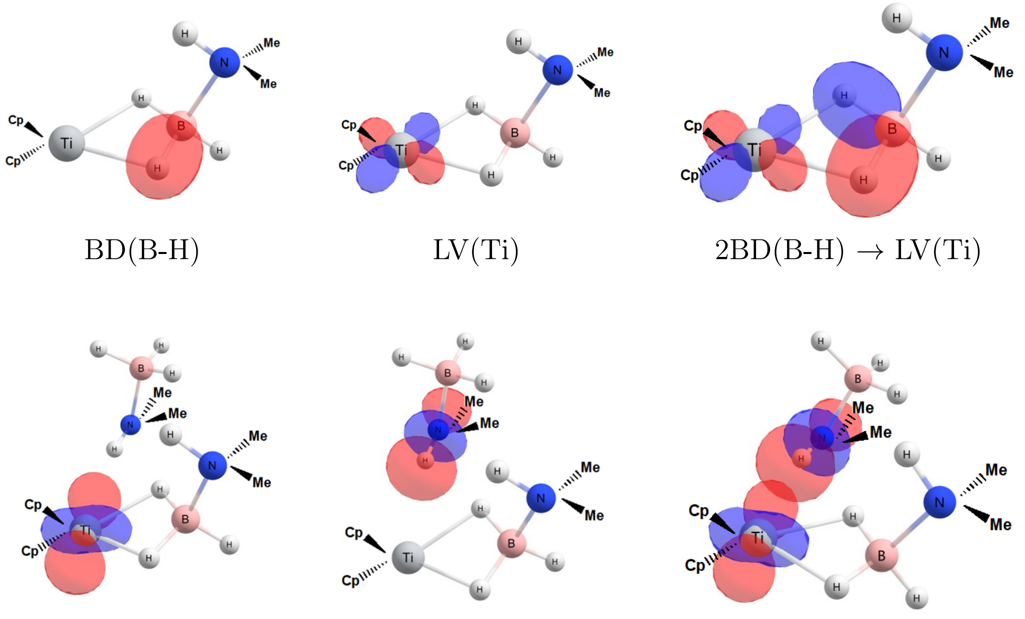

BD(B-H) LV(Ti) 2BD(B-H) → LV(Ti)

LP(Ti) BD*(N-H) LP(Ti) → BD*(N-H)

Figure 7.12: Natural Bond Orbital analysis for the intermolecular interactions involved in $Cp_2Ti{-}\eta^2$-DMAB complex and $S^{II}{}_1$ intermediate. The label BD, LV, LP and BD* represent bonding, lone vacancy, lone pair and antibonding, respectively.

Transformation of $S^{II}{}_1$ to $S^{II}{}_2$ is characterized by a hydrogen transfer from the nitrogen atom to the metal center which leads to the formation of titanium hydride. From energetic point of view, the $S^{II}{}_2$ intermediate evolves towards a new complex ($S^{II}{}_3$) without any energy demand. In the latter complex, dihydride titanium interacts with the linear diborazane fragment via two dihydrogen bonds (ρ[BCP(Ti-H$\cdots$H-C)] = 0.011 a.u. and $\nabla^2\rho$[BCP(Ti-H$\cdots$H-C)] = +0.030 a.u.). It is interesting to notice the presence of a dihydrogen bond (labelled as N1-H$\cdots$H-B2 in $S^{II}{}_3$ in Table 7.10) in the linear diborazane fragment (ρ[BCP(N1-H$\cdots$H-B2)] = 0.032 a.u.) which seems likely to close the six-membered ring in chair-like conformation.

Second catalytic cycle: Dehydrocoupling of linear diborazane intermediate (Path III)

Experimental data also demonstrated that the cyclization of the linear dimer is a catalyzed process. We thus computationally investigated an "on-metal" cyclization of the linear dimer. The calculated energy profiles of this reaction pathway (noted as Path III) are presented in Figure 7.13. The reaction pathway displays the dehydrocoupling process of linear diborazane intermediate to the cyclic diborazane, which is determined to be the final product of the [Cp_2Ti] catalyzed dehydrogenation of DMAB. A similar mechanism was already investigated by Tao and Qi at the DFT level. [59] Their results suggested that this mechanism is highly endothermic. On the contrary, our results obtained within the DFT-D framework demonstrate that this dehydrocoupling pathway is also an exothermic process which is feasible under experimental conditions. (Figure 7.13)

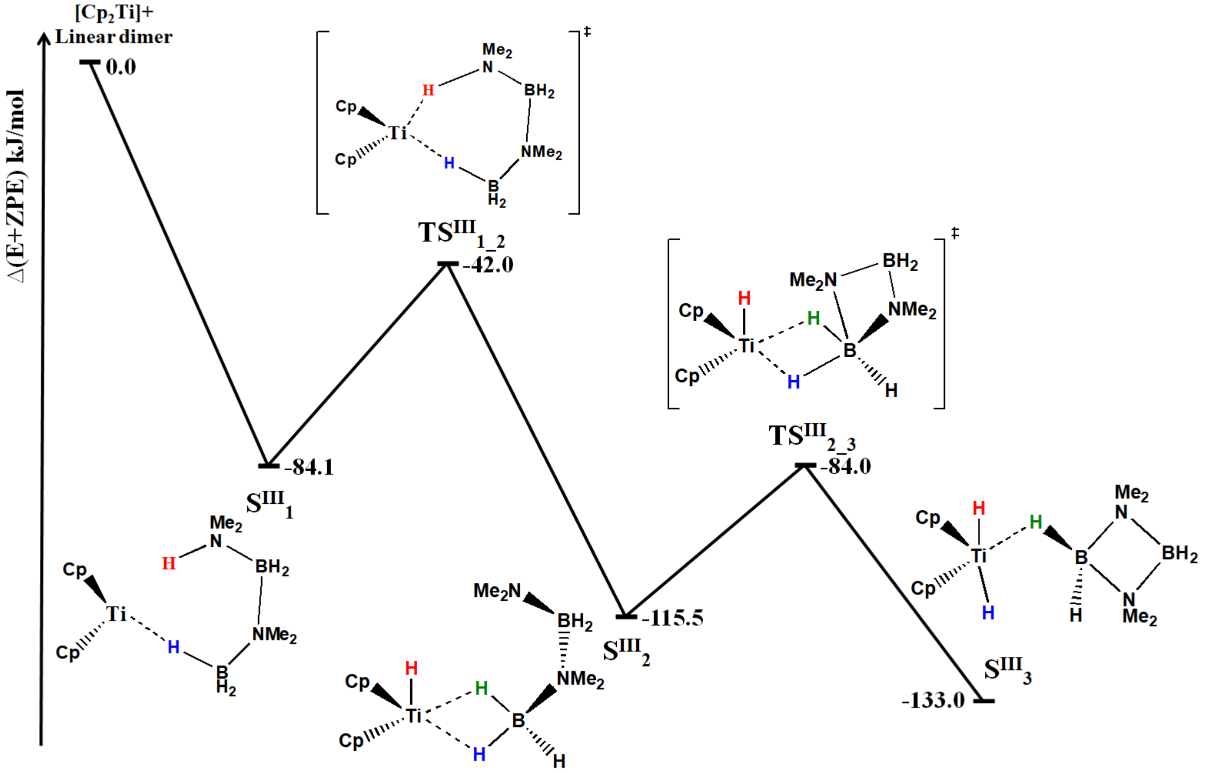
[Cp₂Ti]+
Linear dimer
0.0
Δ(E+ZPE) kJ/mol
TSIII1_2
-42.0
SIII1
-84.1
SIII2
-115.5
TSIII2_3
-84.0
SIII3
-133.0
Cp
Ti
H
Me2
N
BH2
NMe2
B
H2
Me2N
‡

Figure 7.13: Energy profiles for the titanocene-catalyzed dehydrocoupling of linear diborazane: Path III. Relative gas-phase zero-point corrected energies (in kJ/mol) are shown.

Table 7.11: Relative electronic energies with zero point energy (ZPE) correction and Gibbs free energies both in gas phase and in toluene solution with PCM model for Path III.

	Gas phase		PCM with toluene	
Path III	Δ(E+ZPE)	ΔG	Δ(E+ZPE)sol	ΔGsol
Cp_2Ti+ linear diborazane	0.0	0.0	0.0	0.0
S^{III}_1	-84.1	-24.5	-76.5	-11.0
Energy barrier ($TS^{III}_{1\_2}$-S^{III}_1)	**42.1**	**56.1**	**45.3**	**44.8**
$TS^{III}_{1\_2}$	-42.0	31.6	-31.2	33.8
S^{III}_2	-115.5	-47.0	-106.0	-39.9
Energy barrier ($TS^{III}_{2\_3}$-S^{III}_2)	**31.5**	**32.2**	**34.4**	**35.9**
$TS^{III}_{2\_3}$	-84.0	-14.8	-71.6	-4.0
S^{III}_3	-133.0	-65.7	-119.5	-58.4

The cyclization process first involves the coordination of the linear diborazane molecule to the metal center with a stabilization energy of 84.1 kJ/mol (S^{III}_1 intermediate). An η^1-3C/2e intermolecular interaction is identified in this intermediate by the Bader's analysis, with a ρ[BCP(Ti-H(B1)] value of 0.046 a.u. It is interesting to notice that an intramolecular dihydrogen-bond is identified between the protic N$-$H$^{\delta+}$ hydrogen and the hydridic $^{\delta-}$H$-$B hydrogen ρ[BCP(N2-H$^{\delta+}\cdots$ $^{\delta-}$H-B1)] value of 0.021 a.u. A six-membered ring is formed among the linear diborazane molecule with a chair conformation. In the $\mathrm{S^{III}}_2$intermediate, the N-H bond is further activated by the titanium atom by overcoming a 42.1 kJ/mol energy barrier. The cleavage of the N-H bond leads to a titanium hydride intermediate with an asymmetric η^2-3C/2e interactions formed between the titanocene and the amidoborane fragment, characterized by the ρ[BCP(Ti-H(B1)] values of 0.062 and 0.056 a.u. The second titanium hydride is generated by the breakage of one of the B-H bond with an energy barrier of 31.5 kJ/mol while the other one remains connected to the metal center via an intermolecular 3C/2e interaction ($\mathrm{S^{III}}_3$). The QTAIM analysis suggests that this 3C/2e interaction is significantly weaker in the $\mathrm{S^{III}}_3$ intermediate in comparison with the $\mathrm{S^{III}}_2$ intermediate, with ρ[BCP(Ti-H(B1)] values of 0.037 a.u. and 0.062 a.u. in $\mathrm{S^{III}}_3$ and $\mathrm{S^{III}}_2$ respectively.

Concerning the electron flux among different N-B bonds involved in the dehydrocoupling process of linear diborazane to form the cyclic diborazane, Bader's analysis indicates that the two terminal B-N bonds (B1-N1 and B2-N2) are strengthened from $\mathrm{S^{III}}_1$ to$\mathrm{S^{III}}_2$ due to the hydrogen transfer or the formation of intermolecular Ti-H-B interaction. In the case of the $\mathrm{S^{III}}_3$ intermediate where a new B-N bond is formed, the redistribution of electron density among B1-N1-B2-N2 results in the homogenization of these B-N bonds. However, the two B-N bond involved in the Ti-H-B interaction (B1-N1 and B1-N2) are still a little bit reinforced compared to the isolated cyclic diborazane in the same condition (the electron density at all the BCP(B-N) are identical at 0.130 a.u.).

Model of TST (Transition State Theory)

To further predict the kinetic feasibility of these proposed mechanistic in room temperature according to the experimental conditions, the Eyring equation is applied to estimate the rate of the chemical reaction. This equation follows from the the model of Transition State Theory (TST). The general form of Eyring equation is:

$$k = \frac{k_B T}{h} \exp\left(-\frac{\Delta G^{\ddagger}}{RT}\right) \tag{7.4}$$

where

k: reaction rate constant
T: absolute temperature in K, here we take 298 K
k_B: Boltzmann constant, $1.381 \times 10^{-23}\ J \cdot K^{-1}$
h: Planck's constant, $6.626 \times 10^{-34}\ J \cdot K^{-1}$
$\Delta G^{\ddagger}$: Gibbs free energy of activation in $J \cdot mol^{-1}$
R: Gas constant, $8.314\ J \cdot K^{-1} \cdot mol^{-1}$

For an approximative comparison of the possibility of a series of reactions take place at

Table 7.12: QTAIM features of the stationary points of the titanocene-catalyzed dehydrocoupling pathway of linear diborazane. The electron density ρ at BCP, the Laplacian of electron density $\nabla^2\rho$ and the ellipticity ϵ are presented for each BCP in this table and are all in a.u.. The grey, pink, blue and white balls represent the Ti, B, N and H atoms respectively.

	Intermediate	Ti···H(B1)	Ti−H(N2) hydride	Ti−H(B1) hydride	N2-H$^{\delta+}$··· $^{\delta-}$H-B1	B1-N1	B2-N2	N1-B2	N2-B1
S$^{\mathrm{III}}{}_1$	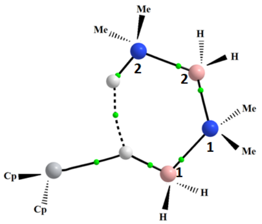	0.046 0.148 1.573			0.021 0.044 0.784	0.126 0.341 0.124	0.123 0.352 0.252	0.139 0.288 0.227	
S$^{\mathrm{III}}{}_2$	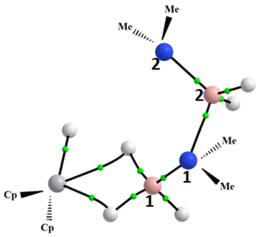	0.062 0.056 0.167 0.161 0.541 0.821	0.122 -0.026 0.033			0.154 0.280 0.114	0.164 0.366 0.091	0.103 0.278 0.070	
S$^{\mathrm{III}}{}_3$	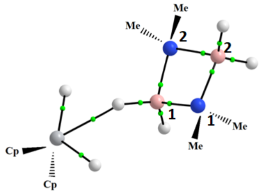	0.037 0.143 0.642	0.108 0.016 0.017	0.018 0.017 0.021		0.137 0.308 0.125	0.129 0.307 0.168	0.129 0.308 0.169	0.137 0.307 0.129

room temperature, we proposed to calculate the estimated reaction rate constant of the turnover limiting step within the TST model. For conciseness, the activation Gibbs free energies of each reaction pathway with their corresponding estimated reaction rate constants using Eyring equation are shown in Table 7.13.

Table 7.13: Relative solvation free activation barriers of the rate-determining step of each process and their estimated reaction rate constant.

	$\Delta\Delta G^{\ddagger}$(kJ/mol) in 298K			Estimated reaction rate constant k (s^{-1})		
	2007	2013	This work	2007	2013	This work
Path I	95.8	90.7	28.3	8.5×10^{-4}	7.8×10^{-4}	6.8×10^{7}
Path II	155.6	140.4	45.6	8.0×10^{-13}	1.5×10^{-12}	6.3×10^{4}
Path III	/	96.1	33.8	/	8.9×10^{-5}	7.4×10^{6}
Off-metal cyclization	119.5	126.2	85.4	7.0×10^{-9}	4.7×10^{-10}	6.7×10^{-3}

The comparison shows that the computational results obtained in this work with an addition of empirical correction of London dispersion can absolutely explain the experimental evidences. Both the two different linear diborazane formation pathways (Path IB and Path II) and the subsequent linear diborazane dehydrocoupling pathway (Path III) are feasible under room temperature according to the relative high reaction rate constant.

Summary

In summary, the titanocene-catalyzed dehydrogenation/dehydrocoupling reaction of DMAB has been computational re-investigated with empirical correction of GD3BJ dispersion. From the Figure 7.14 which summarizes the global mechanisms, we have:

- Two competitive processes were proposed: (1) Path IA: An two-body dehydrogenation starts with the [$Cp_2Ti{-}\eta^1$-$H_3B{\cdot}NMe_2H$] complex leading to an aminoborane $Me_2N{=}BH_2$, which can be converted into cyclic diborazane $[Me_2N{\cdot}BH_2]_2$ by an off-metal dimerization process; (2) Path IB: A 2+1 process through an additive step from agostic intermediate ($S^{I}{}_2$) and a second molecule of DMAB, to generate a linear diborazane *via* a van der Waals complex.
- An three-body intramolecular process Path II starts with a complexation of the catalyst Cp_2Ti with two molecules of DMAB was also feasible. This process also produces the linear diborazane intermediate.
- A subsequent step followed by the catalyzed dehydrocoupling of linear diborazane, the products of both Path II and Path IB, to form the cyclic dimer was also proposed. The cyclic dimer was experimentally observed to be the most common final product (99%).

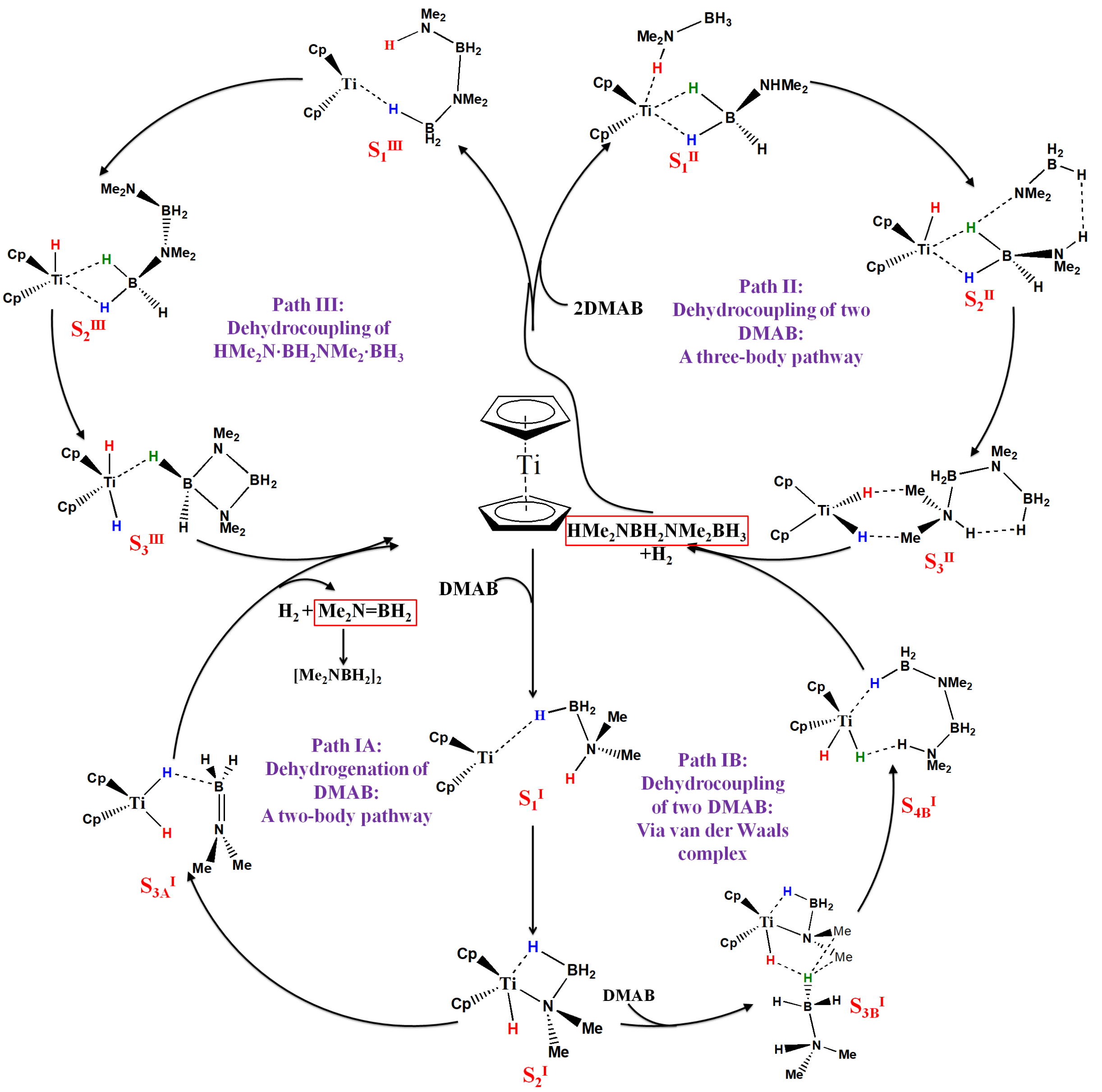
Path III:
Dehydrocoupling of
HMe₂N·BH₂NMe₂·BH₃
Path II:
Dehydrocoupling of two
DMAB:
A three-body pathway
Path IA:
Dehydrogenation of
DMAB:
A two-body pathway
Path IB:
Dehydrocoupling
of two DMAB:
Via van der Waals
complex
2DMAB
DMAB
HMe₂NBH₂NMe₂BH₃
+H₂
H₂ + Me₂N=BH₂
[Me₂NBH₂]₂
Ti
S₁ᴵᴵᴵ
S₂ᴵᴵᴵ
S₃ᴵᴵᴵ
S₁ᴵᴵ
S₂ᴵᴵ
S₃ᴵᴵ
S₁ᴵ
S₂ᴵ
S₃Aᴵ
S₃Bᴵ
S₄Bᴵ

Figure 7.14: Summary of the titanocene-catalyzed dehydrogenation/dehydrocoupling reaction pathways of dimethylamine borane (DMAB).

7.2.2 Titanocene-catalyzed dehydrogenation reaction of other amine borane adducts

As mentioned in the introduction, Manners *et al.* [50] have achieved an overall investigation of the catalytic activity of [Cp_2Ti] under same experimental conditions toward a series of amine-borane adducts: the ammonia borane $H_3N{\cdot}BH_3$, primary amine-borane $H_2MeN{\cdot}BH_3$, secondary amine-boranes with different steric hindrance: $HMeBnN{\cdot}BH_3$, ($Bn{=}CH_2Ph$) and $H^iPr_2N{\cdot}BH_3$. Their results suggested that the activity of the titanocene-catalyzed dehydrogenation reaction depends highly on the nature of amine-borane adducts as well as the substituent group carried by nitrogen atom. As summarized in the Table 7.14, ammonia borane and primary amine-borane showed almost no reactivity with the treatment of 2 mol % [Cp_2Ti] at room temperature after 16 hours. Whereas the catalyst showed a good performance when treated with secondary amine-boranes under the same experimental conditions. It is also interesting to note that the final product of this dehydrogenation reaction various with different substituent groups: the dehydrogenation reaction toward more sterically encumbered amine-borane, the di-isopropylamine borane $H^iPr_2N{\cdot}BH_3$, results in the aminoborane $^iPr_2N{=}BH_3$ instead of the cyclic dimer from $HMe_2N{\cdot}BH_3$ and $HMeBnN{\cdot}BH_3$. To further understand the different reactivity of titanocene catalyst toward different amine-borane adducts, the aim in this section is to explore the performance of titanocene as catalyst for amine-boranes dehydrogenation reactions which were already experimentally studied.

Table 7.14: Main products of the titanocene-catalyzed dehydrogenation/dehydrocoupling reactions of different amine-borane adducts.

Amine-borane : $HR_1R_2N{\cdot}BH_3$	Main products
$R_1 = R_2 = H$	No reaction
$R_1 = H$, $R_2 = Me$	Less than 1% of $[HMeN{\cdot}BH_2]_3$ obtained
$R_1 = R_2 = Me$	$[Me_2N{\cdot}BH_2]_2$
$R_1 = Me$, $R_2 = Bn$	$[MeBnN{\cdot}BH_2]_2$
$R_1 = R_2 = {}^iPr$	$^iPr_2N{=}BH_2$

Titanocene-catalyzed reactivity on ammonia borane and primary amine-borane

Both the experimental results and the theoretical calculations have demonstrated that the proton transfer step from the nitrogen atom to the metallic center is considered as the key stage for the titanocene-catalyzed dehydrogenation reaction of amine-borane.

According to the mechanistic proposition of DMAB dehydrogenation obtained by our DFT-D framework, the transition from the two-body $S^I{}_1$ complex with a η^1 intermolecular interaction to the $S^I{}_2$ intermediate through a hydrogen migration process appears always the turnover limiting step. It is presumed that a transition state $TS^I{}_{1\_2}$ appears along this hydrogen transfer step. This transition state has an approximately con-plane five-member ring structure in which the N-H bond is elongated and the $Ti\cdots H(N)$ interaction is forming. Concerning the initial step of the intramolecular pathway $S^I{}_1$, the coordination of ammonia borane and primary amine-borane ($H_2MeN{\cdot}BH_3$) result in a quasi-symmetric structure with the two hydrogen atoms from the NRH_2 moiety on the opposite and symmetrical positions of the Ti-B-N plane (See structure $S^I{}_1$ in the $H_2RN{\cdot}BH_3$ case in Figure 7.15). The inter-atomic distances between Ti and H from NRH_2 moiety were optimized to be 3.169 Å/3.121 Å and 3.113 Å/3.115 Å respectively for ammonia borane complex and primary amine-borane complex. To further undergo the proton transfer step from NRH_2 (R= H or Me), the formation of the co-plane five-membered ring structure ask energies to overcome the steric strain for further N-H cleavage step. On the contrary, on account of the steric hindrance between the substituent groups of NR_2H moiety ($R_2 = Me_2$, $^iPr_2$ or MeBn) and the catalytic center of the secondary amine-boranes complexes (See $S^I{}_1$ in the $HR_2N{\cdot}BH_3$ case in Figure 7.15), the hydrogen atom of NR_2H moiety tends to approach the metallic center to further undergo the proton transfer process.

Table 7.15: Comparison of the calculated intermolecular distances Ti···H(N) and dihedral angles H-N-B-H of intermediates S_1 and transition states TS_{1_2} respectively for ammonia borane, primary amine-borane and secondary amine-boranes.

Path I	S^{I}_{1}		$TS^{I}_{1\_2}$	
$HR_1R_2N{\cdot}BH_3$	distance Ti···H(N) in Å	Dihedral angle H-N-B-H	distance Ti···H(N) in Å	Dihedral angle H-N-B-H
R_1=R_2=H	3.169/3.121	−59.0°/ + 56.7°	/	/
R_1=HR_2=Me	3.113/3.115	−55.8°/ + 55.8°	/	/
R_1=R_2=Me	2.915	−31.1°	1.819	+4.0°
R_1=MeR_2=Bn	2.888	−32.6°	1.819	+4.0°
R_1=R_2=^{i}Pr	2.906	−31.3°	1.812	+5.1°

To sum up, the presence of the substituent groups in steric hindrance carried by the nitrogen atom allows facilitating a further proton transfer and abstraction by the metal center in this titanocene-catalyzed dehydrogenation of amine-boranes since it diminish strongly the energy barrier. The same process within the ammonia borane or primary amine-borane dehydrogenation demands probably much huger energy to overcome the steric strain. For that reason, no dehydrogenation reaction occurs in the case of ammonia borane and primary amine-borane adducts.

Titanocene-catalyzed dehydrogenation of $H^{i}Pr_2N{\cdot}BH_3$

Experimental investigations have also shown that the di-isopropylamine borane (DiPrAB) is characterized by a fundamentally different reaction with respect to the DMAB. Indeed, instead of the cyclic diborazane product, the dehydrogenation of the DiPrAB leads to the formation of the $^{i}Pr_2N{=}BH_2$. We can therefore reasonably hypothesize that the linear dimer intermediate is not formed from the DiPrAB adducts. The computational results obtained enable us to explain the singularity of DiPrAB dehydrogenation path in two ways.

At the first insight, the key intermediates obtained during the linear diborazane formation of DMAB dehydrogenation may be used to explain the difference in reaction mechanisms caused by the presence of sterically bulky groups on the nitrogen atom. Concerning the formation of linear diborazane, reaction *via* either an three-body intermolecular dehydrocoupling pathway with two equiv. of DiPrAB or a dehydrocoupling step involving amidoborane intermediate ($Cp_2Ti(H)N^{i}Pr_2BH_3$) with a second molecule of DiPrAB *via* a van der Waals complex, the steric hindrance effect become dominant. Even though the presence of isopropyl substituents stabilize the initial coordination complexes with various inter-atomic non-covalent interactions between ligands, the steric encumbered isopropyl substituents prevent the boron atom from the first unit and the nitrogen atom from the second unit to get close each other for a further formation of a B-N bond, as presented in Figure 7.18. Consequently only the monomeric aminoborane was

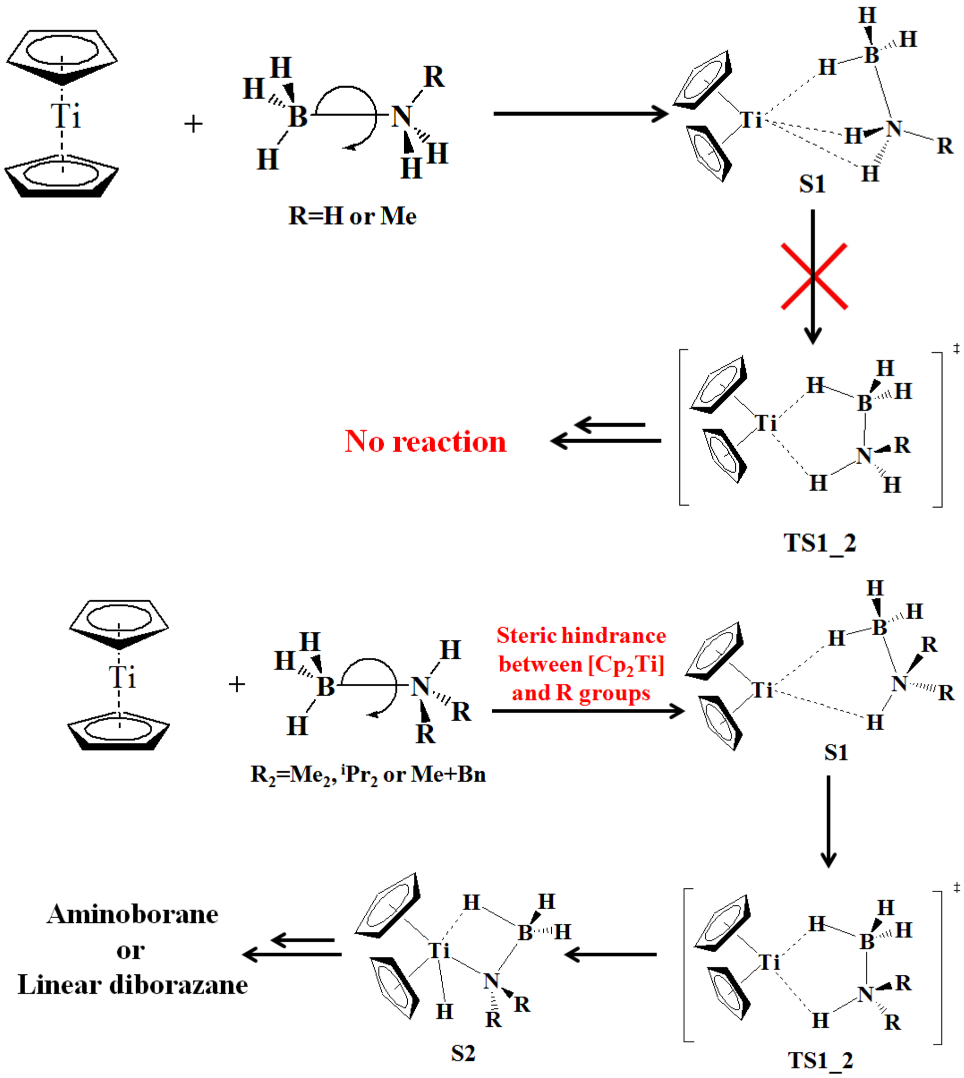
R=H or Me
S1
No reaction
TS1_2
Steric hindrance between [Cp$_2$Ti] and R groups
R$_2$=Me$_2$, ^{i}Pr$_2$ or Me+Bn
S1
Aminoborane or Linear diborazane
S2
TS1_2

Figure 7.15: Schematic presentation of different reactivity of titanocene-catalyzed dehydrogenation reaction of ammonia borane, primary amine-borane and secondary amine-boranes.

observed experimentally.

In addition, in order to explain why only monomeric aminoborane was formed in the case of titanocene-catalyzed dehydrogenation of DiPrAB from the energetic point of view, a comparison of the energy potential surface for Path I between the DMAB and DiPrAB is reported in Figure 7.17. It is demonstrated that in contrast to the case of DMAB, the "Route A" transforming the S_2 structure to the aminoborane (S_3) (red full line) is more favorable than the "Route B" for the DiPrAB.(purple full line)

<table>
<tr><th colspan="2">Path II: Intermolecular Pathway</th></tr>
<tr><td>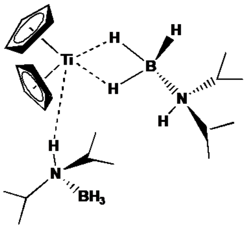</td><td>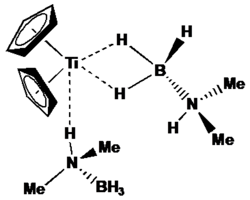</td></tr>
<tr><td>S_1 with R = ^{i}Pr
d(Ti···H(N)) = 3.134 Å</td><td>S_1 with R = Me
d(Ti···H(N)) = 2.722 Å</td></tr>
<tr><th colspan="2">Path IB: 2+1 mechanism *via* vdW complex</th></tr>
<tr><td>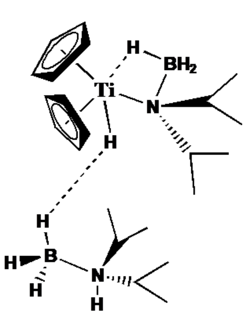</td><td>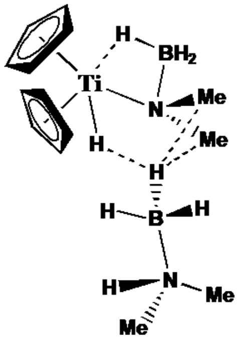</td></tr>
<tr><td>vdW complex with R = ^{i}Pr
d(H(Ti)···H(B2)) = 3.076 Å
d(N1···B2) = 6.546 Å</td><td>vdW complex with R = Me
d(H(Ti)···H(B2)) = 2.844 Å
d(N1···B2) = 4.557 Å</td></tr>
</table>

Figure 7.16: Comparison of structures between key stationary points from dehydrocoupling mechanism of $H^iPr_2N{\cdot}BH_3$ and $HMe_2N{\cdot}BH_3$ respectively.

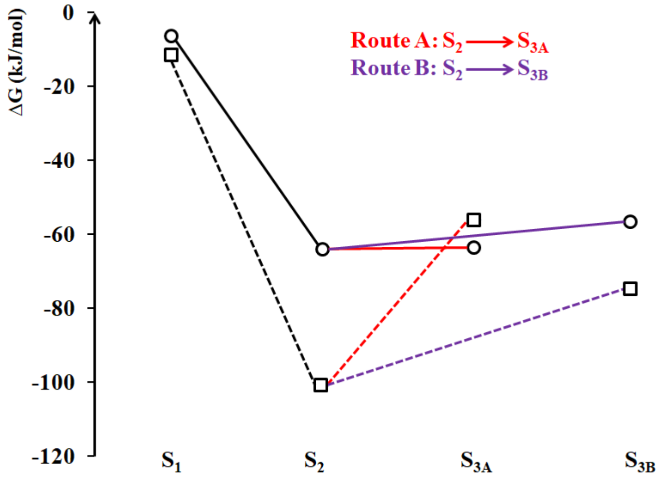

Figure 7.17: Relative Gibbs free energy of four structures along the Path I (see Figure 7.5)for both DMAB (squares, dotted lines) and DiPrAB (circles, full lines) compounds.

Mechanistic investigations showed that the dehydrogenation of DiPrAB undergo the two-body intramolecular stepwise N-H/B-H breakage mechanism (It is the Path I for the dehydrogenation of DMAB), as shown in Figure 7.5.

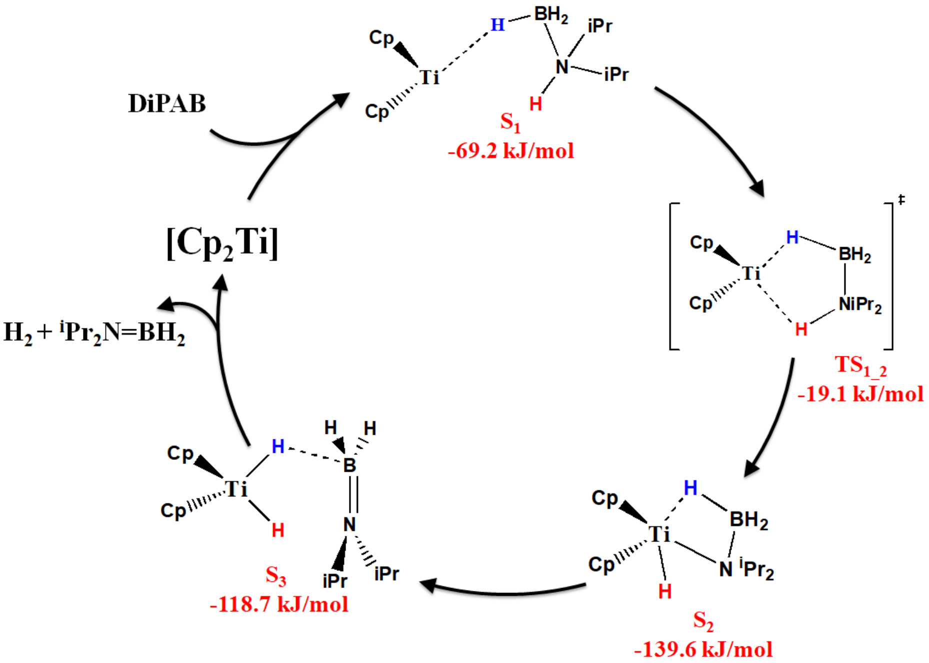

Figure 7.18: Titanocene-catalyzed dehydrogenation reaction of $H^iPr_2N{\cdot}BH_3$. Relative gas-phase electronic energies with zero point energy (ZPE) correction are given in kJ/mol.

Summary

As regards the mechanistic investigations into the titanocene-catalyzed dehydrogenation of DMAB, the inconsistency between theoretical and experimental results has lasted for more than 10 years. Our theoretical calculations within DFT-D framework make it possible to obtain a reaction pathway in perfect agreement with the experimental data: a mechanism involving two catalyzed steps leads to the formation of the cyclic diborazane from the DMAB *via* the linear dimer. Herein, all the steps of this mechanism were elucidated. The cyclization of the intermediate occurs *via* an on-metal mechanism, instead of the off-metal dimerization of aminoborane intermediate proposed by previous DFT calculations. The formation of a van der Waals complex in which one of the DMAB molecules forms a dihydrogen bonding interaction with the hydrogen atom carried by the titanium appears to play a central role in the formation of the linear dimer intermediate. Calculations within the DFT-D framework also show that titanocene is an efficient catalyst for the cyclization of linear dimer. ELF, QTAIM and NBO analyses allowed us to characterize the nature of non-covalent interactions in the reaction intermediates. Numerous weak interactions such as dihydrogen bonding, 3C/2e interactions, electrostatic, and orbital interactions are involved in the catalyzed dehydrocoupling process of DMAB. For a consistent description of these interactions, the consideration of dispersion is fundamental. This is the reason why the DFT-D framework makes it possible to reproduce the experimental data, unlike the DFT framework.

Part IV

Epilogue: General Conclusion and Some Prospect

General Conclusion

This thesis aims at investigating transition-metal catalyzed dehydrogenation of amine-boranes in the context of hydrogen storage for on-board applications. The catalyzed dehydrogenation and regeneration of amine-borane adducts is one of the most promising ways for a hydrogen storage and supply in the hydrogen cycle in line with the green chemistry demands, as it is shown in Figure 7.19.

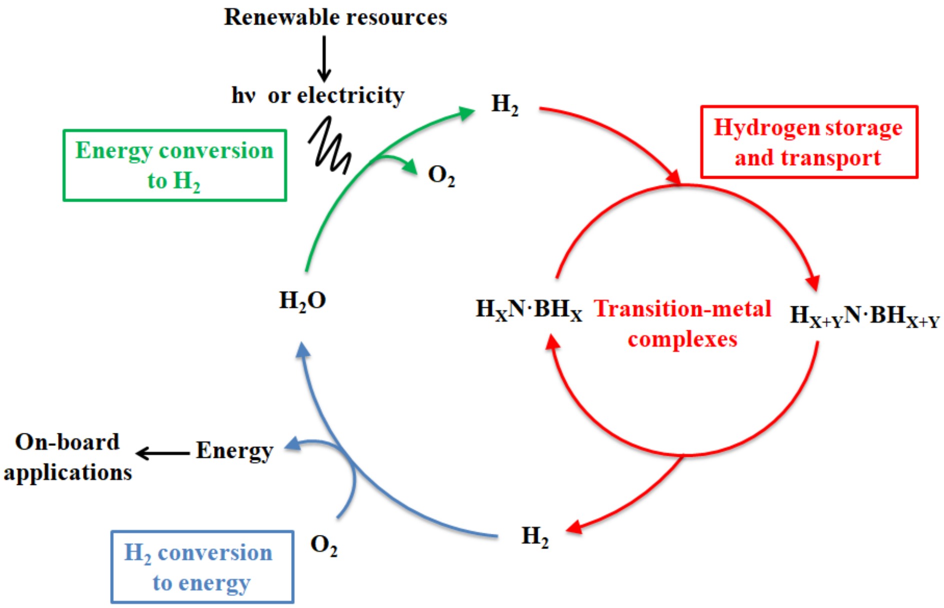
Renewable resources
hν or electricity
Energy conversion to H_2
H_2
O_2
Hydrogen storage and transport
H_2O
$H_XN{\cdot}BH_X$
Transition-metal complexes
$H_{X+Y}N{\cdot}BH_{X+Y}$
On-board applications
Energy
O_2
H_2
H_2 conversion to energy

Figure 7.19: Hydrogen cycle.

A starting point of this thesis work is to focus on the Group IV metallocenes dehydrogenation of amine-boranes for which computational results cannot able to explain the experimental observations. Two categories of reaction intermediates are mainly discussed: the agostic intermediates characterized by an intramolecular 3-center 2-electron (3C/2e) interaction and the σ complexes including intermolecular 3C/2e interactions. Systematic investigations of these intermediates were carried with DFT framework in combination with topological analyses including the QTAIM (Quantum Theory of Atoms in Molecules) and ELF (Electron Localization Function) approaches. Studies demonstrated that not only the nature of metallic center but also the substituent groups carried by the nitrogen atom play a significant role on the strength of the M-H-B 3C/2e interaction. Besides, the magnetic properties of metallic centers or the nature of amine-borane/phosphine-borane may also have impact on the activation of the B-H σ bond. Results also shown that the activation of B-H bond was a crucial step towards the transition-metal catalyzed dehydrogenation of amine-boranes or phosphine-boranes.

Furthermore, the detailed investigation on the titanocene-catalyzed dehydrogenation of amine-borane adducts, especially the dimethylamine borane (DMAB) was carried out. Theoretical calculations within the DFT-D (Density Function Theory corrected with dispersion) framework make it possible to obtain a reaction pathway in perfect agreement with the experimental data. A major conclusion of the mechanistic investigation is that the formation of a van der Waals complex in which a second DMAB molecule interacts with an agostic intermediate subunit *via* dihydrogen bonds appears to play a central role in the formation of the linear dimer intermediate. The topological (ELF and QTAIM) and orbital (NBO: Natural Bond Orbital) analyses allowed us to characterize the natures of non-covalent interactions in the reaction intermediates. Noticeably, we underlined the important role played by weak interactions, such as dihydrogen bonds and 3C/2e interactions, along the catalyzed dehydrocoupling process of DMAB. For a consistent description of these interactions, the coverage of dispersion contribution is fundamental.

Some Prospect

Since the discovery by DW Stephan *et al.* [190] that the Frustrated Lewis Paris (FLPs) can reversibly activate dihydrogen molecule in absence of a transition metal, various attentions have been paid to active small molecules *via* FLPs. FLPs are composed of Lewis acid/base pairs. Because of the steric hindrance ("frustrated"), the Lewis acid and Lewis base cannot combine to form a classic neutral adduct. The cooperation of the active Lewis acid and Lewis base has found to be a surprising way of finding new reactions. [191, 192] Indeed, such catalysts may promote the development of cheaper and more environmentally friendly systems.

Experimental investigations using FLPs to reversibly catalyze the dehydrogenation of amine-boranes have also been performed in the last decade. Duncan F. Wass *et al.* have put forward a series of FLPs involving the cationic metallocene-phosphinoaryloxide (labelled as M/P FLP) complexes. [54, 55] Lewis acidic component is the electrophile transition metal center which provides the potential capacity to activate the reactant. These transition-metal-based FLPs have been shown to rapidly dehydrocouple several amine-borane adducts under ambient conditions to yield the expected products.

As we have been concerned on the catalyzed dehydrogenation of amine-boranes adducts, the further study of the catalytic reaction pathway with transition metal FLP species would be a natural perspective of my work. Fundamentally different reactivity between previously studied analogues, the Group IV metallocenes (Cp_2M), and the M/P FLP systems was found.

The completely different chemical reactivity of catalyzed amine-borane dehydrogenation between the Cp_2M catalysts and the M/P FLP systems would be worth studying using our methodological approach. This comparison of the calculated reaction pathways with the metallocenes and their FLP counterparts may shed some light on how Lewis pairs modify the reaction pathways.

At the first stage, we need to concentrate on the key intermediate(s) by a systematic exploration and characterization using the established methodology. Features that are worth considering are the following points:

- effect of Lewis acidity/basicity, that is the nature of metallic center and Lewis base;
- effect of the electronic properties of substituents and ligands carried by the Lewis acid/base centers;
- effect of the sterically bulky of substituents;
- effect of the solvent.

The second step may be concerned by implementing reaction pathways which are able to explain the experimental observations. The discrepancy of reactivity of metallocene complexes and the FLP analogues should be an entry point for this investigation.

Concerning long-term perspectives, collaborations between theoretical and experimental chemists on the FLP chemistry may lead to the development of ad-hoc catalysts for the dehydrogenation of amine-boranes.

Bibliography

[1] Colin P Morice, John J Kennedy, Nick A Rayner, and Phil D Jones. Quantifying uncertainties in global and regional temperature change using an ensemble of observational estimates: The hadcrut4 data set. *Journal of Geophysical Research: Atmospheres*, 117(D8), 2012.

[2] Pavlos Nikolaidis and Andreas Poullikkas. A comparative overview of hydrogen production processes. *Renewable and sustainable energy reviews*, 67:597–611, 2017.

[3] Sunita Sharma and Sib Krishna Ghoshal. Hydrogen the future transportation fuel: from production to applications. *Renewable and sustainable energy reviews*, 43:1151–1158, 2015.

[4] Seyed Ehsan Hosseini and Mazlan Abdul Wahid. Hydrogen production from renewable and sustainable energy resources: promising green energy carrier for clean development. *Renewable and Sustainable Energy Reviews*, 57:850–866, 2016.

[5] Michael Oertel, Johannes Schmitz, Walter Weirich, Ditmar Jendryssek-Neumann, and Rudolf Schulten. Steam reforming of natural gas with intergrated hydrogen separation for hydrogen production. *Chemical engineering & technology*, 10(1):248–255, 1987.

[6] Meyer Steinberg and Hsing C Cheng. Modern and prospective technologies for hydrogen production from fossil fuels. *International Journal of Hydrogen Energy*, 14(11):797–820, 1989.

[7] Atilla Ersöz. Investigation of hydrocarbon reforming processes for micro-cogeneration systems. *international journal of hydrogen energy*, 33(23):7084–7094, 2008.

[8] Tom Smolinka, Jürgen Garche, Christopher Hebling, and Oliver Ehret. Overview on water electrolysis for hydrogen production and storage. In *International Symposium on Water Electrolysis and Hydrogen as Part of the Future Renewable Energy System, Copenhagen, Denmark, May*, pages 10–11, 2012.

[9] Kai Zeng and Dongke Zhang. Recent progress in alkaline water electrolysis for hydrogen production and applications. *Progress in Energy and Combustion Science*, 36(3):307–326, 2010.

[10] Markus Lehner, Robert Tichler, Horst Steinmüller, and Markus Koppe. Storage options for renewable energy. In *Power-to-Gas: Technology and Business Models*, pages 1–6. Springer, 2014.

[11] Marcelo Carmo, David L Fritz, Jürgen Mergel, and Detlef Stolten. A comprehensive review on pem water electrolysis. *International journal of hydrogen energy*, 38(12):4901–4934, 2013.

[12] John A Kilner, SJ Skinner, SJC Irvine, and PP Edwards. *Functional materials for sustainable energy applications*. Elsevier, 2012.

[13] MA Laguna-Bercero. Recent advances in high temperature electrolysis using solid oxide fuel cells: A review. *Journal of Power Sources*, 203:4–16, 2012.

[14] Meng Ni, Dennis YC Leung, Michael KH Leung, and K Sumathy. An overview of hydrogen production from biomass. *Fuel processing technology*, 87(5):461–472, 2006.

[15] A Demirbas. Thermochemical conversion of mosses and algae to gaseous products. *Energy Sources, Part A*, 31(9):746–753, 2009.

[16] Hyun Tae Hwang and Arvind Varma. Hydrogen storage for fuel cell vehicles. *Current Opinion in Chemical Engineering*, 5:42–48, 2014.

[17] Office of Energy Efficiency & Renewable Energy. Doe technical targets for onboard hydrogen storage for light-duty vehicles, 2017. https://www.energy.gov/eere/fuelcells/doe-technical-targets-onboard-hydrogen-storage-light-duty-vehicles.

[18] Myunghyun Paik Suh, Hye Jeong Park, Thazhe Kootteri Prasad, and Dae-Woon Lim. Hydrogen storage in metal–organic frameworks. *Chemical reviews*, 112(2):782–835, 2011.

[19] R Ströbel, J Garche, PT Moseley, L Jörissen, and G Wolf. Hydrogen storage by carbon materials. *Journal of Power Sources*, 159(2):781–801, 2006.

[20] Billur Sakintuna, Farida Lamari-Darkrim, and Michael Hirscher. Metal hydride materials for solid hydrogen storage: a review. *International journal of hydrogen energy*, 32(9):1121–1140, 2007.

[21] Donald J Siegel, Ch Wolverton, and V Ozoliņš. Thermodynamic guidelines for the prediction of hydrogen storage reactions and their application to destabilized hydride mixtures. *Physical review B*, 76(13):134102, 2007.

[22] CE Wolverton, V Ozoliņš, and M Asta. Hydrogen in aluminum: First-principles calculations of structure and thermodynamics. *Physical Review B*, 69(14):144109, 2004.

[23] Gary Sandrock. A panoramic overview of hydrogen storage alloys from a gas reaction point of view. *Journal of alloys and compounds*, 293:877–888, 1999.

[24] John J Vajo, Sky L Skeith, and Florian Mertens. Reversible storage of hydrogen in destabilized libh4. *The Journal of Physical Chemistry B*, 109(9):3719–3722, 2005.

[25] Philippe Mauron, Florian Buchter, Oliver Friedrichs, Arndt Remhof, Michael Bielmann, Christoph N Zwicky, and Andreas Züttel. Stability and reversibility of libh4. *The Journal of Physical Chemistry B*, 112(3):906–910, 2008.

[26] Nobuko Ohba, Kazutoshi Miwa, Masakazu Aoki, Tatsuo Noritake, Shin-ichi Towata, Yuko Nakamori, Shin-ichi Orimo, and Andreas Züttel. First-principles study on the stability of intermediate compounds of libh 4. *Physical Review B*, 74(7):075110, 2006.

[27] V Ozolins, EH Majzoub, and C Wolverton. First-principles prediction of thermodynamically reversible hydrogen storage reactions in the li-mg-ca-bh system. *Journal of the American Chemical Society*, 131(1):230–237, 2008.

[28] Zhitao Xiong, Jianjiang Hu, Guotao Wu, Ping Chen, Weifang Luo, Karl Gross, and James Wang. Thermodynamic and kinetic investigations of the hydrogen storage in the li–mg–n–h system. *Journal of Alloys and Compounds*, 398(1-2):235–239, 2005.

[29] Jun Yang, Andrea Sudik, Donald J Siegel, Devin Halliday, Andrew Drews, Roscoe O Carter, Christopher Wolverton, Gregory J Lewis, JW Sachtler, John J Low, et al. A self-catalyzing hydrogen-storage material. *Angewandte Chemie International Edition*, 47(5):882–887, 2008.

[30] Borislav Bogdanović, Richard A Brand, Ankica Marjanović, Manfred Schwickardi, and Joachim Tölle. Metal-doped sodium aluminium hydrides as potential new hydrogen storage materials. *Journal of alloys and compounds*, 302(1-2):36–58, 2000.

[31] Wim T Klooster, Thomas F Koetzle, Per EM Siegbahn, Thomas B Richardson, and Robert H Crabtree. Study of the n-h...h-b dihydrogen bond including the crystal structure of bh3nh3 by neutron diffraction. *Journal of the American Chemical Society*, 121(27):6337–6343, 1999.

[32] Radu Custelcean and Zbigniew A Dreger. Dihydrogen bonding under high pressure: a raman study of bh3nh3 molecular crystal. *The Journal of Physical Chemistry B*, 107(35):9231–9235, 2003.

[33] Sheldon G Shore and Robert W Parry. The crystalline compound ammonia-borane, 1 h3nbh3. *Journal of the American Chemical Society*, 77(22):6084–6085, 1955.

[34] David J Heldebrant, Abhi Karkamkar, John C Linehan, and Tom Autrey. Synthesis of ammonia borane for hydrogen storage applications. *Energy & Environmental Science*, 1(1):156–160, 2008.

[35] Sheldon G Shore and Robert W Parry. Chemical evidence for the structure of the âdiammoniate of diborane.â ii. the preparation of ammonia-borane. *Journal of the American Chemical Society*, 80(1):8–12, 1958.

[36] MG Hu, JM Van Paasschen, and RA Geanangel. New synthetic approaches to ammonia-borane and its deuterated derivatives. *Journal of Inorganic and Nuclear Chemistry*, 39(12):2147–2150, 1977.

[37] Sheldon G Shore and KW Boddeker. Large scale synthesis of h2b (nh3) 2+ bh4-and h3nbh3. *Inorganic Chemistry*, 3(6):914–915, 1964.

[38] Roy M Adams, John Beres, Alan Dodds, and Alfred J Morabito. Dimethyl sulfide-borane as a borane carrier. *Inorganic Chemistry*, 10(9):2072–2074, 1971.

[39] Xuenian Chen, Xiaoguang Bao, Beau Billet, Sheldon G Shore, and Ji-Cheng Zhao. Large-scale and facile preparation of pure ammonia borane through displacement reactions. *Chemistry-A European Journal*, 18(38):11994–11999, 2012.

[40] Erwin Mayer. Conversion of dihydridodiammineboron (iii) borohydride to ammonia-borane without hydrogen evolution. *Inorganic Chemistry*, 12(8):1954–1955, 1973.

[41] Melanie C Denney, Vincent Pons, Travis J Hebden, D Michael Heinekey, and Karen I Goldberg. Efficient catalysis of ammonia borane dehydrogenation. *Journal of the American Chemical Society*, 128(37):12048–12049, 2006.

[42] Nicole Blaquiere, Sarah Diallo-Garcia, Serge I Gorelsky, Daniel A Black, and Keith Fagnou. Ruthenium-catalyzed dehydrogenation of ammonia boranes. *Journal of the American Chemical Society*, 130(43):14034–14035, 2008.

[43] Richard J Keaton, Johanna M Blacquiere, and R Tom Baker. Base metal catalyzed dehydrogenation of ammonia- borane for chemical hydrogen storage. *Journal of the American Chemical Society*, 129(7):1844–1845, 2007.

[44] Cédric Boulho and Jean-Pierre Djukic. The dehydrogenation of ammonia–borane catalysed by dicarbonylruthenacyclic (ii) complexes. *Dalton Transactions*, 39(38):8893–8905, 2010.

[45] Brian L Conley and Travis J Williams. Dehydrogenation of ammonia-borane by shvo's catalyst. *Chemical Communications*, 46(26):4815–4817, 2010.

[46] Dominique F Schreiber, Crystal OâConnor, Christian Grave, Yannick Ortin, Helge MuÌller-Bunz, and Andrew D Phillips. Application of β-diketiminato arene-substituted ru (ii) complexes in highly efficient h2 dehydrocoupling of amine boranes. *ACS Catalysis*, 2(12):2505–2511, 2012.

[47] Hassan A Kalviri, Felix Gärtner, Gang Ye, Ilia Korobkov, and R Tom Baker. Probing the second dehydrogenation step in ammonia-borane dehydrocoupling: characterization and reactivity of the key intermediate, b-(cyclotriborazanyl) amine-borane. *Chemical science*, 6(1):618–624, 2015.

[48] Heather C Johnson, Thomas N Hooper, and Andrew S Weller. The catalytic dehydrocoupling of amine–boranes and phosphine–boranes. In *Synthesis and Application of Organoboron Compounds*, pages 153–220. Springer, 2015.

[49] Timothy J Clark, Christopher A Russell, and Ian Manners. Homogeneous, titanocene-catalyzed dehydrocoupling of amine- borane adducts. *Journal of the American Chemical Society*, 128(30):9582–9583, 2006.

[50] Matthew E Sloan, Anne Staubitz, Timothy J Clark, Christopher A Russell, Guy C Lloyd-Jones, and Ian Manners. Homogeneous catalytic dehydrocoupling/dehydrogenation of amine- borane adducts by early transition metal, group 4 metallocene complexes. *Journal of the American Chemical Society*, 132(11):3831–3841, 2010.

[51] Holger Helten, Barnali Dutta, James R Vance, Matthew E Sloan, Mairi F Haddow, Stephen Sproules, David Collison, George R Whittell, Guy C Lloyd-Jones, and Ian Manners. Paramagnetic titanium (iii) and zirconium (iii) metallocene complexes as precatalysts for the dehydrocoupling/dehydrogenation of amine–boranes. *Angewandte Chemie*, 125(1):455–458, 2013.

[52] Doris Pun, Emil Lobkovsky, and Paul J Chirik. Amineborane dehydrogenation promoted by isolable zirconium sandwich, titanium sandwich and n2 complexes. *Chemical Communications*, (31):3297–3299, 2007.

[53] Torsten Beweries, Sven Hansen, Monty Kessler, Marcus Klahn, and Uwe Rosenthal. Catalytic dehydrogenation of dimethylamine borane by group 4 metallocene alkyne complexes and homoleptic amido compounds. *Dalton Transactions*, 40(30):7689–7692, 2011.

[54] Andy M Chapman, Mairi F Haddow, and Duncan F Wass. Frustrated lewis pairs beyond the main group: cationic zirconocene–phosphinoaryloxide complexes and their application in catalytic dehydrogenation of amine boranes. *Journal of the American Chemical Society*, 133(23):8826–8829, 2011.

[55] Andy M Chapman, Mairi F Haddow, and Duncan F Wass. Frustrated lewis pairs beyond the main group: synthesis, reactivity, and small molecule activation with cationic

zirconocene–phosphinoaryloxide complexes. *Journal of the American Chemical Society*, 133(45):18463–18478, 2011.

[56] Marcus Klahn, Dirk Hollmann, Anke Spannenberg, Angelika Brückner, and Torsten Beweries. Titanocene (iii) complexes with 2-phosphinoaryloxide ligands for the catalytic dehydrogenation of dimethylamine borane. *Dalton Transactions*, 44(27):12103–12111, 2015.

[57] Karla A Erickson, John PW Stelmach, Neil T Mucha, and Rory Waterman. Zirconium-catalyzed amine borane dehydrocoupling and transfer hydrogenation. *Organometallics*, 34(19):4693–4699, 2015.

[58] Yi Luo and Koichi Ohno. Computational study of titanocene-catalyzed dehydrocoupling of the adduct me2nhbh3: An intramolecular, stepwise mechanism. *Organometallics*, 26(14):3597–3600, 2007.

[59] Jingcong Tao and Yong Qi. Titanocene-catalyzed dehydrocoupling of the adduct me2nh·bh3 via competitive pathways: A dft study. *Journal of Organometallic Chemistry*, 745:479–486, 2013.

[60] Takamasa Miyazaki, Yoshiaki Tanabe, Masahiro Yuki, Yoshihiro Miyake, and Yoshiaki Nishibayashi. Synthesis of group iv (zr, hf)- group viii (fe, ru) heterobimetallic complexes bearing metallocenyl diphosphine moieties and their application to catalytic dehydrogenation of amine- boranes. *Organometallics*, 30(8):2394–2404, 2011.

[61] Yasuro Kawano, Mikio Uruichi, Mamoru Shimoi, Seitaro Taki, Takayuki Kawaguchi, Taeko Kakizawa, and Hiroshi Ogino. Dehydrocoupling reactions of borane- secondary and- primary amine adducts catalyzed by group-6 carbonyl complexes: formation of aminoboranes and borazines. *Journal of the American Chemical Society*, 131(41):14946–14957, 2009.

[62] Yanfeng Jiang, Olivier Blacque, Thomas Fox, Christian M Frech, and Heinz Berke. Development of rhenium catalysts for amine borane dehydrocoupling and transfer hydrogenation of olefins. *Organometallics*, 28(18):5493–5504, 2009.

[63] James R Vance, AndreÌ SchaÌfer, Alasdair PM Robertson, Kajin Lee, Joshua Turner, George R Whittell, and Ian Manners. Iron-catalyzed dehydrocoupling/dehydrogenation of amine–boranes. *Journal of the American Chemical Society*, 136(8):3048–3064, 2014.

[64] Nathan T Coles, Mary F Mahon, and Ruth L Webster. Phosphine-and amine-borane dehydrocoupling using a three-coordinate iron (ii) β-diketiminate precatalyst. *Organometallics*, 36(11):2262–2268, 2017.

[65] Thomas M Douglas, Adrian B Chaplin, Andrew S Weller, Xinzheng Yang, and Michael B Hall. Monomeric and oligomeric amine- borane σ-complexes of rhodium. intermediates in the catalytic dehydrogenation of amine- boranes. *Journal of the American Chemical Society*, 131(42):15440–15456, 2009.

[66] Marta Rosello-Merino, Joaquin Lopez-Serrano, and Salvador Conejero. Dehydrocoupling reactions of dimethylamine-borane by pt (ii) complexes: a new mechanism involving deprotonation of boronium cations. *Journal of the American Chemical Society*, 135(30):10910–10913, 2013.

[67] Charlotte J Stevens, Romaeo Dallanegra, Adrian B Chaplin, Andrew S Weller, Stuart A Macgregor, Bryan Ward, David McKay, Gilles Alcaraz, and Sylviane Sabo-Etienne. [ir(pcy3)2(h)2(h2bnme2)]+ as a latent source of aminoborane: Probing the role of metal

in the dehydrocoupling of h3bnme2h and retrodimerisation of [h2bnme2] 2. *Chemistry-A European Journal*, 17(10):3011–3020, 2011.

[68] Heather C Johnson, Alasdair PM Robertson, Adrian B Chaplin, Laura J Sewell, Amber L Thompson, Mairi F Haddow, Ian Manners, and Andrew S Weller. Catching the first oligomerization event in the catalytic formation of polyaminoboranes: H3b· nmehbh2· nmeh2 bound to iridium. *Journal of the American Chemical Society*, 133(29):11076–11079, 2011.

[69] Amit Kumar, Heather C Johnson, Thomas N Hooper, Andrew S Weller, Andrés G Algarra, and Stuart A Macgregor. Multiple metal-bound oligomers from ir-catalysed dehydropolymerisation of h 3 b· nh 3 as probed by experiment and computation. *Chemical Science*, 5(6):2546–2553, 2014.

[70] Matthias Vogt, Bas de Bruin, Heinz Berke, Mónica Trincado, and Hansjörg Grützmacher. Amino olefin nickel (i) and nickel (0) complexes as dehydrogenation catalysts for amine boranes. *Chemical Science*, 2(4):723–727, 2011.

[71] Llewellyn H Thomas. The calculation of atomic fields. In *Mathematical Proceedings of the Cambridge Philosophical Society*, volume 23, pages 542–548. Cambridge University Press, 1927.

[72] Enrico Fermi. Un metodo statistico per la determinazione di alcune priorieta dellâatome. *Rend. Accad. Naz. Lincei*, 6(602-607):32, 1927.

[73] Pierre Hohenberg and Walter Kohn. Inhomogeneous electron gas. *Physical review*, 136(3B):B864, 1964.

[74] Walter Kohn and Lu Jeu Sham. Self-consistent equations including exchange and correlation effects. *Physical review*, 140(4A):A1133, 1965.

[75] John C Slater. A simplification of the hartree-fock method. *Physical Review*, 81(3):385, 1951.

[76] Seymour H Vosko, Leslie Wilk, and Marwan Nusair. Accurate spin-dependent electron liquid correlation energies for local spin density calculations: a critical analysis. *Canadian Journal of physics*, 58(8):1200–1211, 1980.

[77] John P Perdew and Alex Zunger. Self-interaction correction to density-functional approximations for many-electron systems. *Physical Review B*, 23(10):5048, 1981.

[78] Thierry Leininger, Hermann Stoll, Hans-Joachim Werner, and Andreas Savin. Combining long-range configuration interaction with short-range density functionals. *Chemical physics letters*, 275(3-4):151–160, 1997.

[79] Iann C Gerber and János G Angyán. Hybrid functional with separated range. *Chemical physics letters*, 415(1-3):100–105, 2005.

[80] Iann C Gerber, János G Ángyán, Martijn Marsman, and Georg Kresse. Range separated hybrid density functional with long-range hartree-fock exchange applied to solids. *The Journal of chemical physics*, 127(5):054101, 2007.

[81] Takeshi Yanai, David P Tew, and Nicholas C Handy. A new hybrid exchange–correlation functional using the coulomb-attenuating method (cam-b3lyp). *Chemical Physics Letters*, 393(1-3):51–57, 2004.

[82] Thomas M Henderson, Artur F Izmaylov, Gustavo E Scuseria, and Andreas Savin. The importance of middle-range hartree-fock-type exchange for hybrid density functionals, 2007.

[83] Thomas M Henderson, Artur F Izmaylov, Gustavo E Scuseria, and Andreas Savin. Assessment of a middle-range hybrid functional. *Journal of chemical theory and computation*, 4(8):1254–1262, 2008.

[84] Hisayoshi Iikura, Takao Tsuneda, Takeshi Yanai, and Kimihiko Hirao. A long-range correction scheme for generalized-gradient-approximation exchange functionals. *The Journal of Chemical Physics*, 115(8):3540–3544, 2001.

[85] John P Perdew, Matthias Ernzerhof, and Kieron Burke. Rationale for mixing exact exchange with density functional approximations. *The Journal of chemical physics*, 105(22):9982–9985, 1996.

[86] Matthias Ernzerhof, John P Perdew, and Kieron Burke. Coupling-constant dependence of atomization energies. *International Journal of Quantum Chemistry*, 64(3):285–295, 1997.

[87] Matthias Ernzerhof and Gustavo E Scuseria. Assessment of the perdew–burke–ernzerhof exchange-correlation functional. *The Journal of chemical physics*, 110(11):5029–5036, 1999.

[88] Carlo Adamo and Vincenzo Barone. Toward reliable density functional methods without adjustable parameters: The pbe0 model. *The Journal of chemical physics*, 110(13):6158–6170, 1999.

[89] John P Perdew, Kieron Burke, and Matthias Ernzerhof. Generalized gradient approximation made simple. *Physical review letters*, 77(18):3865, 1996.

[90] Kieron Burke, JP Perdew, and M Ernzerhof. Generalized gradient approximation made simple [phys. rev. lett. 77, 3865 (1996)]. *Phys. Rev. Lett*, 78:1396, 1997.

[91] Jochen Heyd, Gustavo E Scuseria, and Matthias Ernzerhof. Hybrid functionals based on a screened coulomb potential. *The Journal of chemical physics*, 118(18):8207–8215, 2003.

[92] Aron J Cohen, Paula Mori-Sánchez, and Weitao Yang. Challenges for density functional theory. *Chemical Reviews*, 112(1):289–320, 2011.

[93] Stefan Grimme. Semiempirical gga-type density functional constructed with a long-range dispersion correction. *Journal of computational chemistry*, 27(15):1787–1799, 2006.

[94] Stefan Grimme. Accurate description of van der waals complexes by density functional theory including empirical corrections. *Journal of computational chemistry*, 25(12):1463–1473, 2004.

[95] Stefan Grimme, Stephan Ehrlich, and Lars Goerigk. Effect of the damping function in dispersion corrected density functional theory. *Journal of computational chemistry*, 32(7):1456–1465, 2011.

[96] Amy Austin, George A Petersson, Michael J Frisch, Frank J Dobek, Giovanni Scalmani, and Kyle Throssell. A density functional with spherical atom dispersion terms. *Journal of chemical theory and computation*, 8(12):4989–5007, 2012.

[97] R Eric Stratmann, Gustavo E Scuseria, and Michael J Frisch. Achieving linear scaling in exchange-correlation density functional quadratures. *Chemical physics letters*, 257(3-4):213–223, 1996.

[98] Richard FW Bader. *Atoms in molecules*. Wiley Online Library, 1990.

[99] Chérif F Matta and Russell J Boyd. *An introduction to the quantum theory of atoms in molecules*. Wiley Online Library, 2007.

[100] Philip Coppens. *X-ray charge densities and chemical bonding*, volume 4. International Union of Crystallography, 1997.

[101] Richard FW Bader and Hanno Essén. The characterization of atomic interactions. *The Journal of chemical physics*, 80(5):1943–1960, 1984.

[102] RFW Bader, PJ MacDougall, and CDH Lau. Bonded and nonbonded charge concentrations and their relation to molecular geometry and reactivity. *Journal of the american Chemical Society*, 106(6):1594–1605, 1984.

[103] Axel D Becke and Kenneth E Edgecombe. A simple measure of electron localization in atomic and molecular systems. *The Journal of chemical physics*, 92(9):5397–5403, 1990.

[104] Patricio Fuentealba, E Chamorro, and Juan C Santos. Understanding and using the electron localization function. In *Theoretical and Computational Chemistry*, volume 19, pages 57–85. Elsevier, 2007.

[105] Vladimir Tsirelson and Adam Stash. Determination of the electron localization function from electron density. *Chemical physics letters*, 351(1-2):142–148, 2002.

[106] Bernard Silvi and Andreas Savin. Classification of chemical bonds based on topological analysis of electron localization functions. *Nature*, 371(6499):683, 1994.

[107] C Lepetit, B Silvi, and R Chauvin. Elf analysis of out-of-plane aromaticity and in-plane homoaromaticity in carbo [n] annulenes and [n] pericyclynes. *The Journal of Physical Chemistry A*, 107(4):464–473, 2003.

[108] Franck Fuster and Bernard Silvi. Determination of protonation sites in bases from topological rules. *Chemical Physics*, 252(3):279–287, 2000.

[109] Franck Fuster, Alain Sevin, and Bernard Silvi. Determination of substitutional sites in heterocycles from the topological analysis of the electron localization function (elf). *Journal of Computational Chemistry*, 21(7):509–514, 2000.

[110] Xénophon Krokidis, Stéphane Noury, and Bernard Silvi. Characterization of elementary chemical processes by catastrophe theory. *The Journal of Physical Chemistry A*, 101(39):7277–7282, 1997.

[111] Juan C Santos, Juan Andres, Arie Aizman, Patricio Fuentealba, and Victor Polo. A theoretical study on the reaction mechanism for the bergman cyclization from the perspective of the electron localization function and catastrophe theory. *The Journal of Physical Chemistry A*, 109(16):3687–3693, 2005.

[112] Paul G Mezey. Quantum chemical shape: new density domain relations for the topology of molecular bodies, functional groups, and chemical bonding. *Canadian journal of chemistry*, 72(3):928–935, 1994.

[113] A Savin, B Silvi, and F Colonna. Topological analysis of the electron localization function applied to delocalized bonds. *Canadian journal of chemistry*, 74(6):1088–1096, 1996.

[114] Emilie-Laure Zins, Bernard Silvi, and M Esmaïl Alikhani. Activation of c–h and b–h bonds through agostic bonding: an elf/qtaim insight. *Physical Chemistry Chemical Physics*, 17(14):9258–9281, 2015.

[115] Per-Olov Löwdin. Quantum theory of many-particle systems. i. physical interpretations by means of density matrices, natural spin-orbitals, and convergence problems in the method of configurational interaction. *Physical Review*, 97(6):1474, 1955.

[116] Alan E Reed, Larry A Curtiss, and Frank Weinhold. Intermolecular interactions from a natural bond orbital, donor-acceptor viewpoint. *Chemical Reviews*, 88(6):899–926, 1988.

[117] Eric D Glendening, Clark R Landis, and Frank Weinhold. Natural bond orbital methods. *Wiley interdisciplinary reviews: computational molecular science*, 2(1):1–42, 2012.

[118] Timothy J Clark, Kajin Lee, and Ian Manners. Transition-metal-catalyzed dehydrocoupling: A convenient route to bonds between main-group elements. *Chemistry-A European Journal*, 12(34):8634–8648, 2006.

[119] Zheng Liu, Li Song, Shizhen Zhao, Jiaqi Huang, Lulu Ma, Jiangnan Zhang, Jun Lou, and Pulickel M Ajayan. Direct growth of graphene/hexagonal boron nitride stacked layers. *Nano letters*, 11(5):2032–2037, 2011.

[120] Erin M Leitao, Ian Manners, et al. Catalysis in service of main group chemistry offers a versatile approach to p-block molecules and materials. *Nature chemistry*, 5(10):817, 2013.

[121] Rebecca L Melen. Dehydrocoupling routes to element–element bonds catalysed by main group compounds. *Chemical Society Reviews*, 45(4):775–788, 2016.

[122] George W Crabtree and Mildred S Dresselhaus. The hydrogen fuel alternative. *Mrs Bulletin*, 33(4):421–428, 2008.

[123] Thomas Hügle, Monika Hartl, and Dieter Lentz. The route to a feasible hydrogen-storage material: Mofs versus ammonia borane. *Chemistry-A European Journal*, 17(37):10184–10207, 2011.

[124] Anne Staubitz, Alasdair PM Robertson, Matthew E Sloan, and Ian Manners. Amine- and phosphine- borane adducts: new interest in old molecules. *Chemical reviews*, 110(7):4023–4078, 2010.

[125] Anne Staubitz, Alasdair PM Robertson, and Ian Manners. Ammonia-borane and related compounds as dihydrogen sources. *Chemical reviews*, 110(7):4079–4124, 2010.

[126] Cory A Jaska, Karen Temple, Alan J Lough, and Ian Manners. Rhodium-catalyzed formation of boron–nitrogen bonds: a mild route to cyclic aminoboranes and borazines. *Chemical Communications*, (11):962–963, 2001.

[127] Laura J Sewell, Guy C Lloyd-Jones, and Andrew S Weller. Development of a generic mechanism for the dehydrocoupling of amine-boranes: a stoichiometric, catalytic, and kinetic study of h3b· nme2h using the [rh (pcy3) 2]+ fragment. *Journal of the American Chemical Society*, 134(7):3598–3610, 2012.

[128] Richard A Collins, Adam F Russell, and Philip Mountford. Group 4 metal complexes for homogeneous olefin polymerisation: a short tutorial review. *Applied Petrochemical Research*, 5(3):153–171, 2015.

[129] Andrea Rossin and Maurizio Peruzzini. Ammonia–borane and amine–borane dehydrogenation mediated by complex metal hydrides. *Chemical reviews*, 116(15):8848–8872, 2016.

[130] Maurice Brookhart and Malcolm LH Green. Carbon-hydrogen-transition metal bonds. *Journal of Organometallic Chemistry*, 250(1):395–408, 1983.

[131] Maurice Brookhart, Malcolm LH Green, and Luet-Lok Wong. Carbon-hydrogen-transition metal bonds. *Progress in Inorganic Chemistry, Volume 36*, pages 1–124, 1988.

[132] PLA Popelier and G Logothetis. Characterization of an agostic bond on the basis of the electron density. *Journal of organometallic chemistry*, 555(1):101–111, 1998.

[133] Matthias Lein. Characterization of agostic interactions in theory and computation. *Coordination Chemistry Reviews*, 253(5-6):625–634, 2009.

[134] Wolfgang Scherer and G Sean McGrady. Agostic interactions in d0 metal alkyl complexes. *Angewandte Chemie International Edition*, 43(14):1782–1806, 2004.

[135] David J Wolstenholme, Kyle T Traboulsee, Andreas Decken, and G Sean McGrady. Structure and bonding of titanocene amidoborane complexes: a common bonding motif with their β-agostic organometallic counterparts. *Organometallics*, 29(22):5769–5772, 2010.

[136] Virginia Montiel-Palma, Miguel A Muñoz-Hernández, Tahra Ayed, Jean-Claude Barthelat, Mary Grellier, Laure Vendier, and Sylviane Sabo-Etienne. Agostic si–h bond coordination assists c–h bond activation at ruthenium in bis (phosphinobenzylsilane) complexes. *Chemical Communications*, (38):3963–3965, 2007.

[137] Michel Etienne and Andrew S Weller. Intramolecular c–c agostic complexes: C–c sigma interactions by another name. *Chemical Society Reviews*, 43(1):242–259, 2014.

[138] Wim T Klooster, Lee Brammer, Colin J Schaverien, and Peter HM Budzelaar. C- h bonds are not elongated by coordination to lanthanide metals: Single-crystal neutron diffraction structures of (c5me5) y (oc6h3tbu2) ch (sime3) 2 at 20 k and (c5me5) la {CH (SiMe3) 2} 2 at 15 k. *Journal of the American Chemical Society*, 121(6):1381–1382, 1999.

[139] Maurice Brookhart, Malcolm LH Green, and Gerard Parkin. Agostic interactions in transition metal compounds. *Proceedings of the National Academy of Sciences of the United States of America*, 104(17):6908, 2007.

[140] U Koch and Paul LA Popelier. Characterization of cho hydrogen bonds on the basis of the charge density. *The Journal of Physical Chemistry*, 99(24):9747–9754, 1995.

[141] Matthias Lein, John A Harrison, and Alastair J Nielson. Identification of non-classical c-h...m interactions in early and late transition metal complexes containing the $CH(ArO)_3$ ligand. *Dalton Transactions*, 42(30):10939–10951, 2013.

[142] Vincent Tognetti, Laurent Joubert, Roman Raucoules, Theodorus De Bruin, and Carlo Adamo. Characterizing agosticity using the quantum theory of atoms in molecules: bond critical points and their local properties. *The Journal of Physical Chemistry A*, 116(22):5472–5479, 2012.

[143] Miguel Castro, Julián Cruz, Horacio López-Sandoval, and Norah Barba-Behrens. On the ch...cu agostic interaction: chiral copper (ii) compounds with ephedrine and pseudoephedrine derivatives. *Chemical Communications*, (30):3779–3781, 2005.

[144] Tejender S Thakur and Gautam R Desiraju. Misassigned c–h...cu agostic interaction in a copper (ii) ephedrine derivative is actually a weak, multicentred hydrogen bond. *Chemical Communications*, (5):552–554, 2006.

[145] Christine Lepetit, Jordi Poater, M Esmail Alikhani, Bernard Silvi, Yves Canac, Julia Contreras-García, Miquel SolaÌ, and Remi Chauvin. The missing entry in the agostic–anagostic series: Rh (i)–η1-c interactions in p (ch) p pincer complexes. *Inorganic chemistry*, 54(6):2960–2969, 2015.

[146] Taryn D Forster, Heikki M Tuononen, Masood Parvez, and Roland Roesler. Characterization of β-b-agostic isomers in zirconocene amidoborane complexes. *Journal of the American Chemical Society*, 131(19):6689–6691, 2009.

[147] U Flierler and D Stalke. More than just distances from electron density studies. In *Electron Density and Chemical Bonding I*, pages 1–20. Springer, 2012.

[148] Marvin Douglas and Norman M Kroll. Quantum electrodynamical corrections to the fine structure of helium. *Annals of Physics*, 82(1):89–155, 1974.

[149] Bernd A Hess. Applicability of the no-pair equation with free-particle projection operators to atomic and molecular structure calculations. *Physical Review A*, 32(2):756, 1985.

[150] Georg Jansen and Bernd A Heß. Revision of the douglas-kroll transformation. *Physical Review A*, 39(11):6016, 1989.

[151] Cory A Jaska and Ian Manners. Heterogeneous or homogeneous catalysis? mechanistic studies of the rhodium-catalyzed dehydrocoupling of amine-borane and phosphine-borane adducts. *Journal of the American Chemical Society*, 126(31):9776–9785, 2004.

[152] Thomas M Douglas, Adrian B Chaplin, and Andrew S Weller. Amine-borane σ-complexes of rhodium. relevance to the catalytic dehydrogenation of amine-boranes. *Journal of the American Chemical Society*, 130(44):14432–14433, 2008.

[153] Romaeo Dallanegra, Adrian B Chaplin, and Andrew S Weller. Bis (σ-amine–borane) complexes: An unusual binding mode at a transition-metal center. *Angewandte Chemie International Edition*, 48(37):6875–6878, 2009.

[154] Edward S Bretschneider and Christopher W Allen. Reactions of the cis-1, 2-dicyanoethylenedithiolate ion with disubtituted group iv organometallic compounds. *Inorganic Chemistry*, 12(3):623–627, 1973.

[155] Fu-Chen Liu, Christine E Plečnik, Shengming Liu, Jianping Liu, Edward A Meyers, and Sheldon G Shore. Cyclic organohydroborate complexes of metallocenes: Part vi. syntheses and structures of cp2m {(μ-H) 2BR2}(m= ti, nb; r2= c4h8, c5h10, c8h14). *Journal of Organometallic Chemistry*, 627(1):109–120, 2001.

[156] Preston A Chase, Warren E Piers, and Masood Parvez. Reactions of bis (pentafluorophenyl) borane with titanocene dialkyls: Synthesis and structure of cp2ti [η2-h2b (c6f5) 2]. *Organometallics*, 19(10):2040–2042, 2000.

[157] James M Morse Jr, Gregory H Parker, and Theodore J Burkey. Enthalpy of carbonyl dissociation from metal hexacarbonyls m (co) 6 (m= chromium, molybdenum, tungsten) in alkane solvent: determination of intermolecular agostic bond strengths. *Organometallics*, 8(10):2471–2474, 1989.

[158] Tom Ziegler and Jochen Autschbach. Theoretical methods of potential use for studies of inorganic reaction mechanisms. *Chemical reviews*, 105(6):2695–2722, 2005.

[159] Christopher J Cramer and Donald G Truhlar. Density functional theory for transition metals and transition metal chemistry. *Physical Chemistry Chemical Physics*, 11(46):10757–10816, 2009.

[160] Lutz Ackermann. Carboxylate-assisted transition-metal-catalyzed c-h bond functionalizations: mechanism and scope. *Chemical reviews*, 111(3):1315–1345, 2011.

[161] Yuanyuan Sun and Hui Chen. Performance of density functionals for activation energies of zr-mediated reactions. *Journal of chemical theory and computation*, 9(11):4735–4743, 2013.

[162] Yihua Sun and Hui Chen. Dft methods to study the reaction mechanism of iridium-catalyzed hydrogenation of olefins: Which functional should be chosen? *ChemPhysChem*, 17(1):119–127, 2016.

[163] David J Liptrot and Philip P Power. London dispersion forces in sterically crowded inorganic and organometallic molecules. *Nature Reviews Chemistry*, 1(1):0004, 2017.

[164] Stefan Grimme and Marc Steinmetz. Effects of london dispersion correction in density functional theory on the structures of organic molecules in the gas phase. *Physical Chemistry Chemical Physics*, 15(38):16031–16042, 2013.

[165] Axel D Becke. Density-functional exchange-energy approximation with correct asymptotic behavior. *Physical review A*, 38(6):3098, 1988.

[166] Chengteh Lee, Weitao Yang, and Robert G Parr. Development of the colle-salvetti correlation-energy formula into a functional of the electron density. *Physical review B*, 37(2):785, 1988.

[167] Oleg A Vydrov and Gustavo E Scuseria. Assessment of a long-range corrected hybrid functional. *The Journal of chemical physics*, 125(23):234109, 2006.

[168] Oleg A Vydrov, Gustavo E Scuseria, and John P Perdew. Tests of functionals for systems with fractional electron number. *The Journal of chemical physics*, 126(15):154109, 2007.

[169] Jeng-Da Chai and Martin Head-Gordon. Long-range corrected hybrid density functionals with damped atom–atom dispersion corrections. *Physical Chemistry Chemical Physics*, 10(44):6615–6620, 2008.

[170] Jeng-Da Chai and Martin Head-Gordon. Systematic optimization of long-range corrected hybrid density functionals. *The Journal of chemical physics*, 128(8):084106, 2008.

[171] George D Purvis III and Rodney J Bartlett. A full coupled-cluster singles and doubles model: The inclusion of disconnected triples. *The Journal of Chemical Physics*, 76(4):1910–1918, 1982.

[172] John A Pople, Martin Head-Gordon, and Krishnan Raghavachari. Quadratic configuration interaction. a general technique for determining electron correlation energies. *The Journal of chemical physics*, 87(10):5968–5975, 1987.

[173] RFW Bader and TT Nguyen-Dang. Quantum theory of atoms in molecules–dalton revisited. In *Advances in Quantum Chemistry*, volume 14, pages 63–124. Elsevier, 1981.

[174] Richard FW Bader. The quantum mechanical basis of conceptual chemistry. *Monatshefte für Chemie/Chemical Monthly*, 136(6):819–854, 2005.

[175] Bernard Silvi. The synaptic order: a key concept to understand multicenter bonding. *Journal of molecular structure*, 614(1-3):3–10, 2002.

[176] Frank Weinhold and Clark R Landis. Natural bond orbitals and extensions of localized bonding concepts. *Chemistry Education Research and Practice*, 2(2):91–104, 2001.

[177] M. J. Frisch, G. W. Trucks, H. B. Schlegel, G. E. Scuseria, M. A. Robb, J. R. Cheeseman, G. Scalmani, V. Barone, B. Mennucci, G. A. Petersson, H. Nakatsuji, M. Caricato, X. Li, H. P. Hratchian, A. F. Izmaylov, J. Bloino, G. Zheng, J. L. Sonnenberg, M. Hada, M. Ehara, K. Toyota, R. Fukuda, J. Hasegawa, M. Ishida, T. Nakajima, Y. Honda, O. Kitao, H. Nakai, T. Vreven, J. A. Montgomery, Jr., J. E. Peralta, F. Ogliaro, M. Bearpark, J. J. Heyd, E. Brothers, K. N. Kudin, V. N. Staroverov, R. Kobayashi, J. Normand, K. Raghavachari, A. Rendell, J. C. Burant, S. S. Iyengar, J. Tomasi, M. Cossi, N. Rega, J. M. Millam, M. Klene, J. E. Knox, J. B. Cross, V. Bakken, C. Adamo, J. Jaramillo, R. Gomperts, R. E. Stratmann, O. Yazyev, A. J. Austin, R. Cammi, C. Pomelli, J. W. Ochterski, R. L. Martin, K. Morokuma, V. G. Zakrzewski, G. A. Voth, P. Salvador, J. J. Dannenberg, S. Dapprich, A. D. Daniels, Ã. Farkas, J. B. Foresman, J. V. Ortiz, J. Cioslowski, and D. J. Fox. Gaussian 09 Revision D.01. Gaussian Inc. Wallingford CT 2009.

[178] Giovanni Scalmani and Michael J Frisch. Continuous surface charge polarizable continuum models of solvation. i. general formalism. *The Journal of chemical physics*, 132(11):114110, 2010.

[179] FE Jorge, A Canal Neto, GG Camiletti, and SF Machado. Contracted gaussian basis sets for douglas–kroll–hess calculations: estimating scalar relativistic effects of some atomic and molecular properties. *The Journal of chemical physics*, 130(6):064108, 2009.

[180] CT Campos and FE Jorge. Triple zeta quality basis sets for atoms rb through xe: application in ccsd (t) atomic and molecular property calculations. *Molecular Physics*, 111(2):167–173, 2013.

[181] A Canal Neto and FE Jorge. All-electron double zeta basis sets for the most fifth-row atoms: Application in dft spectroscopic constant calculations. *Chemical Physics Letters*, 582:158–162, 2013.

[182] ED Glendening, JK Badenhoop, AE Reed, JE Carpenter, JA Bohmann, CM Morales, CR Landis, and F Weinhold. Natural bond orbital analysis program: Nbo 6.0. *Theoretical Chemistry Institute, University of Wisconsin, Madison, WI*, 2013.

[183] Rory Waterman. Mechanisms of metal-catalyzed dehydrocoupling reactions. *Chemical Society Reviews*, 42(13):5629–5641, 2013.

[184] David J Wolstenholme, Kyle T Traboulsee, Ye Hua, Larry A Calhoun, and G Sean McGrady. Thermal desorption of hydrogen from ammonia borane: unexpected role of homopolar b–h...h–b interactions. *Chemical Communications*, 48(20):2597–2599, 2012.

[185] Damir A Safin, Maria G Babashkina, Koen Robeyns, Mariusz P Mitoraj, Piotr Kubisiak, and Yann Garcia. Influence of the homopolar dihydrogen bonding c-h...h-c on coordination geometry: Experimental and theoretical studies. *Chemistry-A European Journal*, 21(46):16679–16687, 2015.

[186] David J Wolstenholme, Jessica L Dobson, and G Sean McGrady. Homopolar dihydrogen bonding in main group hydrides: discovery, consequences, and applications. *Dalton Transactions*, 44(21):9718–9731, 2015.

[187] Lina M Epstein and Elena S Shubina. New types of hydrogen bonding in organometallic chemistry. *Coordination chemistry reviews*, 231(1-2):165–181, 2002.

[188] Natalia V Belkova, Elena S Shubina, and Lina M Epstein. Diverse world of unconventional hydrogen bonds. *Accounts of chemical research*, 38(8):624–631, 2005.

[189] Heiko Jacobsen. Hydrogen and dihydrogen bonding of transition metal hydrides. *Chemical Physics*, 345(1):95–102, 2008.

[190] Gregory C Welch, Ronan R San Juan, Jason D Masuda, and Douglas W Stephan. Reversible, metal-free hydrogen activation. *Science*, 314(5802):1124–1126, 2006.

[191] Zhi-Xiang Wang, Lili Zhao, Gang Lu, Haixia Li, and Fang Huang. Computational design of metal-free molecules for activation of small molecules, hydrogenation, and hydroamination. In *Frustrated Lewis Pairs I*, pages 231–266. Springer, 2012.

[192] Douglas W Stephan and Gerhard Erker. Frustrated lewis pair chemistry: development and perspectives. *Angewandte Chemie International Edition*, 54(22):6400–6441, 2015.

List of Figures

1.1 Average annual temperature difference trend through time with the average temperature during 1961-1990 period as baseline. [1] 13
1.2 Summary of hydrogen production, storage and applications. 21

2.1 Low temperature crystal structure of solid state ammonia borane. [32] The yellow, blue and white balls represent the B, N and H atoms, respectively. The dihydrogen bonds are delineated by dashed lines. 24
2.2 Metal-catalyzed dehydrogenation of ammonia borane. [47] 27
2.3 Summary of catalyzed dehydrogenation/dehydrocoupling pathways from primary amine-borane. [48] 27
2.4 Possible catalyzed dehydrogenation/dehydrocoupling pathways of secondary amine-boranes. 28
2.5 Proposed mechanism for the dehydrogenation of $HMe_2N{\cdot}BH_3$ catalyzed by Zr-Ru heterobimetallic complex. [60] 30
2.6 Proposed mechanism of dehydrogenation of amine-boranes by $(N_3N)ZrNMe_2$ complex. [57] 31
2.7 Calculated mechanistic proposal for dehydrogenation of $HMe_2N{\cdot}BH_3$ by $[Cr(CO)_6]$ precatalyst. [61] 32
2.8 Proposed mechanism for the dehydrogenation of $HMe_2N{\cdot}BH_3$ catalyzed by $[Re(Br)(H)(NO)(PCy_3)_2]$. [62] 33
2.9 Proposed two-step mechanistic cycle of the dehydrogenation of $HMe_2N{\cdot}BH_3$ catalyzed by $CpFe(CO)_2I$ under photo-irradiation. [63] 34

3.1 Illustration of SCF. 40

4.1 2D isosurface of electron density of C_2H_4. 51
4.2 Laplacian of electron density isosurface of C_2H_4. Blue solid lines: $\nabla^2\rho < 0$ (Charge concentration region); red solid line: $\nabla^2\rho > 0$ (Charge depletion region). 53
4.3 Laplacian of electron density isosurface of $Al{-}C_2H_4$ system. Blue solid lines: $\nabla^2\rho < 0$ (Charge concentration region); red solid line: $\nabla^2\rho > 0$ (Charge depletion region). 53
4.4 Localization domains of benzene molecule for different ELF isosurface values. The B3LYP/6-31G** level of theory was used for this example. 57

4.5 Bifurcation diagram corresponding to the ELF analysis of benzene molecule optimized with B3LYP/6-31G** level of theory. 57
4.6 QTAIM and ELF basin analysis for CH_3CN molecule. For clarity, only two QTAIM atomic surfaces (H and N) are shown. [114] 58
4.7 Overview of the basis sets between atomic orbitals and molecular orbitals. 59
4.8 Two-electron stabilizing interaction between an occupied donor orbital $\Phi_i^{(0)}$ and an empty acceptor orbital $\Phi_{j^*}^{(0)}$. 60

5.1 Two-cycle model of catalytic dehydrocoupling of DMAB proposed by Manners *et al.* 67
5.2 The intramolecular (Path I) and intermolecular (Path II) catalytic dehydrocoupling of DMAB by [Cp_2Ti] proposed by Luo and Ohno with their calculated relative free energies (in kJ/mol) that takes into account the solvation effect is shown. The calculated off-metal 2+2 dimerization of aminoborane $Me_2N{=}BH_2$ to form the cyclic diborazane $[Me_2N{\cdot}BH_2]_2$ is also given. 69
5.3 The titanocene-catalyzed dehydrocoupling of linear diborazane calculated by Tao and Qi in 2013 with their calculated relative free energies (in kJ/mol) including solvation effect. The B3LYP functional associated with the 6-31G(d) basis set for Cp groups, the 6-311++G(d,p) basis set for all the DMAB atoms and a modified LanL2DZ relativistic pseudo-potential for Ti atom was used. 70

6.1 Illustration of C-H agostic interaction and different types of C-H agostic interactions. For clarity purposes, all the agostic interactions and other non-covalent interactions will be marked as dotted lines in the following sections. (For example M···H-X for an agostic interaction) 74
6.2 X-ray crystallography study [143] as well as QTAIM and ELF topological characterization of the C-H···M interaction in the Cu(II) compound. 77
6.3 The paramagnetic $Cp_2TiNH_2BH_3$ complex which was characterized by X-ray diffraction and the diamagnetic $Cp_2Ti(H)NH_2BH_3$. 78
6.4 Deviations between calculated and experimental geometric features for the $Cp_2TiNH_2BH_3$ complex. 81
6.5 Total deviations between calculated geometric values (with B3LYP functional in combination with different basis sets) and experimental values for the $Cp_2TiNH_2BH_3$ complex. 88
6.6 Z-matrix representation for the partial optimization of the $Cp_2TiNH_2BH_3$ complex. 88
6.7 Group IV metallocene compounds involving a 3C/2e intramolecular M-H-B interaction that were considered for the present study. 91
6.8 Variation of ρ[BCP(M-Ha)] as a function of M-Ha distances involved in $Cp_2MXR_2BH_3$ and $Cp_2M(H)XR_2BH_3$ complexes. 92
6.9 Simplified pathway for dehydrogenation of amine-borane adducts. 93
6.10 σ complex that contains a cationic metallocene and an anionic hydroborate ligand. 93

6.11 Representation of the experimental B-H($\cdots$M) and M-H(B) distances in the {metallocene + hydroborate} complexes. 95
6.12 Combinations of cationic metallocenes and anionic hydroborates selected for the present study of the M-H-B interactions involved in $Cp_2M{-}H_2BR_2$ complexes. . 96
6.13 B-H distances as a function of M-H distances involved in the titanocene complexes. 97
6.14 Evolution calculated B-H distance as function of M-H distance. 98
6.15 2D representation of Laplacian of electron density of $Cp_2Ti{-}H_2BH_2$ complex. . . 98
6.16 Effects of the substituent groups carried by boron atom on the strength of B-H bonds in isolated hydroborate and in the hydroborates interacting with titanocene cation. 99
6.17 Quantification of the strength of the M-H interaction for differently substituted hydroborates interacting with titanocene. 100
6.18 Influence of the metal center on the strength of the M-H interaction. 101
6.19 Graphical representation of contribution of metal center (M=Ti) to the basin ($100\times\frac{C(M)}{V(H)}$) as function of geometric properties ($\frac{d(B-H)}{d(M-H)}$). 103
6.20 Graphical representation of contribution of metal center (M=Ti, Zr, V and Nb) to the protonated basin ($100\times\frac{C(M)}{V(H)}$) as a function of geometric properties ($\frac{d(B-H)}{d(M-H)}$). 104
6.21 Some important geometrical parameters of optimized $Cp_2Ti{-}H_2BH_2$ complex (a) and its modified structure (b). The relative energy of (b) compared to (a) is also given. 105

7.1 DMAB dehydrocoupling mechanism from both experimental (Exp.) and theoretical (DFT) points of view. 109
7.2 Effect of the dispersion correction on the energy profile associated with the intramolecular and intermolecular pathways: comparison of relative electronic energies (in kJ/mol) without or with GD3BJ corrections 112
7.3 Contributions of the GD3BJ dispersion correction energy to relative electronic energy (in kJ/mol) of each intermediate involved in both the Path I and Path II proposed by Luo and Ohno. 114
7.4 Energy profile for the intramolecular dehydrogenation mechanism of DMAB: Path I. Relative gas-phase zero-point corrected energies (E+ZPE) are given in kJ/mol. 118
7.5 Energy profiles for the titanocene-catalyzed dehydrogenation/dehydrocoupling of DMAB. Relative gas-phase zero-point corrected energies (in kJ/mol) are shown. . 120
7.6 Transition state for a 2+1 dehydrocoupling process proposed by Waterman to complement the Manners' mechanistic model. 120
7.7 Bond critical points and Bader's charge analyses in the ${S^I}_{3B}$ and ${S^I}_{4B}$ intermediate. 123
7.8 First catalytic cycle from $[Cp_2Ti{-}\eta^1\text{-}H_3B{\cdot}NMe_2H]$ complex to linear diborazane *via* a van der Waals complex. Relative energies calculated in the gas-phase including zero-point energy (ZPE) correction in kJ/mol are mentioned. 124
7.9 Two-body complex $Cp_2Ti{-}\eta^2$-DMAB involving the η^2 Ti$\cdots$H$-$B interactions between Cp_2Ti and DMAB molecule. 125

7.10 Energy profiles for the titanocene-catalyzed dehydrocoupling of two DMAB molecules: a three-body intermolecular pathway. Relative gas-phase zero-point corrected energies (in kJ/mol) are shown. 126
7.11 Geometric features of 3C/2e interactions in ${S^{II}}_1$. 127
7.12 Natural Bond Orbital analysis for the intermolecular interactions involved in $Cp_2Ti-\eta^2$-DMAB complex and ${S^{II}}_1$ intermediate. The label BD, LV, LP and BD* represent bonding, lone vacancy, lone pair and antibonding, respectively. . . 129
7.13 Energy profiles for the titanocene-catalyzed dehydrocoupling of linear diborazane: Path III. Relative gas-phase zero-point corrected energies (in kJ/mol) are shown. 130
7.14 Summary of the titanocene-catalyzed dehydrogenation/dehydrocoupling reaction pathways of dimethylamine borane (DMAB). 134
7.15 Schematic presentation of different reactivity of titanocene-catalyzed dehydrogenation reaction of ammonia borane, primary amine-borane and secondary amine-boranes. 137
7.16 Comparison of structures between key stationary points from dehydrocoupling mechanism of $H^iPr_2N{\cdot}BH_3$ and $HMe_2N{\cdot}BH_3$ respectively. 138
7.17 Relative Gibbs free energy of four structures along the Path I (see Figure 7.5)for both DMAB (squares, dotted lines) and DiPrAB (circles, full lines) compounds. . 138
7.18 Titanocene-catalyzed dehydrogenation reaction of $H^iPr_2N{\cdot}BH_3$. Relative gas-phase electronic energies with zero point energy (ZPE) correction are given in kJ/mol. 139
7.19 Hydrogen cycle. 143

List of Tables

1.1 Comparison of different hydrocarbon reforming methods. 15
1.2 Characters of different water electrolysis methods. [8] 16
1.3 Summary of hydrogen production technologies [4] 17
1.4 Technical system targets for on-board hydrogen storage for Light-Duty Fuel Cell Vehicles (Update May 2017) (wt.%=kg H_2/kg system, gge: gallon gasoline equivalent) [17] 18
1.5 Examples of different type of metal hydrides for hydrogen storage with their theoretical weight percentage of hydrogen wt.%, reversibility, binding energies (ΔH in kJ/(mol H_2)). 19

2.1 Examples of early transition metal catalysts for amine-boranes dehydrogenation reactions. 29
2.2 Examples of mid-transition metal catalysts for amine-boranes dehydrogenation reactions. 31
2.3 Examples of late transition metal catalysts for amine-boranes dehydrogenation reactions. 33

4.1 Descriptions of different types of critical point 50

5.1 Phenomenological k_H/k_D value of the catalytic dehydrocoupling reactions of different deuterated DMAB. Reaction time for 100% conversion for each reactant are also given. 66
5.2 Summary of experimental and theoretical results and conclusions of the titanocene-catalyzed dehydrogenation of DMAB reaction. 71

6.1 Different geometric features to distinguish the M-H-C agostic and anagostic interactions. 75
6.2 QTAIM features of hydrogen bonds and agostic interactions proposed by Popelier *et al.* [132, 140, 141] All the values presented here are in atomic unit. (a.u.) 76
6.3 Selected exchange-correlation functionals for the calibration study of the agostic systems. 79
6.4 Influence of the functionals on the geometric description of the $Cp_2TiNH_2BH_3$ complex 80

6.5 Influence of the GD3BJ dispersion correction on the geometric description of the $Cp_2TiNH_2BH_3$ complex: relative deviation δ_{X-Y}^{GD3BJ} and $\delta_{X-\widehat{Y}-Z}^{GD3BJ}$ are given in %. . 82
6.6 Influence of the functionals on the ELF topological description of the protonated basin involved in the agostic interaction of the $Cp_2TiNH_2BH_3$ complex. 83
6.7 Effect of functionals on the QTAIM topological description of the agostic interaction and other important interactions involved in the $Cp_2TiNH_2BH_3$ complex. All the values are given in atomic units. 84
6.8 Effect of the basis set on the geometric description of the $Cp_2TiNH_2BH_3$ complex. The distances are given in Å. 87
6.9 Effect of different combinations of basis set on the ELF topological description of the protonated basin involved in the Ti-H-B interaction in $Cp_2TiNH_2BH_3$ compound. All the calculations were carried out with the B3LYP functional and all the values are given in e. 89
6.10 Characteristic distances involved in the M-H-B iterations in the Cp_2M-hydroborate complexes identified with diffraction techniques (Exp). Calculations (Calc) were carried out by geometry optimization at B3LYP/6-311++G(2d,2p)+LanL2DZ level of theory. All the distances are given in Å. 94
6.11 Calculated B-H distances in the isolated hydroborate ligands as well as the B-H and M-H distances involved in the $Cp_2Ti-H_2BR_2$ complexes. 97
6.12 ELF features of Ti-H-B interactions involved in $Cp_2Ti-H_2BR_2$ including the population of protonated basin V(H), the atomic contribution of each atom to this basin, all of them are given in e. The contributions of metal center to the protonated basin $100\times\frac{C(M)}{V(H)}$ are also given. 102
6.13 Energies of highest occupied molecular orbital (HOMO) of each isolated hydroborate ligand. 106
6.14 Geometric and topological descriptors to estimate the strength of the 3C/2e interactions. 107

7.1 Selected inter-atomic distances and their relative deviations involved in S_1 intermediate. 111
7.2 E_{GD3BJ}^{corr} values (in kJ/mol) for each intermediate and transition state involved in Path I and Path II 113
7.3 Gas-phase relative electronic energies and free energies (in kJ/mol) are given. (a) Basis set: 6-31G*/6-31++G**/LanL2DZ. (b) ΔG for all the single-point calculations are obtained by the addition of the reference value (that is the value with B3LYP-GD3BJ method) to their corresponding relative electronic energies. . . . 115
7.4 Main inter-atomic distances (in Å) of calculated intermediates and transition state of Path I 119
7.5 Relative electronic energies with zero point energy (ZPE) correction and Gibbs free energies (in kJ/mol) both in gas phase and in toluene solution with PCM model for Path I. 119

7.7 Topological characterization of the dehydrocoupling of DMAB via the van der Waals complex: the ELF protonated basins interacting with the titanium atom and the atomic contribution of each atom are presented. 121

7.6 QTAIM features of the stationary points of the titanocene-catalyzed dehydrocoupling pathway of DMAB *via* the van der Waals complex. The electron density ρ at BCP, the Laplacian of electron density $\nabla^2\rho$ and the ellipticity ϵ are presented for each BCP in this table are all in a.u.. The gray, pink, blue and white balls represent the Ti, B, N and H atoms respectively. (a): Values at BCPs from top to bottom in the $S^{I}{}_{3B}$ intermediate are written from left to right. 122

7.8 Relative electronic energies with zero point energy (ZPE) correction and Gibbs free energies both in gas phase and in toluene solution with PCM model for Path II.125

7.9 ELF characters of the intermolecular interactions involved in $Cp_2Ti{-}\eta^2$-DMAB complex and $S^{II}{}_1$ intermediate. 127

7.10 QTAIM features of the stationary points of the titanocene-catalyzed intermolecular dehydrocoupling pathway of two DMABs . The electron density ρ at BCP, the Laplacian of electron density $\nabla^2\rho$ and the ellipticity ϵ are presented for each BCP in this table and are all in a.u.. The grey, pink, blue and white balls represent the Ti, B, N and H atoms respectively. 128

7.11 Relative electronic energies with zero point energy (ZPE) correction and Gibbs free energies both in gas phase and in toluene solution with PCM model for Path III. 130

7.12 QTAIM features of the stationary points of the titanocene-catalyzed dehydrocoupling pathway of linear diborazane. The electron density ρ at BCP, the Laplacian of electron density $\nabla^2\rho$ and the ellipticity ϵ are presented for each BCP in this table and are all in a.u.. The grey, pink, blue and white balls represent the Ti, B, N and H atoms respectively. 132

7.13 Relative solvation free activation barriers of the rate-determining step of each process and their estimated reaction rate constant. 133

7.14 Main products of the titanocene-catalyzed dehydrogenation/dehydrocoupling reactions of different amine-borane adducts. 135

7.15 Comparison of the calculated intermolecular distances Ti$\cdots$H(N) and dihedral angles H-N-B-H of intermediates S_1 and transition states TS_{1_2} respectively for ammonia borane, primary amine-borane and secondary amine-boranes. 136

Scientific production

Published articles

1. Zhu, J., Zins, E. L., & Alikhani, M. E. (2018). Dehydrocoupling of dimethylamine borane by titanocene: Elucidation of ten years of inconsistency between theoretical and experimental descriptions. Physical Chemistry Chemical Physics.
2. Zhu, J., Zins, E. L., & Alikhani, M. E. (2017). Toward a quantitative evaluation of the strength of $\mathrm{Cp_2M}\cdots\eta^2$–borate interactions. Theoretical Chemistry Accounts, 136(12), 133.
3. Zhu, J., Zins, E. L., & Alikhani, M. E. (2016). Characterization of B-H agostic compounds involved in the dehydrogenation of amine-boranes by group 4 metallocenes. Journal of molecular modeling, 22(12), 294.

Communications

Oral presentations

1. Jingwen Zhu, Emilie-Laure Zins and Mohammad Esmaïl Alikhani; **Caractérisation d'interactions 3-centres/2-électrons pour le stockage de l'hydrogène.** *43rd CHITEL (Congress of Theoretical Chemists of Latin Expression)*, 2017, Paris, France.
2. Jingwen Zhu, Emilie-Laure Zins and Mohammad Esmaïl Alikhani; **Activation and dehydrogenation of Amine Borane catalyzed by group 4 metallocene: On the topological point of view.** *ESCB1 (First European Symposium on Chemical Bonding)*, 2016, Rouen, France.

Posters

1. Jingwen Zhu, Emilie-Laure Zins and Mohammad Esmaïl Alikhani; **Investigation of Catalytic Dehydrocoupling of Dimethylamine-borane by Titanocene: A DFT and Topologic Study.** *11th WATOC (Triennial Congress of the World Association of Theoretical and Computational Chemists)*, 2017, Munich, Germany.
2. Jingwen Zhu, Emilie-Laure Zins and Mohammad Esmaïl Alikhani; Activation of B-H bond of Amine-Borane catalyzed by group 4 metallocene: On the topological point of view. *15th RCTF2016 (Rencontre de Chimistes Théoriciens Francophones 2016)*, Lyon, France.

Etude des interactions B-H agostiques et conséquences pour le stockage de l'hydrogène

Résumé : Dans le cadre de la recherche de vecteurs d'énergie "propres", le borazane et ses dérivés amine-boranes sont devenus des candidats intéressants en tant que matériaux de stockage de l'hydrogène en raison de leur pourcentage massique relativement élevé en hydrogène (19,6% pour borazane) et de la réversibilité potentielle de la réaction de déshydrogénation. Pour des applications réelles, le contrôle des réactions se produisant à la température ambiante est fondamental. Dans ce contexte, la compréhension du processus de la déshydrogénation/déshydrocouplage catalytique de l'amine-borane apparaît comme un élément important. Dans cette thèse, les catalyseurs de types métallocènes du Groupe IV (Cp_2M, M = Ti, Zr et Hf) sont étudiés en détail. Le déshydrocouplage de $HMe_2N{\cdot}BH_3$ catalysé par le titanocène a été étudié à la fois expérimentalement et théoriquement mais aucun accord n'avait été atteint auparavant. Dans ce travail, les caractérisations systématiques des interactions 3-centre 2-électron $M{\cdots}H\text{-}B$ impliquées dans les intermédiaires réactionnels ont été réalisées avec des approches topologiques QTAIM et ELF. Par la suite, des mécanismes réactionnels détaillés ont été étudiés. Les résultats théoriques ont démontré que la méthode DFT corrigée avec la dispersion (DFT-D) étaient nécessaires et suffisantes pour une description énergétique correcte des chemins réactionnel. Mon travail a également permis l'identification d'un complexe de van der Waals jouant un rôle clé dans le mécanisme réactionnel en accord avec les observations expérimentales.

Mots clés : Stockage de l'hydrogène, interactions 3-centre 2-électron, échelle moléculaire, réactions catalytiques, DFT-D, QTAIM, ELF

Study of B-H agostic interactions and consequences for hydrogen storage

Abstract: With the increasing demand of clean energy carriers, ammonia borane and its related amine-borane compounds have emerged as attractive candidates for hydrogen storage materials due to their relatively high weight percentage of available hydrogen (19.6% for ammonia borane) as well as the potential reversibility for the hydrogen release reactions. Actual applications would benefit from controlled reactions occurring close to room-temperature. In this context, catalytic dehydrogenation/dehydrocoupling of amine-borane appears as a promising solution. In this thesis the Group IV metallocene (Cp_2M, M = Ti, Zr and Hf) are mainly discussed. The dehydrocoupling of $HMe_2N{\cdot}BH_3$ catalyzed by titanocene was investigated both experimentally and theoretically but no agreement were reached. In this work, systematic characterizations of $M{\cdots}H\text{-}B$ 3-center 2-electron interactions involved in reaction intermediates were carried out with QTAIM and ELF topological approaches. Afterwards, detailed mechanisms were further studied. Computational results have demonstrated that the dispersion corrected DFT (DFT-D) method was indispensable for a correct energetic prediction for reaction pathways. The identification of a van der Waals complex also plays a central role for a reaction mechanism with good agreement with experimental observations.

Keywords: Hydrogen storage, 3-center 2-electron interactions, molecular scale, catalytic reactions, DFT-D, QTAIM, ELF